APPLIED COMPUTATIONAL ELECTROMAGNETICS SOCIETY JOURNAL

February 2024
Vol. 39 No. 2
ISSN 1054-4887

The ACES Journal is abstracted in INSPEC, in Engineering Index, DTIC, Science Citation Index Expanded, the Research Alert, and to Current Contents/Engineering, Computing & Technology.

The illustrations on the front cover have been obtained from the ARC research group at the Department of Electrical Engineering, Colorado School of Mines

Published, sold and distributed by: River Publishers, Alsbjergvej 10, 9260 Gistrup, Denmark

FEBRUARY 2024 REVIEWERS

Serkan Aksoy
Gaowei Cai
James B. Cole
Vinh Dang
Ravi Kumar Goyal
Serkan Günel
Lida Kouhalvandi
Anubhav Kumar
Layla
Yunlong Mao
Edis Mekic
Michel M. Ney
Andrew Peterson
Javier Rivero
Zhonggen Wang
Marian Wnuk
Yanlin Xu
Tao Yuan
Xingqiu Yuan
BoWen Zhang
Wei-Hua Zong
Yanchun Zuo

THE APPLIED COMPUTATIONAL ELECTROMAGNETICS SOCIETY JOURNAL

Vol. 39 No. 2 February 2024

TABLE OF CONTENTS

Compressed Fast Multipole Representations for Homogeneous 3-D Kernels

R. J. Adams[1], J. C. Young[1], and S. D. Gedney[2]

[1]Electrical & Computer Engineering
University of Kentucky, Lexington, KY, USA
rjadams@uky.edu, john.c.young@uky.edu

[2]Electrical Engineering
University of Colorado Denver, Denver, CO, USA
stephen.gedney@ucdenver.edu

***Abstract* –** For homogeneous kernels, the memory requirements associated with H^2 representations of integral equation matrices can be reduced by incorporating translational invariance. Starting with a non-translationally invariant H^2 representation, this can be accomplished using a left/right iterative algorithm. In this paper, it is shown that a similar algorithm can also be used to compress an existing fast multipole method (FMM). It is observed that the iterative compression converges faster when used to compress an FMM than when it is applied to an H^2 representation. Resulting savings in floating-point operations are indicated, and extensions of the reported method are discussed.

***Index Terms* –** fast multipole method, integral equation.

I. INTRODUCTION

Integral equation (IE) based formulations provide an effective method for formulating 3D electromagnetic interaction problems over a range of frequencies. When modeling fields on large and/or complex domains, it is necessary to use compressed representations of the generally dense system matrix that results from the use of an IE formulation. For static and low-frequency electromagnetic applications, fast multipole methods (FMM) [1, 2] and the H^2 representations [3] provide controllably accurate representations of IE system matrices and have $O(N)$ complexity, where N indicates the number of unknowns in the discretized IE formulation.

Although similar in many ways, the FMM and H^2 representations of integral equation matrices differ in how they represent interactions between source and field groups. In an FMM, all interactions are represented using a common (e.g., multipole) basis. For translationally invariant kernels, this enables significant time and memory savings when building the FMM since only a relatively small number of unique translators are needed at each level of an octree decomposition (at most 316 for a homogeneous kernel).

In contrast, the H^2 representation is often developed from sparse samples of the underlying matrix [4]. (The H^2 representation in [4] is therein referred to as an MLSSM representation; the MLSSM is equivalent to an H^2, as indicated by equation (21) of [4].) Since the underlying geometry is not translationally invariant, the H^2 representation obtained via sparse matrix samples does not retain the translational invariance of the underlying kernel, and each translation matrix is unique. A result is that the time required to build an H^2 representation can be significantly longer than the time required to build a similarly accurate FMM.

Although the time required to build an FMM can be much less than the time required to build a similarly accurate H^2, this saving comes at the expense of requiring larger translation matrices. This increased dimension of the FMM translators can lead to higher costs for matrix-vector product operations when using an FMM versus an H^2 representation. Furthermore, when fast direct solvers such as the $O(N)$ H^2 factorization of [4] are used, the larger translators of the FMM can also yield increased factorization costs relative to an H^2. These additional costs can offset the relative computational savings provided by an FMM when constructing a sparse representation of the system matrix.

It was recently shown that, for translationally invariant kernels, it is possible to reduce memory costs associated with an H^2 representation by converting a non-translationally invariant H^2 matrix into a translationally invariant H^2 representation using an iterative procedure [5, 6]. However, the computational costs of the algorithms used to compress the H^2 have been found to be too large to be practically useful.

In the remainder, a similar algorithm is reported for compressing an existing FMM representation [2]. It is found that the computational costs to compress an FMM

Submitted On: August 1, 2023
Accepted On: March 27, 2024

https://doi.org/10.13052/2024.ACES.J.390201

are significantly less than the costs reported in [5, 6] for compressing an H^2.

II. SHIFT INVARIANT FORM

At a given level of an octree, the interactions between non-touching groups in an FMM can be represented as:

$$\mathbf{Z}_{\text{far}} = \mathbf{U}\,\mathbf{T}_{SI}\,\mathbf{V}^h, \tag{1}$$

where $\mathbf{U}$ and $\mathbf{V}$ are block-diagonal matrices containing the FMM aggregation and disaggregation operators that map between the multipole representations of parent and child groups (or between multipole representation and the unknowns, if at the finest level). The matrix $\mathbf{T}_{SI}$ contains all translators at the level, of which only 316 (at most) are unique. Further details are provided in [2].

To compress the FMM, we first compute a compressed representation $\mathbf{T}$ from $\mathbf{T}_{SI}$. The matrix $\mathbf{T}$ is obtained by computing the $O(\tau)$ truncated SVD of column- and row-blocks of the FMM translation matrix $\mathbf{T}_{SI}$. The resulting singular vectors are then used to project the column-/row-blocks of $\mathbf{T}_{SI}$ yielding $\mathbf{T}$. Herein, the SVD truncation tolerance τ is selected to be equal to the accuracy of the FMM representation divided by 10. (In the numerical examples below, τ=1e-7.)

Once $\mathbf{T}$ is obtained, block diagonal matrices $\mathbf{L}$ and $\mathbf{R}$ are computed such that:

$$\mathbf{T} = \mathbf{L}\mathbf{T}_{\text{SI}}\mathbf{R}, \tag{2}$$

which has the same structure as equation (4) of [6].

III. SOLVING FOR L AND R

In the following, an iterative algorithm is outlined for determining the blocks of the block-diagonal matrices $\mathbf{L}$ and $\mathbf{R}$. It is noted that, if the singular vectors obtained in the column-/row-block analysis outlined above are used to form $\mathbf{L}$ and $\mathbf{R}$, then (2) holds; this is the initialization used in the following algorithm. It is noted that this initialization for $\mathbf{L}$ and $\mathbf{R}$ does not provide an effective compression of the FMM for the following reasons.

First, if the matrices $\mathbf{L}\mathbf{T}_{SI}\,\mathbf{R}$ are multiplied together in (2), then the redundancy of $\mathbf{T}_{SI}$ is lost (the individual translators that constitute the global translation matrix $\mathbf{T}$ are each unique, whereas $\mathbf{T}_{SI}$ is comprised of at most 316 unique submatrices). Second, if the representation on the right side of (2) is used without multiplying the matrices together, then the cost to apply $\mathbf{T}_{SI}$ to a vector during an iterative solve is not reduced relative to a standard FMM. The purpose of the algorithm outlined below is to find alternative diagonal blocks for $\mathbf{L}$ and $\mathbf{R}$ that utilize only a fraction of the FMM DOF space, thus reducing the cost to apply $\mathbf{T}_{SI}$ without increasing the cost to store $\mathbf{T}_{SI}$. (In this paper, the terms FMM DOF and DOF are used to indicate the dimension of the FMM translator blocks and the corresponding dimensions of the diagonal blocks in $\mathbf{L}$ and $\mathbf{R}$. This terminology differs from that used in [7].)

The algorithm used to compute the diagonal blocks of $\mathbf{L}$ and $\mathbf{R}$ is summarized in Fig. 1, which is a reverse-bootstrapping procedure This is a modified version of the bootstrapping algorithm reported in [5, 6]. The algorithm begins with the initialization summarized above.

In Fig. 1, matrices $\mathbf{L}_g$ and $\mathbf{R}_g$ are the diagonal blocks of $\mathbf{L}$ and $\mathbf{R}$, and subscript g implies a loop over the groups at this level of the octree. The integer m is the size of each block of $\mathbf{T}_{SI}$ and is equal to the number of columns/rows in each diagonal block of $\mathbf{L}$ and $\mathbf{R}$. The decrement d is the size of the reduction in the number of FMM DOF to be tested in the current iteration of the WHILE loop.

It has been observed that the compression converges to nearly identical values of m for arbitrarily large values of d for cases tested. This property makes the algorithm of Fig. 1 significantly more efficient than the bootstrapping algorithms previously reported for compressing H^2 representations [5, 6], which required d=1. The difference between those methods and the current application to an FMM is likely due to the fact that, in developing a translationally invariant representation from an existing H^2, one starts with an inaccurate representation that is iteratively improved by adding additional DOF. In contrast, when compressing an existing FMM, one starts with an accurate representation, that is compressed by removing DOF.

- n=# DOF in FMM basis; err=0; d = round(n/4)
- while $err < \tau$
  1. $m = n - d$
  2. for k = 1:n_steps (n_steps=2 here)
     a. fix $\mathbf{L}$ and compute a least squares (LS) solution for $\mathbf{R}_g$ using only the first m DOF
        - when k=1, this reduces the number of rows in the $\mathbf{R}_g$ to m
        - when k>1, the $\mathbf{R}_g$ do not change in size
     b. fix $\mathbf{R}$ and compute a LS solution for $\mathbf{L}_g$
        - when k=1, this reduces the number of columns in the $\mathbf{L}_g$ to m
        - when k>1, the $\mathbf{L}_g$ do not change in size
  3. $err\_new = \| \mathbf{T} - \mathbf{L}\,\mathbf{T}_{\text{SI}}\,\mathbf{R} \| / \|\mathbf{T}\|$
  4. If ($err\_new < \tau$), $n = m$; $err = err\_new$; else,
     - if d>1, m=n; d = round(d/2)
     - else, m=n; end while

Fig. 1. Algorithm for compressing an existing FMM.

IV. EXAMPLES

The following examples compress the black-box FMM (bbFMM) [2] representation of the static Green's function, $G(\vec{r},\vec{r}') = 1/|\vec{r}-\vec{r}'|$. Due to the scale-invariance of the homogeneous kernel, the total number of unique translation matrices needed in the bbFMM representation of G across all levels of the octree is 316.

The bbFMM representation of G is constructed with an accuracy of 1e-6. The Chebyshev order and SVD truncation tolerance [2] of the underlying bbFMM required to obtain 1e-6 accuracy were determined as follows. A dense (i.e., no empty groups), five-level octree was formed, and source and observer points were densely distributed over the surfaces of all octree boxes at the finest level of the tree. The relative RMS error in the bbFMM representation (versus the exact kernel evaluations) was computed for all interactions between non-touching groups at the finest level. Table 1 shows the resulting error as a function of the SVD truncation tolerance when a 729-point bbFMM was used (9 points in the x-, y-, and z-directions for each group). An RMS error less than 1e-6 is obtained when the SVD truncation tolerance is 1e-7, resulting in approximately 157 FMM DOF (the size of each translation matrix is 157-by-157). This is the base FMM representation used in the following examples.

Table 1: Number of FMM DOF remaining after the global SVD compression step outlined in [2] as a function of the SVD tolerance. A 729-point grid of Chebyshev nodes is used, so that the total number of FMM DOF prior to the SVD compression step is 729. Lower order Chebyshev grids fail to provide sufficient accuracy, and higher order grids did not reduce the number of FMM DOF required to achieve 1e-6 accuracy below 157.

SVD Tolerance	# DOF Before SVD	# DOF After SVD	Base-10 log of Error
1e-4	729	44	5.0e-4
1e-5	729	73	9.6e-5
1e-6	729	109	9.6e-6
1e-7	729	157	8.0e-7

A. Example: Points on a line

To illustrate the performance of the compression algorithm, we first consider the static kernel $G(\vec{r},\vec{r}')$ when N=50000 points are distributed along the line defined by x=0, y=0, -1<z<1. A six-level octree is used to decompose the problem, with level-1 being the root box. There are 8, 16, 32, and 64 non-empty groups at levels 3, 4, 5, and 6 of the octree for this geometry.

After the bbFMM representation described above is built, at each level the matrix **T** is constructed as discussed above, and the diagonal blocks of **L** and **R** in (2) are found using the algorithm summarized in Fig. 1. When the iteration completes, the number of remaining FMM DOF at a given level is m. The values of m at each level of the octree for this example are reported in the third column of Table 2. The last column of the table indicates the savings in the floating point costs required to apply the compressed translation matrix $\mathbf{T}_{SI}$ to a vector. The resulting block-diagonal matrices **L** and **R** of (2) are multiplied into the block-diagonal **U** and $\mathbf{V}^h$ matrices shown in (1), effectively compressing the basis matrices (in addition to the translator matrix) at each level.

Table 2: Results of compressing the 1e-6 bbFMM for points on a line. The initial number of FMM DOF at all levels is 157. The last column indicates the reduction in floating-point operations to apply that level's translation matrix to a vector

Octree Level	# FMM DOF Before Compression (n)	# FMM DOF After Compression (m)	FP Savings Factor $(n/m)^2$
3	157	7	503
4	157	17	85
5	157	21	56
6	157	23	47

Finally, it is noted that the relative RMS error in the compressed FMM representation at each level (and globally) is less than 1e-6 (see Step 3 of the algorithm reported in Fig. 1). This ensures that the accuracy of the original FMM representation is retained by the compressed FMM representation.

B. Example: Points on a plane

Table 3 reports the result of applying the FMM compression of Fig. 1 to the static kernel for the case of source/observer points distributed on the square surface shown in Fig. 2. For this geometry, each group has a larger interaction list than for the line example, and more FMM DOF are needed to retain an accuracy of 1e-6. This yields a savings of slightly more than 4.5 in the floating-

Table 3: Results of compressing the 1e-6 bbFMM for the square surface geometry illustrated in Fig. 2. The initial number of FMM DOF at all levels is 157. The last column indicates the reduction in floating-point operations to apply that level's translation matrix to a vector

Octree Level	# FMM DOF Before Compression (n)	# FMM DOF After Compression (m)	FP Savings Factor $(n/m)^2$
3	157	47	11
4	157	71	4.9
5	157	74	4.6
6	157	74	4.6

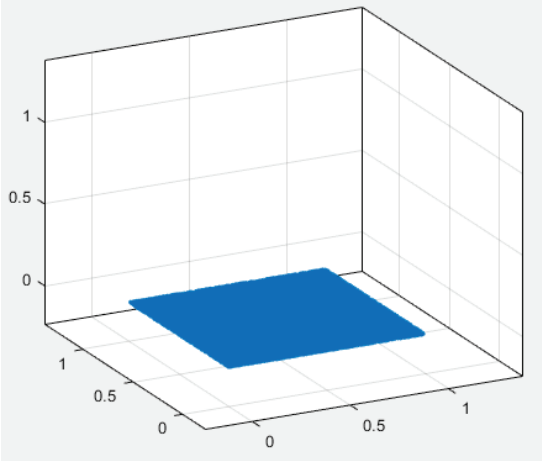

Fig. 2. Surface point distribution (N=1e5 points).

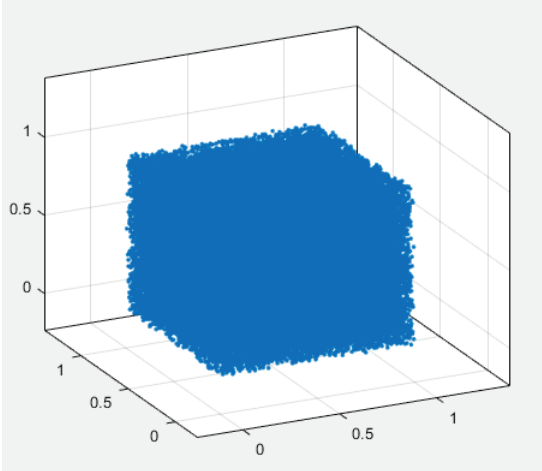

Fig. 3. Volumetric point distribution (N=1e5 points).

point cost to apply the translation matrix to a vector (relative to the original, 1e-6 bbFMM representation).

C. Example: Points in a volume

Table 4 reports the result of applying the FMM compression of Fig. 1 to the static kernel for the case of source/observer points distributed within the cubic volume shown in Fig. 3. For this geometry, each group has a larger interaction list than in the previous two examples, and more FMM DOF are needed to retain an accuracy of 1e-6. For this reason, the floating-point savings provided by the FMM compression is limited to a factor of approximately 2, as indicated by the last column of the table.

D. Example: Coil lattice

Finally, consider the 4-by-4 coil lattice geometry shown in Fig. 4. There are a total of N=80000 point sources/observers in this geometry, and the static kernel, $G(\vec{r},\vec{r}')$, is compressed using a six-level octree with results shown in Table 5.

Table 4: Results of compressing the 1e-6 bbFMM for the volumetric point distribution illustrated in Fig. 2. The initial number of FMM DOF at all levels is 157. The last column indicates the reduction in floating-point operations to apply that level's translation matrix to a vector

Octree Level	**# FMM DOF Before Compression (n)**	**# FMM DOF After Compression (m)**	**FP Savings Factor $(n/m)^2$**
3	157	91	3.0
4	157	108	2.1
5	157	109	2.1

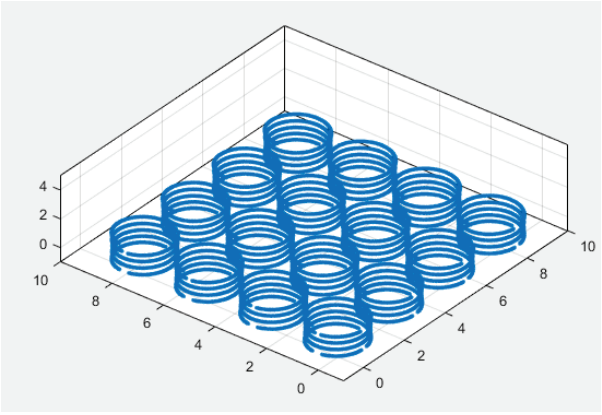

Fig. 4. Coil lattice geometry (N=8e4 points).

Table 5: Results of compressing the 1e-6 bbFMM for the coil lattice geometry illustrated in Fig. 4. The initial number of FMM DOF at all levels is 157. The last column indicates the reduction in floating-point operations to apply that level's translation matrix to a vector

Octree Level	**# DOF Before Compression (n)**	**# DOF After Compression (m)**	**FP Savings Factor $(n/m)^2$**
3	157	52	9.1
4	157	76	4.3
5	157	64	6.0
6	157	58	7.3

V. CONCLUSION

A method for compressing an existing FMM representation of point-to-point interactions for homogeneous kernels in three dimensions has been reported.

Previously reported methods for compressing an existing H^2 representation [5, 6] relied on a bootstrapping method, which caused them to be computationally inefficient. The method reported here is a modified form of [5, 6] and utilizes a reverse-bootstrapping algorithm. The compression has been observed to be insensitive to the reverse-bootstrapping step size that is used to reduce the FMM DOF space. This insensitivity to step-size renders the proposed method computationally efficient for practical 3-D applications.

The FMM compression algorithm has been applied to the bbFMM representation of $G(\vec{r},\vec{r}') = 1/|\vec{r}-\vec{r}'|$ for four different 3-D point distribution examples consisting of points on a line, a surface, a volume and a coil lattice. Significant compression is observed in several cases, with the volumetric point distribution resulting in the least amount of compression relative to the original bbFMM representation. This result is expected, since the bbFMM is already optimized for volumetric point distributions.

Finally, we briefly consider the application of the compression algorithm of Fig. 1 to more complex point distributions, such as that shown in Fig. 5. Unlike the other examples considered above, the point distribution in Fig. 5 has different types of point distributions in different spatial regions. In one corner of the domain, points are distributed along three intersecting lines; in another corner of the domain, points are densely distributed throughout a cubic sub-volume. Assuming that the point distributions are dense, an application of the algorithm in Fig. 1 to this problem at fine levels of the octree can be expected to yield compression results more similar to those shown in Table 4 than those shown in Table 2. This is because the number of FMM DOF, m, retained by the compression algorithm of Fig. 1 is the same for all groups at a given level, and m must be sufficiently large to represent the interactions between groups having dense interaction lists (i.e., octree groups located in the region containing the volumetric point distribution).

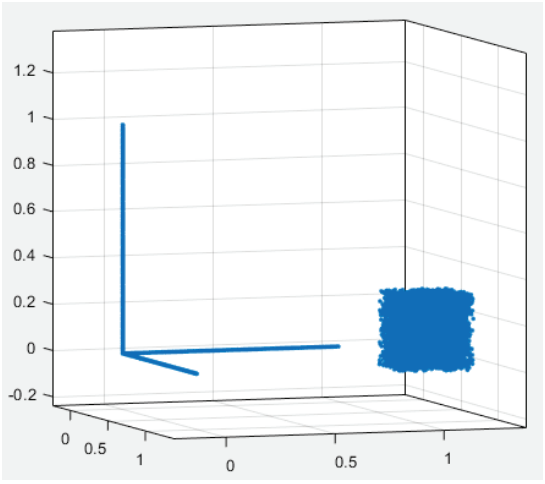

Fig. 5. Example of a mixed DOF distribution containing a region with a dense set of volumetric points and a region with three intersecting lines of points.

However, it has been observed that significant additional compression can be obtained for problems involving non-uniform point distributions (such as Fig. 5) through a straightforward extension the algorithm reported in Fig. 1. The extension is achieved by allowing the number of FMM DOF used for each source/field group at a given level of the octree to vary independently of one another, which leads to non-square translation matrices while retaining translational redundancy. This extended version of the algorithm will be reported separately elsewhere.

ACKNOWLEDGMENT

This work was supported in part by Office of Naval Research Grants N00014-16-1-3066 and N00014-21-1-2599.

REFERENCES

[1] L. Greengard and V. Rokhlin, "A fast algorithm for particle simulations," *J. Comput. Phys.*, vol. 73, no. 2, pp. 325-348, 1987.

[2] W. Fong and E. Darve, "The black-box fast multipole method," *J. Comput. Phys.*, vol. 228, no. 23, pp. 8712-8725, Dec. 2009.

[3] W. Hackbusch, *Hierarchical Matrices: Algorithms and Analysis* (Springer Series in Computational Mathematics). Berlin: Springer-Verlag, p. 511, 2015.

[4] X. Xu and R. J. Adams, "Sparse matrix factorization using overlapped localizing LOGOS modes on a shifted grid," *IEEE T. Antenn. Propag.*, vol. 60, no. 3, pp. 1414-1424, 2012.

[5] R. J. Adams, J. C. Young, and S. D. Gedney, "Compressing H2 matrices for translationally invariant kernels," *Applied Computational Electromagnetics Society (ACES) Journal*, vol. 35, no. 11, pp. 1392-1393, Nov. 2020.

[6] R. J. Adams, J. C. Young, and S. D. Gedney, "Efficiency improvements in compressing H2 matrices for translationally invariant kernels," presented at the *2022 IEEE International Symposium on Antennas and Propagation and USNC-URSI Radio Science Meeting*, Denver, CO, July 10-15, 2022.

[7] R. J. Adams, J. C. Young, and S. D. Gedney, "Compressing a fast multipole method representation of an integral equation matrix," presented at the 2023 *International Applied Computational Electromagnetics Society Symposium*, Monterey/Seaside, CA, 2023.

Robert J. Adams received the B.S. degree from Michigan Technological University, Houghton, MI, USA, in 1993, and the M.S. and Ph.D. degrees in electrical engineering from Virginia Polytechnic Institute and State University (Virginia Tech), Blacksburg, VA, USA, in 1995 and 1998, respectively.

From 1999 to 2000, he was a Research Assistant Professor with Virginia Tech. Dr. Adams joined the University of Kentucky in 2001, where he is currently a Professor with the Department of Electrical and Computer Engineering.

Dr. Adams has made novel contributions to mesh and frequency stable integral equation formulations of electromagnetic problems, constraint-based methods for high-order MOM discretizations, spectral splitting methods for implementing shadowing effects in integral equations at high frequencies, and sparse direct solution methods for low-to-moderate frequency electromagnetics applications. Dr. Adams' group developed the first $O(N)$ sparse direct solver for 3-D H^2 and FMM representations of static and low-frequency EM problems. Dr. Adams is a senior member of the IEEE.

John C. Young received the B.E.E. degree in electrical engineering from Auburn University in 1997, the M.S. degree in electrical engineering from Clemson University in 2000, and the Ph.D. degree in electrical engineering also from Clemson University in 2002.

From January 2003 to April 2003, he served as a post-doctoral researcher at Clemson University, and from 2003 to 2005, he served as a post-doctoral researcher at Tokyo Institute of Technology, Tokyo, Japan. From 2005 to 2008, he worked at Japan Radio Co. Since 2008, he has been with the Department of Electrical and Computer Engineering at the University of Kentucky, Lexington, KY, where he is currently an associate professor.

Dr. Young's research interests include integral equation methods, finite element methods, electromagnetic theory, waveguides, array antennas, and magnetic signature modeling of hysteretic materials. He is a member of IEEE, the Applied Electromagnetics Society (ACES), and URSI Commission B. He currently serves as an Associate Editor for the IEEE Transactions on Antennas and Propagation and on the Education Committee of the Antennas and Propagation Society. He also served (2020-2023) on the Board of Directors of ACES where he is currently Secretary.

Stephen D. Gedney received the B.Eng.-Honors degree from McGill University, Montreal, P.Q., in 1985, and the M.S. and Ph.D. degrees in Electrical Engineering from the University of Illinois, Urbana-Champaign, IL, in 1987 and 1991, respectively.

He is currently the Don and Karen White Professor of the Department of Electrical Engineering at the University of Colorado Denver (CUD). Previously he was a Professor of Electrical Engineering at the University of Kentucky from 1991-2014. He worked for the U.S. Army Corps of Engineers, Champaign, IL (1985-1987). He was a visiting Professor at the Jet Propulsion Laboratory, (1992-1993), HRL laboratories (1996-1997) and Alpha Omega Electromagnetics (2004-2005). He received the Tau Beta Pi Outstanding Teacher Award in 1995 and 2013. From 2002-2014, he was the Reese Terry Professor of Electrical and Computer Engineering at the University of Kentucky. He was titled as a Distinguished Professor of the University of Colorado in 2022. He is a past Associate Editor of the IEEE Transactions on Antennas and Propagation (1997-2004), a member of the IEEE Antennas and Propagation Society ADCOM (2000-2003), and served as the chair of the IEEE Antennas and Propagation Society Membership Committee (1995-2002). He is a Fellow of the IEEE and member of Tau Beta Pi.

An IGFBM-SAA Fast Algorithm for Solving Electromagnetic Scattering from Layered Media Rough Surfaces

Lilan Lei

School of Mathematics and Computer Science
Yichun University, Yichun 336000, China
lilanlei0320@126.com

Abstract – This article proposes a new fast solution algorithm (IGFBM-SAA), which combines the Improved Generalized Forward and Backward Method (IGFBM) with Spectral Acceleration Approach (SAA), which can effectively solve the electromagnetic scattering problem of layered rough surface. In this article, the electric field integral equations (EFIE) for layered rough surfaces is established, and the traditional forward and backward method (FBM) is introduced. Then, based on the traditional FBM algorithm, an Improved Generalized Forward and Backward Method is proposed and, by using the SAA technique in its iterative process, the computation of matrix-vector multiplication is accelerated, thus enabling rapid solution. In the algorithm validation, the same rough surface was calculated using the MoM, FBM, and IGFBM-SAA. The study found that when root mean square (RMS) heights are $h_1 = h_2 = 0.1\lambda$, the convergence accuracy can reach $\tau = 10^{-7}$ after 14 iterations. However, as the roughness increases to $h_1 = h_2 = 0.3\lambda$ and $h_1 = h_2 = 0.5\lambda$, the convergence accuracy falling to $\tau = 10^{-5}$ and $\tau = 10^{-5}$, respectively. This indicates that it is necessary to adjust the integration parameters to improve the convergence accuracy. In addition, it was found that when the size of the rough surface is 25.6λ, the computational times for calculations are 91 s (IGFBM-SAA), 197 s (FBM), and 410 s (MoM), respectively. When the size of the rough surface increases to 51.2λ, the computational time differences become more significant, with 236 s, 756 s, and 2547 s being the respective values. This indicates that the proposed algorithm in this article has significant computational speed advantages when dealing with larger rough surfaces. Based on this algorithm, this article studied the electromagnetic scattering characteristics of layered rough surfaces with different parameters (RMS height, dielectric constant, and correlation length), and relevant research results can provide valuable references for areas such as radar target recognition and radar stealth technology, thereby enhancing the accuracy and reliability of radar detection as well as radar stealth performance.

Index Terms – electric field integral equations, electromagnetic scattering, Improved Generalized Forward and Backward Method, layered rough surface, Spectral Acceleration Approach.

I. INTRODUCTION

Rough surface electromagnetic scattering has important application value in radar remote sensing and communication fields. In practical applications, accurately predicting and modeling the electromagnetic scattering characteristics of rough surfaces have shown important practical significance for optimizing radar image interpretation and improving the performance of communication systems. However, despite the existence of some classical methods such as the large-scale Kirchhoff approximation [1–4], the small-scale perturbation method [5–8], and the general Rayleigh method [9–11], these methods typically rely on certain simplifying assumptions, have limited applicability, and impose specific limitations on the parameters of the rough surface. Therefore, studying computation methods for rough surface electromagnetic scattering with universal applicability and high accuracy has important theoretical and practical significance.

In recent years, with the continuous development of computer technology, numerical calculation methods such as the method of moment (MoM) [12–15], the finite difference time domain method (FDTD) [16–19], and the finite element method (FEM) [20–22] have been widely used in the study of rough surface electromagnetic scattering. These methods can provide high-precision calculation results and have no specific limitations on the parameters of the rough surface. However, because numerical methods require discretizing the rough surface, the resulting unknowns are numerous, leading to high computational complexity. Currently, most numerical methods have a computational cost that grows cubically with the number of unknowns ($o(N^3)$) when dealing with rough surface electromagnetic scattering problems, which limits their practical applications to some extent.

Submitted On: September 28, 2023
Accepted On: January 12, 2024

https://doi.org/10.13052/2024.ACES.J.390202

In addition, accurate calculation of rough surface electromagnetic scattering requires not only high-precision numerical calculation methods but also efficient numerical optimization techniques. Although many researchers have conducted extensive and in-depth research in this field, there are still many problems that need to be addressed, for example how to improve computational accuracy and efficiency.

Article [23] mainly investigated the electromagnetic scattering problem based on the composite rough surface modeling method and the improved SBR-FBSSA algorithm. They placed objects in a canyon/valley environment and analyzed the electromagnetic scattering characteristics of that environment. This study extended the environmental complexity of scattering research by applying the composite rough surface modeling method and the improved SBR-FBSSA algorithm to solve the electromagnetic scattering problems in canyon/valley environments. Article [24] proposed an efficient and accurate method using the MoM-SMCG method combined with adaptive integration to solve the electromagnetic scattering problem of random rough surfaces. The main contribution of this work included using MoM to calculate the electromagnetic scattering coefficients of rough surfaces, and then using the adaptive selection integration point method (SMCG) to integrate and solve the electromagnetic scattering of rough surfaces. This study applied the MoM-SMCG method to the electromagnetic scattering problem of random rough surfaces, improving the computational efficiency and accuracy. Article [25] used the discrete two-level complex image method (DSCM) to calculate the electromagnetic scattering of completely conducting periodic rough surfaces. A model of completely conducting periodic rough surfaces was established and DSCM was used to calculate the electromagnetic scattering coefficients of rough surfaces. Then, the FDTD method was used to solve the electromagnetic scattering problems of rough surfaces. This study applied DSCM to the electromagnetic scattering problems of completely conducting periodic rough surfaces, improving the understanding of these scattering problems. Article [26] mainly studied an innovative method in the engineering field, the hybrid AMCFFM-MAE method, which can quickly simulate the electromagnetic scattering of one-dimensional rough surfaces over a frequency band. The importance of this research lies in that it provides a new engineering tool to better understand and solve practical electromagnetic scattering problems involving rough surfaces. Article [27] proposed a hybrid method for solving the composite scattering problem of targets and rough ground. The uniqueness of this method lies in that it combines the physical optics method and physical basis function method, which can accurately simulate and solve the electromagnetic scattering characteristics of rough surfaces. This study has made important extensions and improvements to the application of physical optics methods in complex environments. Article [28] proposed a fast algorithm mainly for calculating the electromagnetic scattering of one-dimensional rough surfaces. This algorithm is based on integral equation methods and basis function expansion methods, and can effectively simulate the electromagnetic scattering characteristics of complex rough surfaces. The development of this algorithm provides important theoretical basis and practical guidance for understanding and solving electromagnetic scattering problems involving rough surfaces in practical environments. Compared to that, the layered rough surfaces studied in this paper are more common in nature, such as the surface of a sea covered with floating ice, ground covered with snow or leaves, etc. Therefore, studying the electromagnetic scattering characteristics of layered rough surfaces is of great significance. However, the computational volume for calculating layered rough surfaces using numerical methods is very large, so fast algorithms need to be applied. The algorithm proposed in this paper can effectively solve this problem and save a lot of time, improving computational efficiency. This advantage is more prominent when the rough surface length is large.

This article proposes an efficient Improved Generalized Forward and Backward Method-Spectral Acceleration Approach (IGFBM-SAA) algorithm for electromagnetic scattering from layered rough surfaces, aiming to improve computational efficiency and thereby enhance research efficiency. Firstly, an electric field integral equation (EFIE) for layered rough surfaces is established, and the traditional forward and backward method (FBM) is modified to propose the innovative IGFBM method. At the same time, in order to reduce the error caused by the artificial truncation of the rough surface, a conical wave is used as the incident wave. This wave has Gaussian characteristics, which gradually decrease to zero as it approaches the boundary. This property effectively avoids the abrupt change of surface current, thereby improving the accuracy of the calculation. Then, SAA technology is combined to accelerate the calculation to achieve rapid solution. Subsequently, the computational results of the IGFBM-SAA algorithm are compared with those of MoM to verify the effectiveness and accuracy of the proposed algorithm. Finally, the electromagnetic scattering characteristics of different layered rough surfaces are studied through several examples. The results show that the IGFBM-SAA algorithm has significant advantages when calculating scattering from long layered rough surfaces. The research findings in this article have positive contributions to the technological progress in areas such as target recogni-

tion, target detection, radar stealth, and other related fields.

II. IGFBM-SAA FAST ALGORITHM MODEL

Ground covered with leaves or snow, grassland, and the sea surface covered with ice chunks can all be regarded as layered rough media surfaces. Therefore, studying the composite scattering of layered rough media surfaces and targets has important significance.

A. Electric field integral equations (EFIE) for layered rough surface

The rough surface of the three-layer medium is shown in Fig. 1. The upper and lower rough surfaces divide the medium into three layers, with parameters (ε_0,μ_0), (ε_1,μ_1), and (ε_2,μ_2) for each region. The contour S_1 of the upper rough surface is represented by $z_1=f_1(x)$, and the contour S_2 of the lower rough surface is represented by $z_2=f_2(x)$. The incident field is ψ^{inc}. ψ_0, ψ_1, and ψ_2 represent the fields within each region of the medium, and they satisfy the following boundary equations:

$$\frac{\psi_0(\mathbf{r})}{2}-\int_{S_1}\left[\psi_0(\mathbf{r}')\frac{\partial G_0(\mathbf{r},\mathbf{r}')}{\partial \mathbf{n}'} -G_0(\mathbf{r},\mathbf{r}')\frac{\partial \psi_0(\mathbf{r}')}{\partial \mathbf{n}'}\right]ds'=\psi^{\mathrm{inc}}(\mathbf{r}) \quad \mathbf{r}\in S_1\ , \tag{1}$$

$$\frac{\psi_1(\mathbf{r}')}{2}-\int_{S_2}\left[\psi_1(\mathbf{r}')\frac{\partial G_1(\mathbf{r},\mathbf{r}')}{\partial \mathbf{n}'}-G_1(\mathbf{r},\mathbf{r}')\frac{\partial \psi_1(\mathbf{r}')}{\partial \mathbf{n}'}\right]ds' +\int_{S_1}\left[\psi_1(\mathbf{r}')\frac{\partial G_1(\mathbf{r},\mathbf{r}')}{\partial \mathbf{n}'}-G_1(\mathbf{r},\mathbf{r}')\frac{\partial \psi_1(\mathbf{r}')}{\partial \mathbf{n}'}\right]ds'=0 \tag{2}$$

$$\mathbf{r}\in S_1 \text{ or } \mathbf{r}\in \mathrm{S}_2,$$

$$\frac{\psi_2(\mathbf{r})}{2}+\int_{S_2}\psi_2(\mathbf{r}')\frac{\partial G_2(\mathbf{r},\mathbf{r}')}{\partial \mathbf{n}'}-G_2(\mathbf{r},\mathbf{r}')\frac{\partial \psi_2(\mathbf{r})}{\partial \mathbf{n}'}ds'=0 \quad \mathbf{r}\in S_2, \tag{3}$$

where $\int_S$ represents the integration over the rough surface, $G_0(\mathbf{r},\mathbf{r}')$ represents the Green's function in free space, and $G_1(\mathbf{r},\mathbf{r}')$ and $G_2(\mathbf{r},\mathbf{r}')$ represent the Green's functions in medium 1 and medium 2, respectively. At the same time, the fields in each region satisfy the following boundary conditions:

$$\psi_i(\mathbf{r})=\psi_{i+1}(\mathbf{r}), \tag{4}$$

$$\frac{\partial \psi_{i+1}(\mathbf{r})}{\partial n}=\rho\frac{\partial \psi_i(\mathbf{r})}{\partial n}\ \ (i=0,1). \tag{5}$$

For TE wave, $\rho=\mu_{i+1}/\mu_i$. For TM wave, $\rho=\varepsilon_{i+1}/\varepsilon_0$.

Assuming that the length of the rough surface is L and the discrete density Δx is uniform, equations (1-3) can be simplified as follows:

$$\mathbf{A}^{(0,1,1)}U_1+\mathbf{B}^{(0,1,1)}\psi_1=\psi^{inc}, \tag{6}$$

$$\rho_1\mathbf{A}^{(1,1,1)}U_1+\mathbf{B}^{(1,1,1)}\psi_1+\mathbf{A}^{(1,1,2)}U_2+\mathbf{B}^{(1,1,2)}\psi_2=0, \tag{7}$$

$$\rho_1\mathbf{A}^{(1,2,1)}U_1+\mathbf{B}^{(1,2,1)}\psi_1+\mathbf{A}^{(1,2,2)}U_2+\mathbf{B}^{(1,2,2)}\psi_2=0, \tag{8}$$

$$\rho_2\mathbf{A}^{(2,2,2)}U_2+\mathbf{B}^{(2,2,2)}\psi_2=0. \tag{9}$$

The expression for each matrix element is as follows [29]:

$$\mathbf{A}_{mn}^{(a,b,c)}=\begin{cases} w^{(a,c)}\frac{i\Delta x}{4}H_0^{(1)}\left(k_a\left|\mathbf{r}_{m,b}-\mathbf{r}_{n,c}\right|\right)\Delta l_{m,b} \\ \quad (b=c,m\neq n) \text{ or } b\neq c \\ w^{(a,c)}\frac{i\Delta x}{4}\left[1+\frac{i2}{\pi}\ln\left(\frac{e^{\gamma}k_a\Delta x\Delta l_{m,b}}{4e}\right)\right] \\ \quad (b=c,m=n)\end{cases}, \tag{10}$$

$$\mathbf{B}_{mn}^{(a,b,c)}=\begin{cases} -w^{(a,c)}\frac{ik_a\Delta x}{4}\frac{H_1^{(1)}\left(k_a\left|\mathbf{r}_{m,b}-\mathbf{r}_{n,c}\right|\right)}{\left|\left|\mathbf{r}_{m,b}-\mathbf{r}_{n,c}\right|\right|}\times \\ (f_c'(x_n)(x_n-x_m)-(f_c(x_n)-f_b(x_m))) \\ \quad (b=c,m\neq n) \text{ or } b\neq c \\ \frac{1}{2}-w^{(a,c)}\frac{f_b''(x_m)}{4\pi}\frac{\Delta x}{1+f_b'(x_m)^2} \\ \quad (b=c,m=n)\end{cases}, \tag{11}$$

where

$$w^{(a,c)}=\begin{cases}1 & a=c\\ -1 & a\neq c\end{cases}, \tag{12}$$

$$U_{i,m}=\sqrt{1+(f_i'(x_m))^2}\,\partial\psi_i(x_m)\Big/\partial n\ \ (i=1,2,3)\,. \tag{13}$$

In the equations above, the first superscript indicates the region, the second superscript indicates the roughness location where the field point is located, and the third superscript indicates the roughness location where the source point is located.

Therefore, equations (6-9) can be transformed into a matrix equation:

$$\begin{bmatrix}\mathbf{A}^{(0,1,1)} & \mathbf{B}^{(0,1,1)} & 0 & 0\\ \rho_1\mathbf{A}^{(1,1,1)} & \mathbf{B}^{(1,1,1)} & \mathbf{A}^{(1,1,2)} & \mathbf{B}^{(1,1,2)}\\ \rho_1\mathbf{A}^{(1,2,1)} & \mathbf{B}^{(1,2,1)} & \mathbf{A}^{(1,2,2)} & \mathbf{B}^{(1,2,2)}\\ 0 & 0 & \rho_2\mathbf{A}^{(2,2,2)} & \mathbf{B}^{(2,2,2)}\end{bmatrix}\cdot\begin{bmatrix}\mathbf{U}_1\\ \psi_1\\ \mathbf{U}_2\\ \psi_2\end{bmatrix}=\begin{bmatrix}\psi^{inc}\\ 0\\ 0\\ 0\end{bmatrix}. \tag{14}$$

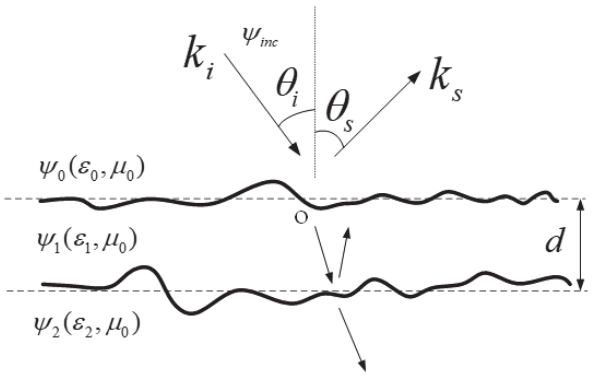

Fig. 1. Schematic diagram of layered rough surface.

B. Forward and backward method (FBM)

Solving scattering problems using numerical algorithms ultimately requires transforming them into matrix equation solutions:

$$\mathbf{ZI} = \mathbf{V}, \tag{15}$$

where $\boldsymbol{Z}$ is the impedance matrix, $\boldsymbol{V}$ is the excitation vector, and $\boldsymbol{I}$ is the unknown vector to be solved. The traditional method for solving this system is to invert the impedance matrix, which requires a computational cost and storage cost of $o(N^3)$ (where N is the number of unknowns). When the number of unknowns is large, this approach requires significant memory and computation time.

FBM [29–31] has good convergence properties for problems involving scattering from rough surfaces. It divides the induced current of each discrete element on the rough surface into forward and backward contributions to the scattering field. The forward contribution is generated by the incident electromagnetic wave and the induced current of the source element located in front of the receiving field element, while the backward contribution is generated by the induced current of the source element located behind the receiving field element. The calculation process follows.

First, divide the impedance matrix into three matrices:

$$\mathbf{Z} = \mathbf{Z}_f + \mathbf{Z}_s + \mathbf{Z}_b. \tag{16}$$

Among them, $\mathbf{Z}_f$ is a lower triangular matrix representing the contributions of all source currents located before the receiving unit, $\mathbf{Z}_b$ is an upper triangular matrix representing the contributions of all source currents located behind the receiving unit, and $\mathbf{Z}_s$ is a diagonal matrix representing the contributions of each point on the rough surface to itself.

Divide the unknown vector $\boldsymbol{I}$ to be solved into two parts:

$$\mathbf{I} = \mathbf{I}_f + \mathbf{I}_b, \tag{17}$$

where $\boldsymbol{I}_f$ is the induced current on the rough surface contributing to the forward propagation of electromagnetic waves, and $\boldsymbol{I}_b$ is the induced current on the rough surface contributing to the backward propagation of electromagnetic waves.

The following equation system can be obtained from the three equations above:

$$\mathbf{Z}_s\mathbf{I}_f = \mathbf{Z} - \mathbf{Z}_f\left[\mathbf{I}_f + \mathbf{I}_b\right], \tag{18}$$

$$\mathbf{Z}_s\mathbf{I}_b = -\mathbf{Z}_b\left[\mathbf{I}_f + \mathbf{I}_b\right]. \tag{19}$$

It can be transformed into the following iterative form:

$$\left[\mathbf{Z}_s + \mathbf{Z}_f\right]\mathbf{I}_f^{(n)} = \mathbf{Z} - \mathbf{Z}_f\mathbf{I}_b^{(n-1)}, \tag{20}$$

$$\left[\mathbf{Z}_s + \mathbf{Z}_b\right]\mathbf{I}_b^{(n)} = -\mathbf{Z}_b\mathbf{I}_f^{(n)}. \tag{21}$$

Define the convergence accuracy as follows:

$$\tau = \frac{\mathbf{Z}\left[(\mathbf{I}_f^{(n)} + \mathbf{I}_b^{(n)}) - (\mathbf{I}_f^{(n-1)} + \mathbf{I}_b^{(n-1)})\right]}{\mathbf{Z}} < \varepsilon. \tag{22}$$

The iterative process starts with $\mathbf{I}_b^{(0)} = 0$ as the initial value, and first calculates $\mathbf{I}_f^{(1)}$ using equation (20), then calculates $\mathbf{I}_b^{(1)}$ using equation (21). This process iterates until the specified convergence accuracy is met. The computational cost of this algorithm is $o(N^2)$, and it has fast convergence speed, making it an effective algorithm for solving scattering problems of rough surfaces.

However, if we want to use FBM to solve the matrix equation (14), we need to improve the FBM method. Next, we will introduce IGFBM.

C. Improved Generalized Forward and Backward Method (IGFBM)

Decompose the impedance matrix into upper, lower, and diagonal matrices denoted by U, L, and D, respectively. For example, the submatrix denoted by (l,l,l) has the following form:

$$\mathbf{A}^{(l,l,l)} = \mathbf{A}^{\mathrm{U},(l,l,l)} + \mathbf{A}^{\mathrm{L},(l,l,l)} + \mathbf{A}^{\mathrm{D},(l,l,l)}, \tag{23}$$

$$\mathbf{B}^{(l,l,l)} = \mathbf{B}^{\mathrm{U},(l,l,l)} + \mathbf{B}^{\mathrm{L},(l,l,l)} + \mathbf{B}^{\mathrm{D},(l,l,l)}. \tag{24}$$

The unknown vector is decomposed into forward and backward components, $\mathbf{U}_i = \mathbf{U}_i^{\mathrm{f}} + \mathbf{U}_i^{\mathrm{b}}$ and $\psi_i = \psi_i^{\mathrm{f}} + \psi_i^{\mathrm{b}}$, where $\mathbf{U}_i^{\mathrm{f}}$ and ψ_i^{f} are the forward components, and $\mathbf{U}_i^{\mathrm{b}}$ and ψ_i^{b} are the backward components. Therefore, the forward current iteration formula in equation (14) is written as:

$$\begin{aligned}\mathbf{A}^{\mathrm{L},(0,1,1)}\mathbf{U}_1^{\mathrm{f}} + \mathbf{B}^{\mathrm{L},(0,1,1)}\psi_1^{\mathrm{f}} &= \psi^{inc} \\ &- \mathbf{A}^{\mathrm{D},(0,1,1)}(\mathbf{U}_1^{\mathrm{f}} + \mathbf{U}_1^{\mathrm{b}}) - \mathbf{B}^{\mathrm{D},(0,1,1)}(\psi_1^{\mathrm{f}} + \psi_1^{\mathrm{b}}),\end{aligned} \tag{25}$$

$$\begin{aligned}\rho_1\mathbf{A}^{\mathrm{L},(1,1,1)}\mathbf{U}_1^{\mathrm{f}} + \mathbf{B}^{\mathrm{L},(1,1,1)}\psi_1^{\mathrm{f}} + \mathbf{A}^{\mathrm{L},(1,1,2)}\mathbf{U}_2^{\mathrm{f}} + \mathbf{B}^{\mathrm{L},(1,1,2)}\psi_2^{\mathrm{f}} \\ = -\rho_1\mathbf{A}^{\mathrm{D},(1,1,1)}(\mathbf{U}_1^{\mathrm{f}} + \mathbf{U}_1^{\mathrm{b}}) - \mathbf{B}^{\mathrm{D},(1,1,1)}(\psi_1^{\mathrm{f}} + \psi_1^{\mathrm{b}}) \\ - \mathbf{A}^{\mathrm{D},(1,1,2)}(\mathbf{U}_2^{\mathrm{f}} + \mathbf{U}_2^{\mathrm{b}}) - \mathbf{B}^{\mathrm{D},(1,1,2)}(\psi_2^{\mathrm{f}} + \psi_2^{\mathrm{b}}),\end{aligned} \tag{26}$$

$$\begin{aligned}\rho_1\mathbf{A}^{\mathrm{L},(1,1,1)}\mathbf{U}_1^{\mathrm{f}} + \mathbf{B}^{\mathrm{L},(1,1,1)}\psi_1^{\mathrm{f}} + \mathbf{A}^{\mathrm{L},(1,1,2)}\mathbf{U}_2^{\mathrm{f}} + \mathbf{B}^{\mathrm{L},(1,1,2)}\psi_2^{\mathrm{f}} \\ = -\rho_1\mathbf{A}^{\mathrm{D},(1,2,1)}(\mathbf{U}_1^{\mathrm{f}} + \mathbf{U}_1^{\mathrm{b}}) - \mathbf{B}^{\mathrm{D},(1,2,1)}(\psi_1^{\mathrm{f}} + \psi_1^{\mathrm{b}}) \\ - \mathbf{A}^{\mathrm{D},(1,2,2)}(\mathbf{U}_2^{\mathrm{f}} + \mathbf{U}_2^{\mathrm{b}}) - \mathbf{B}^{\mathrm{D},(1,2,2)}(\psi_2^{\mathrm{f}} + \psi_2^{\mathrm{b}}),\end{aligned} \tag{27}$$

$$\begin{aligned}\rho_2\mathbf{A}^{\mathrm{L},(2,2,2)}\mathbf{U}_1^{\mathrm{f}} + \mathbf{B}^{\mathrm{L},(2,2,2)}\psi_1^{\mathrm{f}} = \\ - \rho_2\mathbf{A}^{\mathrm{D},(2,2,2)}(\mathbf{U}_2^{\mathrm{f}} + \mathbf{U}_2^{\mathrm{b}}) - \mathbf{B}^{\mathrm{D},(2,2,2)}(\psi_2^{\mathrm{f}} + \psi_2^{\mathrm{b}}).\end{aligned} \tag{28}$$

The iterative formula for obtaining the backward current can be obtained analogously. By iterative solution, the unknown variables at the i-th iteration are $\mathbf{U}_1^{\mathrm{f},(i)}$, $\mathbf{U}_1^{\mathrm{b},(i)}$, $\psi_1^{\mathrm{f},(i)}$, $\psi_1^{\mathrm{b},(i)}$, $\mathbf{U}_2^{\mathrm{f},(i)}$, $\mathbf{U}_2^{\mathrm{b},(i)}$, $\psi_2^{\mathrm{f},(i)}$, $\psi_2^{\mathrm{b},(i)}$, and the iterative algorithm starts with initial values of $\mathbf{U}_1^{\mathrm{b},(0)} = 0$, $\psi_1^{\mathrm{b},(0)} = 0$, $\mathbf{U}_2^{\mathrm{b},(0)} = 0$, and $\psi_2^{\mathrm{b},(0)} = 0$, and calculates iteratively until the specified convergence accuracy is reached.

For the forward iteration process of IGFBM, the matrix-vector multiplication needs to be repeated, and

the process can be expressed as:

$$V_f^{(1)}(\mathbf{r}_n)=\sum_{m=1}^{n-1}A_{\mathrm{mn}}^{(0,1,1)}\cdot U_{1,m}+\sum_{m=1}^{n-1}B_{\mathrm{mn}}^{(0,1,1)}\cdot\psi_{1,m}, \tag{29}$$

$$V_f^{(2)}(\mathbf{r}_n)=\sum_{m=1}^{n-1}A_{\mathrm{mn}}^{(1,1,1)}\cdot \mathrm{U}_{1,m} + \sum_{m=1}^{n-1}B_{\mathrm{mn}}^{(1,1,1)}\cdot\psi_{1,m}+\sum_{m=1}^{n-1}A_{\mathrm{mn}}^{(1,1,2)}\cdot U_{2,m}+\sum_{m=1}^{n-1}B_{\mathrm{mn}}^{(1,1,2)}\cdot\psi_{2,m}, \tag{30}$$

$$V_f^{(3)}(\mathbf{r}_n)=\sum_{m=1}^{n-1}A_{\mathrm{mn}}^{(1,2,1)}\cdot U_{1,m}+\sum_{m=1}^{n-1}B_{\mathrm{mn}}^{(1,2,1)}\cdot\psi_{1,m} + \sum_{m=1}^{n-1}A_{\mathrm{mn}}^{(1,2,2)}\cdot U_{2,m}+\sum_{m=1}^{n-1}B_{\mathrm{mn}}^{(1,2,2)}\cdot\psi_{2,m}, \tag{31}$$

$$V_f^{(4)}(\mathbf{r}_n)=\sum_{m=1}^{n-1}A_{\mathrm{mn}}^{(2,2,2)}\cdot U_{1,m}+\sum_{m=1}^{n-1}B_{\mathrm{mn}}^{(2,2,2)}\cdot\psi_{1,m}, \tag{32}$$

where $n=1,2,...,N$. $V_f^{(i)}(\mathbf{r}_n)$ $(i=1,2,3,4)$ represents the radiation contribution generated by the source current in the n-th receiving element upstream of the interface, and the computational effort required for each iteration is $o(N^2)$. Therefore, the SAA algorithm can be used to accelerate the calculation and improve computational efficiency.

D. Spectral Acceleration Approach (SAA)

If SAA is applied to the calculation of equation (29), both the computational load and memory requirements are reduced to $o(N)$. The basic principle is to define a neighboring region L_s, where if a source element and a receiver element are within a certain distance, they are referred to as strong interaction group and produce strong interaction V_s, otherwise they are referred to as weak interaction group and produce weak interaction V_w. Equation (29) can be rewritten as:

$$V_f^{(1)}(\mathbf{r}_n)=V_s^{(1)}+V_w^{(1)}=\sum_{m=n-N_s}^{n-1}(A_{mn}^{(1,1,1)}\cdot U_{1,m}+B_{mn}^{(1,1,1)}\cdot\psi_{1,m}) + \sum_{m=1}^{n-N_s-1}(A_{mn}^{(1,1,1)}\cdot U_{1,m}+B_{mn}^{(1,1,1)}\cdot\psi_{1,m}). \tag{33}$$

The $V_s^{(1)}$ at position r_n is the contribution from the collective action of N_s source elements within a distance L_s of the field element receiving at position r_n, computed accurately using MOM. The contribution $V_w^{(1)}$ is from the collective action of $n-N_s-1$ source elements outside a distance L_s, which involves a large computational cost and reduces computational efficiency. Next, we discuss acceleration methods for this contribution.

Based on the spectral integral form of the Green's function [32], we can derive:

$$V_w^{(1)}(\mathbf{r}_n)=\sum_{m=1}^{n-N_s-1}(A_{mn}^{(1,1,1)}\cdot U_{1,m}+B_{mn}^{(1,1,1)}\cdot\psi_{1,m}) =\frac{i\Delta x}{4\pi}\int_{C_\theta}F_n(\theta)\exp(ik_1z_{1,n}\sin\theta)d\theta, \tag{34}$$

$$F_n(\theta)=F_{n-1}(\theta)\cdot\exp(ik_1\Delta x\cos\theta) + [-ik_1(-\sin\theta+\xi_x\cos\theta)\psi_{1,n-N_s-1}+\mathrm{U}_{1,n-N_s-1}] \cdot\exp[ik_1(N_s+1)\Delta x\cos\theta]\cdot\exp[-ik_1z_{1,n-N_s-1}\sin\theta]. \tag{35}$$

Similarly, we can obtain the spectral integral forms of $V_w^{(2)}$, $V_w^{(3)}$, and $V_w^{(4)}$. C_θ is the integration path. It can be seen that the weak contributions of all far-field elements $F_n(\theta)$ are now continuously recursively calculated by equation (35), with slowly changing field modes on the integration path making the SAA algorithm efficient.

Due to the weak contribution of the far field on the longer rough surface, $F_n(\theta)$ tends to have a narrow main lobe and multiple narrow side lobes in the complex plane. The choice of the integration path in equation (35) can be considered from C_θ to C_δ, such that $F_n(\theta)$ has a slowly varying mode with C_δ. The efficiency of the SAA algorithm lies in this slowly varying far field mode. The parameters chosen in Fig. 2 are as follows [31]:

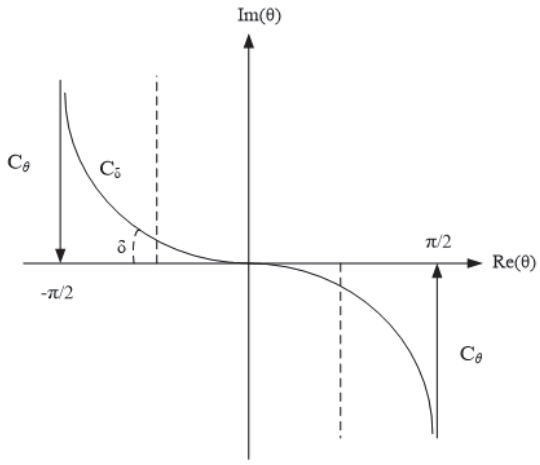

Fig. 2. Schematic diagram of spectral integration path.

where $\delta=\tan^{-1}(1/b)$, $b=\max(\sqrt{kR_s/20}\cdot\theta_s-1,1)$, $\theta_{s,\max}=\tan^{-1}(\frac{z_{\max}-z_{\min}+d}{R_s})$, $R_s=\sqrt{L_s^2+(z_{\max}-z_{\min}+d)^2}$.

Finally, choosing appropriate parameters, the discrete spectral integral form of the far-field can be obtained, for example, for A:

$$V_w^{(1)}=\frac{i\Delta x e^{-i\delta}}{4\pi}\sum_{p=-Q}^{Q}W(\theta_p)F_n(\theta_p)e^{ik_1z_{1,n}\sin\theta_p}\Delta\theta. \tag{36}$$

E. Conical incident wave

In simulation calculations, it is not practical to deal with the scattering of infinitely long rough surfaces, so the size of the rough surface is usually limited to a certain range. To avoid the effects of reflection and edge-bending caused by abrupt truncation of the rough surface edge, a conical incident wave [33] is used instead

of traditional plane wave incidence. This conical wave gradually decreases to zero as it approaches the boundary, effectively avoiding abrupt changes in surface current and significantly improving the accuracy of the calculation.

For the TE incident wave, the electromagnetic field expressions are:

$$\mathbf{E}_{inc}(\mathbf{r}) = \int_{-\infty}^{+\infty}\int_{-\infty}^{+\infty} \exp(\mathrm{j}k_x x + \mathrm{j}k_y y - \mathrm{j}k_z z) \cdot E(k_x,k_y)\, h_i(-k_z)\, dk_x dk_y, \tag{37}$$

$$\mathbf{H}_{inc}(\mathbf{r}) = -\frac{1}{\eta_0}\int_{-\infty}^{+\infty}\int_{-\infty}^{+\infty} \exp(\mathrm{j}k_x x + \mathrm{j}k_y y - \mathrm{j}k_z z) \cdot E(k_x,k_y)\, v_i(-k_z)\, dk_x dk_y. \tag{38}$$

For the TM incident wave, the electromagnetic field expressions are:

$$\mathbf{E}_{inc}(\mathbf{r}) = \int_{-\infty}^{+\infty}\int_{-\infty}^{+\infty} \exp(jk_x x + jk_y y - jk_z z) \cdot E(k_x,k_y)\, v_i(-k_z)\, dk_x dk_y, \tag{39}$$

$$\mathbf{H}_{inc}(\mathbf{r}) = -\frac{1}{\eta_0}\int_{-\infty}^{+\infty}\int_{-\infty}^{+\infty} \exp(jk_x x + jk_y y - jk_z z) \cdot E(k_x,k_y)\, h_i(-k_z)\, dk_x dk_y, \tag{40}$$

where $E(k_x,k_y)$ is the incident spectrum, $\mathbf{h}_i$ is the horizontal polarization direction, v_i is the vertical polarization direction, η_0 is the free space wave impedance, and k_i is the spatial spectral domains in the i directions, respectively, $k_\rho = \sqrt{k_x^2 + k_y^2}$.

The two-dimensional normalized conical incident wave amplitude is shown in Fig. 3. It can be seen from this that the magnetic field is strongest from the center of the rough surface and slowly returns to zero at the edges. Therefore, the tapered incident wave can be used to reduce the error caused by truncating the rough surface.

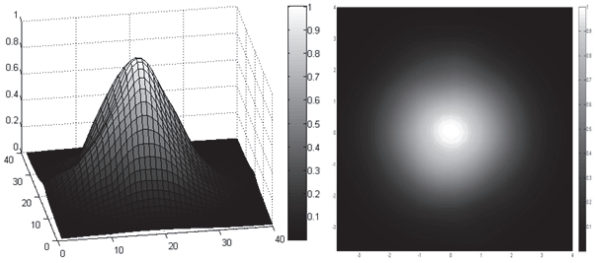

(a) (b)

Fig. 3. Normalized conical wave schematic.

III. VALIDATION OF ALGORITHM

Before applying the proposed IGFBM-SAA algorithm to practical situations, we need to verify its effectiveness and accuracy in calculating scattering from layered rough surfaces. To avoid overlap for different rough surfaces, all interfaces are modeled using Gaussian rough surfaces with the same parameters. The characteristics of these rough surfaces, including the root mean square (RMS) height and correlation length of the upper and lower layers, are described by parameters h_1, l_1, h_2, and l_2. In addition, we also need to consider the dielectric constants of the media, which are $\varepsilon_{r1} = 2.0 + i0.05$ and $\varepsilon_{r2} = 25 + i0$. Furthermore, we set the following parameters: rough surface length $L = 51.2\lambda$, correlation length $l_1 = l_2 = 1.0\lambda$, upper rough surface thickness $d = 10\lambda$, incident frequency $f = 1$ GHz, and incident angle $\theta_i = 60^\circ$.

In the verification process, we used this algorithm to calculate an example of scattering from a layered rough surface and stored the calculated results in Fig. 4. For comparison of the accuracy of the algorithm, we used traditional MoM as validation algorithms. This algorithm is relatively slow in calculation speed, but with high accuracy. We used MoM to calculate the same example and plotted the calculated results on the same graph for comparison.

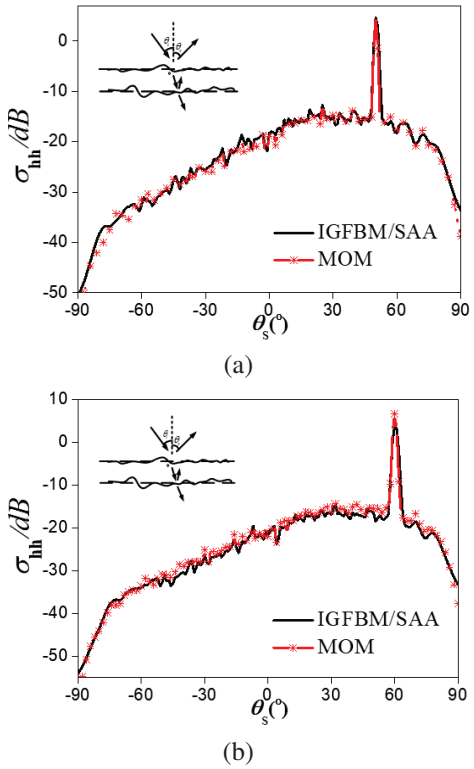

Fig. 4. Validation of algorithm: (a) horizontal polarization and (b) vertical polarization.

From Fig. 4 we can see that the calculated results of the three methods are in good agreement, which indicates that the IGFBM-SAA algorithm is effective in calculating scattering from layered rough surfaces.

To more accurately evaluate the performance of the algorithm, we used different rough surface lengths, 12.8λ, 25.6λ, and 51.2λ, corresponding to different dimensions of the impedance matrix, 512, 1024, and 2048, respectively. Other parameters were kept constant. Then we compared the computational time of the IGFBM-SAA algorithm with that of FBM and MoM. To ensure accurate statistical analysis, we averaged the time taken for 20 calculations. As shown in Fig. 5, we conducted a detailed comparison between the IGFBM/SAA algorithm, traditional MoM, and FBM. The results showed that the IGFBM/SAA algorithm exhibited significant advantages in computational speed compared to traditional MoM and FBM. This advantage was even more pronounced when dealing with large-scale rough surfaces. This enabled the algorithm to complete tasks more efficiently when dealing with large-scale rough surface scattering problems, providing strong support for practical engineering applications.

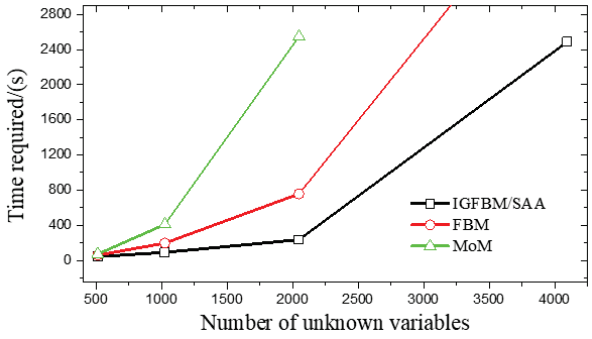

Fig. 5. Computational time.

During the above computations and validation process, we used a simulation computer with a CPU frequency of 3.4 GHz and 8 GB of memory. These parameters are sufficient for running large-scale rough surface scattering calculations. However, for more complex or larger-scale computational requirements, higher-performance computers or parallel computing techniques may be required to meet computational needs.

We conducted research on the convergence performance of this algorithm for different values of rough surface RMS height. As shown in Fig. 6 (a), when TE wave is incident, the algorithm achieves $\tau = 10^{-7}$ after 14 iterations when the roughness is $h_1 = h_2 = 0.1\lambda$, and the error increases to $\tau = 10^{-5}$ after the same number of iterations when the roughness is $h_1 = h_2 = 0.3\lambda$. However, when the roughness is $h_1 = h_2 = 0.5\lambda$, the convergence accuracy can only reach $\tau = 10^{-3}$, indicating that as the roughness increases, the convergence performance of IGFBM-SAA decreases. This is mainly due to the increase in error in solving spectral integral equation

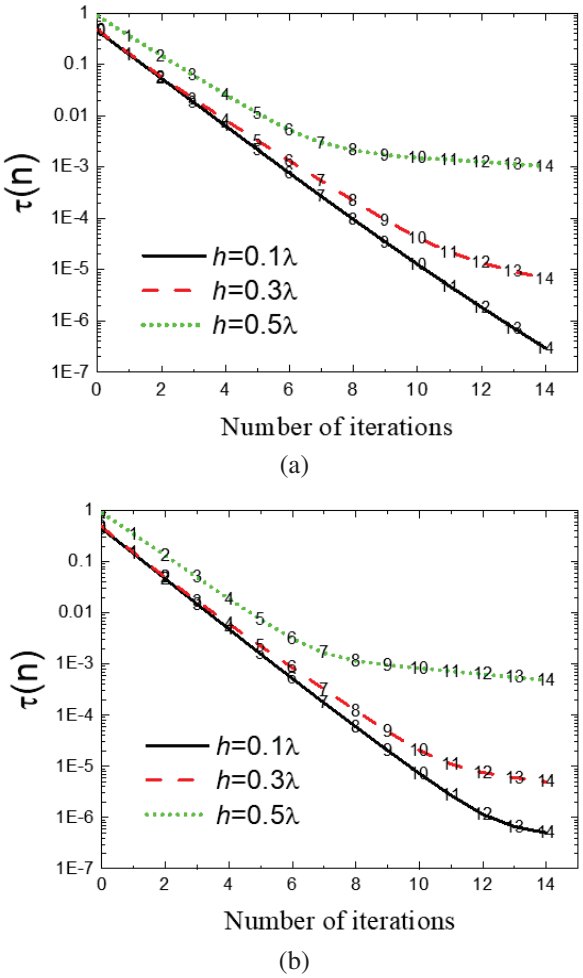

Fig. 6. Algorithmic convergence analysis chart: (a) TE incident wave and (b) TM incident wave.

(36) with increasing roughness. To improve the convergence accuracy, it is necessary to reselect integral parameters. In addition, it was found that the characteristics of TM wave incidence are different from those of TE wave incidence. As shown in Fig. 6 (b), it can be clearly seen that the convergence speed of TM wave is faster, but its convergence accuracy is lower than that of TE wave incidence.

In summary, when studying rough surface scattering problems, appropriate algorithms and parameter settings need to be carefully selected for different incident waves and roughness to ensure good convergence performance and computational accuracy of the algorithm. Especially when the roughness increases, it may be necessary to readjust parameters of the algorithm to reduce the error in spectral integral solution and improve convergence accuracy. This finding has important guiding significance for practical applications in dealing with complex rough surface scattering problems.

IV. CALCULATION RESULTS AND ANALYSIS

This section mainly studies and analyzes the electromagnetic scattering characteristics of layered rough surfaces under different parameters. Unless otherwise specified, the relevant parameters are set as: dielectric constants of the media $\varepsilon_{r1} = 2.0 + i0.05$ and $\varepsilon_{r2} = 25 + i0$, rough surface length $L = 51.2\lambda$, $h_1 = h_2 = 0.2\lambda$, correlation length $l_1 = l_2 = 1.0\lambda$, upper rough surface thickness $d = 6\lambda$, incident frequency $f = 1GHz$, and incident angle $\theta_i = 40^\circ$.

Figure 7 demonstrates the impact of changes in the RMS height of a layered rough surface on the bistatic scattering coefficient under TM wave incidence, with RMS heights chosen as $h_1 = h_2 = 0.2$, $h_1 = h_2 = 0.5$, and $h_1 = h_2 = 1.0$, respectively. The correlation length of the rough surface follows $l_1 = l_2 = 1.0\lambda$, and the incident angle is $\theta_i = 40^\circ$. Upon close examination, it is observed that the bistatic scattering coefficient of the layered rough surface tends to decrease in the specular direction with increasing RMS height, particularly evident when the RMS height is $h_1 = h_2 = 0.2$ and $h_1 = h_2 = 0.5$. Conversely, in the non-specular scattering directions, the bistatic scattering coefficient increases with increasing RMS height, particularly prominent when the RMS height is $h_1 = h_2 = 1.0$. Additionally, compared to the specular direction, the bistatic scattering coefficient is generally smaller in the non-specular directions, indicating a stronger scattering ability of the layered rough surface in the specular direction.

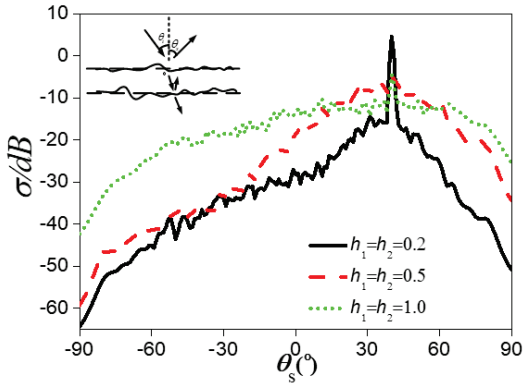

Fig. 7. Scattering coefficient comparison chart for different root mean square (RMS) heights.

This observed phenomenon indicates that the RMS height of rough surfaces has a significant impact on bistatic scattering coefficients that depends on the direction of scattering. This finding can provide valuable reference and applications in areas such as electromagnetic scattering and radar target characterization. For example, in radar target recognition, by studying the scattering characteristics of layered rough surfaces, targets can be identified and classified more accurately, thereby enhancing the accuracy and reliability of radar detection. Additionally, in radar stealth technology, surface structures with lower scattering coefficients can be designed and implemented based on studies of layered rough surfaces to decrease the probability of targets being detected by radar, thus enhancing their radar stealth performance. Furthermore, this research can also be applied to electromagnetic compatibility analysis and prediction.

Figure 8 shows the dependence of the scattering coefficient of a layered rough surface on the correlation length when TM wave incidence. As seen from the figure, the scattering coefficient increases with increasing correlation length in the specular direction. However, at large scattering angles, the scattering coefficient decreases with increasing correlation length. This observation is consistent with the conclusions of many electromagnetic scattering studies, indicating that the scattering characteristics of rough surfaces are not only determined by their surface structure but also affected by the incident conditions of electromagnetic waves.

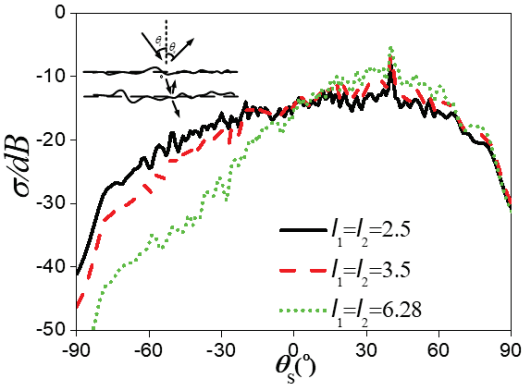

Fig. 8. Scattering coefficient comparison chart for different correlation lengths.

In the specular direction, as the correlation length increases, the details and fluctuations of the surface structure become more significant, which leads to an increase in the scattering coefficient. This trend can be understood as follows: as the surface structure changes, the complexity of scattering increases, causing more electromagnetic energy to be scattered into different directions.

However, in the region of large scattering angles, the situation is different. In this region, the decrease in scattering coefficient is related to the increase in surface structure size and the propagation characteristics of electromagnetic waves. More specifically, when electromagnetic waves propagate from regions with larger surface structures, the coherence of the wave may be affected,

leading to a decrease in scattering coefficient. Additionally, larger surface structures may provide more propagation paths for electromagnetic waves, causing some waves to bypass the surface structure rather than undergo strong scattering.

In the subsequent study, we applied the IGFBM-SAA method to deeply explore the impact of the changes in the dielectric constant ε_2 of the lower rough surface on electromagnetic scattering coefficients. In the simulation calculations, both the upper and lower media were lossless, with the dielectric constant of the upper medium being $\varepsilon_1 = 5.0$ and the dielectric constants of the lower media being $\varepsilon_2 = 5.0$, $\varepsilon_2 = 10.0$, and $\varepsilon_2 = 20.0$, respectively. The rms and correlation length of the upper-lower interface were $h_1 = h_2 = 0.5$ and $l_1 = l_2 = 1.0\lambda$, respectively, and the incident angle was $\theta_i = 40°$.

To visually present the changes in the scattering coefficients, we plotted Fig. 9 (a), which demonstrated the trend of the scattering coefficient varying with the dielectric constant ε_2 throughout the entire scattering angle range. It could be clearly observed from the figure that with the increase in the dielectric constant ε_2, the scattering coefficient changed at each scattering angle but this change was not monotonous. At some specific scattering angles, a significant peak was observed in the scattering coefficient; at other angles, it might decrease. This complex trend reflected the complex impact of the dielectric constant ε_2 on the scattering process.

To better reveal the changing rules of the scattering coefficient with respect to the dielectric constant, we plotted Fig. 9 (b), which presented the changes in the scattering coefficient within the scattering angle range -90°∼75°. In particular, when the dielectric constant was $\varepsilon_2 = 5.0$, the electromagnetic scattering of the layered rough surface would simplify to that of a single rough surface. It could be seen from Fig. 9 (b) that at large scattering angles, the scattering coefficient of the layered rough surface was always greater than that of a single rough surface. Additionally, with the increase in $|\varepsilon_1 - \varepsilon_2|$, the scattering coefficient of the layered rough surface also showed an increasing trend. This trend might be attributed to the gradually enhanced scattering effect of electromagnetic waves by the lower medium as $|\varepsilon_1 - \varepsilon_2|$ increased.

In summary, through applying the IGFBM-SAA method, we conducted an in-depth investigation into the impact of changes in the dielectric constant on the scattering process of rough surfaces. The investigation revealed that, regardless of how the dielectric constant changed, the scattering coefficient of the layered rough surface at some specific scattering angles was always greater than that of a single rough surface. Especially at large scattering angles, the scattering coefficient of the layered rough surface showed an increasing trend. This trend might be because the layered rough surface exhibits more complex scattering characteristics during the propagation of electromagnetic waves.

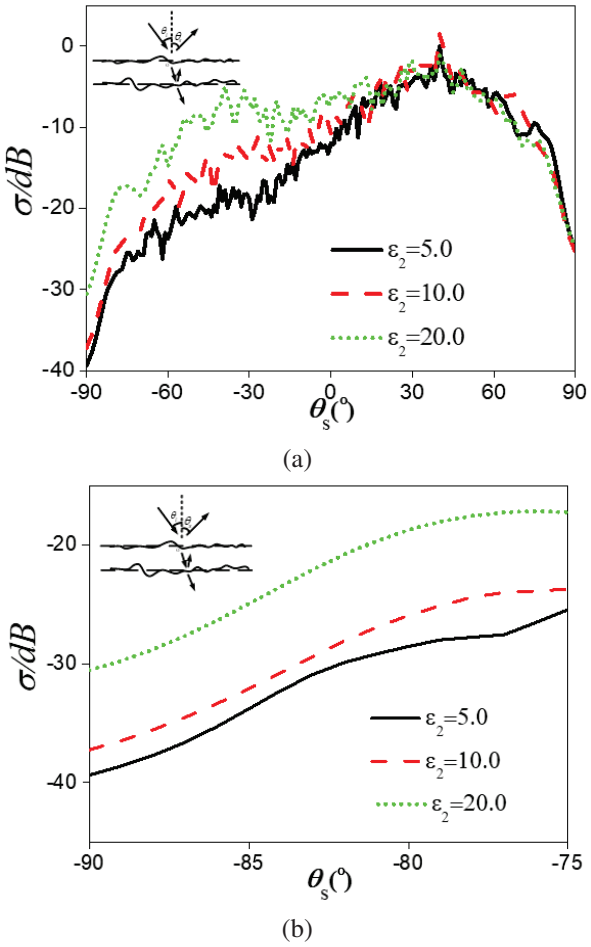

Fig. 9. Scattering coefficient comparison chart for different lower rough surface permittivity values: (a)-90°∼90° and (b) -90°∼75°.

V. CONCLUSION

This article proposes an innovative I-GFBM-SAA algorithm for effectively solving the electromagnetic scattering problem of rough surfaces. This algorithm significantly reduces the calculation workload from $o(N^3)$ to $o(N)$, thereby greatly saving computational time and improving computational efficiency. At the same time, this algorithm exhibits good convergence behavior under different calculation conditions, making it able to meet the computational needs of different application scenarios. The next research direction will be to incorporate targets (conductors and dielectrics) into the environment to further improve the electromagnetic scattering model and study composite electromagnetic scattering problems.

REFERENCES

[1] B. Wang, W. H. Wang, J. Fan, K. Q. Zhao, F. L. Zhou, and L. W. Tan, "Modeling of bistatic scattering from an underwater non-penetrable target using a Kirchhoff approximation method," *Defence Technology,* vol. 18, no. 7, pp. 1097-1106, 2022.

[2] P. Nicolas, B. L. Cedric, and B. Christophe, "Modeling of EM wave coherent scattering from a rough multilayered medium with the scalar Kirchhoff approximation for GPR applications," *IEEE Transactions on Geoscience and Remote Sensing,* vol. 58, no. 3, pp. 1654-1664, 2020.

[3] L. E. Richards, C. H. Song, and S. W. Hodgkiss, "Acoustic scattering comparison of Kirchhoff approximation to Rayleigh-Fourier method for sinusoidal surface waves at low grazing angles," *The Journal of the Acoustical Society of America,* vol. 144, no. 3, pp. 1269-1278, 2018.

[4] J. Tian, J. Tong, J. Shi, and L. Gui, "A new approximate fast method of computing the scattering from multilayer rough surfaces based on the Kirchhoff approximation," *Radio Science,* vol. 52, no. 2, pp. 186-195, 2017.

[5] W. Qing, L. Chen, Z. L. Ya, H. J. Qiang, and L. Lei, "High-order small perturbation method of arbitrary order for conducting rough surface scattering under TE incidence," *Applied Computational Electromagnetics Society (ACES) Journal,* vol. 35, no. 6, pp. 601-612, 2020.

[6] M. F. Arshad, A. Anwar, and M. A. Aqueel, "Perturbation method to study scattering from a dielectric-chiral rough interface," *Waves in Random and Complex Media,* vol. 31, no. 4, pp. 712-730, 2019.

[7] A. Saddek and D. Richard, "Scattering from 2-D perfect electromagnetic conductor rough surface: Analysis with the small perturbation method and the small-slope approximation," *IEEE Transactions on Antennas and Propagation,* vol. 66, no. 1, pp. 340-346, 2018.

[8] M. Sanamzadeh, L. Tsang, J. Johnson, R. Burkholder, and S. Tan, "Electromagnetic scattering from one dimensional random rough surfaces of dielectric layered media with waveguide modes using second order small perturbation method," *Progress In Electromagnetics Research B,* vol. 80, pp. 1-17, 2018.

[9] B. Auguié, W. R. C. Somerville, S. Roache, and E. C. L. Re, "Numerical investigation of the Rayleigh hypothesis for electromagnetic scattering by a particle," *Journal of Optics,* vol. 18, no. 7, 2016.

[10] C. Q. Shang, S. Z. Wu, T. Qu, and Z. J. Li, "Rayleigh model for electromagnetic scattering from a chiral sphere," *Procedia Engineering,* vol. 102, pp. 226-232, 2015.

[11] X. C. Li, X. Min, and D. D. Liu, "Rayleigh approximation for the scattering of small partially charged sand particles," *Journal of the Optical Society of America. A, Optics, Image Science, and Vision,* vol. 31, no. 7, pp. 1495-1501, 2014.

[12] K. C. Wang, Z. He, D. Z. Ding, and R. S. Chen, "Uncertainty scattering analysis of 3-D objects with varying shape based on method of moments," *IEEE Transactions on Antennas and Propagation,* vol. 67, no. 4, pp. 2835-2840, 2019.

[13] J. Chen, M. Zhu, M. Wang, S. Li, and X. Li, "A hybrid MoM-PO method combining ACA technique for electromagnetic scattering from target above a rough surface," *Applied Computational Electromagnetics Society (ACES) Journal,* vol. 29, no. 4, pp. 301-306, 2014.

[14] N. Basta and D. I. Olćan, "Scattering from anisotropic surfaces analyzed with method of moments," *Microwave and Optical Technology Letters,* vol. 60, no. 7, pp. 1782-1787, 2018.

[15] A. M. Mojtaba, S. S. H. Hesamedin, and D. A. Mojtaba, "A method of moments for analysis of electromagnetic scattering from inhomogeneous anisotropic bodies of revolution," *IEEE Transactions on Antennas and Propagation,* vol. 66, no. 6, pp. 2976-2986, 2018.

[16] S. Liu, B. Zou, and L. M. Zhang, "An FDTD-based method for difference scattering from a target above a randomly rough surface," *IEEE Transactions on Antennas and Propagation,* vol. 69, no. 4, pp. 2427-2432, 2021.

[17] H. Zamani, P. Dehkhoda, and A. Tavakoli, "Scattering by a three-dimensional buried object beneath multilayered rough surface illuminated by a collimated microwave Gaussian pulse," *AEUE - International Journal of Electronics and Communications,* vol. 123, 2020.

[18] R. C. Bollimuntha, F. M. Hadi, J. M. Piket-May, and A. Z. Elsherbeni, "Dispersion optimised plane wave sources for scattering analysis with integral based high order finite difference time domain methods," *IET Microwaves, Antennas & Propagation,* vol. 10, no. 9, pp. 976-982, 2016.

[19] J. Li, X. L. Guo, and H. Zeng, "FDTD investigation on electromagnetic scattering from two-dimensional layered rough surfaces," *Applied Computational Electromagnetics Society (ACES) Journal,* vol. 25, no. 5, pp. 450-457, 2010.

[20] D. Hrvoje, P. Dragan, and C. Mario, "On the edge element boundary element method/finite element method coupling for time harmonic electromagnetic scattering problems," *International Journal*

for Numerical Methods in Engineering, vol. 122, no. 14, pp. 3613-3652, 2021.

[21] J. J. Harman, C. Key, D. Estep, T. Butler, and B. M. Notaros, "Adjoint-based accelerated adaptive refinement in frequency domain 3-D finite element method scattering problems," *IEEE Transactions on Antennas and Propagation,* vol. 69, no. 2, pp. 940-949, 2021.

[22] X. Xu, C. Brekke, A. P. Doulgeris, and F. Melandsø, "Numerical analysis of microwave scattering from layered sea ice based on the finite element method," *Remote Sensing,* vol. 10, no. 9, p. 1332, 2018.

[23] Y. J. Wang, C. M. Tong, T. Wang, X. M. Li, and Q. K. Wang, "EM scattering of a target above canyon/valley environment based on composite rough surface modeling method and modified SBR-FBSSA algorithm," *Applied Sciences,* vol. 13, no. 7, p. 4427, 2023.

[24] Y. L. Du, J. J. Yin, X. Li, F. Gao, and J. Yang, "Accurate and efficient solution of electromagnetic scattering from randomly rough surface using MoM-SMCG with adaptive quadrature," *Electronics Letters,* vol. 57, no. 18, pp. 694-696, 2021.

[25] L. Li and J. Xu, "Electromagnetic scattering from perfectly conducting periodic rough surfaces using discrete two-level complex images method," *IOP Conference Series Materials Science and Engineering,* vol. 780, no. 5, 2020.

[26] A. Wang, J. Wang, Z. Huang, L. Guo, and T. Jian, "Fast simulations of electromagnetic scattering from one-dimensional rough surface over a frequency band using hybrid AMCBFM-Maehly method," *Journal of Engineering,* vol. 7, pp. 184622-184628, 2020.

[27] X. M. Li, J. J. Li, G. Qian, and P. C. Gao, "A hybrid method of solving near-zone composite electromagnetic scattering from targets and underlying rough surface," *Chinese Physics B,* vol. 29, no. 2, 2020.

[28] J. J. Wang, A. Q. Wang, T. Z. Jiang, and Z. X. Huang, "A fast algorithm for electromagnetic scattering from one-dimensional rough surface," *International Journal of Antennas and Propagation,* vol. 2019, no. 11, pp. 1-7, 2019.

[29] C. D. Moss, T. K. Grzegorczyk, H. C. Han, and A. K. Jin, "Forward-backward method with spectral acceleration for scattering from layered rough surfaces," *IEEE Trans Antennas Propagation,* vol. 54, no. 3, pp. 1006-1016, 2006.

[30] A. Iodice, "Forward-backward method for scattering from dielectric rough surfaces," *IEEE Trans. Antennas Propagation,* vol. 50, no. 7, pp. 901-911, 2002.

[31] D. Torrungrueng, H. T. Chou, and J. T. Johnson, "A novel acceleration algorithm for the computation of scattering from two-dimensional large-scale perfectly conducting random rough surfaces with the forward-backward method," *IEEE Trans. on Geoscience and Remote Sensing,* vol. 38, no. 4, pp. 1656-1668, 2000.

[32] H. T. Chou and J. T. Johnson, "A novel acceleration algorithm for the computation of scattering from rough surfaces with a forward-backward method," *Radio Science,* vol. 33, no. 5, pp. 1277-1287, 1998.

[33] A. Thorsos, "The validity of the Kirchhoff approximation for rough surface scattering using a Gaussian roughness spectrum," *Journal of the Acoustical Society of America,* vol. 83, no. 1, pp. 78-92, 1988.

Lilan Lei was born in Jiangxi, China. She received the bachelor's and master's degrees from Jiangxi Normal University, Jiangxi, China, in 2002 and 2009, respectively. Her research interests include computer applications and computer communication.

Solving Surface-volume Integral Equations for PEC and Inhomogeneous/Anisotropic Materials with Multibranch Basis Functions

Rui Liu, Gaobiao Xiao, and Yuyang Hu

State Key Laboratory of Radio Frequency Heterogeneous Integration, Department of Electronic Engineering
Shanghai Jiao Tong University, Shanghai, 200240, China
Liurui_sjtu@sjtu.edu.cn, gaobiaoxiao@sjtu.edu.cn

***Abstract* –** Multibranch basis functions have been confirmed to be effective for local refinement of domain decomposition methods in the application of solving surface and volume integral equations. Surface-volume integral equations (SVIEs) are applied for solving the hybrid electromagnetic scattering problems involving perfect electric conductors (PEC) and dielectrics, especially inhomogeneous and anisotropic media. In this paper, multibranch Rao-Wilton-Glisson basis functions (MB-RWGs) are applied in conjunction with multibranch Schaubert-Wilton-Glisson basis functions (MB-SWGs) for solving the SVIEs. Block diagonal preconditioners (BDPs) are used to accelerate the iteration convergence based on generalized minimum residual (GMRES) algorithms. The numerical results demonstrate the accuracy of the multibranch basis functions in solving SVIEs, and also show that proper BDPs can accelerate the iteration convergency.

***Index Terms* –** block diagonal preconditioner, MB-RWG, MB-SWG, surface-volume integral equations (SVIEs).

I. INTRODUCTION

With the increasing complexity of electronic structures and material characteristics, the analysis of scattering problems becomes more and more challenging. We need to consider hybrid structures with perfect electric conductors (PEC) and dielectric scatterers, or even including inhomogeneous and anisotropic media. Integral equation methods have been widely used for electromagnetic scattering problems. PEC and simple medium can be efficiently analyzed with surface integral equations (SIEs) [1–4], while for anisotropic and inhomogeneous media, volume integral equations (VIEs) [5–8] may have to be used. To solve these two types of integral equations (IEs), Rao-Wilton-Glisson basis functions (RWGs) [1] and Schaubert-Wilton-Glisson basis functions (SWGs) [5] have been widely applied for over four decades. Recently, as an extension of the two kinds of basis functions, multibranch Rao-Wilton-Glisson (MB-RWGs) and multibranch Schaubert-Wilton-Glisson (MB-SWGs) basis functions are proposed for domain decomposition and local refinement [3][7]. It has been confirmed that these two kinds of basis functions have almost the same characteristics of the related traditional basis functions and have advantages in flexibility when applied for solving SIEs and VIEs. In this paper, we focus on analyzing hybrid objects that include inhomogeneous and anisotropic dielectric scattering objects. Both MB-RWGs and MB-SWGs are applied, together with traditional RWGs and SWGs, to solve the surface-volume integral equations (SVIEs) [9–12] for these objects.

When applying method of moments (MoM), the impedance matrix is usually a dense matrix and it is time-consuming to solve the matrix equation with LU decomposition directly. Iterative algorithms, like the generalized minimum residual (GMRES) algorithm, conjugate gradient (CG) algorithm, and so on, are well used as solvers. However, with more complex structures and diversified materials, the characteristics of the impedance matrix becomes worse. It is difficult to converge even using iterative algorithms. An effective approach to improve the behavior of the matrix is to apply preconditioners [13–15]. In this paper, we use block diagonal preconditioners (BDP) to accelerate the iterative process.

The remainder of this paper is organized as follows: SVIEs are introduced in Section II, along with the matrix equations applied with (MB-)RWGs/SWGs and the method to generate BDPs. Two numerical examples are shown in Section III, with a conclusion in Section IV.

II. SVIES FORMULATION

Consider an arbitrary hybrid PEC and anisotropic dielectric scattering body (S_{pec} and V_D) illuminated by an incident field $\left(E^{inc}\mathbf{H}^{inc}\right)$. The relative tensor permittivity and permeability of the dielectric are $\bar{\varepsilon}_r$ and $\bar{\mu}_r$. The SVIEs can be written as:

$$\mathscr{L}_E\left(\mathbf{J}\left(\mathbf{r}'\right)\right)+\mathscr{K}\left(\mathbf{M}\left(\mathbf{r}'\right)\right)+\mathscr{L}_E\left(\mathbf{J}_S\left(\mathbf{r}'\right)\right)+\mathbf{E}^{\text{tot}}\left(\mathbf{r}\right) = \mathbf{E}^{inc}(\mathbf{r}), \mathbf{r}\in V_D,$$

Submitted On: June 30, 2023
Accepted On: April 1, 2024

https://doi.org/10.13052/2024.ACES.J.390203

$$\begin{aligned}
&\mathscr{L}_M\left(\mathbf{M}\left(\mathbf{r}'\right)\right)-\mathscr{K}\left(\mathbf{J}\left(\mathbf{r}'\right)\right)-\mathscr{K}\left(\mathbf{J}_S\left(\mathbf{r}'\right)\right)+\mathbf{H}^{\text{tot}}\left(\mathbf{r}\right)\\
&\quad=\mathbf{H}^{inc}(\mathbf{r}),\mathbf{r}\in V_D,\\
&\hat{\mathbf{n}}\times\left\{\mathscr{L}_E\left(\mathbf{J}\left(\mathbf{r}'\right)\right)+\mathscr{K}\left(\mathbf{M}\left(\mathbf{r}'\right)\right)+\mathscr{L}_E\left(\mathbf{J}_S\left(\mathbf{r}'\right)\right)\right\}\\
&\quad=\hat{\mathbf{n}}\times\mathbf{E}^{inc}(\mathbf{r}),\mathbf{r}\in S_{pec},
\end{aligned}\tag{1}$$

where the operators are formulated as:

$$\begin{aligned}
\mathscr{L}_E(\mathbf{f})&=j\omega\mu_0\int_\Omega\left(\bar{I}+\frac{\nabla\nabla}{k_0^2}\right)g_0\bullet\mathbf{f}d\mathbf{r}',\\
\mathscr{L}_M(\mathbf{f})&=j\omega\varepsilon_0\int_\Omega\left(\bar{I}+\frac{\nabla\nabla}{k_0^2}\right)g_0\bullet\mathbf{f}d\mathbf{r}',\\
\mathscr{K}(\mathbf{f})&=p\cdot v\cdot\nabla\times\int_\Omega\mathbf{f}\cdot g_0d\mathbf{r}',
\end{aligned}\tag{2}$$

and $g_0=e^{-jkR}/4\pi R, R=|\mathbf{r}-\mathbf{r}'|$is three dimensional Green's function in free space, $\mathbf{r}$ and $\mathbf{r}'$ represent the field point and source point, respectively. The integration region Ω is V_D and S_{pec} means volume integral for dielectric scatterer and surface integral for PEC scatter, respectively. In equation (1), $\mathbf{J}$, $\mathbf{M}$, $\mathbf{J}_s$ are polarized electric current, polarized magnetic current, and equivalent surface current, respectively. E^{tot} and $\mathbf{H}^{tot}$ are total electric and magnetic fields in the interior region of the dielectric scattering object. According to the constitutive relation, $\mathbf{J}$, $\mathbf{M}$, E^{tot}, and $\mathbf{H}^{tot}$ can be replaced by polarized electric displacement $\mathbf{D}$and polarized magnetic flux density $\mathbf{B}$ as:

$$\begin{aligned}
\mathbf{J}&=j\omega\left(\bar{\varepsilon}_r-\bar{I}\right)\mathrm{g}\bar{\varepsilon}_r^{-1}\mathbf{gD}\\
\mathbf{M}&=j\omega\left(\bar{\mu}_r-\bar{I}\right)\mathrm{g}\bar{\mu}_r^{-1}\mathrm{gB}\\
\mathbf{E}^{tot}&=\bar{\varepsilon}_r^{-1}\,\mathrm{g}\mathbf{D}/\varepsilon_0\\
\mathbf{H}^{\text{tot}}&=\bar{\mu}_r^{-1}\mathrm{gB}/\mu_0
\end{aligned}.\tag{3}$$

To solve the SVIEs, traditional RWG and SWG basis functions are defined as:

$$\mathbf{f}(\mathbf{r})=\begin{cases}\frac{l}{2A^+}\left(\mathbf{r}-\mathbf{r}_0^+\right),r\in S^+\\ \frac{l}{2A^-}\left(\mathbf{r}-\mathbf{r}_0^-\right),r\in S^-\\ 0,\ \text{otherwise}\end{cases},$$

$$\mathbf{h}(\mathbf{r})=\begin{cases}\frac{s}{3W^+}\left(\mathbf{r}-\mathbf{r}_0^+\right),r\in T^+\\ \frac{s}{3W^-}\left(\mathbf{r}-\mathbf{r}_0^-\right),r\in T^-\\ 0,\ \text{otherwise}\end{cases},\tag{4}$$

where $S^\pm$ and $T^\pm$ response to positive/negative triangle and tetrahedron in RWGs and SWGs, $\mathbf{r}_0^\pm$ is the positive/negative free node in both basis functions, l and $A^\pm$ are the length of common line and the area of positive/negative triangle for RWGs, meanwhile s and $W^\pm$ are the area of common surface and the volume of positive/negative tetrahedron for SWGs. The MB-RWGs and MB-SWGs are defined with similar formulation as shown in equations (5) and (6) [3], [7]:

$$\mathbf{f}^{MB}(\mathbf{r})=\begin{cases}\frac{l_i^+}{2A_i^+}\left(\mathbf{r}-\mathbf{r}_i^+\right),r\in S_i^+,i=1,\ \mathrm{L},N^+\\ \frac{l_j^-}{2A_j^-}\left(\mathbf{r}-\mathbf{r}_j^-\right),r\in S_j^-,j=1,\ \mathrm{L},N^-\\ 0,\ \text{otherwise}\end{cases},\tag{5}$$

$$\mathbf{h}^{MB}(\mathbf{r})=\begin{cases}\frac{s_i^+}{3W_i^+}\left(\mathbf{r}-\mathbf{r}_i^+\right),r\in T_i^+,i=1,\ \mathrm{L},N^+\\ \frac{s_j^-}{3W_j^-}\left(\mathbf{r}-\mathbf{r}_j^-\right),r\in T_j^-,j=1,\ \mathrm{L},N^-\\ 0,\ \text{otherwise}\end{cases}.\tag{6}$$

If meshing the PEC surface and the dielectric separately, we may encounter nonconformal meshes on the interface between them. It is also possible to use half SWG basis functions (HSWGs) $\mathbf{h}^H$ in the analysis [6]. Then, $\mathbf{D}$, $\mathbf{B}$, and $\mathbf{J}_s$, are expanded by these basis functions (shorted as $\mathbf{b}$ in total) mentioned above and formulated as:

$$\begin{aligned}
\mathbf{D}(\mathbf{r})&=\sum_{i=1}^{N^S}c_{D,i}^{N^S}\mathbf{h}_i(\mathbf{r})+\sum_{i=1}^{N^{HS}}c_{D,i}^{N^{HS}}\mathbf{h}_i^H(\mathbf{r})+\sum_{i=1}^{N^{MBS}}c_{D,i}^{N^{MGS}}\mathbf{h}_i^{MB}(\mathbf{r}),\\
\mathbf{B}(\mathbf{r})&=\sum_{i=1}^{N^S}c_{B,i}^{N^S}\mathbf{h}_i(\mathbf{r})+\sum_{i=1}^{N^{HS}}c_{B,i}^{N^{HS}}\mathbf{h}_i^H(\mathbf{r})+\sum_{i=1}^{N^{MBS}}c_{B,i}^{N^{MGS}}\mathbf{h}_i^{MB}(\mathbf{r}),\\
\mathbf{J}_s(\mathbf{r})&=\sum_{i=1}^{N^R}c_{J,i}^{N^R}\mathbf{f}_i(\mathbf{r})+\sum_{i=1}^{N^{MBR}}c_{J,i}^{N^{MBR}}\mathbf{f}_i^{MB}(\mathbf{r}),
\end{aligned}\tag{7}$$

where S, HS, MBS, R, and MBR are the labels to represent related SWG, HSWG, MBSWGs RWG, and MBRWG basis functions (shorted as BF in total), N^{BF} are the numbers of basis functions, respectively, and $c_m^{N^{BF}}$, where $m=D,B,J$, are the coefficients of different sources and basis functions.

According to MoM, testing the first two equations in equation (1) by SWG series functions and testing the tangential components of the fields in the last equation in equation (1) by the tangential components of RWG series functions, we can convert it in matrix formulation as equation (8), with elements formulas listed under it

$$\begin{pmatrix}
Z_1^{S,S} & Z_2^{S,S} & Z_1^{S,HS} & Z_2^{S,HS} & Z_1^{S,MBS} & Z_2^{S,MBS} & Z_E^{S,R} & Z_E^{S,MBR}\\
Z_3^{S,S} & Z_4^{S,S} & Z_3^{S,HS} & Z_4^{S,HS} & Z_3^{S,MBS} & Z_4^{S,MBS} & Z_H^{S,R} & Z_E^{S,MBR}\\
Z_1^{HS,S} & Z_2^{HS,S} & Z_1^{HS,HS} & Z_2^{HS,HS} & Z_1^{HS,MBS} & Z_2^{HS,MBS} & Z_E^{HS,R} & Z_E^{HS,MBR}\\
Z_3^{HS,S} & Z_4^{HS,S} & Z_3^{HS,HS} & Z_4^{HS,HS} & Z_3^{HS,MBS} & Z_4^{HS,MBS} & Z_H^{HS,R} & Z_H^{HS,MBR}\\
Z_1^{MBS,S} & Z_2^{MBS,S} & Z_1^{MBS,HS} & Z_2^{MBS,HS} & Z_1^{MBS,MBS} & Z_2^{MBS,MBS} & Z_E^{MBS,R} & Z_E^{MBS,MBR}\\
Z_3^{MBS,S} & Z_4^{MBS,S} & Z_3^{MBS,HS} & Z_4^{MBS,HS} & Z_3^{MBS,MBS} & Z_4^{MBS,MBS} & Z_H^{MBS,R} & Z_H^{MBS,MBR}\\
Z_1^{R,S} & Z_2^{R,S} & Z_1^{R,HS} & Z_2^{R,HS} & Z_1^{R,MBS} & Z_2^{R,MBS} & Z_E^{R,R} & Z_E^{R,MBR}\\
Z_1^{MBR,S} & Z_2^{MBR,S} & Z_1^{MBR,HS} & Z_2^{MBR,HS} & Z_1^{MBR,MBS} & Z_2^{MBR,MBS} & Z_E^{MBR,R} & Z_E^{MBR,MBR}
\end{pmatrix}\bullet\begin{pmatrix}C_D^S\\ C_B^S\\ C_D^{HS}\\ C_B^{HS}\\ C_D^{MBS}\\ C_B^{MBS}\\ C^R\\ C^{MBR}\end{pmatrix}=\begin{pmatrix}E^S\\ H^S\\ E^{HS}\\ H^{HS}\\ E^{MBS}\\ H^{MBS}\\ E^R\\ E^{MBR}\end{pmatrix}.\tag{8}$$

$$
\begin{aligned}
Z_1^{S,S}(\mathbf{h}_m,\mathbf{h}_n) &= \left\langle \mathbf{h}_m, j\omega\mathscr{L}_E\left((\bar{\varepsilon}_r-\bar{I})\bullet\bar{\varepsilon}_r^{-1}\bullet h_n\right)\right. \\
&\quad \left. +\bar{\varepsilon}_r^{-1}\bullet h_n/\varepsilon_0\right\rangle, \\
Z_1^{R,S}(\mathbf{f}_m,\mathbf{h}_n) &= \left\langle \mathbf{f}_m, j\omega\mathscr{L}_E\left((\bar{\varepsilon}_r-\bar{I})\bullet\bar{\varepsilon}_r^{-1}\bullet h_n\right)\right\rangle, \\
Z_2^{S,S}(\mathbf{h}_m,\mathbf{h}_n) &= \left\langle \mathbf{h}_m, j\omega\mathscr{K}\left((\bar{\mu}_r-\bar{I})\bullet\bar{\mu}_r^{-1}\bullet h_n\right)\right\rangle, \\
Z_2^{R,S}(\mathbf{f}_m,\mathbf{h}_n) &= \left\langle \mathbf{f}_m, j\omega\mathscr{K}\left((\bar{\mu}_r-\bar{I})\bullet\bar{\mu}_r^{-1}\bullet h_n\right)\right\rangle, \\
Z_3^{S,S}(\mathbf{h}_m,\mathbf{h}_n) &= \left\langle \mathbf{h}_m, j\omega\mathscr{K}\left((\bar{\mu}_r-\bar{I})\bullet\bar{\mu}_r^{-1}\bullet h_n\right)\right\rangle, \\
Z_4^{S,S}(\mathbf{h}_m,\mathbf{h}_n) &= \left\langle \mathbf{h}_m, j\omega\mathscr{L}_M\left((\bar{\mu}_r-\bar{I})\bullet\bar{\mu}_r^{-1}\bullet h_n\right)\right. \\
&\quad \left. +\bar{\mu}_r^{-1}\bullet h_n/\mu_0\right\rangle, \\
Z_E^{R,R}(\mathbf{f}_m,\mathbf{f}_n) &= \left\langle \mathbf{f}_m, \mathscr{L}_E(f_n)\right\rangle, \\
Z_E^{S,R}(\mathbf{h}_m,\mathbf{f}_n) &= \left\langle \mathbf{h}_m, \mathscr{L}_E(f_n)\right\rangle, \\
Z_H^{S,R}(\mathbf{h}_m,\mathbf{f}_n) &= \left\langle \mathbf{h}_m, -\mathscr{K}(f_n)\right\rangle,
\end{aligned}
$$

where $\langle \mathbf{a},\mathbf{b}\rangle$ is the inner product of vector $\mathbf{a}$ and $\mathbf{b}$. The number of test functions is subscripts $m=1,\cdots,N^S$ for SWGs and $m=1,\cdots,N^R$ for RWGs as test functions, $n=1,\cdots,N^S$ for SWGs and $n=1,\cdots,N^R$ for RWGs as basis functions.

If we rearrange the variables according to the type of the basis functions, the impedance matrix can be simply denoted by:

$$
\bar{Z}=\begin{pmatrix}
Z^{S,S} & Z^{S,HS} & Z^{S,MBS} & Z^{S,R} & Z^{S,MBR} \\
Z^{HS,S} & Z^{HS,HS} & Z^{HS,MBS} & Z^{HS,R} & Z^{HS,MBR} \\
Z^{MBS,S} & Z^{MBS,HS} & Z^{MBS,MBS} & Z^{MBS,R} & Z^{MBS,MBR} \\
Z^{R,S} & Z^{R,HS} & Z^{R,MBS} & Z^{R,R} & Z^{R,MBR} \\
Z^{MBR,S} & Z^{MBR,HS} & Z^{MBR,MBS} & Z^{MBR,R} & Z^{MBR,MBR}
\end{pmatrix}. \tag{9}
$$

To accelerate the iterative progress, it is important to establish a proper precondition matrix $\bar{P}$ to improve the convergence rate of the iterative solver. In this paper, a left BDP matrix is used to transform:

$$
\bar{Z}\bullet\mathbf{C}=\mathbf{E}, \tag{10}
$$

into:

$$
(\bar{P})^{-1}\bullet\bar{Z}\bullet\mathbf{C}=(\bar{P})^{-1}\bullet\mathbf{E}. \tag{11}
$$

The left BDP matrix has different formulations. Here, four different BDPs are constructed and applied to the matrix function independently.

The first preconditioner is constructed by the block matrix along the diagonal line in equation (9) and formulated as:

$$
\bar{P}_{1a}=diag\left(Z^{S,S}\ Z^{HS,HS}\ Z^{MBS,MBS}\ Z^{R,R}\ Z^{MBR,MBR}\right). \tag{12}
$$

According to the difference between **J** (**M**) and **D** (**B**) in equation (3), in order to balance the elements of dielectric part and PEC part, the second preconditioner is constructed by dividing the $j\omega$ and formulated as:

$$
\bar{P}_{1b}=diag\left(\frac{Z^{S,S}}{j\omega}\ \frac{Z^{HS,HS}}{j\omega}\ \frac{Z^{MBS,MBS}}{j\omega}\ Z^{R,R}\ Z^{MBR,MBR}\right). \tag{13}
$$

Similarly, the third and the fourth preconditioners are constructed by the block matrix along the diagonal line in equation (8) with $j\omega$ only divided in the fourth preconditioner, and formulated as:

$$
\bar{P}_{2a}=diag\left(Z_1^{S,S}\ \cdots\ Z_4^{MBS,MBS}\ Z_E^{R,R}\ Z_E^{MBR,MBR}\right), \tag{14}
$$

$$
\bar{P}_{2b}=diag\left(\frac{Z_1^{S,S}}{j\omega}\ \cdots\ \frac{Z_4^{MBS,MBS}}{j\omega}\ Z_E^{R,R}\ Z_E^{MBR,MBR}\right). \tag{15}
$$

Finally, according to equations (10) and (11), these four BDPs are applied to original matrix equation independently.

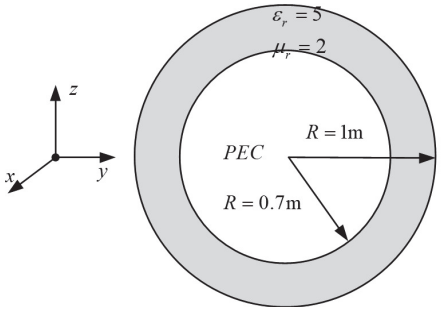

Fig. 1. Two-layered sphere with a PEC core and a dielectric shell.

III. NUMERICAL EXAMPLES

Two numerical examples are considered. In both cases, the scattering objects consist of a PEC part and a dielectric part. They are illuminated by a x-polarized plane wave travelling in -z axis. The PEC part and the dielectric part are independently constructed and meshed using COMSOL software. The relative error is defined as $20\log\left(\|\bar{x}-\bar{x}_0\|_2 / \|\bar{x}_0\|_2\right)$ to calculate the difference between results $\bar{x}$ and reference results $\bar{x}_0$.

We use the first numerical example to verify the accuracy of the algorithm and the effect of the preconditioners. The object is a two-layer sphere, centered at (000). The radius of the outer surface is 1.0 m, while the radius of the inner surface is 0.7 m. The frequency of the incident plane wave is 30 MHz. The inner part is a PEC sphere and the outer layer is a dielectric with relative permittivity and permeability as 5.0 and 2.0, respectively.

We have used two mesh structures to compare the accuracy and the convergence behavior. In case 1, the PEC surface and the dielectric part are meshed into 1320 triangles and 1946 tetrahedrons, respectively. The average length of the triangles is about $0.01\lambda_0$, λ_0 is the wavelength in free space. The average length of tetrahedrons is about $0.0763\lambda_D$, λ_D is the wavelength in the interior region of dielectric part. The mesh structure generates 1980 RWGs, 3543 SWGs, and 698 HSWGs. Hence, the dimension of the impedance matrix is 10462×10462. The mesh in case 2 is generated based on the mesh of case 1. From the meshes in case 1, we have selected the 162 triangles and 244 tetrahedrons in the region $x\geq 0$, $y\geq 0$, and $z\leq 0$ for local refinement. By

adding 3 additional nodes at the middle of the 3 edges of the triangle, each selected triangle is divided into 4 small triangles. Similarly, by adding 6 additional nodes at the middle of the 6 edges of the tetrahedron, each selected tetrahedron is divided into 8 small tetrahedrons. Hence, the refined meshes generate 2664 RWGs, 6692 SWGs, 962 HSWGs, 30 MBRWGs, and 54 MBSWGs in total. The dimension of the impedance matrix is changed to 18110×18110.

To reduce the number of iterations, the four preconditioners, discussed in Section II, are applied. All the preconditioners can greatly accelerate the convergence of the GMRES iteration solver under nearly the same accuracy. The Bi-RCSs, obtained for the two mesh structures, are compared with those obtained by Mie series, as illustrated in Fig. 2. The relative error is -17.65 dB in case 1 and -25.05 dB in case 2. Moreover, we have applied four BDPs in case 2.

The relative error stays the same when different BDPs are applied. The iteration property and singular values of the impedance matrix in different cases are illustrated in Figs. 3 and 4, respectively. The condition numbers of case 2 with or without different BDPs and numbers of iterations to achieve a residual error of 0.005 are listed in Table 1. Obviously, the singular values are more clustered and the number of iterations is smaller after application of preconditioners [16][17].

The second example is used to show the effect of local refinement for different materials. We consider a PEC cuboid, surrounded by two different materials and illuminated by a plane wave with frequency of 260 MHz, as shown in Fig. 5. The lengths of PEC cuboid along x, y, and z axis are 0.6 m, 0.1 m, and 0.1 m, respectively. The thickness of dielectric shell is 0.05 m. It consists of two kinds of materials. The dielectric in region 1 is

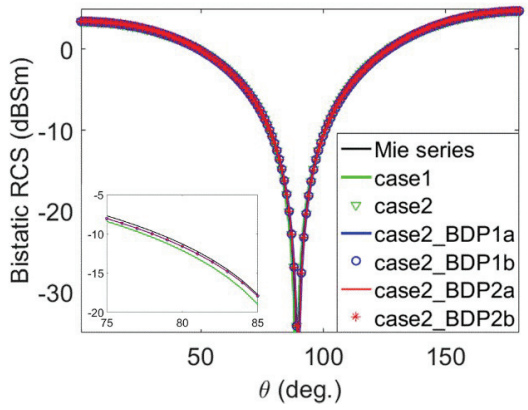

Fig. 2. Bistatic RCSs for case 1, case 2, and case 2 with two BDPs, Mie series.

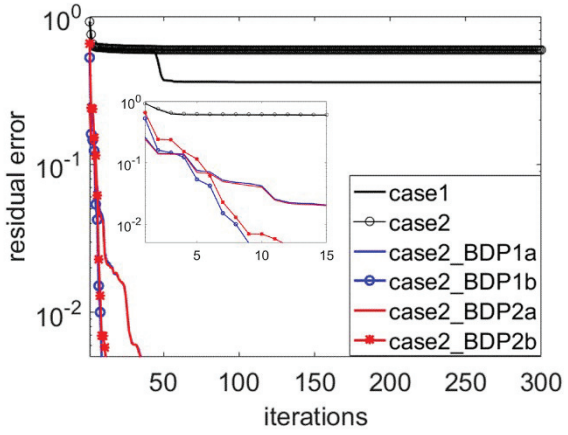

Fig. 3. Iteration convergencies for different methods.

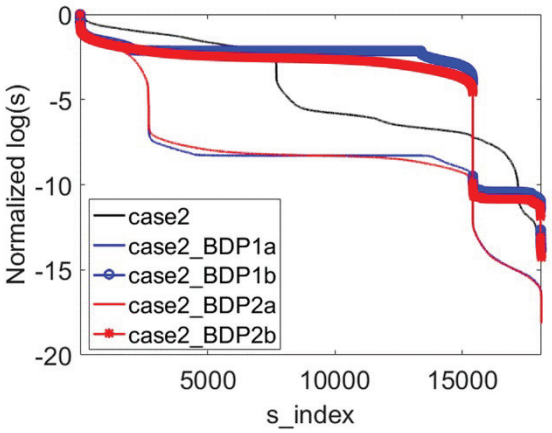

Fig. 4. The s values of SVD for different methods.

Table 1: Condition numbers and numbers of iterations

Case 2	Condition Number	Number of Iterations
without BDP	1.438×10^{13}	/
with BDP1a	1.356×10^{18}	35
with BDP1b	7.250×10^{13}	9
with BDP2a	1.356×10^{18}	35
with BDP2b	1.842×10^{14}	12

anisotropic materials, with parameters of:

$$\bar{\varepsilon}_{r1} = \begin{bmatrix} 8+0.2j & -0.4j & 0 \\ 0.4j & 8+0.2j & 0 \\ 0 & 0 & 8-0.1j \end{bmatrix},$$

$\mu_{r1} = 2$. The parameters of region 2 are $\varepsilon_{r2} = 2$, $\mu_{r2} = 1.5$. The wavelengths in the dielectric part are labeled as λ_n, where $n = 1, 2$ for different regions.

Firstly, we generate a fine mesh structure as a base for comparison. The surface of the PEC part is divided into 360 triangles, and the dielectric part is divided into

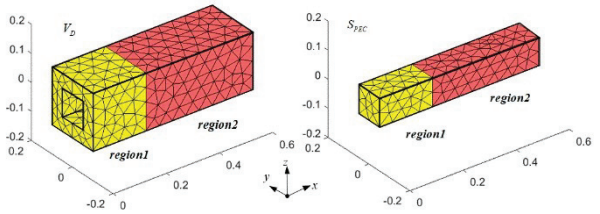

(a) (b)

Fig. 5. Model of the cuboid scatterer divided in w regions: (a) dielectric part and (b) PEC part.

2462 tetrahedrons. The fine mesh structure generates 4449 SWGs, 950 HSWGs, and 540 RWGs. The dimension of the impedance matrix is 11338×11338. The average lengths are $0.036\lambda_0$ for the PEC part, $0.19\lambda_1$ and $0.089\lambda_2$ for the dielectric part.

Secondly, we generate a coarse mesh structure as the base for local refinement, where the surface of the PEC part is divided into 104 triangles, and the dielectric part is divided into 402 tetrahedrons. The coarse mesh structure generates 658 SWGs, 292 HSWGs, and 156 RWGs. The dimension of the impedance matrix is 2056×2056. The average lengths are $0.066\lambda_0$ for the PEC part, $0.37\lambda_1$ and $0.16\lambda_2$ for the dielectric part.

Thirdly, based on the coarse mesh structure, progressive local refinements are considered to show the effect of different local refinement strategies. The refining approach for the selected part of meshes is the same as that in the first example.

In case 1, we only select the triangles/tetrahedrons in region 1 of PEC/dielectric part for local refinement, generating 2326 SWGs, 592 HSWGs, 12 MBSWGs, 312 RWGs, and 4 MBRWGs. The dimension of the impedance matrix is 6176×6176.

Case 2 is based on case 1. We find the 4 triangles on the PEC surface in region 2 that have one side locating on the bordering line with region 1, and then add them as additional region for local refinement. The numbers of RWGs, MBRWGs, and the dimension of the impedance matrix are changed to 324, 8, and 6192×6192, respectively.

Case 3 is also based on case 1. We find the 50 tetrahedrons in region 1 and region 3 of dielectric part that have a surface locating at the interface with region 2, then we add them for local refinement. The numbers of SWGs, HSWGs, MBSWGs, and the dimension of the impedance matrix are changed to 2446, 628, 24, and 6512×6512, respectively.

In case 4, both of the additional meshes in case 2 and case 3 are selected for local refinement. The dimension of the impedance matrix is changed to 6528×6528.

Obviously, the local refinement in case 1 has abrupt variation in mesh sizes in different material regions; in case 2, a transition region on the PEC surface is added; in case 3, a transition region in the dielectric region is added; and in case 4, both the transition regions are added. This is to show the effect of the different local refining strategies.

The results of the surface current on the PEC part and the Bi-RCSs of the object in the *xoz* plane in different cases are shown in Figs. 6 and 7, respectively. The

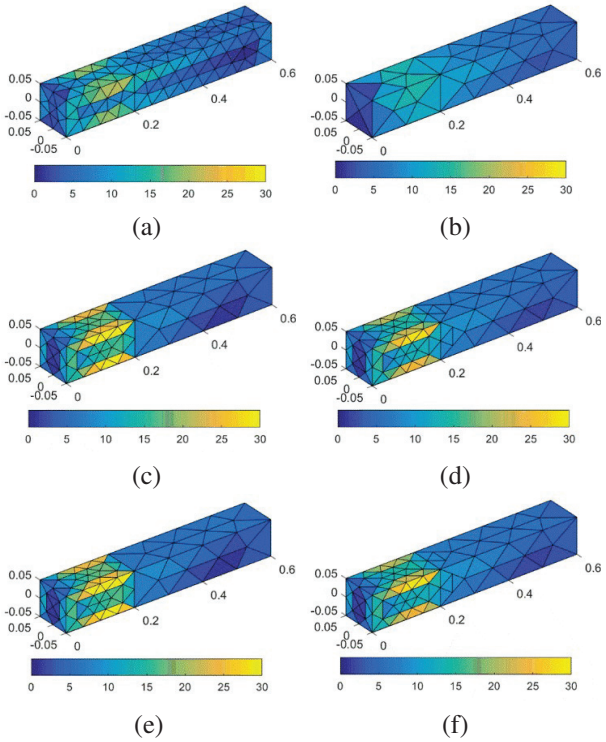

(a) (b) (c) (d) (e) (f)

Fig. 6. The surface currents of different cases (unit: mA/m): (a) fine case, (b) coarse case, and (c-f) case 1-4.

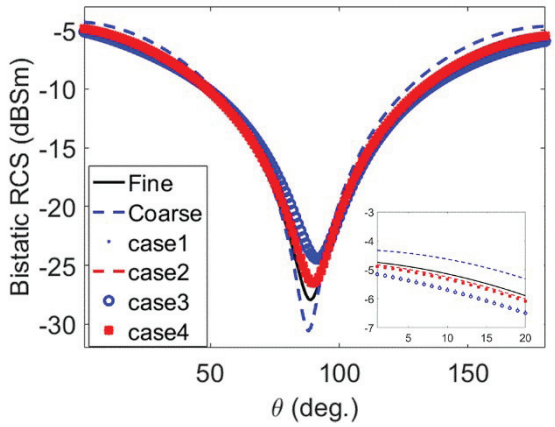

Fig. 7. The results of bistatic RCSs of different cases in *xoz* plane.

relative errors of Bi-RCSs of the coarse mesh and cases 1-4 are -24.47 dB, -21.44 dB, -30.31 dB, -20.52 dB, and -28.61 dB compared with the Bi-RCSs of the fine mesh as a reference result.

It can be seen that surface current on the PEC surface is greatly affected by the discontinuity between different materials where there is no transition area on the surface of the PEC object. The local refinement in coarse meshes improves the Bi-RCSs result. Hence, the MBSWGs and MBRWGs can be applied for hybrid PEC and dielectric structures, especially when local refinement is needed.

IV. CONCLUSION

MB-RWGs can be applied for solving SIEs, and MB-SWGs can be applied for solving VIEs. Both have nearly the same accuracy as that of using traditional RWGs and SWGs [3][7]. In this paper, it is demonstrated that MB-RWG and MB-SWG can also be applied for solving SVIEs in hybrid systems even consisting of inhomogeneous and anisotropic materials.

Although MB-RWGs and MB-SWGs are flexible for local refinement, numerical examples show that, when performing local refinement among different types of materials, it would be better to refine the regions in a progressive way so that the scale of the mesh structures between neighboring elements is not too different.

ACKNOWLEDGMENT

This work was supported by the National Science Foundation of China under Grant 62188102.

REFERENCES

[1] S. M. Rao, D. R. Wilton, and A. W. Glisson, "Electromagnetic scattering by surfaces of arbitrary shape," *IEEE Trans. Antennas Propagat*., vol. 30, no. 3, pp. 409-418, 1982.

[2] P. Yla-Oijala and M. Taskinen, "Well-conditioned Müller formulation for electromagnetic scattering by dielectric objects," *IEEE Trans. Antennas Propagat.*, vol. 53, no. 10, pp. 3316-3323, Oct. 2005.

[3] S. Huang, G. Xiao, Y. Hu, R. Liu, and J. Mao, "Multibranch Rao-Wilton-Glisson basis functions for electromagnetic scattering problems," *IEEE Trans. Antennas Propagat*., vol. 69, no. 10, pp. 6624-6634, Oct. 2021.

[4] F. P. Andriulli, F. Vipiana, and G. Vecchi, "Hierarchical bases for nonhierarchic 3-D triangular meshes," *IEEE Trans. Antennas Propagat.*, vol. 56, no. 8, pp. 2288-2297, Aug. 2008.

[5] D. H. Schaubert, D. R. Wilton, and A. W. Glisson, "A tetrahedral modeling method for electromagnetic scattering by arbitrarily shaped inhomogeneous dielectric bodies," *IEEE Trans. Antennas Propagat*., vol. 32, no. 1, pp. 77-85, Apr. 1984.

[6] L. M. Zhang and X. Q. Sheng, "Solving volume electric current integral equation with full- and half-SWG functions," *IEEE Antennas and Wirel. Propaga. Lett.*, vol. 14, pp. 682-685, 2015.

[7] R. Liu, G. Xiao, S. Huang, and Y. Hu, "Multibranch Schaubert-Wilton-Glisson basis functions for electromagnetic scattering problem," *IEEE Trans. Antennas Propagat*., vol. 70, no. 4, pp. 3100-3105, Apr. 2022.

[8] R. R. Chang, K. Chen, J. Wei, and M. S. Tong, "Reducing volume integrals to line integrals for some functions associated with Schaubert-Wilton-Glisson basis functions," *IEEE Trans. Antennas Propagat*., vol. 69, no. 5, pp. 3033-3038, May 2021.

[9] C. C. Lu and W. C. Chew, "A coupled surface-volume integral equation approach for the calculation of electromagnetic scattering from composite metallic and material targets," *IEEE Trans. Antennas Propagat.*, vol. 48, no. 12, pp. 1866-1868, Dec. 2000.

[10] Q. M. Cai, Y. W. Zhao, W. F. Huang, Y. T. Zheng, Z. P. Zhang, Z. P. Nie, and Q. H. Liu, "Volume surface integral equation method based on higher order hierarchical vector basis functions for EM scattering and radiation from composite metallic and dielectric structures," *IEEE Trans. Antennas Propagat.*, vol. 64, no. 12, pp. 5359-5372, Dec. 2016.

[11] A. C. Yucel, L. J. Gomez, and E. Michielssen, "Internally combined volume-surface integral equation for EM analysis of inhomogeneous negative permittivity plasma scatterers," *IEEE Trans. Antennas Propagat*., vol. 66, no. 4, pp. 1903-1913, Apr. 2018.

[12] B. J. Ward, "Hybrid surface electric field volume magnetic field integral equations for electromagnetic analysis of heterogeneous dielectric bodies with embedded electrically conducting structures," *IEEE Trans. Antennas Propagat*., vol. 69, no. 3, pp. 1545-1552, Mar. 2021.

[13] W. D. Li, W. Hong, and H. X. Zhou, "An IE-ODDM-MLFMA scheme with DILU preconditioner for analysis of electromagnetic scattering from large complex objects," *IEEE Trans. Antennas Propagat*., vol. 56, no. 5, pp. 1368-1380, May 2008.

[14] B. Kong, X. W. Huang, and X. Q. Sheng, "A discontinuous Galerkin surface integral solution for scattering from homogeneous objects with high dielectric constant," *IEEE Trans. Antennas*

Propagat., vol. 68, no. 1, pp. 598-603, Jan. 2020.

[15] S. Z. Gu, L. Zhang, D. M. Yu, K. W. Xu, L. M. Si, and X. M. Pan, "On preconditioners of the FFT-JVIE for inhomogeneous dielectric objects," *IEEE Trans. Antennas Propagat*., vol. 71, no. 6, pp. 5493-5497, June 2023.

[16] S. B. Adrian, A. Dely, D. Consoli, A. Merlini, and F. P. Andriulli, "Electromagnetic integral equations: Insights in conditioning and preconditioning," *IEEE Open Journal of Antennas and Propagation*, vol. 2, pp. 1143-1174, Dec. 2021.

[17] X. Antoine and M. Darbas, "An introduction to operator preconditioning for the fast iterative integral equation solution of time-harmonic scattering problems," *Multiscale Sci. Eng.*, vol. 3, pp. 1-35, Feb. 2021.

Rui Liu received B.S. degree from Shanghai Jiao Tong University, Shanghai, China, in 2017. He is currently pursuing Ph.D. degree in electronic engineering in Shanghai Jiao Tong University. His research interests include computational electromagnetics and inverse scattering problems.

Gaobiao Xiao received the B.S. degree from Huazhong University of Science and Technology, Wuhan, China, in 1988, M.S. degree from the National University of Defense Technology, Changsha, China, in 1991, and Ph.D. degree from Chiba University, Chiba, Japan, in 2002.

He has been a faculty member since 2004 in the Department of Electronic Engineering, Shanghai Jiao Tong University, Shanghai, China. His research interests are computational electromagnetics, coupled thermo-electromagnetic analysis, microwave filter designs, fiber-optic filter designs, phased array antennas, and inverse scattering problems.

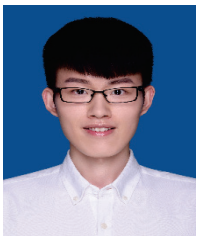

Yuyang Hu received B.S. degree in telecommunications engineering from Xidian University, Xi'an, China, in 2018. He is currently pursuing Ph.D. degree with the State Key Laboratory of Radio Frequency Heterogeneous Integration, Shanghai Jiao Tong University, Shanghai. His current research interests include computational electromagnetics and its application in scattering and radiation problems.

A Numerical Analysis of Conformal Energy Selective Surface Array with Synthetic Functions Expansion

Ning Hu[1], Yanlin Xu[2], and Peiguo Liu[2]

[1]Information Engineering University
Zhengzhou 450001, China
1141832906@qq.com

[2]College of Electronic Science of National University of Defense Technology
Changsha 410073, China
13298656824@163.com, pg731@qq.com

***Abstract* –** Energy selective surface (ESS) is a special kind of metasurface with great potential in high-power microwave protection. In this paper, the electromagnetic (EM) properties of an ESS array are analyzed with synthetic functions expansion (SFX) method. A cylindrical conformal ESS array based on an I-shape element is designed for demonstration. The Bistatic RCS as well as electric field distribution of the ESS array is calculated with SFX and traditional full-wave numerical methods. The results show that SFX exhibits great advantages in memory cost while maintaining the same level of accuracy and efficiency with the multi-layer fast multipole method (MLFMM). Besides, the EM performance of the designed ESS is calculated with an array with finite elements and unit cell with periodic boundaries, respectively. The results show a good agreement. The proposed method can also be applied to the analysis of other kinds of metasurfaces whose elements share similar geometries with periodic or quasi-periodic arrangement. Especially for large-scale arrays, this method could well overcome the difficulty of balancing accuracy, efficiency, and resource consumption.

***Index Terms* –** Energy selective surface (ESS), large-scale arrays, metasurface, method of moment (MoM), synthetic functions expansion (SFX).

I. INTRODUCTION

Energy selective surface (ESS) is a special kind of metasurface posing nonlinear transmission characteristics with respect to the field intensity of incident waves [1]. More specifically, ESS is supposed to be transparent to low-power microwaves but shield high-power microwaves adaptively. Therefore, ESS is regarded as a potential method in the fields of high-power microwave protection [2].

In the past several years, ESS has attracted great interest and significant progresses have been made [3–8]. In terms of the analytical and numerical modeling of ESS, an approximation method based on periodic boundary conditions is mostly adopted. In that case, ESS is regarded as an infinite array and its electromagnetic (EM) properties are obtained using Floquet model analysis [6]. However, this method is not valid for finite and conformal arrays [7]. On the one hand, the edge effects of a finite array should be taken into account. On the other hand, for most conformal arrays, they do not strictly satisfy the periodic boundary conditions. Thinking of this, full-wave numerical methods are usually adopted to simulate the EM properties of a finite conformal ESS array.

Nevertheless, traditional full-wave algorithms face several difficulties such as a tremendous cost of memory, low computational efficiency, and so on, when applied to large-scale arrays. For instance, method of moment (MoM) is a classic frequency-domain full-wave numerical method which is well known for high accuracy and pretty good adaptability for arbitrary 3D objects. When it comes to large-scale arrays, MoM requires significant memory cost which is usually unbearable for a single PC because of the complex dense matrix equations. Furthermore, the computational complexity is terrible. In contrast, time-domain full-wave numerical methods like finite difference time domain (FDTD) and finite integration technique (FIT) perform better than frequency-domain methods in memory consumption and computational efficiency in general. As a tradeoff, computational accuracy of time-domain methods is usually less than frequency-domain methods. Hence, for the modeling and analysis of large-scale conformal ESS arrays, an efficient and accurate full-wave numerical method is what we desire [9–12].

In this paper, an improved method of MoM called synthetic functions expansion (SFX) is used to analyze

Submitted On: July 23, 2023
Accepted On: March 18, 2024

https://doi.org/10.13052/2024.ACES.J.390204

the EM properties of a large-scale cylindrical conformal ESS array. SFX is first presented by Matekovits et al., the core idea of which is using synthetic functions instead of low order basis functions to discretize EM integral equations [13–14]. After that, several meaningful works on SFX have been published which mainly focus on the following topics such as the construction of synthetic functions [15–16], the unsolved integral equations [17–18], and the parallel algorithm [12]. Compared to traditional full-wave numerical methods, the advantages of SFX are:

1) Since synthetic functions are adopted to discretize the integral equations, memory cost and efficiency of SFX will perform much better than MoM.

2) For an ESS array, synthetic functions defined on different elements can be reused because of the geometrical similarity between these elements. This feature is of vital importance in the analysis of large-scale arrays which can improve the computational efficiency greatly.

3) For a cylindrical conformal array, SFX only needs to mesh the surface of objects rather than the total space which means the memory cost of SFX will be less than traditional time-domain numerical methods.

The paper is arranged as follows. In Section II, a cylindrical conformal ESS array working at 10 GHz is designed and analyzed based on periodic boundary conditions. In Section III, we introduce the basic theory of SFX, then the modeling of ESS and the construction of synthetic functions are discussed. In Section IV, Bistatic RCS, electric field distribution, and high-power microwave protection performance of the designed cylindrical conformal ESS array are calculated using SFX and other numerical methods. Furthermore, the computational performance are discussed, from which we can see that SFX exhibits great advantages in memory consumption while maintaining the same level of computational accuracy and efficiency compared to traditional full-wave numerical methods.

II. MODEL DESIGN

For demonstration, a cylindrical conformal ESS array is designed and analyzed, and the detailed geometry parameters are shown in Fig. 1. The array includes 21*10=210 unit cells covering an azimuth angle of 180^0. The radius of the conformal array is $1.27\lambda_0$ (λ_0=30 mm at 10 GHz) and the height is about $2\lambda_0$. The unit cell is composed of an I-shaped metal structure with two diodes loaded on the vertical arm.

Transmission properties of the unit cell, shown in Fig. 2, are obtained with a commercial full-wave software (CST MWS 2021) under periodic boundary conditions where diodes are modeled as lumped elements, namely, a capacitor C=0.018pf and a resistor R=2Ωfor OFF and ON states, respectively [4]. It is not difficult

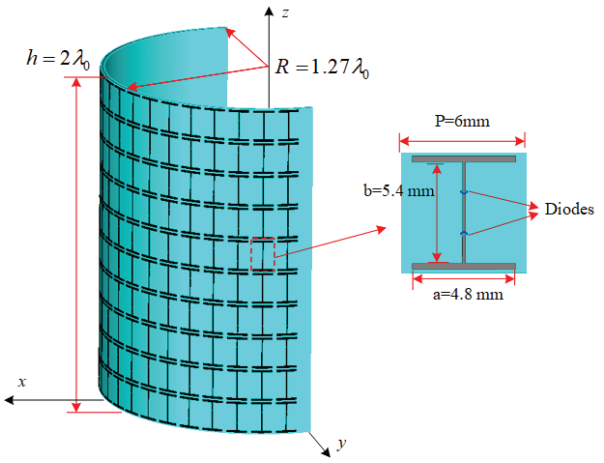

Fig. 1. Illustration of the cylindrical conformal ESS array.

to see that the transmission coefficient is near to 0 dB and smaller than -20 dB at the central frequency (10 GHz) when the diodes are in different states. The physical mechanism may be illustrated briefly by the shift of the resonance frequency. When the diodes are OFF under low-power EM waves, the resonance frequency is much higher than 10 GHz and the structure is supposed to be transparent to low-power EM waves. By contrast, when the structure is illuminated by high-power EM waves, the diodes will be triggered on by the induced voltage, and the ESS structure will resonate at 10 GHz. Then, the high-power EM waves will be reflected. By this way, electronic equipment in the area enclosed by the ESS array is able to receive low-power EM waves, which is the working signals. Meanwhile, high power EM waves are shielded by the ESS array adaptively to protect the electronic equipment.

In this work, our focus is not on the design method of the ESS structure or the underlined mechanism. We aim at the fast and accurate numerical analysis of a designed ESS array. In previous works, the performance of ESS is mainly evaluated by two important indexes - the insertion loss (IL) and the shielding effectiveness (SE) - which are defined as the transmission coefficient of the ESS under different states (Diodes OFF for IL and Diodes ON for SE). However, the transmission coefficients used in these definitions are obtained from an infinite array with periodic boundary conditions, which only illustrate an ideal situation. Thus, from a more practical perspective, we define the IL/SE as the average attenuation of the electric field in the area enclosed by the ESS array in different states. In more detail, IL and SE are defined as:

$$\mathrm{IL/SE} = 20\log\left(\frac{\oint_s |E_{inc}|\,ds}{\oint_s |E_t|\,ds}\right), \tag{1}$$

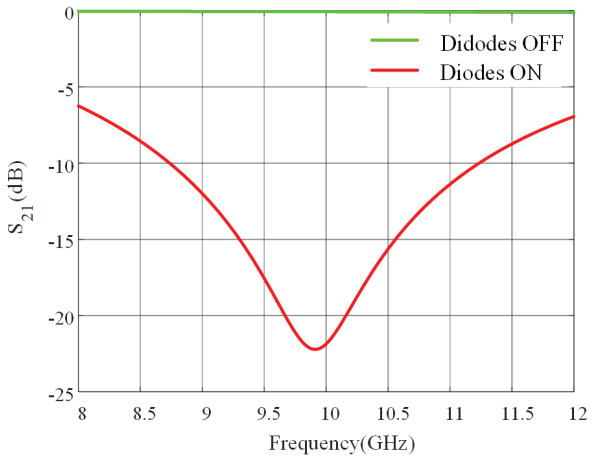

Fig. 2. The transmission properties of the unit cell of ESS under periodic boundary condition.

where $\boldsymbol{S}$ is the area enclosed by ESS array; $E_{inc}$and E_t indicate the electric field with and without ESS array. In this paper, considering the ESS array is half-open, we select a semi-circle $\boldsymbol{S}$ in the transverse (to z) plane at z=30 mm as the area to calculate IL and SE. That is:

$$x^2+y^2 \le R, x \ge 0, z = 30mm. \tag{2}$$

III. SFX ANALYSIS

A. Theory

Since SFX is an improved approach of MoM, we will begin with a brief introduction of MoM and the electric field integral equation (EFIE) is adopted for example.

Usually, EFIE can be compactly written as:

$$\hat{n} \times L(J) = \hat{n} \times E_{inc}, \tag{3}$$

where $J$and $\hat{n}$ are the surface current and a unit vector, respectively. For a vector $\boldsymbol{X}$ (Xcircled by S), L is the electric integral operator and defined as:

$$L(X) = j\omega\mu \int_S [X + \frac{1}{k^2}\nabla(\nabla \cdot X)]gdS, \tag{4}$$

where ω,$\mu$and k are the frequency, the permeability, and the wave number in the free space, respectively. In addition, g is the Green's function in the free space.

To solve the vector integral equation using MoM, we first need to use Rao-Wilton-Glisson (RWG) functions to discretize the unknown vector $\boldsymbol{J}$ and then to make Galerkin test. Then, (3) can be transformed into a linear scalar matrix equation as:

$$ZI=V, \tag{5}$$

where $\boldsymbol{Z}$ is the impedance matrix, $\boldsymbol{V}$ is the excitation vector, and $\boldsymbol{I}$ is the current coefficient vector of basis functions.

Elements in $\boldsymbol{Z}$ and $\boldsymbol{V}$ can be calculated as:

$$\begin{cases} z_{mn} = < f_m, L(f_n) > \\ v_m = < f_m, E_{inc} > \end{cases}, \tag{6}$$

where $\boldsymbol{f}_m$ and $\boldsymbol{f}_n$ are the basis functions (RWG functions in general), $\boldsymbol{E}_{inc}$ stands for the electric field of the incident wave, $<\boldsymbol{A}, \boldsymbol{B}>$ represents the inner product of $\boldsymbol{A}$ and $\boldsymbol{B}$.

Different with the case in MoM, synthetic functions are used in SFX to discretize the surface current $\boldsymbol{J}$ and to make Galerkin test which will yield the following linear scalar matrix equation, as shown in the following term [19]:

$$\begin{cases} [W_{SBF}][Y] = [G_{SBF}] \\ [W_{SBF}] = [P]^H [Z][P] \\ [G_{SBF}] = [P]^H [V] \end{cases}, \tag{7}$$

where [$\boldsymbol{P}$] and [$\boldsymbol{Y}$] are expansion coefficients and current coefficients of synthetic functions; [$\boldsymbol{Z}$] and [$\boldsymbol{V}$] are impedance matrix and exciting matrix of the traditional MoM.

From (7) we can see that impedance matrix [$\boldsymbol{W}_{SBF}$] and exciting matrix [$\boldsymbol{G}_{SBF}$] of SFX can be got on the basis of [$\boldsymbol{Z}$] and [$\boldsymbol{V}$] once [$\boldsymbol{P}$] is obtained. In SBFM, synthetic functions are usually defined as linear combinations of RWG functions, as shown in the following equation:

$$F_m(r) = \sum_{k=1}^{N} P_k f_k(r); \ m = 1, \cdots, M, \tag{8}$$

where N is the number of RWG functions, M is the number of synthetic functions; $\boldsymbol{F}_m$ represents the m-th synthetic functions, and P_k is the expansion coefficient of the k-th RWG function.

Thus, [$\boldsymbol{P}$]=$\{P_k\}_{N\times M}$ can be viewed as the expansion coefficient matrix of synthetic functions.

In [14], Matekovits et al. propose a concrete way to calculate [$\boldsymbol{P}$] and we conclude it as the following three steps:

Step 1: setting a series of auxiliary exciting sources around the target, as shown in Fig. 3.

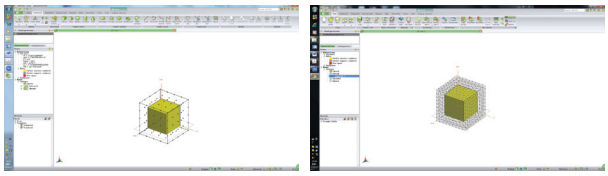

(a) (b)

Fig. 3. A cube is surrounded by a series of auxiliary exciting sources: (a) auxiliary exciting sources are defined on a series of discrete small RWG functions and (b) auxiliary exciting sources are defined on a meshed surface (shown in the wire-frame model).

Initially, Matekovits et al. define auxiliary exciting sources on a series of discrete small RWG functions around the target, as shown in Fig. 3 (a). After that, Bo Zhang et al. define auxiliary exciting sources on a

meshed surface [17], as shown in Fig. 3 (b). Since the surface is meshed into triangular patches in an irregular way, auxiliary exciting source defined on them will be with diverse polarizations which is helpful for improving accuracy. In the following work, the second method of setting auxiliary exciting sources will be adopted.

Step 2: solving the responses of targets to exciting sources to get a solution space (both natural exciting source and auxiliary exciting source are included).

If we define the mutual coupling impedance matrix between the target and auxiliary exciting sources as $\boldsymbol{V}^e$, the solution space $\boldsymbol{R}$ of synthetic functions can be computed as:

$$[R]_{N\times(Q+1)} = Z^{-1}(V+V^e), \tag{9}$$

where N is the number of RWG functions defined on the target, and Q is the number of RWG functions defined on auxiliary exciting sources.

Notably, (9) indicates that the solution space contains two parts:

1) response to natural excitations (incident wave)

$$r^1 = Z^{-1}V, \tag{10}$$

2) responses to auxiliary exciting sources

$$[r^2 r^3 \ldots r^{Q+1}] = Z^{-1}V^e, \tag{11}$$

where $\boldsymbol{r}^i$ (i=1,2,…,Q+1) represent the i-th column of solution space $\boldsymbol{R}$.

Step 3: extracting independent items from solution space.

To extract independent items (expansion coefficients of synthetic functions) from the solution space $\boldsymbol{R}$, singular value decomposition (SVD) is usually adopted:

$$R = U\rho V^H, \rho = diag(\rho_1, \rho_2, ..., \rho_N), \tag{12}$$

where ρ_i is the i-th singular value of R and $\rho_1 > \rho_2 > \cdots > \rho_N$

$\boldsymbol{U}$ is a unitary matrix, and if $\rho_M/\rho_1 < \rho_{SBF}$ (truncation error), we will take the first M columns of $\boldsymbol{U}$ as the expansion coefficients [$\boldsymbol{P}$] of synthetic functions. Thus, it will be:

$$[P]_{N\times M} = U_{N\times N}\begin{bmatrix} I_M \\ 0 \end{bmatrix}_{N\times M}, \tag{13}$$

where $\boldsymbol{I}_M$ is the identity matrix.

The truncation error ρ_{SBF} is usually determined by the operator and, in different applications, ρ_{SBF} is also usually different.

Having got the expansion coefficients [$\boldsymbol{P}$] of synthetic functions, we can compute the current coefficients [$\boldsymbol{Y}$] of synthetic functions according to (7):

$$[Y] = [W_{SBF}]^{-1}[G_{SBF}] = \left[P^H Z P\right]^{-1}[P]^H[V]. \tag{14}$$

Then, according to (8), we can obtain the current coefficients of RWG functions defined on the surface of targets:

$$[I] = [P][Y] = [P]\left[P^H Z P\right]^{-1}[P]^H[V]. \tag{15}$$

Finally, based on the current coefficients of RWG functions, it is not difficult to calculate other EM properties of the target. As it is similar to the traditional MoM, we are not going to explain it in detail.

B. ESS Modeling

In SFX, triangular meshes and RWG functions are usually adopted. For the ESS array shown in Fig. 1, each element is divided into 164 triangular meshes and 188 RWG functions are defined on these meshes, as shown in Fig. 4. Thus, there are 188*210=39480 unknowns in total for the whole ESS array. In traditional MoM, the impedance matrix is a N*N (the number of unknowns) dense matrix of complex coefficients which means the memory cost impedance matrix will be 39480*39480*2*4 Byte/float≈11.6 GByte. To decrease the number of unknowns, synthetic functions are used to compress the scale of the matrix equation.

To construct synthetic functions, a virtual meshed surface is created around each element and 288 RWG functions are defined on these meshes working as the auxiliary sources, as shown in Fig. 4.

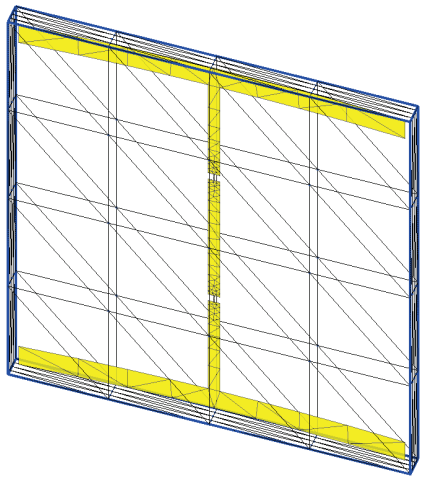

Fig. 4. Each element is divided into 164 triangular meshes and a virtual meshed surface is created around the element.

Fortunately, for the ESS array, synthetic functions defined on different elements can be reused based on the geometric similarities between these elements [10]. This feature is rather appealing to us, especially in the analysis of quasi-periodic structures. It means the construction of synthetic functions only needs to be carried out once, which is helpful to improve efficiency for large-scale arrays. In this paper, after optimization, only 5 synthetic functions for each element are enough to get a

satisfying accuracy. Thus, for the whole ESS array, the number of unknowns will be only 210*5=1050 for SFX. So, the scale of the matrix equation in (7) is 1050*1050, which is much smaller than that of traditional MoM.

For the analysis of ESS, another emphasis is on the modeling of diodes. In this paper, a thin strip is used to approximate the feeder line and the diodes are viewed as a complex impedance in the middle of the feeder line, as shown in Fig. 5. Technically, arbitrary two-port equivalent circuit models could be handled in this method.

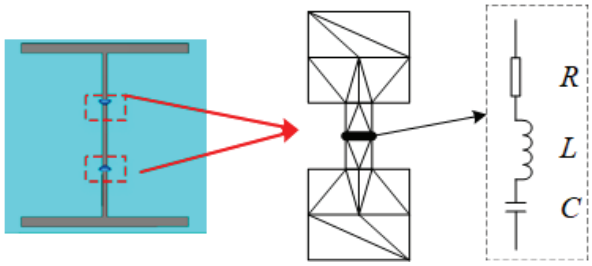

Fig. 5. A thin strip is used to approximate the feeder line and the diodes can be viewed as a complex impedance in the middle of the feeder line.

To take the diodes into consideration, we need to modify the diagonal elements of the impedance matrix, as shown in (16):

$$\begin{aligned} &\text{Diode OFF}: z_{nn} \to z_{nn} + l_n^2(1/j\omega C) \\ &\text{Diode ON}: z_{nn} \to z_{nn} + l_n^2 R \end{aligned} \tag{16}$$

where $R = 2.0\Omega$,$C = 0.018$pF, which are consistent with the simulation setup in the Section II.

Compared to the simulating model in Feko, the model used in this paper can transform the connection from a wire-surface problem to a surface-surface problem and can be perfectly addressed by RWG functions, shown in Fig. 6.

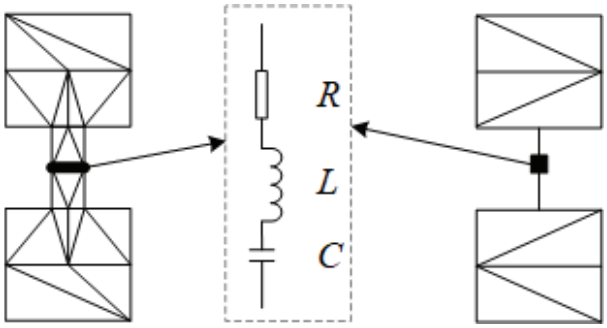

Fig. 6. The diode simulating model in Feko (right) and in this paper (left).

IV. RESULTS

To illustrate the accuracy and efficiency of SFX, the EM properties of the ESS array are numerically analyzed with different methods based on commercial software for comparison. Specifically, the following numerical methods are adopted: MOM and multi-layer fast multipole method (MLFMM) with Feko (Altair Feko 2020), FIT with CST (CST Studio Suite 2021). Considering that the boundary conditions play a critical role in the accuracy in time domain calculations, the boundary conditions in CST are set as open boundary conditions (perfectly matched layers, PML) with a minimum distance to structures of 4λ, and the estimated refection level is 0.0001. The outer excitation is a plane wave which comes from +x axis and polarizes +z axis with its frequency being 10 GHz. Both the far-field (Bistatic RCS) and near field (electric field at z=0 mm cut-plane) are calculated. All the simulations are carried on a computer poses 8 Intel Core i7-7700K Processors with 4 cores per CPU running at 4.2 GHz.

The results of the Bistatic RCS of the ESS array obtained by different methods are shown in Figs. 7 and 8 with diodes in different states, respectively. When the diodes are in OFF state, the transmission coefficient of ESS is high and almost transparent to the incident waves. Therefore, the RCS is supposed to be low and the results are smaller than -20 dB (Fig. 7). On the contrary, the RCS is much larger because the incident wave is strongly reflected when the diodes are in ON state (Fig. 8). Notably, in Fig. 7, when the diodes are OFF, the RCS of ESS array obtained by different methods shows a similar trend with an error smaller than 2.6 dB. On the main lobe, the largest RCS value comes from Feko (MLFMM) (-20.4 dB) and then follows CST (FIT) (-20.9 dB) and SFX (-23.0 dB). Because the absolute value of RCS is very low, the real error between different methods is actually small. As the RCS becomes much larger

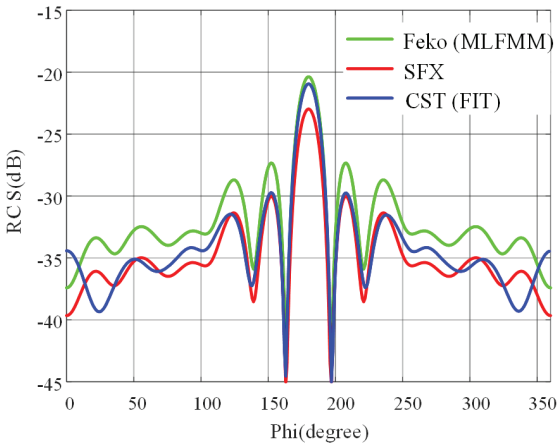

Fig. 7. The RCS of the cylindrical conformal ESS array calculated by different methods when diodes are in OFF state.

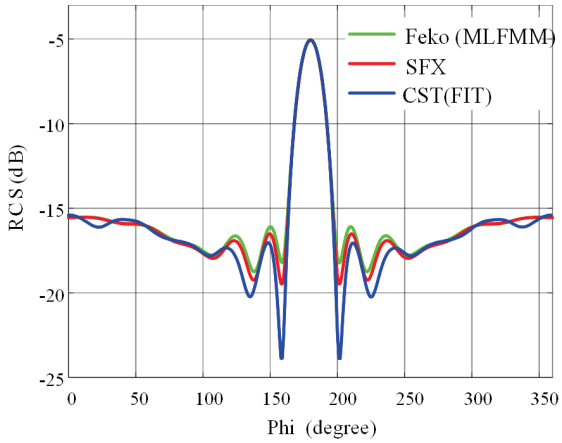

Fig. 8. The RCS of the cylindrical conformal ESS array calculated by different methods when diodes are in ON state.

in Fig. 8, the results obtained with different values are in good agreement, which confirms the accuracy of SFX. It should be pointed out that the results of Feko (MoM) and Feko (MLFMM) are the same, therefore, only Feko (MLFMM) is presented.

The distribution of electric field obtained with different methods at the cut-plane z=30 mm are demonstrated in Figs. 9, 10, and 11. As we can see, the electric field is more uniform when the diodes are OFF, which means the ESS array generates a minor influence on the incident waves. However, when the diodes are ON, the incident wave is reflected rather than propagate through the ESS array from the left to the right. As a result, the electric field at the right side of ESS array is much smaller than that at the left side. That is to say, the incident wave will be isolated out of the ESS array.

Furthermore, the IL and SE of the ESS array are calculated with different methods, as given in Table 1. Results obtained with the periodic boundary conditions are also provided here for comparison. Obviously, the results show a significant difference between IL and SE,

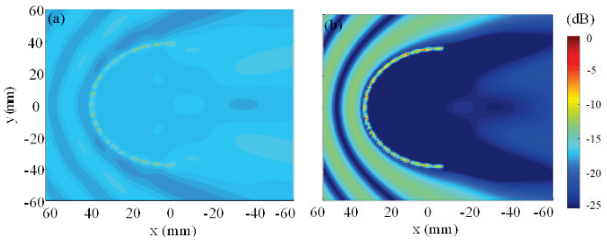

(a) (b)

Fig. 9. The electric field distribution of the cylindrical conformal ESS array calculated with SFX when the diodes are in different states (a) OFF and (b) ON.

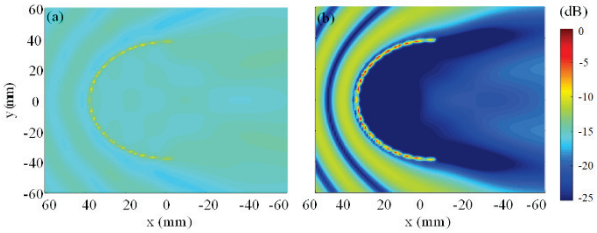

(a) (b)

Fig. 10. The electric field distribution of the cylindrical conformal ESS array calculated with Feko (MLFMM) when the diodes are in different states (a) OFF and (b) ON.

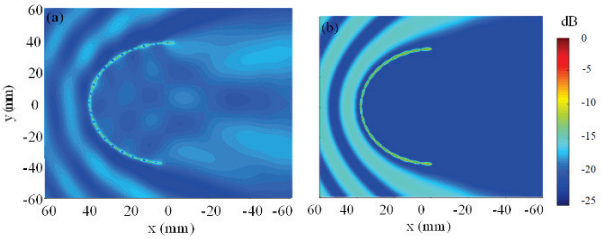

(a) (b)

Fig. 11. The electric field distribution of the cylindrical conformal ESS array calculated with CST (FIT) when the diodes are in different states (a) OFF and (b) ON.

Table 1: The IL and SE of ESS obtained with different methods

	IL (dB)	**SE (dB)**
SFX	-0.45	-16.5
CST (FIT)	-1.26	-18.4
Feko (MoM)	-0.3	-17.7
Feko (MLFMM)	-0.3	-17.7
Unit cell	-0.1	-20

confirming the capability of ESS for high-power EM wave protection. As we can see, the IL obtained from the finite ESS array is larger but the SE is smaller than that of the unit cell, where ESS is regarded as infinite arrays. The results can be attributed to several reasons. Firstly, the array is not a strictly enclosed one, which may lead to some EM leaks. Secondly, the IL and SE are obtained based on the field intensity in the near field area of the ESS array while that of the unit cell are calculated with field intensity in the far field area, which also leads to some error. Generally, the results obtained by different methods are in agreement.

Table 2 illustrates the computational performance of different methods in terms of time consumption, peak memory cost, and root mean square error (RMSE). Notably, the peak memory cost and time consumption of Feko and CST are obtained from the software log-file. It is not difficult to see that the proposed SFX

exhibits outstanding performance in accuracy, efficiency, and memory cost. More concretely:

1) According to the RMSE in Table 2, SFX has the same level of accuracy with CST (FIT) and Feko (MLFMM).

2) As for the computational efficiency, according to the indexes of time consumption, SFX is slightly lower than CST (FIT) and Feko (MLFMM), but exceeds traditional Feko (MoM).

3) When it comes to memory cost, SFX shows a huge advantage over other methods, especially CST (FIT) and Feko (MoM).

It is not difficult to draw the conclusion that SFX is especially suitable for the analysis of ESS. Compared to traditional full-wave numerical methods, SFX well overcomes the difficulty of balancing accuracy, efficiency, and resource consumption.

Table 2: Performance and comparison of different algorithms (RMSE is obtained in comparison with the results of Feko)

	Elapsed Time	**Peak Memory Cost**	**RMSE**
SFX	387.56 s	8.41 MByte	0.13
CST (FIT)	266 s	1.11 GByte	0.47
Feko (MoM)	2350.95 s	6.55 GByte	-
Feko (MLFMM)	262.16 s	618.25 Mbyte	-

V. CONCLUSIONS

ESS is a potential method of high-power EM protection. In this paper, SFX is adopted to numerically analyze the EM properties of ESS and an I-shape cylindrical conformal ESS array is designed for demonstration. Compared to traditional full-wave numerical methods, SFX exhibits great advantages in memory cost while maintaining the same level of accuracy and efficiency with MLFMM and FIT. Moreover, this method not only suits ESS, but also suits other quasi-periodic arrays whose elements share similar geometries. Especially for large-scale array, this method can well overcome the difficulty of balancing accuracy, efficiency, and resource consumption.

REFERENCES

[1] P. Liu, C. Liu, J. Tan, Y. Dong, and B. Yi, "Analysis of the research development on HPM/EMP protection," *Chinese Journal of Ship Research*, vol. 10, no. 2, pp. 2-6, 2015 [in Chinese].

[2] C. Yang, P. Liu, and X. Huang, "A novel method of energy selective surface for adaptive HPM/EMP protection," *IEEE Antennas Wireless Propag. Lett.*, vol. 12, pp. 112-115, 2013.

[3] N. Hu, Y. Zhao, J. Zhang, P. Liu, H. Xu, and F. Costa, "High-performance energy selective surface based on equivalent circuit design approach," *IEEE Trans. Antennas Propag.*, vol. 70, no. 6, pp. 4526-4538, 2022.

[4] N. Hu, K. Wang, J. H. Zhang, S. Zha, Z. F. Wu, C. Liu, and P. Liu, "Design of ultrawideband energy-selective surface for high-power microwave protection," *IEEE Antennas Wireless Propag. Lett.*, vol. 18, no. 4, pp. 669-673, 2019.

[5] N. Hu, S. Zha, T. Tian, and P. Liu, "Design and analysis of multiband energy selective surface based on semiconductors," *IEEE Trans. Electromagn. Compat.,* vol. 64, no. 4, pp. 1076-1085, 2022.

[6] Z. Wu, Y. Xu, P. Liu, T. Tian, and M Lin, "An ultra-broadband energy selective surface design method: From filter circuits to metamaterials," *IEEE Trans. Antennas Propag.*, vol. 71, no. 7, pp. 5865-5873, 2023.

[7] W. Kui, X. Huang, T. Tian, W. Huang, and P. Liu, -1447283793-1447283793"Design and demonstration of high-power density infrared nonlinear filtering window with EM shielding," *Opt. Express.*, vol. 32, pp. 5956-5968, 2024.

[8] T. Tian, X. Huang, Y. Xu, P. Liu, C. Liu, N. Hu, J. Zhang, and Z. Wu, "A wideband energy selective surface with quasi-elliptic bandpass response and high-power microwave shielding," *IEEE Trans. Electromagn. Compat.*, vol. 61, no. 1, pp. 224-233, 2024.

[9] L. Tarricone, "A genetic approach for the efficient numerical analysis of microwave circuits," *Applied Computational Electromagnetics Society (ACES) Journal*, vol. 1, no. 1, pp. 87-93, 2000.

[10] Z. Jiang, Y. Sha, X. Xuan, and L. Nie, "An omnidirectional antenna with multi-taper conformal structure," *Applied Computational Electromagnetics Society (ACES) Journal*, vol. 38, no. 3, pp. 184-192, 2023.

[11] G. Sener, "Antenna synthesis by Levin's method using a novel optimization algorithm for knot placement," *Applied Computational Electromagnetics Society (ACES) Journal*, vol. 38, no. 7, pp. 482-488, 2023.

[12] Y. Xu, X. Huang, C. Liu, S. Zha, and J. Liu, "Synthetic functions expansion: Automation, reuse, and parallel," *IEEE Trans. Antennas Propag.*, vol. 69, no. 3, pp. 1825-1830, 2021.

[13] L. Matekovits, G. Vecchi, G. Dassano, and M. Orefice, "Synthetic function analysis of large printed structures: The solution space sampling

approach," *Proc. IEEE AP-S Int. Symp.*, Boston, MA, pp. 568-571, 2001.

[14] L. Matekovits, V. A. Laza, and G. Vecchi, "Analysis of large complex structures with the synthetic-functions approach," *IEEE Trans. Antennas Propag.*, vol. 55, no. 3, pp. 2509-2521, 2007.

[15] W. C. Chen, G. B. Xiao, S. Xiang, and J. F. Mao. "A note on the construction of synthetic basis functions for antenna arrays," *IEEE Trans. Antennas Propag.*, vol. 60, no. 7, pp. 3509-3512, 2012.

[16] Y. L. Xu, H. Yang, W. K. Yu, and J. Zhu. "An automatic scheme for synthetic basis functions method," *IEEE Trans. Antennas Propag.*, vol. 66, no. 3, pp. 1601-1606, 2018.

[17] B. Zhang, G. B. Xiao, J. Mao, and Y. Wang, "Analyzing large-scale non-periodic arrays with synthetic basis functions," *IEEE Trans. Antennas Propag.*, vol. 58, no. 11, pp. 3576-3584, 2010.

[18] L. Matekovits, G. Vecchi, M. Bercigli, and M. Bandinelli, "Synthetic-functions analysis of large aperture-coupled antennas," *IEEE Trans. Antennas Propag.*, vol. 57, no. 7, pp. 1936-1943, 2009.

[19] Y. L. Xu, H. Yang, D. Peng, and R. J. Shen, "Efficient numerical analysis of dielectric resonator antenna arrays," *IEEE Antennas Wireless Propag. Lett.*, vol. 27, no. 4, pp. 670-674, 2018.

Ning Hu received the B.S. degree in electronic engineering and the M.S. degree in electronic science and technology from National University of Defense Technology (NUDT), Changsha, Hunan, P. R. China, in 2017 and 2019, respectively. And he received the Ph.D. degree in information and communication engineering from NUDT in 2023. His research interests include electromagnetic compatibility and protection, metamaterials and antennas.

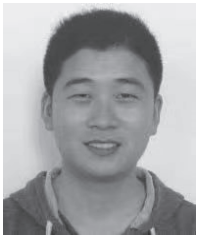

Yanlin Xu was born in Tianchang, Anhui, China, in 1990. He received the B.S. and M.S. degrees in electronic science and technology from National University of Defense Technology (NUDT), Chang-sha, China, in 2013 and 2015, respectively. He received the Ph.D. degree in information and communication engineering from NUDT in 2018. His current research interests include electromagnetic compatibility and protection, computational electromagnetics and its applications in scattering analysis.

Peiguo Liu received the Ph.D. degree in information engineering from the National University of Defense Technology, Changsha, China, in 1995. He is currently a Professor with the College of Electrical Science and Engineering, National University of Defense Technology. His current research interests include electromagnetic compatibility and protection.

A 3-D Global FDTD Courant-limit Model of the Earth for Long-time-span and High-altitude Applications

Yisong Zhang[1], Dallin R. Smith[2], and Jamesina J. Simpson[1]

[1]Department of Electrical and Computer Engineering
University of Utah, Salt Lake City, UT, USA
yisong.zhang.ee@gmail.com, jamesina.simpson@utah.edu

[2]Air Force Research Labs
Albuquerque, NM, USA
dallinsmith9@gmail.com

***Abstract* –** A new global 3-D finite-difference time-domain (FDTD) model is introduced to simulate electromagnetic wave propagation around the Earth, including the lithosphere, oceans, atmosphere, and ionosphere regions. This model has several advantages over existing global models, which include grids that follow lines of latitude and longitude and geodesic grids comprised of hexagons and pentagons. The advantages of the new model include: (1) it may be run at the Courant-Friedrichs-Lewy (CFL) time step (as a result, it is termed the Courant-limit model); (2) subgrids may be added to specific regions of the model as needed in a straight-forward manner; and (3) the grid cells do not become infinitely larger as the grid is extended higher in altitude. As a result, this model is a better candidate than the others for investigating electromagnetic phenomena over long time spans of interest and for investigating atmosphere-ionosphere-magnetosphere coupling. The new model is first described and then validated by comparing results for extremely low frequency (ELF) propagation attenuation with corresponding analytical and measurement results reported in the literature.

***Index Terms* –** ELF, electromagnetic wave propagation, FDTD, global propagation, long-time and high-altitude simulations, scattering.

I. INTRODUCTION

The Earth-ionosphere waveguide is defined as the spherical cavity between the Earth's surface and the bottom side of the ionosphere [1]. Within this waveguide, ultra-low frequency (ULF:<3 Hz) and extremely low frequency (ELF: 3 Hz–3 kHz) electromagnetic waves are capable of propagating globally as quasi-transverse electromagnetic (TEM) waves that experience very little attenuation. TEM and higher-order waveguide modes can also propagate globally in the Earth-ionosphere waveguide at frequencies ranging from the upper ELF band to very low frequencies (VLF: 3-30 kHz) [2] and even high frequencies (HF: 3–30 MHz) [3]. The propagation of electromagnetic waves in the Earth-ionosphere waveguide has been of interest for a wide variety of applications, including communications (e.g. [4]), geolocation and communications with submarines (e.g. [5]), studying lightning and sprites (e.g. [6, 7]), and remote sensing (e.g. [8]).

Two generations of 3-D global finite-difference time-domain (FDTD) models [9] of electromagnetic wave propagation in the Earth-ionosphere waveguide have been generated over the years: (1) latitude-longitude models (e.g. [10, 11]) and (2) geodesic models (e.g. [12]). Both generations of models have been used for a variety of applications (e.g. [13]), including Schumann resonances, hypothetical earthquake precursors, remote-sensing of ionospheric anomalies, space weather hazards to electric power grids, and remote sensing of oil fields.

In order to model beyond the Earth-ionosphere waveguide and to also pursue applications beyond those listed above, a new generation of global FDTD models is required. The reasons are three-fold:

(1) Both the latitude-longitude and geodesic grid cell arrangements require a time step increment that is smaller than the Courant-Friedrichs-Lewy (CFL) limit [9]. In the case of the latitude-longitude grid, this is due to the polar regions and the merging of cells [11]. For the case of the geodesic grid, the reduced time step is due to the reduction in the grid cell dimensions as any of the smaller 12 pentagons are approached (there are 12 pentagons in the model, regardless of the grid resolution) [12]. As a result of the reduced time step increment of these grid arrangements, many simulations of interest are challenging, if not infeasible, even using today's supercomputing capabilities. An example scenario

Submitted On: May 2, 2023
Accepted On: February 6, 2024
https://doi.org/10.13052/2024.ACES.J.390205

wherein a large number of time steps is required includes the generation of geomagnetically-induced currents (GICs) during geomagnetic storms. GICs are capable of causing blackouts to electric power grids. These storms can last days at a time, although the evolution of the storm over time spans of 30 minutes to two hours is often of most interest [14, 15]. Another example includes the global propagation of VLF to HF waves. It would take a large number of time steps for a wave to propagate around the entire Earth at the required grid resolution for VLF and HF waves. We note that the alternating direction implicit (ADI) FDTD approach [16–18] was used to generate a global FDTD model of the Earth-ionosphere waveguide [19]. However, that model was found to exhibit a late time instability, which limited the model's utility, particularly for long time spans of interest.

(2) Adding efficient and stable subgrids to FDTD models continues to be a challenge. Many approaches have been proposed over the years, but an approach that is accurate and efficient for a wide variety of scenarios and for long time spans has not been established. Both the latitude-longitude grid and geodesic grids have the added complexity that the subgrids would have non-uniform cell sizes and domain edges. Further, the strategy for adding a subgrid to the geodesic model would need to change depending on whether the subgrid includes a pentagon or not.

(3) Both the latitude-longitude and geodesic grid cell arrangements are comprised of grid cells that become larger in the horizontal (East-West and North-South) directions as the grid is extended to higher altitudes. This becomes an issue for applications in which electromagnetic waves may couple into and propagate through the ionosphere and even into the magnetosphere (e.g. [20]). It is also an issue when studying the effects of space weather since the sources of electromagnetic waves (i.e., disturbed currents) occur throughout the ionosphere and magnetosphere regions [21].

In this paper, a new "global Courant-limit" FDTD model is presented that does not suffer from the above issues because all of the grid cells in the grid are Cartesian-based and identical. This allows the model to be run at the Courant limit, which is advantageous for long time spans. Furthermore, since all of the cells are uniform, the cells do not increase in size with increasing altitude. Finally, if at any point any subgrids are added to the model, the standard approach for regular Cartesian FDTD models may be utilized.

One disadvantage of the global Courant-limit model is that material interfaces, such as the Earth's surface, are stair-cased. However, the staircasing is minimal because the grid resolution (5 km in this paper) is small compared to the radius of the Earth ($\sim$6.4 Mm). Further, the staircasing reduces with increasing grid resolution, the surface of the Earth, in reality, is already not completely smooth, and techniques exist that may be used to mitigate the impact of staircasing as needed [22, 23].

The next section includes a description of the global Courant-limit model. Section III then provides details of the validation of the model. Section IV concludes the paper.

II. METHODOLOGY

A. Global Courant-limit model description

An example two-dimensional (2-D) slice of a low-resolution version of the three-dimensional (3-D) global Courant-limit model is shown in Fig. 1 (a). A higher-resolution 3-D view of the grid is shown in Fig. 1 (b). Although the grid is uniformly comprised of regular cubic grid cells, there are special considerations for the model, such as how to efficiently store the grid in computer memory, how to best center the grid, and how to assign boundary conditions and varying material parameters.

In the first part of the code (Part A), the grid is generated, and all of the updating coefficients are computed. The second part of the code (Part B) includes the time-stepping loop and any output from the model.

In Part A, the altitude range of the grid and the resolution of the cells are first defined. Thereafter, any Cartesian cells that are positioned within the altitude range of the model are assigned positive integer grid cell numbers. In the example slice of the grid shown in Fig. 1 (a), there are 28 total cells to be included in the model. The cells are positioned such that there are electric fields radiating outwards from the center of the Earth, as shown in Fig. 1 (a) (the center of the Earth is unlikely to be included in the model, so the electric field vectors shown at the center of the Earth are for illustrative purposes only). This field arrangement is optimal for dealing with the boundary conditions at the surface of the Earth. That is, using this arrangement the interface between the conductive lithosphere and the atmosphere is spherically symmetric, and it is comprised of a continuous string of tangential electric field components.

When generating the grid, there are two primary challenges. One of the biggest challenges is to ensure that there are not too many "ghost" cells (this was also true for the previous latitude-longitude model). Ghost cells take up memory but are not used in the time-stepping loop. The second challenge is to ensure that each processor is assigned the same number of grid cells

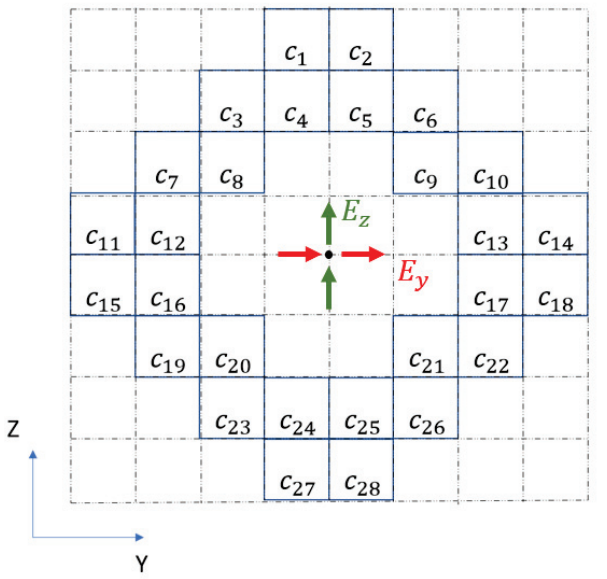

(a)

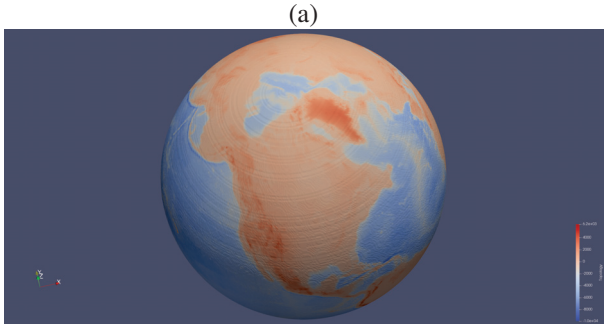

(b)

Fig. 1. (a) Example 2-D slice of the 3-D grid cells along the prime meridian for the global Courant-limit model at a very low spatial resolution. Each cell ("c") included in the model is labeled c_n, where n represents the cell number. The arrows represent electric fields oriented radially from the center of the Earth, which is indicated by a black dot. (b) Illustration of the outer layer of the 3-D FDTD grid at a resolution of $5 \times 5 \times 5$ km with the Earth's topography superimposed. Staircasing is minimal due to the size of the Earth, although this is difficult to fully visualize in an image of so many cells.

such that the time-stepping loop is efficient. To address both of these issues, the field components in the global Courant-limit model are stored in 1-D arrays instead of 3-D matrices. This allows us to assign the same number of cells to each processor and prevents any ghost cells from being included. An effort is made to assign neighboring grid cells to the same processor to limit the number of communications required between processors (this is described further in Section IIB).

In order to implement a source or to record field values at specific locations, a weighted average approach is used on neighboring field components. This approach was also used in the latitude-longitude and geodesic grids. Special care must be taken across the air-lithosphere boundary (i.e., if a field observation in the atmosphere is desired, then only field values above the Earth's surface should be utilized in the weighted average calculation).

Finally, for the second part of the code (Part B), the global Courant-limit model uses the same update equations in the time-stepping loop as found in regular Cartesian FDTD models [9]. The main difference is that the update equations use cell numbers in order to locate the neighboring cells since the data is stored in 1-D arrays instead of 3-D matrices. The updating coefficients and information about neighboring field components are all determined and stored in memory during the first part of the code (Part A) before time-stepping begins.

B. Parallelization of the grid

Message passing interface (MPI) is used to communicate between processors. In general, MPI communications are slow relative to the types of computations performed by each processor during the time-stepping loop. As a result, the goal when parallelizing the model is to minimize the amount of information that must be passed between processors using MPI. This is accomplished by assigning neighboring grid cells to the same processor as much as possible.

There are several methodologies that could be used to equally divide the cells onto different processors. One approach, which we followed, is to divide the grid first using a specific number of lines of longitude (with the number depending on how many processors will be used for the simulation). Thereafter, the grid is divided along the lines of latitude in a manner that assigns each processor the same volume of space. If a further division of the grid is needed, the volume of space may also be divided in the radial direction so that additional processors may be employed.

III. VALIDATION

The global Courant-limit model is validated by comparing the predicted ELF propagation attenuation with the data reported in [24]. As for the validation performed for the latitude-longitude model [25], the altitude range is set to be from -100 to +100 km, and the daytime exponential conductivity profile from [26] is used globally. Initially, the ground is considered to be a homogeneous perfect electric conductor (PEC) in order to test the model for spherical symmetry. The global Courant-limit model is run at a resolution of $5 \times 5 \times 5$ km (rather than the $40 \times 40 \times 5$ km resolution used in the latitude-longitude model of [11]). This grid resolution is chosen to match the 5-km resolution used in the radial direction of the latitude-longitude model.

The source is a radial, 5-km-long current pulse having a Gaussian time-waveform with a 1/e full-width of 1.44 *ms*. This current pulse is located just above the Earth's surface on the equator and at the prime meridian. To ensure a smooth onset of the excitation, the temporal center of this pulse is 2.88 *ms*.

The radial electric field is sampled along the surface of the Earth in order to study its propagation characteristics. A few steps are required in order to obtain this data. Due to the staggering of the electric field components in the FDTD model, spatial averaging is first applied to the x-, y-, and z-electric field components in order to obtain the corresponding co-located values of these components at the specific observation points of interest. Specifically, up to eight electric fields closest to the observation point of interest are employed and averaged using an inverse-distance weighting (IDW) approach [27]. Once these co-located Cartesian components are obtained, they are converted to spherical coordinates in order to obtain the radial electric field.

A snapshot of the radial electric fields along the surface of the Earth is plotted in Fig. 2 after the pulse has propagated around the world and is in the process of converging at the antipode. The snapshot is obtained by recording the field values at 720x360 locations on the longitude-latitude grid. The black circles superimposed on the figure illustrate the model's spherical symmetry very well.

The radial electric field is also recorded vs. time at several observation points along four different propagation paths between the source and its antipode. Point A along each propagation path corresponds to 1/4 of the distance to the antipode. Point B is $3/8^{th}$, Point C is 1/2, and Point D is 3/4 of the distance to the antipode. The orientations of these propagation paths are shown in Fig. 2 by the white dashed lines. Note that in 3-D, each of these propagation paths includes wave propagation along a variety of directions across the Cartesian-based grid cells.

Figure 3 shows the time waveforms of the FDTD-calculated radial electric fields at the A, B, C, and D observation points of all four propagation paths. Since the waveforms at each distance overlap, this plot also demonstrates the spherical symmetry of the model.

Next, the topographic and bathymetric data from NOAA-NGDC is imported into the model, and lithosphere conductivities are assigned depending on whether a grid cell is located directly below an ocean or within a continent. A daytime profile is used globally as for the propagation attenuation study presented in [11].

Figure 4 compares the FDTD-calculated ELF propagation attenuation as calculated from the global Courant-limit model versus frequency over the $A_{1E}B_{1E}$ and $A_{1W}B_{1W}$ propagation paths of Fig. 3 with the analytical results presented in [24] (which were also compared with measurements). The FDTD data are obtained by forming the ratio of the discrete Fourier transforms (DFTs) of the time-domain responses at the corresponding observa-

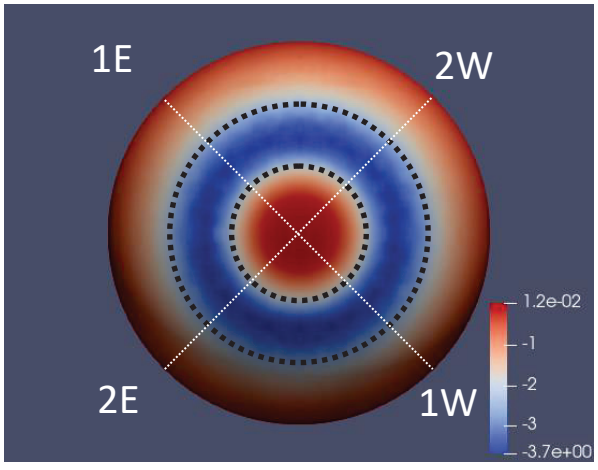

Fig. 2. Visualization of the radial electric field projected onto the surface of the Earth-sphere after the pulse has propagated around the entire Earth and is converging at the antipode. The units for the electric field are $\mu V/m$. The spherical symmetry in the region of the antipode is apparent from the black dashed circles superimposed on the image.

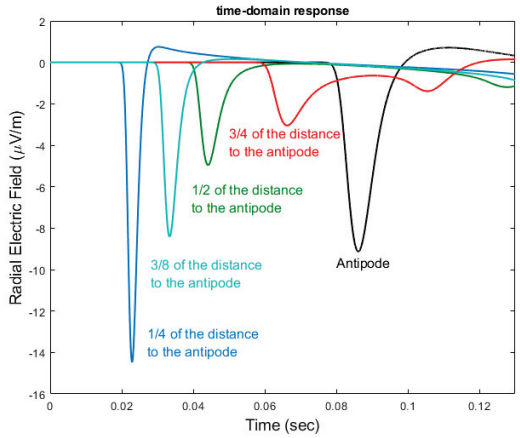

Fig. 3. The FDTD-calculated time-domain response of the radial electric field along the four white dashed propagation paths shown in Fig. 2. The radial electric fields at observation points to the East of the source (along paths 1E and 2E) are labeled as solid lines, and the fields at points to the West of the source (along paths 1W and 2W) are labeled as dashed lines. All of the lines at each distance overlap, which indicates the global Courant-limit model's spherical symmetrical.

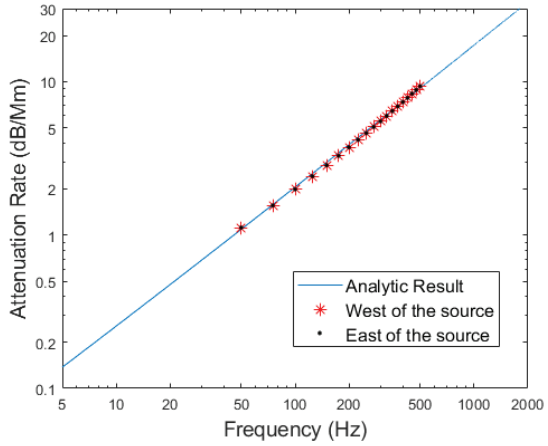

Fig. 4. Comparison between the FDTD-calculated ELF propagation attenuation versus frequency over paths $A_{1E}B_{1E}$ and $A_{1W}B_{1W}$ with analytical results reported in [24], where the subscripts refer to the different propagation paths shown in Fig. 2.

tion points. Note that the time-domain responses at each observation point are truncated at each zero-crossing preceding the slow-tail response in order to exclude the signal arriving from the long propagation path relative to the source.

As seen in Fig. 4, over the frequency range of 50–500 Hz, the FDTD-calculated propagation attenuation agrees with the results in [24] within $\pm 0.2\ dB/Mm$.

IV. CONCLUSION

A new global FDTD model was introduced that is advantageous for long-time-span applications as well as applications that will extend over large radial distances (a wide range of altitudes). This grid arrangement is termed the global Courant-limit model because it runs at the Courant limit, the maximum permissible time step that is free from instabilities. The model was described and validated by comparing the FDTD-calculated frequency attenuation with corresponding analytical and measurement data in the literature [24].

As part of our ongoing work, we are using this model to investigate magnetotelluric and geoelectric fields at the surface of the Earth during geomagnetic storms. By coupling this model with other models, such as the Block Adaptive Tree Solar wind Roe-type Upwind Scheme (BATS-R-US) model [28–31], this model may help serve as an essential forecasting tool for predicting space weather hazards to near-Earth electrotechnologies [32].

ACKNOWLEDGMENT

This material is based upon work sponsored by the National Science Foundation under Grant 1662318. The authors would like to acknowledge high-performance computing support from Cheyenne (doi:10.5065/D6RX99HX) provided by NCAR's Computational and Information Systems Laboratory. Also, the support and resources from the Center for High Performance Computing at the University of Utah are gratefully acknowledged.

REFERENCES

[1] K. G. Budden, *The Wave-Guide Mode Theory of Wave Propagation*, London: Logos Press, 1961.

[2] P. B. Morris, R. R. Gupta, R. S. Warren, and P. M. Creamer, *Omega Navigation System Course Book Vols. 1 and 2. Reading*, MA: Analytical Sciences Corp.

[3] M. A. Tyler, "Round-the-world high frequency propagation: A synoptic study, DSTO-RR-0059," 1995.

[4] R. W. Moses, "The high-latitude ionosphere and its effects on radio propagation," *Eos, Transactions American Geophysical Union*, vol. 85, no. 19, p. 192, 2004.

[5] M. B. Cohen, U. S. Inan, R. K. Said, and T. Gjestland, "Geolocation of terrestrial gamma-ray flash source lightning," *Geophysical Research Letters*, vol. 37, no. 2, 2010.

[6] L. Liebermann, "Extremely low-frequency electromagnetic waves. I. Reception from lightning," *Journal of Applied Physics*, vol. 27, no. 12, pp. 1473-1476, 2004.

[7] S. A. Cummer, U. S. Inan, T. F. Bell, and C. P. Barrington-Leigh, "ELF radiation produced by electrical currents in sprites," *Geophysical Research Letters*, vol. 25, no. 8, pp. 1281-1284, 1998.

[8] S. A. Cummer, U. S. Inan, and T. F. Bell, "Ionospheric D region remote sensing using VLF radio atmospherics," *Radio Science*, vol. 33, no. 6, pp. 1781-1792, 1998.

[9] A. Taflove and S. C. Hagness, "Computational Electromagnetics: The Finite-Difference Time-Domain Method," 3rd ed. Norwood, MA: Artech House, Inc., p. 1038, 2005.

[10] M. Hayakawa and T. Otsuyama, "FDTD analysis of ELF wave propagation in inhomogeneous subionospheric waveguide models," *Applied Computational Electromagnetics Society (ACES) Journal*, vol. 17, no. 3, pp. 239-244, 2002.

[11] J. J. Simpson and A. Taflove, "Three-dimensional FDTD modeling of impulsive ELF propagation about the Earth-sphere," *IEEE Transactions on Antennas and Propagation*, vol. 52, no. 2, pp. 443-451, 2004.

[12] J. J. Simpson, R. P. Heikes, and A. Taflove, "FDTD modeling of a novel ELF radar for major oil deposits using a three-dimensional geodesic grid of the Earth-ionosphere waveguide," *IEEE Transactions on Antennas and Propagation*, vol. 54, no. 6, pp. 1734-1741, 2006.

[13] J. J. Simpson, "Current and future applications of 3-D global Earth-ionosphere models based on the full-vector Maxwell's equations FDTD method," *Surveys in Geophysics*, vol. 30, no. 2, pp. 105-130, 2009.

[14] C. Yue and Q. Zong, "Solar wind parameters and geomagnetic indices for four different interplanetary shock/ICME structures," *Journal of Geophysical Research: Space Physics*, vol. 116, no. A12, 2011.

[15] J. T. Gosling, "The solar flare myth," *Journal of Geophysical Research: Space Physics*, vol. 98, no. A11, pp. 18937-18949, 1993.

[16] F. Zheng, Z. Chen, and J. Zhang, "A finite-difference time-domain method without the Courant stability conditions," *IEEE Microwave and Guided Wave Letters*, vol. 9, no. 11, pp. 441-443, 1999.

[17] C. C.-P. Chen, T.-W. Lee, N. Murugesan, and S. C. Hagness, "Generalized FDTD-ADI: An unconditionally stable full-wave Maxwell's equations solver for VLSI interconnect modeling," in IEEE/ACM International Conference on Computer Aided Design. ICCAD - 2000. IEEE/ACM Digest of Technical Papers (Cat. No.00CH37140) IEEE [Online]. Available: https://ieeexplore.ieee.org/document/896466/.

[18] Y. Yang, R. S. Chen, Z. B. Ye, and Z. B. Wang, "Analysis of planar antennas using unconditionally stable three-dimensional ADI-FDTD method," in *2005 IEEE Antennas and Propagation Society International Symposium*, 2005: IEEE [Online]. Available: https://ieeexplore.ieee.org/document/1551512/.

[19] D. L. Paul and C. J. Railton, "Spherical ADI FDTD method with application to propagation in the Earth ionosphere cavity," *IEEE Transactions on Antennas and Propagation*, vol. 60, no. 1, pp. 310-317, 2012.

[20] M. A. Clilverd, C. J. Rodger, R. Gamble, N. P. Meredith, M. Parrot, J.-J. Berthelier, and N. R. Thomson, "Ground-based transmitter signals observed from space: Ducted or nonducted?," *Journal of Geophysical Research: Space Physics*, vol. 113, no. A4, 2008.

[21] G. V. Khazanov, M. W. Chen, C. L. Lemon, and D. G. Sibeck, "The magnetosphere-ionosphere electron precipitation dynamics and their geospace consequences during the 17 March 2013 storm," *Journal of Geophysical Research: Space Physics*, vol. 124, no. 8, pp. 6504-6523, 2019.

[22] T. Xiao and Q. H. Liu, "A Staggered Upwind Embedded Boundary (SUEB) method to eliminate the FDTD staircasing error," *IEEE Transactions on Antennas and Propagation*, vol. 52, no. 3, pp. 730-741, 2004.

[23] K. H. Dridi, J. S. Hesthaven, and A. Ditkowski, "Staircase-free finite-difference time-domain formulation for general materials in complex geometries," *IEEE Transactions on Antennas and Propagation*, vol. 49, no. 5, pp. 749-756, 2001.

[24] P. R. Bannister, "ELF propagation update," *IEEE Journal of Oceanic Engineering*, vol. 9, 1984.

[25] J. J. Simpson and A. Taflove, "Efficient modeling of impulsive ELF antipodal propagation about the Earth sphere using an optimized two-dimensional geodesic FDTD grid," *IEEE Antennas and Wireless Propagation Letters*, vol. 3, no. 1, pp. 215-218, 2004.

[26] P. R. Bannister, "The determination of representative ionospheric conductivity parameters for ELF propagation in the Earth-ionosphere waveguide," *Radio Science*, vol. 20, no. 4, pp. 977-984, 1985.

[27] D. Shepard, "A two-dimensional interpolation function for irregularly-spaced data," in *Proceedings of the 1968 23rd ACM National Conference*, New York: ACM Press, 1968.

[28] G. Tóth, D. L. De Zeeuw, T. I. Gombosi, W. B. Manchester, A. J. Ridley, I. V. Sokolov, and I. I. Roussev, "Sun-to-thermosphere simulation of the 28-30 October 2003 storm with the Space Weather Modeling Framework," *Space Weather*, vol. 5, no. 6, 2007.

[29] K. G. Powell, P. L. Roe, T. J. Linde, T. I. Gombosi, and D. L. De Zeeuw, "A solution-adaptive upwind scheme for ideal magnetohydrodynamics," *Journal of Computational Physics*, vol. 154, no. 2, pp. 284-309, 1999.

[30] T. I. Gombosi, G. Tóth, D. L. De Zeeuw, K. C. Hansen, K. Kabin, and K. G. Powell, "Semirelativistic magnetohydrodynamics and physics-based convergence acceleration," *Journal of Computational Physics*, vol. 177, no. 1, pp. 176-205, 2002.

[31] T. I. Gombosi, K. G. Powell, D. L. De Zeeuw, C. R. Clauer, K. C. Hansen, W. B. Manchester, A. J. Ridley, I. I. Roussev, I. V. Sokolov, Q. F. Stout, and G. Toth, "Solution-adaptive magnetohydrodynamics for space plasmas: Sun-to-Earth simulations," *Computing in Science & Engineering*, vol. 6, no. 2, pp. 14-35, 2004.

[32] M. W. Liemohn, D. T. Welling, J. J. Simpson, R. Ilie, B. J. Anderson, S. Zou, N. Y. Ganushkina, A. J. Ridley, J. W. Gjerloev, A. Kelbert, M. Burleigh, A.

Mukhopadhyay, and H. Xu, "CHARGED: Understanding the Physics of Extreme Geomagnetically Induced Currents," presented at the American Geophysical Union Fall Meeting December 01, 2018 [Online]. Available: https://ui.adsabs.harvard.edu/abs/2018AGUFMNH31C0993L

Yisong Zhang received the B.S. and M.S. degrees in electrical and computer engineering from University of Utah, Salt Lake City, UT, USA, in 2017 and 2021, respectively. He is currently pursuing the Ph.D. degree in electrical and computer engineering at University of Utah.

His current research interests include finite-different time-domain modeling of geomagnetic induced current, numerical model acceleration.

Dallin R. Smith received the B.S. degree in physics from Brighton Young University at Provo, Provo, UT, USA, in 2016, and the M.S. and Ph.D. degrees in electrical and computer engineering from the University of Utah, Salt Lake City, UT, USA, in 2019 and 2020, respectively.

He is currently with the Air Force Research Laboratory, Kirkland Air Force Base, Albuquerque, NM, USA. He is currently a Research Electrical Engineer with the Ionospheric Impacts Branch, Space Vehicles Directorate. His current research involves full-wave analysis of radio wave propagation in perturbed ionosphere conditions at high and equatorial latitudes of the Earth.

Jamesina J. Simpson received the B.S. and Ph.D. degrees in electrical engineering from Northwestern University, Evanston, IL, USA, in 2003 and 2007, respectively. She is currently a Professor in the Electrical and Computer Engineering Department, University of Utah, Salt Lake City, USA. Her research lab encompasses the application of Maxwell's equations finite-difference time-domain (FDTD) method to a wide variety of scientific and engineering applications across the electromagnetic spectrum.

Dr. Simpson received a 2010 NSF CAREER award, the 2012 IEEE AP-S Donald G. Dudley, Jr. Undergraduate Teaching Award, the 2017 International Union of Radio Science (URSI) Santimay Basu Medal, and the 2020 IEEE AP-S Lot Shafai Mid-Career Award.

Near-fields of Butterfly Nanoantennas: A Comparative Simulation and Experimental Study

Saswatee Banerjee[1], Nicolas Marquez Peraca[2], and Alexander Franke[1]

[1]Meta
Cork, Ireland
saswateeb@meta.com, alexfranke@meta.com

[2]Department of Physics and Astronomy
Rice University, Houston, Texas 77005, USA
nmarquez@rice.edu

***Abstract* –** Optical nanoantennas demonstrate the ability to confine and enhance electromagnetic fields. This ability makes nanoantennas essential tools for high-resolution microscopy. The nanoantenna resonance and response can be tuned by changing their size, shape, and material as well as adjusting the probing conditions, e.g. excitation wavelength. In this paper we simulated the propagation and interaction of visible light with computer generated models of butterfly nanoantenna arrays using the finite-difference time-domain (FDTD) method. The simulations were used to understand and predict the experimental results obtained with scanning near-field microscopy (SNOM) on commercially available samples. Simulation parameters are chosen carefully to reflect the measurement conditions.

***Index Terms* –** finite-difference time-domain method, Fischer nanostructures, near-field, resolution, SNOM.

I. INTRODUCTION

The interaction of light with metallic nanostructures is of great research interest. Studies have shown that metal-dielectric nanostructures are capable of manipulating light in subwavelength-scale. For example, nanoantennas have been successfully utilized as near-field apertures that work as localized evanescent sources, effectively suppressing the background illumination [1]. Arrays of butterfly nanoantennas such as Fischer patterns [2] have been used as platforms for surface-enhanced Raman spectroscopy (SERS) [3].

In this study we investigate metallic Fischer patterns using a combination of simulations and measurements. The simulations are carried out using finite-difference time-domain (FDTD) method while scanning near-field optical microscopy (SNOM) is used to measure the near-field intensity distributions with nm-resolution beyond the classical Abbe diffraction limit for microscopy.

In the paper we (i) study the fundamental light interaction, in particular the field enhancement and localization, and (ii) demonstrate the feasibility of SNOM to resolve field intensity distributions beyond the classical resolution limit for optical microscopy.

Simulations are conducted creating a model for one unit of the Fischer pattern. The model consists of triangular nanostructures in a hexagonal arrangement. Different simulation and structural parameters such as the electromagnetic field polarization, the distance of the field monitor from the surface of the nanoantennas or the structural size are considered. These simulation results show the light localization, light enhancement or the surface plasmon resonance behavior of such a nanoantenna array as a response to changes in structural, material properties, and illumination conditions. The simulations are also used to predict and analyze the measurements obtained by SNOM.

The resolution of a microscope is one of the key performance parameters that qualify the system performance. The Abbe diffraction limit, in particular, sets a physical limit to the minimum resolvable distance that a microscope can achieve. It is defined by the numerical aperture (NA) and the wavelength of the excitation source (λ_{exc}) used in the following manner: dAbbe$\sim\lambda_{exc}$/2NA [4]. For visible light of 500 nm and assuming a NA of common high magnification objective lenses around 0.9, the diffraction limited resolution is $\sim$300 nm.

Therefore, in order to investigate smaller feature sizes, switching to electron microscopy for probing the sample, or techniques such as SNOM, are needed.

We utilize the transmission SNOM technique to investigate periodic nanoantenna calibration patterns far below the Abbe diffraction limit. The commercially available Fischer pattern samples consist of arrays of butterfly nanoantennas in a hexagonal arrangement.

Submitted On: July 11, 2023
Accepted On: February 26, 2024

https://doi.org/10.13052/2024.ACES.J.390206

Each nanoantenna consists of a pair of metallic triangles/hexagons. In our study the diameter of the center aperture was changed from ∼200 nm to 1.1 um. It allows us to study light-matter interaction effects in the Mie regime, where the excitation wavelength λ_{exc} is comparable to the pattern size d.

The paper is outlined as follows. The modeling and simulation of the Fischer pattern using the FDTD method is discussed in Section II. Section III describes the experimental setup, followed by the presentation of the measurement results in Section IV. In Section V we discuss the experimental observation in the light of simulation results. Our main findings are concluded in Section VI.

II. FDTD MODELING OF FISCHER NANOSTRUCTURES

A computer model is generated based on one unit cell of the patterned nanostructures. The model features three butterfly nanoantennas in a hexagonal arrangement. Each nanoantenna consists of a pair of equilateral triangular elements.

Two main model variants with different structural parameters are considered. For the first model the material of the nanoantennas is gold (Au) and the diameter of the central aperture is 420 nm. The second variant consists of aluminum (Al) nanoantennas with central aperture diameters of 500 nm and 1.1 um, respectively.

The light propagation through each of the models is simulated using the FDTD method. FDTD is a numerical method based on the Yee algorithm that solves Maxwell's equations [5–6]. In this paper we use a commercial FDTD solver from Lumerical to compute the near-field [7].

An electric dipole is created to represent the illumination source to mimic the SNOM measurements [2]. The dipole is placed immediately below the structure at the center of the xy-plane. The dispersive complex refractive indices for both Au and Al used in simulations are obtained from published reference data [7]. The FDTD mesh is a nonuniform one that uses approximately 29.6 grid points/wavelength within the structure and 16.6 grid points/wavelength in the PML (absorbing boundary condition) region.

Figure 1 (a) shows the first computer model. A side of any of the nano triangles is 200 nm and the gap between the tips of two adjacent triangles is ∼25 nm. A constant thickness of the nanotriangles of 15 nm was assumed for all simulations.

The distribution of the electric field intensity in the xy-plane, parallel to the surface of the structure, is computed for x and y orientations of the dipole, respectively. The field distributions are recorded at a monitor set at a height of 5 nm from the structure surface. In order to model an unpolarised illumination condition, we

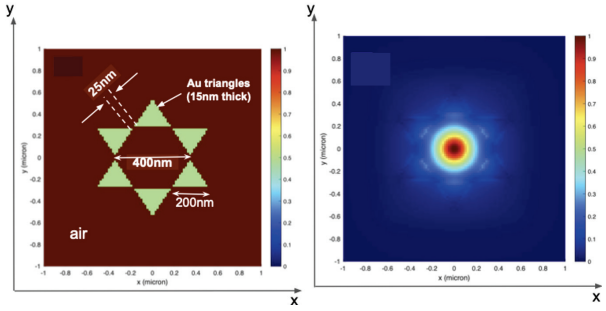

(a) (b)

Fig. 1. FDTD simulation of Au model: (a) First computer model of one unit cell of the Fischer pattern and (b) xy-plane distribution of the electric field intensity recorded 5 nm above the surface of the structure in (a).

averaged the electric field intensities obtained with the two orthogonal orientations of the dipole. The normalized and averaged electric field intensity distribution for an excitation wavelength of 532 nm is shown in Fig. 1 (b). The field distribution reveals a partial light penetration into the metal covered areas. As a result, the metallic elements cast partial shadows in the transmitted light.

The dependance of the near-field on the orientation of the dipole is shown in Fig. 2. The electric field distribution in Fig. 1 (b) is an average over all six orientations of the dipole shown in Fig. 2. The average intensity is representative of the unpolarised incident illumination condition used in the experiments.

As seen in Fig. 2, the near-field intensity patterns depend on the orientation of the dipole. In particular the near-field pattern generated when the dipole orientation is parallel and perpendicular to the gap between the tips of adjacent triangular nanoelements. For example, orientations parallel to the gaps (−30deg (Fig. 2 (a)), 30deg (Fig. 2 (c)), and 90deg (Fig. 2 (e))) appear to be different from orientations perpendicular to the gaps (60deg (Fig. 2 (b)), 120deg (Fig. 2 (d)), and 180deg (Fig. 2 (f))).

Averaging over any two pairs of orthogonal dipole orientations yields identical results. However, if we consider a structural anisotropy of the modeled structures, e.g. unequal gap distances between two adjacent elements, the effect of anisotropy in the simulation results can be ameliorated by averaging over all six polarization orientations. Averaging also makes the pattern more symmetric with regards to the central aperture. Nevertheless, penetration of light in metal covered areas, and light confinement in the central aperture region with similar intensities, is observed for all the considered dipole configurations irrespective of their alignment relative to the butterfly antennas.

The dependence of the field distribution on the monitor distance is studied by increasing the monitor height

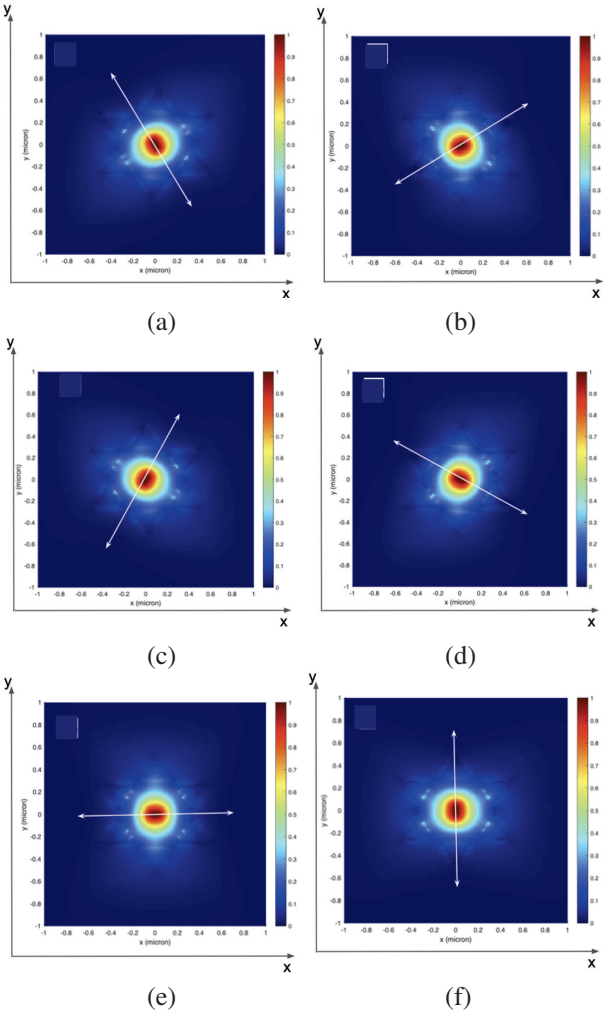

Fig. 2. Field dependence on dipole orientation. Electric field intensity distribution in the xy-plane at a monitor height of 5 nm from the surface of the structure. Dipoles are oriented along directions parallel and perpendicular to each pair of gaps between adjacent nanotriangles. The dipole orientations are (a) −30deg, (b) 60deg, (c) 30deg, (d) 120deg, (e) 90deg, and (f) 180deg from the +y-axis, respectively.

in four steps from 10 nm to 200 nm from the surface of the structure. At each step (height along the z-axis), the corresponding electric field pattern is recorded for the three pairs of orthogonal in-plane orientations of the dipole excitation source, and averaged to mimic an unpolarised illumination condition. The aim of this study is to better predict the SNOM measurement conditions where the field distribution is recorded by an objective lens in the um-range away from the sample surface.

The normalized average intensity profiles for the four monitor heights of 10 nm, 50 nm, 100 nm, and 200 nm are shown in Fig. 3.

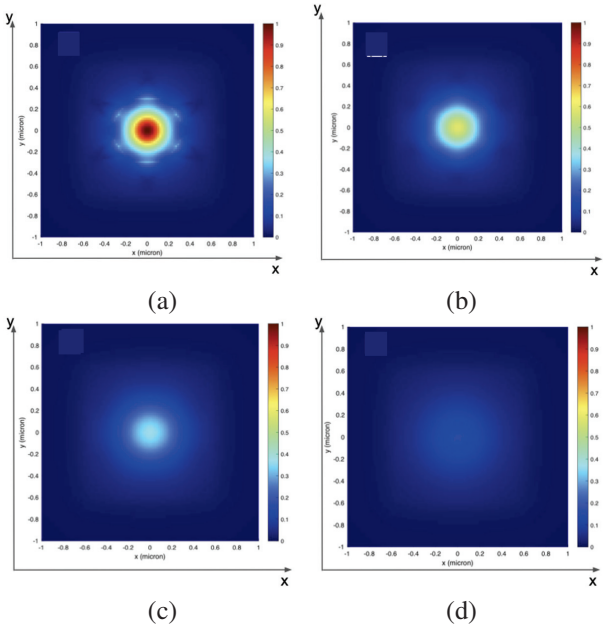

Fig. 3. Field dependence on monitor height. Evolution of the field pattern with increasing height of the monitor from the surface of the structure. The averaged and normalized distribution of the electric field intensity in the xy-plane was calculated for a monitor z-distance of (a) 10 nm, (b) 50 nm, (c) 100 nm, and (d) 200 nm.

At a distance of less than 10 nm, light confinement is most pronounced and the shape of the center hexagonal aperture is more discernible. As the distance of the monitor is increased, the finer details of intensity variations gradually disappear from the near-field pattern. It indicates that the light confinement seen in the near-field is due to evanescent waves that dissipate with increasing the distance of the monitor from the surface of the nanostructure.

A third main parameter influencing the near-field behavior of the nanoantenna is the pattern dimension compared to the excitation wavelength. The simulated field distribution of the first model (Fig. 1 (a)), obtained with an excitation wavelength of 405 nm, is shown in Fig. 4. In order to directly compare the result with the earlier shown intensity pattern after 532 nm laser excitation in Fig. 1 (b), the 405 nm intensity pattern (Fig. 4 (b)) is normalized using the maximum intensity found in Fig. 1 (b). Compared to Fig. 1 (b), Fig. 4 (b) shows that, at 405 nm excitation, the central higher intensity lobe diminishes both in size and intensity.

Figure 5 (a) shows the second computer model of an Al Fischer nanostructure with a larger central aperture of 1.1 um in diameter. A side of any of the triangular elements is 300 nm, the gap between the tips of two adjacent triangles is 250 nm, and the metal thickness of 15 nm is

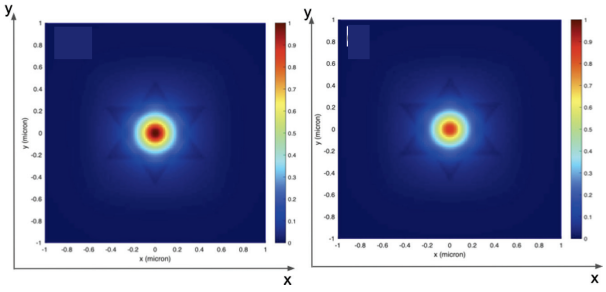

(a) (b)

Fig. 4. Field distribution with 405 nm excitation. The averaged and normalized field intensity distribution simulated for the geometry in Fig. 1 (a) for an excitation wavelength of 405 nm, at a monitor height of 5 nm. Field intensity pattern normalized to (a) the maximum intensity and (b) the maximum intensity found at 532 nm excitation from Fig. 1 (b).

the same as used for the first model. Figure 5 (b) shows the normalized electric field intensity averaged over three pairs of orthogonal orientations of the dipole at an excitation wavelength of 532 nm and recorded at a monitor height of 5 nm.

Figure 5 (b) shows that light penetrates into metal covered antenna elements partially as in the case of the Au model (Fig. 1 (b)). However, the intensity and lateral depth of penetration is less. Most of the transmitted light intensity in Fig. 5 (b) originates from the central aperture, while only a small fraction is passed through the gaps in Fig. 5 (a).

Figure 6 (a) shows a slight variation of the second computer model where the central aperture diameter is changed to 500 nm. Figure 6 (b) depicts the corresponding distribution of intensity pattern. The intensity pattern

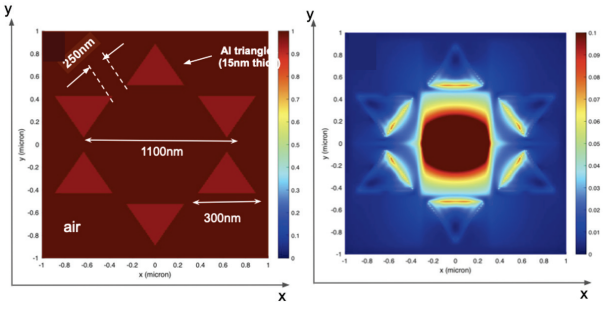

(a) (b)

Fig. 5. Second computed model of a 1.1 um Al pattern: (a) Computer generated model of a hexagonal arrangement of Al antenna elements with a central aperture diameter of 1.1 um and (b) xy-plane distribution of the electric field intensity at a monitor height of 5 nm for the structure in (a).

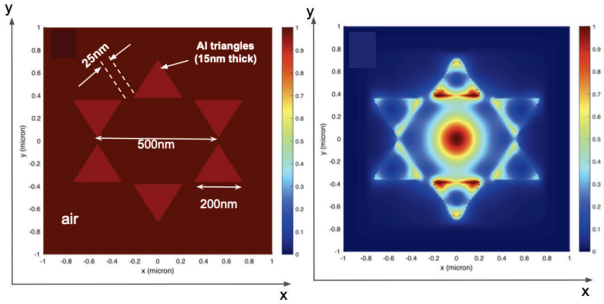

(a) (b)

Fig. 6. Second model of Al with reduced pattern diameter of 500 nm: (a) Geometry of nanoantenna elements with a central aperture diameter of 500 nm and (b) xy-plane distribution of the averaged and normalized electric field intensity at a monitor height of 5 nm from the structure surface.

shows strong enhancements along the edges and at the tips of the metallic antenna elements.

III. SNOM SETUP

A commercially available Raman/SNOM system based on a confocal microscope (WITec alpha300) [8] was used to study microscopy resolution and electric field enhancement effects. In the Raman and Photoluminescence mode the maximum spatial resolution is diffraction limited by the chosen objective lens and restricted to ∼300-400 nm (532 nm excitation wavelength, 100x objective lens with NA=0.9) [4, 10]. However, confining the excitation spot by introducing an aperture can help to overcome the diffraction limit. This principle is used in the SNOM mode, where a hollow truncated pyramid is scanned in contact mode across the sample surface. The height control is achieved by an atomic force microscopy-like feedback loop, allowing to simultaneously record the sample topography (height information) and SNOM intensity [9–10].

SNOM was performed in the transmission geometry (Fig. 7). An excitation laser is focused by a 20x objective lens (NA=0.4) on the backside of an aluminum coated silicon cantilever which acts as a near-field SNOM excitation probe [9–10]. The apex opening of the cantilever directly defines the spatial resolution. For our study, two different tip sizes of 90 nm and 150 nm were used to investigate the maximum achievable spatial resolution and the influence on the signal-to-noise ratio (SNR).

The transmitted light from the sample is collected by a long-range 100x (NA=0.75) objective lens and detected using a photomultiplier tube (PMT). By lateral scanning of the sample under the SNOM tip, spatially resolved maps of the transmitted SNOM intensity and topography across the sample could be generated. To analyze the multidimensional dataset as well as to

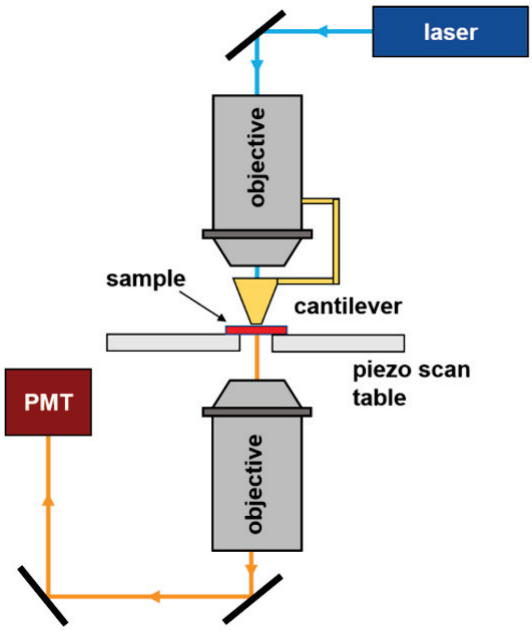

Fig. 7. Schematics of the transmission SNOM setup used in our experiments.

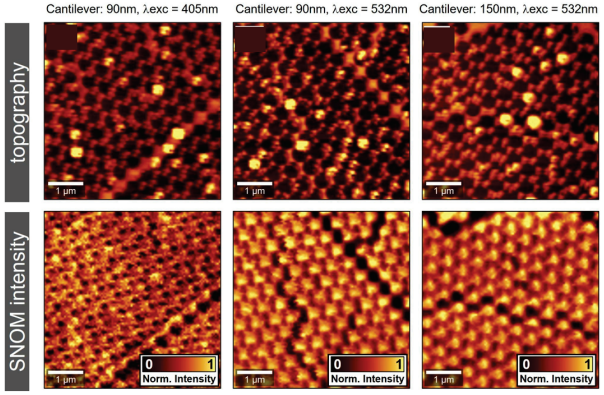

(a) (b) (c)

Fig. 8. Cantilever tip size and excitation wavelength dependency. Topography (top row) and SNOM intensity (bottom row) for a hexagonal Au pattern having a central aperture diameter of d∼400 nm. Different excitation and scan conditions were investigated: (a) 90 nm cantilever opening in conjunction with an excitation wavelength of 405 nm, (b) 532 nm, and (c) a 150 nm tip together with $\lambda_{exc} = 532$ nm.

control the microscope system, WITec software Control 6 and Project 5 were used.

IV. MEASUREMENT RESULTS

Achieving a high image quality and lateral resolution in a SNOM system most importantly relies on the cantilever tip size and quality as well as the chosen excitation conditions. The influence of those parameters were investigated on commercially available metallic projection patterns provided by Kentax GmbH [11]. To fabricate these samples, monolayers of hexagonal closely packed latex spheres are used as a mask for physical vapor deposition of a ∼10 nm Al or Au layer. After removal of the latex spheres, the resulting structure consists of a periodic hexagonal metal array deposited on a 0.15 mm-thick glass substrate.

Lower resolution scans covering an area of 5 um × 5 um (scan resolution 50 nm) on Au Fischer pattern featuring a central aperture diameter of about 400 nm are depicted in Fig. 8. The top row shows the sample topography (height map) while the SNOM intensity profile is visualized in the bottom row. The images are complementary. Metal coated areas are opaque for the excitation laser and light is backscattered towards the incident direction. Those regions appear as black dots, while bright areas originate mainly from areas not covered by metal.

The SNOM resolution is basically defined by the geometric confinement (tip aperture). Any scattering and diffraction loss at the cantilever tip is expected to have a negligible effect. This is because the tip is scanned in contact mode across the sample surface, exciting the near-field. Changing the excitation laser wavelength and keeping the tip opening aperture constant should have a negligible influence on the resolution since both laser wavelength are almost similar ($\Delta\lambda_{exc}$<d), and pass the same tip aperture. These expectations are confirmed by the scans shown in Fig. 8. Altering the excitation wavelength from 405 nm (Fig. 8 (a)) to 532 nm (Fig. 8 (b)) doesn't change the SNOM intensity pattern significantly. On the other hand, the chosen cantilever opening is seen to mainly determine the lateral SNOM resolution. Smaller and more crisp features are obtained using the smaller 90 nm tip (Fig. 8 (b)) compared to the more than twice as large 150 nm tip (Fig. 8 (c)).

Besides the resolution, the achievable SNR is an important SNOM parameter. A higher SNR enables faster, more stable, scans (less sample drift), and stronger SNOM intensity signals. Due to a higher output power of the 532 nm laser, the SNR after 532 nm excitation (Fig. 8 (b)) is increased compared to 405 nm (Fig. 8 (a)). For the 405 nm laser (Fig. 8 (a)), an almost constant background intensity over the whole scan area is detected, at 532 nm excitation the dominant SNOM signal originates from the center part of the hexagonal shaped Fischer pattern. A closer look at the edges and gap regions between the butterfly pattern reveal fine details which could not be resolved at 405 nm excitation. This observation reveals the importance and influence of the SNR on the resolution.

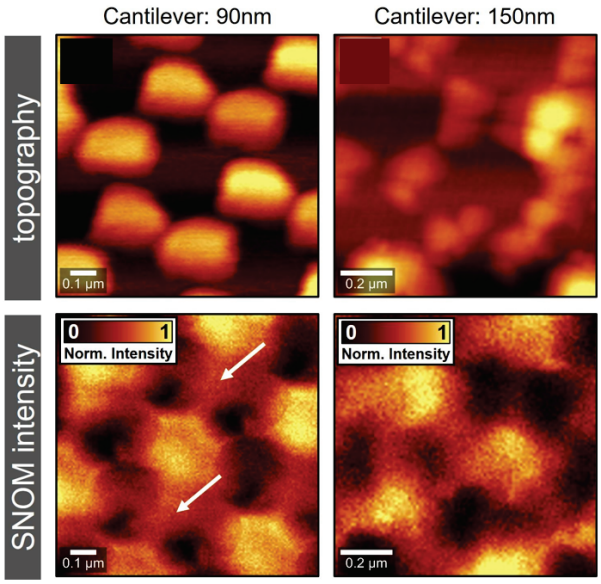

Fig. 9. High resolution SNOM measurements. Topography (top) and SNOM intensity (bottom) for the same Au sample investigated in Fig. 8 using (a) 90 nm and (b) 150 nm tip opening.

Figure 9 shows the images of a 2 um × 2 um scan with two different tip sizes. A clear superior topography height contrast (top row of Fig. 9), and a significantly improved SNOM resolution was achieved using the 90 nm cantilever. Edges appear fuzzy in the SNOM intensity image using the 150 nm tip (Fig. 9 (b)). In comparison, fine lines connecting adjacent hexagonal transmissive parts as well as light from metal covered areas are resolved using the 90 nm cantilever (Fig. 9 (a)). It should be highlighted that there is a small lateral shift expected between the topography and SNOM intensity images. Due to the finite cantilever thickness at the apex (rim), the topography signal will respond first to any height change at the metal pattern edge, followed by the intensity signal when light is transmitted through the cantilever tip opening [9].

Summarizing our instrument related SNOM study, the optimum measurement conditions to achieve high resolution and a high SNR for our system are found for a cantilever with the smallest available opening of 90 nm and using a high power laser emitting at $\lambda_{exc} = 532$ nm.

The influence of pattern size on light-matter interaction is highlighted in size series in Fig. 10. Aluminum Fischer pattern with an intended central aperture diameter ranging from 230 nm ($d<\lambda_{exc}$) up to 1.1 um ($d>\lambda_{exc}$) were investigated. First it should be noted that the smallest pattern with an intended central aperture diameter of

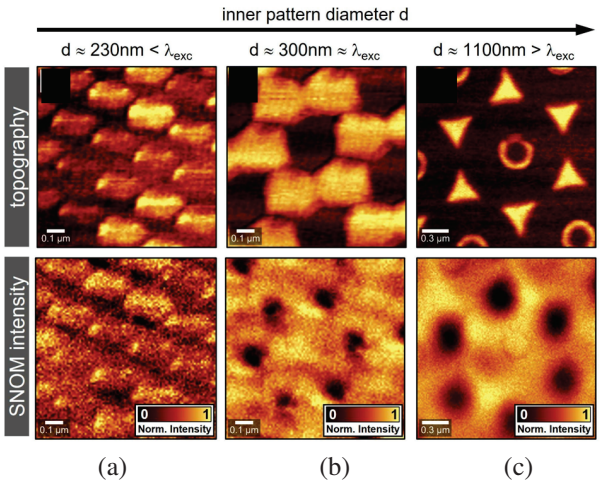

Fig. 10. Aluminium Fischer pattern size series. Fischer patterns with a central aperture diameter ranging from (a) intended 230 nm to (c) 1.1 um were investigated using the best known SNOM conditions: 90 nm tip and 532 nm laser excitation.

230 nm shows the potential of SNOM in terms of resolution. Features below the theoretical diffraction limit for optical microscopy are observed. The topography images in the top row of Fig. 10 as well as SNOM intensity (bottom row) reveal features on a lateral length scale below 100 nm. However, due to fabrication inhomogeneities and absent hexagonal features, the 230 nm pattern cannot be used to study the change of the near-field intensity as the Fischer pattern size increases.

By enhancing the pattern size from 300 nm to 1.1 um, a change in the morphology is observed. The 1.1 um structure (Fig. 10 (c)) exhibits a well separated triangular pattern with noticeable gaps in between. For 300 nm (Fig. 10 (b)), the gaps are nearly closed and a hexagonal symmetry of the metal parts is present. Classically one would expect almost no light transmitting through the small or almost closed gaps between the pattern. However, in the SNOM intensity image (Fig. 10 (b), bottom), transmitted light is also detected in areas covered by metal. We attribute this to a field enhancement effect which is expected to be more pronounced when the feature size is close to the laser wavelength. This hypothesis is confirmed by the measurement at the d∼400 nm gold pattern shown in Fig. 9 (a). The light enhancement and propagation in the metal covered area is even more pronounced. Note the extended bright lines/features exceeding the expected gap opening between adjacent hexagonal metal patterns and connecting different bright hexagonal openings (examples highlighted by arrow in Fig. 9 (a)).

A further increase of the pattern size to $d>\lambda_{exc}$ (Fig. 10 (c)) marks the transition to the classical regime

in which the transmitted light originates mainly from the center aperture of the Fischer pattern and the larger gap openings between adjacent metal structures.

V. DISCUSSION

As highlighted in Section II, partial light penetration and confinement is observed for the metallic nanoantenna array at a monitor distance less than 10 nm from the surface of the nanostructures (Fig. 1 (b), 3 (a)). Light is predominantly transmitted through the transparent, central aperture of the Fischer pattern for all investigated diameter sizes, ranging from ∼300 nm to 1.1 um (Figs. 1 (b), 5 (b), and 6 (b)). In addition, antenna elements cast a partial shadow blocking the light from passing through these areas. Those findings are validated by SNOM measurement results depicted in Figs. 9 and 10.

In order to allow for a comparison between our simulations and the measurements, the modeled conditions were adjusted to the experimental ones. A main difference between the simulated and measured intensity maps is the occurrence of more details or finer intensity gradations in the simulated patterns. This is most pronounced for the light transmitted through the central aperture. While the measurement results, e.g. Fig. 9 (a), show only a weak intensity reduction from the center of the inner aperture to the outer regions close to the metal pattern, the computed center field distribution in Fig. 1 (b) consists of concentric rings with gradually reduced intensity. Starting at a maximum intensity of 100% in the middle of the center aperture, the value drops to ∼40% close to the edges of the metal covered regions adjacent to the center aperture.

This observation could be explained considering the change of the near-field intensity distribution with increasing monitor height, summarized in Fig. 3. As the monitor height increases to 50 nm and 100 nm, the finer intensity variations in the center aperture area slowly disappear and the absolute intensity value reduces significantly. For the measurement configuration used, the objective lens to collect the transmitted light is actually at a larger distance compared to the maximum simulated monitor distance of 200 nm (Fig. 3 (d)). Therefore only a small intensity variation in the center aperture part as well as a reduced overall intensity is expected.

Furthermore the chosen excitation wavelength and power will affect the intensity gradation observed in the center aperture part. Lowering the excitation wavelength from 532 nm (Fig. 1 (b)) to 405 nm (Fig. 4 (b)) results in a smaller lateral extension of the center intensity distribution, which reduces the ability to resolve finer intensity features. Evidence for an experimental confirmation of this simulation result are given in Figs. 8 (a) and (b). Only a very small intensity enhancement in the center of the clear aperture region of the Fischer pattern is found for 405 nm excitation. The transmitted SNOM intensity is almost homogeneously distributed across the whole scanned area, in contrast to the 532 nm laser scan (Fig. 8 (b)). The center part of the aperture is clearly of highest intensity and the intensity is reduced towards the edges of the center aperture. This observation is in good agreement with the simulation shown in Fig. 1 (b) for the pattern center region.

However, in experimental investigations the laser power and therefore the achieved signal-to-noise ratio needs to be considered. Since the output power for the 532 nm laser is larger compared to that of the 405 nm laser, the transmitted SNOM intensity and SNR is enhanced in the first case. This will help to resolve finer intensity details in the SNOM image as seen in Figs. 8 (a) and (b). Consequently, our best measurement conditions are found at high power 532 nm excitation using a small cantilever tip size, which was 90 nm in our case.

Finally we discuss the role of the pattern size on the simulated and measured field distribution. Of particular interest are light-matter interaction effects like field enhancement, and surface plasmonic resonances.

With Al nanostructure, two different pattern sizes with 1.1 um and 500 nm center aperture diameter, excited at 532 nm were considered. When the diameter is larger than the excitation wavelength (d=1.1 um, Fig. 5), light is mainly transmitted through the center part and less from the gap regions between adjacent triangles of the butterfly antennas. However, light originating from areas covered by metal is predicted. Those regions are localized at the lower edges of the triangles closest to the center aperture.

Reducing the diameter size to a regime comparable to the excitation wavelength ($d \approx 500\ nm \approx \lambda_{exc}$) increases the probability of observing phenomena like light penetration in metal covered areas and plasmonic effects. For the 500 nm Al Fischer pattern in Fig. 6, light coming from the lower triangular sides is strongly intensified, while the transmission through the center aperture is more localized featuring a clear intensity gradient towards the edges of the center aperture. In addition, localized spots of highest intensity, which is comparable to the one observed in the aperture center, are forming at the tips of the triangles. This behavior could be related to a localized surface plasmon resonance (LSPR).

The Fisher pattern size dependent SNOM measurements in Fig. 10 show indications which support the simulation results. In the case $d > \lambda_{exc}$ (Fig. 10 (c)), dominant emission is observed from the aperture center and the gap regions of the triangles. In contrast, for a smaller center

aperture diameter (d≈λ_{exc} in Fig. 10 (b)), the transmitted light seems to be more centered to the aperture origin and weaker in the gap regions between adjacent triangles. This observation is supported and even more pronounced for the d≈400 nm≈λ_{exc} gold pattern depicted in Fig. 9 (a). Light from the gap regions is suppressed and mainly transmitted in the center part of the aperture. Furthermore, indications of a higher intensity at the lower triangle edges close to the central aperture can be assumed, which is predicted by the simulation in Fig. 1 (a). However, an experimental verification of fine details of the field intensity distribution as projected by the simulation is challenging. Besides the cantilever tip size, its quality, and the excitation wavelength, mainly the distance of the collecting objective lens from the sample reduces the lateral resolution substantially. This phenomena was discussed earlier and is in agreement with the simulation data in Fig. 3.

VI. CONCLUSION

In summary, we investigated the near-field intensity distribution generated through light interaction with butterfly nanoantennas, both using FDTD simulations with computer generated models, and SNOM measurements at commercially available Fischer patterns. Essential agreement between the simulation and the key experimental observations are found.

Of special interest was the light enhancement by the nanoantennas. Light confinement, field enhancement, and light intensity from metal covered areas are observed in the d≤λ_{exc} regime. For large patterns (d>λ_{exc}), the intensity distribution is seen to be dominated by fundamental transmission and reflection from the metal pattern.

The best experimental conditions to achieve highest lateral resolution and investigate light-matter interaction signatures can be achieved by using the smallest SNOM cantilever size available, high power excitation (high signal-to-noise ratio), and beneficially a small detector distance relative to the sample. A maximum lateral resolution smaller than 100 nm and well below the diffraction limit for optical microscopy was achieved using a 90 nm SNOM cantilever opening and 532 nm excitation.

ACKNOWLEDGMENT

The authors would like to thank our Meta colleagues Kathryn M. Kelchner, John Roberts, Guillaume Lheureux, Yaniv Vinish, Shuyu Bao, and Matthias Finger from WITec (Oxford Instruments) for the useful discussions. N.M.P. would like to gratefully acknowledge Prof. Junichiro Kono and Prof. Geoff Wehmeyer from Rice University for their support during his internship.

REFERENCES

[1] T. H. Taminiau, F. B. Segerink, R. J. Moerland, L. (Kobus) Kuipers, and N. F. van Hulst, "Near-field driving of a optical monopole antenna," *Journal of Optics A: Pure and Applied Optics*, vol. 9, no. 9, p. S315, Apr. 2007.

[2] U. C. Fischer, J. Heimel, H.-J. Maas, H. Fuchs, J. C. Weeber, and A. Dereux, "Super-resolution scanning near-field optical microscopy," in *Optical Nanotechnologies*, J. Tominaga and D. P. Tsai, Eds. Berlin Heidelberg: Springer-Verlag, 2003, pp. 141-153.

[3] L. E. Hennemann, A. Kolloch, A. Kern, J. Mihaljevic, J. Boneberg, P. Leiderer, A. J. Meixner, and D. Zhang, "Assessing the plasmonics of gold nanotriangles with higher order laser modes," *Beilstein Journal of Nanotechnology*, vol. 3, pp. 674-683, 2012.

[4] J. Toporski, T. Dieing, and O. Hollricher, *Confocal Raman Microscopy*, 2nd ed. New York: Springer, 2018.

[5] K. S. Yee, "Numerical solution of initial boundary value problems involving Maxwell's equations in isotropic media," *IEEE Trans. Antennas Propagat.*, vol. AP-14, pp. 302-307, 1966.

[6] A. Z. Elsherbeni, *FDTD Course Notes*, Department of Electrical Engineering, The University of Mississippi, MS, Spring 2001.

[7] Ansys Lumerical FDTD [Online]. Available: https://www.ansys.com/en-gb/products/photonics/fdtd.

[8] Oxford Instruments, "alpha300 S - SNOM microscope" [Online]. Available: https://raman.oxinst.com/products/scanning-probe-microscopes/snom-alpha300s.

[9] WITec Project FIVE, software 5.5, suite help function.

[10] Oxford Instruments, "Scanning near-field optical microscopy (SNOM)" [Online]. Available: https://raman.oxinst.com/techniques/snom.

[11] Kentax.de UHV equipment, "Projection pattern" [Online]. Available: https://www.kentax.de/projection-pattern.html.

Saswatee Banerjee is currently working as Research Scientist at Meta Ireland, Cork, Republic of Ireland. Her research interests include optical design, simulation methods and light propagation in nano-optic and photonic components. Before joining Meta, she worked in Japan for 20 years in both industrial R&D and academia.

Nicolas Marquez Peraca is a 5th year Ph.D. Candidate in the Department of Physics and Astronomy at Rice University in Houston, TX, USA. Before coming to Rice in 2018, he was a Guest Researcher for 2 years at the National Institute of Standards and Technology, where he worked on the electric and opto-electronic characterization of multi-junction solar cells. He joined Meta's Display & Optics team in Cork, Republic of Ireland, in the fall of 2022 as a Research Scientist Intern. His current research interests include ultrafast phenomena in condensed matter physics, THz magneto-spectroscopy of quantum materials, and AR/VR metrology.

Alexander Franke is currently working in the Display & Optics team of Meta in Cork, Republic of Ireland. Prior to joining Meta he worked in academia and R&D at various locations in Germany and USA, including the University of Magdeburg, TU Berlin, North Carolina State University, and the Fraunhofer Institute for Solar Energy Systems in Freiburg, Germany. His research interests are wide spread ranging from crystal growth (epitaxy), optoelectronic devices, photonics, nanostructures, to metrology and especially optical characterization by various spectroscopic methods.

PSSFSS—An Open-source Code for Analysis of Polarization and Frequency Selective Surfaces

Peter S. Simon

Retired Antenna Engineer
Camarillo, California, USA
peter_simon@ieee.org

***Abstract* –** The open-source code PSSFSS for analysis and design of polarization selective surfaces (PSSs), and frequency selective surfaces (FSSs) is presented, beginning with an introduction to the Julia programming language in which the code is written. Analysis methods and algorithms used in PSSFSS are described, highlighting features of Julia that make it attractive for developing this type of application. Usage examples illustrate the code's ease of use, speed, and accuracy.

***Index Terms* –** computer code, frequency selective surface, FSS, Julia programming language, open-source, polarization selective surface, radome, reflectarray.

I. INTRODUCTION

PSSFSS [1] is a free, open-source code for analysis and design of polarization selective surfaces (PSSs), frequency selective surfaces (FSSs), radomes, reflectarray elements, and similar devices. It is written in Julia [2], a recently developed language for high-performance technical computing. Its speed, accuracy, and ease of use make PSSFSS useful and accessible to both students and working engineers. Section II of this paper briefly introduces the Julia programming language. Section III describes the PSSFSS program, including information on its deployment as a standard Julia package. It then goes on to outline the steps in the analytical formulation used in PSSFSS. Some of the key steps are detailed and their realization in Julia code is presented. In the process, a few of the features of Julia that make it well-suited for this type of application are highlighted. Section IV provides several usage examples, including timing and convergence studies, with comparisons to exact solutions or results of other simulation tools. Finally, conclusions are presented in Section V.

II. THE JULIA LANGUAGE

Julia [2] is a recently developed, free and open-source computer programming language intended for high-performance technical computing. A modern, dynamic, high-level language, Julia was specifically created to address perceived shortcomings of existing languages like R, C, C++, Fortran, Matlab, and Python. Notably, the developers of Julia were awarded the 2019 James H. Wilkinson Prize for Numerical Software. Although Julia can be used interactively where it "feels" like an interpreted language, it transparently compiles code to machine language prior to execution ("JIT" or just in time compilation), resulting in execution speed competitive with Fortran or C. Indeed, in 2017 Julia joined C, C++, and Fortran as the only languages to have achieved petaflop performance [3]. Support for parallelism (both distributed and threaded) is built into the language, as is support for multidimensional arrays of any dimensions and types. The syntax for performing linear algebra is similar to Matlab's. Installation of Julia is a simple process on Windows, Linux, or Macintosh computers. The language fully supports Unicode, so that symbols such as `ϵᵣ`, `μᵣ`, and `tanδ` can be used for Julia variable names, if desired.

Most of Julia's core code and its standard libraries are written in Julia itself, making it easy for users to read, understand, and contribute improvements. User-written packages employing custom types can be just as performant as functions and standard libraries supplied with the language, since all are written in Julia. In this way, Julia solves the so-called "two-language problem" wherein packages for dynamic languages like Python or Matlab that require maximum performance must either be partially written in C or Fortran, or be restricted to a compilable subset of the full language.

Additional comments about specific features of Julia that were found to be useful in developing PSSFSS are included below in Section III.

III. DESCRIPTION OF PSSFSS

A. Packaging

PSSFSS has been released as a registered Julia package. As such it can be installed via a single command at the Julia REPL[1]. Doing so causes Julia to download the

[1]"REPL" is an acronym for Read-Evaluate-Print Loop, the interactive terminal environment where the user types inputs that are then evaluated and printed back by Julia.

Submitted On: April 26, 2023
Accepted On: March 27, 2024

https://doi.org/10.13052/2024.ACES.J.390207

Git repository [1] containing the PSSFSS source code, along with repositories of dependent packages. Similarly, updates published to the PSSFSS Github repository can be automatically retrieved by the user with another simple Julia update command.

Besides its on-line user manual [4], PSSFSS includes a detailed, 86 page theory document [5] that derives from first principles the formulas and algorithms implemented in the code. The code is heavily commented with references to specific sections and equation numbers in the theory document to promote code transparency.

B. Analysis methods and algorithms used

1. Overview

PSSFSS solves for the electric and/or magnetic surface currents on planar FSS/PSS sheets located within a stratified medium consisting of any number of dielectric layers. Currents are represented using modified Rao-Wilton-Glisson (RWG) basis functions [6] and are determined via a periodic moment method (PMM) solution of the mixed-potential integral equation (MPIE) in the space domain. The potential Green's functions are computed using a wide-band expansion [7] that, for normal incidence, permits the most expensive part of matrix assembly to be performed once only, regardless of the number of analysis frequencies performed. Multiple FSS/PSS sheets are accommodated by cascading their generalized scattering matrices (GSMs). The number of Floquet modes retained in the GSMs is calculated automatically such that excluded modes must encounter at least 30 dB of attenuation between neighboring sheets. The following subsections describe some of these analysis steps in more detail, and describe their Julia implementation.

2. Surface representation

As in other surface-based moment method (MoM) formulations, in PSSFSS a conducting surface (in the case of a capacitive FSS) or aperture (in the case of inductive FSS) must be triangulated as a preliminary step in forming the RWG basis functions. Triangulation is accomplished using the `Triangulate` package, a convenient Julia interface to the well-known, planar mesh generator `Triangle` [8]. Polygon and triangle vertex locations in the plane are stored in one-dimensional arrays, each element of which is of type `SVector{2,Float64}` as defined in the `StaticArrays` [9] package. Here the type parameters `2` and `Float64` mean that each planar vertex is represented by a length-2 "static vector" consisting of two 64-bit floating point values (the x and y coordinates of the point). Since the length of an `SVector` is encoded statically into its type, this length is known to the Julia compiler, allowing optimizations at compile time such as CPU register or stack allocation (rather than slower heap allocation), and efficient packing in memory and retrieval from arrays of these objects. For example, an array of n `SVectors` requires exactly the same amount of memory as is required for a contiguous array of $2n$ 64-bit floating point numbers. Furthermore, linear algebra operations on `StaticArray` objects of small orders are specialized via unrolling and other optimizations to be many times faster than those on an ordinary, heap-allocated arrays.

Besides speed of computation, static vectors (and matrices) inherit all the convenient array syntax of the language. By way of illustration, given a pair of `SVectors` `r` and `s`, the expression `3r - 2s` will perform the indicated scalar multiplications[2] of each vector followed by a vector difference. The result will be another `SVector`. With the `LinearAlgebra` standard library package, many additional operations are defined. E.g., we may compute the dot product of the two vectors by writing `r ⋅ s`. The centered dot is the infix form of the two-argument `dot` function and is typed at the Julia REPL (or within an appropriately configured editor) as `\cdot` (LaTeX notation) followed by a `Tab` character.

3. Green's function calculation

Discretization of the MPIEs via MoM in the spatial domain requires calculation of the potential Green's functions for currents flowing in a stratified medium, subject to quasi-periodic (Floquet) boundary conditions in the lateral directions. For efficient numerical evaluation, each potential Green's function is represented as a sum of modal series and quasi-static, spatial series, as derived in detail in [5]. As an example, consider an electric surface current flowing in the interface plane z_s, located between dielectric layers s and $s+1$ of the stratified media. The $\hat{\boldsymbol{x}}\hat{\boldsymbol{x}}$ component of magnetic vector potential dyadic Green's function evaluated at $\boldsymbol{r} = \boldsymbol{\rho} + z_s\hat{\boldsymbol{z}} = (x, y, z_s)$ due to a point current source at $\boldsymbol{r}' = \boldsymbol{\rho}' + z_s\hat{\boldsymbol{z}} = (x', y', z_s)$ is

$$G^A_{xx}(\boldsymbol{\rho}-\boldsymbol{\rho}', z_s, z_s) = \tilde{\mu}\Big\{\Sigma_{M1}(\boldsymbol{\rho}-\boldsymbol{\rho}') + \\ + \frac{u}{4\pi}\big[\Sigma_{S1}(\boldsymbol{\rho}-\boldsymbol{\rho}') + c_3\Sigma_{S2}(\boldsymbol{\rho}-\boldsymbol{\rho}')\big]\Big\}, \quad (1)$$

where $u > 0$ is an appropriately chosen smoothing factor with units of wavenumber, $\tilde{\mu} = \mu_s\mu_{s+1}/(\mu_s + \mu_{s+1})$, μ_n is the permeability of dielectric region n, ω is the radian frequency, and c_3 is a constant that depends on frequency, u, and the electrical parameters of regions s and $s+1$. Σ_{S1} and Σ_{S2} are quasi-static, spatial series, and Σ_{M1} is a modal series. All series are double sums $\sum_{m=-\infty}^{\infty}\sum_{n=-\infty}^{\infty}$ which is abbreviated as $\sum_{m,n}$ hereafter.

[2] A numeric literal prepended to a variable or parenthesized expression implies multiplication.

Spatial series

The spatial series are

$$\Sigma_{S1}(\boldsymbol{\rho}-\boldsymbol{\rho}') = \sum_{m,n} \frac{e^{-u\rho_{mn}}}{u\rho_{mn}} e^{-j(m\psi_1+n\psi_2)}, \qquad (2)$$

$$\Sigma_{S2}(\boldsymbol{\rho}-\boldsymbol{\rho}') = \sum_{m,n} e^{-u\rho_{mn}} e^{-j(m\psi_1+n\psi_2)}, \qquad (3)$$

where $\rho_{mn} = \|\boldsymbol{\rho}-\boldsymbol{\rho}'-m\boldsymbol{s}_1-n\boldsymbol{s}_2\|$, $\boldsymbol{s}_1$ and $\boldsymbol{s}_2$ are the direct lattice vectors of the periodic metalization pattern, and ψ_1 and ψ_2 are the incremental phase shifts associated with the Floquet boundary conditions in the $\boldsymbol{s}_1$ and $\boldsymbol{s}_2$ directions, respectively. It is evident that these rapidly (exponentially) convergent series are independent of frequency whenever the incremental phase shifts are. This occurs for normally incident illumination of the FSS ($\psi_1 = \psi_2 = 0$) or when simulating an FSS placed within a rectangular waveguide. When either of these is the case, and a swept-frequency analysis is desired, the contributions of the spatial series can be calculated a single time and reused at each new analysis frequency, achieving substantial execution time savings. It should also be noted that Σ_{S1} contains the known $1/\|\boldsymbol{\rho}-\boldsymbol{\rho}'\|$ static singularity in the $(m,n) = (0,0)$ term, permitting singularity subtraction and closed-form integration [10] as part of the MoM procedure.

It is of interest to see how these series are evaluated in Julia. The following code fragment is taken from the PSSFSS package:

```
# Sum over the r'th ring:
for (m, n) in Ring(r)
    uρmn = norm(uρ⃗00 - (m * us⃗1 + n * us⃗2))
    phase = -(m*ψ1 + n*ψ2)
    ...
end
```

The `for` loop iterates over the `(m,n)` tuples of integer indices comprising the `r`th concentric ring of the summation lattice. For example, `Ring(0)` generates the single tuple `(0,0)`, while `Ring(1)` iterates over the eight tuples `(1, -1)`, `(1, 0)`, `(1, 1)`, `(-1, -1)`, `(-1, 0)`, `(-1, 1)`, `(0, -1)`, and `(0, 1)`. In the code base `Ring` is a `struct` defined simply as

```
struct Ring
    r::Int
end
```

where the double colon is a type declaration for field `r`. The capability to iterate on `Ring(r)` as in the `for` loop above comes from defining a method for the base Julia `iterate` function that accepts two inputs: a variable of type `Ring`, and the current state of the iterator. It provides as outputs the next iterate and updated state. Each tuple is then efficiently generated iteratively in turn (i.e., lazily) in the `for` loop, avoiding unnecessary heap allocations. The above `for` loop is actually embedded in an outer loop over the ring index `r`, where convergence is checked after summing the contributions over each ring—the natural and rigorously correct way to form partial sums of such series. Thus the `Ring` type, straightforwardly implemented using Julia's standard iteration protocol, enhances the simplicity and readability of the Green's function code.

Calculation of the scalar variable `uρmn` within the body of the `for` loop above shows how closely Julia code can resemble the mathematics that it is implementing. Variables `uρ⃗00`, `us⃗1`, and `us⃗2` are all of type `SVector{2,Float64}`, representing in this case dimensionless 2-vectors. Again, such variable names incorporating Unicode symbols are easily typed using LaTeX notation. The expression passed as the argument to the `norm` function above will be evaluated prior to the call, resulting in a new `SVector`, stored either in the CPU stack or CPU registers (without any heap allocation). The function `norm` computes the 2-norm of a vector or matrix, and is exported by the `LinearAlgebra` package. However, a method specifically for arguments of type `SVector{2,Float64}` is provided at compile time by the `StaticArrays` package. Both the construction of the argument and calculation of its norm in the specialized method avoid (via unrolling) the loops that would otherwise be needed for dealing with standard arrays.

Modal Series

The modal series is

$$\Sigma_{M1}(\boldsymbol{\rho}-\boldsymbol{\rho}') = \sum_{m,n} f_{(m,n)} e^{-j\boldsymbol{\beta}_{mn}\cdot(\boldsymbol{\rho}-\boldsymbol{\rho}')}, \qquad (4)$$

where

$$f_{(m,n)} = \frac{1}{2A}\left[\frac{2V_{\mathrm{i}}^{\mathrm{TE}}(\beta_{mn})}{j\omega\tilde{\mu}} - \frac{1}{\kappa_{mn}} - \frac{c_3}{\kappa_{mn}^3}\right]. \qquad (5)$$

Here A is the area of the unit cell, $V_{\mathrm{i}}^{\mathrm{TE}}$ is the spectral transmission line Green's function as defined in [11], $\boldsymbol{\beta}_{mn} = \boldsymbol{\beta}_{00} + m\boldsymbol{\beta}_1 + n\boldsymbol{\beta}_2$, $\boldsymbol{\beta}_{00} = (\psi_1\boldsymbol{\beta}_1 + \psi_2\boldsymbol{\beta}_2)/(2\pi)$, $\kappa_{mn} = \sqrt{\boldsymbol{\beta}_{mn}\cdot\boldsymbol{\beta}_{mn} + u^2}$, and $\boldsymbol{\beta}_1 = (2\pi/A)\boldsymbol{s}_2 \times \hat{\boldsymbol{z}}$ and $\boldsymbol{\beta}_2 = (2\pi)/A\hat{\boldsymbol{z}} \times \boldsymbol{s}_1$ are the reciprocal lattice vectors. The modal series is very smooth as a function of $\boldsymbol{\rho}-\boldsymbol{\rho}'$ and rapidly converging, since the summand decays as β_{mn}^{-5}. Using the change of variables $\boldsymbol{\rho}-\boldsymbol{\rho}' = \xi_1\boldsymbol{s}_1 + \xi_2\boldsymbol{s}_2$ and using the fact that

$$\xi_i = \frac{1}{2\pi}\boldsymbol{\beta}_i\cdot(\boldsymbol{\rho}-\boldsymbol{\rho}'), \quad i = 1,2 \qquad (6)$$

the series can be rewritten in the form

$$\Sigma_{M1}(\xi_1\boldsymbol{s}_1 + \xi_2\boldsymbol{s}_2) = e^{-j(\xi_1\psi_1+\xi_2\psi_2)} \sum_{m,n} f_{(m,n)} e^{-j2\pi(m\xi_1+n\xi_2)}. \qquad (7)$$

If we restrict evaluation to a discrete, regular grid of ξ_1 and ξ_2 points, and assume that the summand is negligibly small outside some maximal ring index, it is straightforward to recast the series above into the form of a two-dimensional discrete Fourier transform, which is efficiently evaluated using the fast Fourier transform (FFT).

Low-order bivariate polynomial interpolation is used to allow evaluation of the modal series at arbitrary points within the grid.

In the Julia implementation of the modal series, it is convenient when tabulating $f_{(m,n)}$ to use an array whose indices can range over both positive and negative integers. This is accomplished by use of the `OffsetArrays` package, which provides Julia with arrays that have arbitrary indices, similar to those found in some other programming languages like Fortran. Consider the following code fragment, taken from the modal series code:

```
parent = zeros(ComplexF64, 2mg + 1, 2mg + 1)
table1g = OffsetArray(parent, -mg:mg, -mg:mg)
```

The `zeros` call returns a two-dimensional array of 64-bit, complex, floating-point numbers initialized to zero. The indices range from `1` to `2*mg + 1` (native Julia arrays use 1-based indexing). The `OffsetArray` call returns an array sharing the same memory as `parent`, but whose indices range from `-mg` to `mg`. There is no performance penalty associated with indexing into `table1g` versus `parent`. Both `StaticArrays` and `OffsetArrays` were originally contributed by the Julia user community, and both are written entirely in Julia, showing the power and flexibility inherent in the language.

Tabulation of $f_{(m,n)}$ is performed in a parallel (multithreaded) loop. Here is a fragment from the relevant code:

```
# Fill the tables:
@threads for r in (mmax_oldo2+1):mmaxo2
    ringsum1 = zero(eltype(table1g))
    ....
    for (m, n) in Ring(r)
        β⃗mn = β⃗00 + m * β⃗1 + n * β⃗2
        β² = β⃗mn ⋅ β⃗mn # magnitude squared
        ...
    end
    ...
    table1g[m,n] += ringsum1
    ...
end
```

The outer loop over ring index is parallelized (threaded) by a call to `@threads` of the built-in threading library `Threads`. The `@` symbol denotes a Julia *macro*, which can arbitrarily transform Julia source prior to compilation. The two lines shown in the inner loop over summation ring indices, where $\boldsymbol{\beta}_{mn}$ and $\|\boldsymbol{\beta}_{mn}\|^2$ are computed, exemplify once again how the use of Unicode symbols in variable names can enhance clarity when translating a mathematical formulation to Julia code. $\vec{\beta}_{00}$, $\vec{\beta}_1$, and $\vec{\beta}_2$ are all defined previously in the code and have type `SVector{2,Float64}`. The assignment causes $\vec{\beta}_{mn}$ to also have the same type without requiring any type declaration, an example of type inference performed by the Julia compiler.

Following tabulation, the FFT is performed in-place by a call to the function `FFT!` from the `FFTW` package. The latter provides convenient Julia bindings to the popular FFTW library [12].

4. GSM representation and cascading

A GSM is represented in the Julia code by the `GSM` type, defined as

```
struct GSM
    s11::Matrix{ComplexF64}
    s12::Matrix{ComplexF64}
    s21::Matrix{ComplexF64}
    s22::Matrix{ComplexF64}
end
```

The `s11`, `s12`, `s21`, and `s22` fields store the four partitions of the full GSM. In Julia, an array is indexed using square brackets, e.g. `s[1,2]` to select the element of array `s` in the first row and second column. The Julia compiler converts this syntax into the call `getindex(s, 1, 2)`. By extending the `getindex` function with a new method for the `GSM` type, one can enable indexing into a variable of this type:

```
function Base.getindex(gsm::GSM, i, j)
    (i, j) == (1, 1) && (return gsm.s11)
    (i, j) == (1, 2) && (return gsm.s12)
    (i, j) == (2, 1) && (return gsm.s21)
    (i, j) == (2, 2) && (return gsm.s22)
    throw(BoundsError(gsm, (i, j)))
end
```

Here the short-circuit logical "and" operator `&&` is used as a concise if-then construct, a common Julia idiom. Given `g::GSM`, the above definition allows, e.g., `g[1,2]` to be used in lieu of `g.s12`. Since Julia functions use "pass-by-sharing" semantics, such indexing does not cause any unwanted copying of the GSM partitions.

Cascading of GSMs is accomplished by use of the Redheffer star product [13–14]. If A and B are scattering matrices for two linear networks, the scattering matrix of the cascaded network is given by the (scattering) star product $A \star B$. If A and B are the block matrices

$$A = \begin{bmatrix} A_{11} & A_{12} \\ A_{21} & A_{22} \end{bmatrix}, \quad B = \begin{bmatrix} B_{11} & B_{12} \\ B_{21} & B_{22} \end{bmatrix}, \tag{8}$$

then their star product is

$$A \star B = \begin{bmatrix} (A \star B)_{11} & (A \star B)_{12} \\ (A \star B)_{21} & (A \star B)_{22} \end{bmatrix}, \tag{9}$$

where

$$(A \star B)_{11} = A_{11} + A_{12}B_{11}(I - A_{22}B_{11})^{-1}A_{21}, \tag{10a}$$

$$(A \star B)_{12} = A_{12}(I - B_{11}A_{22})^{-1}B_{12}, \tag{10b}$$

$$(A \star B)_{21} = B_{21}(I - A_{22}B_{11})^{-1}A_{21}, \tag{10c}$$

$$(A \star B)_{22} = B_{22} + B_{21}A_{22}(I - B_{11}A_{22})^{-1}B_{12}, \tag{10d}$$

and I is the identity matrix. The star product is implemented in PSSFSS in the `cascade` function:

```
function cascade(a::GSM, b::GSM)
  n2a = size(a[2,2], 2)
  n1b = size(b[1,1], 1)
  n1b ≠ n2a && error("Non-conformable GSMs")
```

```
    gprod1 = (I - a[2,2] * b[1,1]) \ a[2,1]
    s21 = b[2,1] * gprod1
    s11 = a[1,1] + (a[1,2] * b[1,1] * gprod1)
    gprod2 = (I - b[1,1] * a[2,2]) \ b[1,2]
    s12 = a[1,2] * gprod2
    s22 = b[2,2] + (b[2,1] * a[2,2] * gprod2)
    return GSM(s11, s12, s21, s22)
end
```

The backslash operator `\` and the symbol `I` used above are from the `LinearAlgebra` package. `I` is an object that represents an identity matrix of any order. The backslash, as in Matlab, performs matrix division using a polyalgorithm that depends on the array types on both sides. For the dense, square matrices occuring on the left-hand sides here, it calls a LAPACK solver based on LU factorization. By including the function definition

```
⋆(a,b) = cascade(a,b)
```

it is now possible to compute the cascade of `GSM`s `s` and `t` and store the result in `c` by simply typing `c = s ⋆ t`.

The GSM of a dielectric layer has the form $\left[\begin{smallmatrix} 0 & D \\ D & 0 \end{smallmatrix}\right]$, where D is a diagonal matrix. Therefore, when cascading some general GSM with that of a dielectric layer, the calculations needed are significantly simpler than the general case described by Eqs. (10). PSSFSS defines the `Layer` type for dielectric layers, along with several additional methods of the `cascade` function, with signatures `cascade(a::GSM, b::Layer)` and `cascade(a::Layer, b::GSM)`, wherein the appropriate, simplified calculations are encoded. This is an example of *multiple dispatch*, one of the fundamental paradigms of Julia programming. The correct method to be called for a function is selected from the available methods at compile time based on the types of *all* of the call site arguments. This is in contrast to standard object-oriented programming, where the selected method depends only on the first argument (single dispatch). Multiple dispatch is clearly more powerful, and it can be argued that it is a better fit to the needs of scientific computing. For example, given conformable arrays `A`, `B`, and `C`, the expression `A * B * C` is transformed by the Julia compiler into the call `*(A, B, C)`, a three-argument method for the `*` (multiplication) function. Within that method, the number of multiplications needed for `(A * B) * C` is compared to that for `A * (B * C)` to choose which of these to execute. Users can add their own methods as needed for their custom types.

5. Fast sweep algorithm

The default method for frequency sweeps is an extremely robust, diagonal rational function interpolation using the Stoer-Bulirsch [15] ("fast sweep") algorithm. Applied to the final, composite GSM of the structure being analyzed, it eliminates the need for a full PMM solution at each frequency (a "discrete sweep"), often producing speedups of 10× to 20×. The algorithm starts by analyzing the structure at five equally spaced frequencies (interpolation "knots") across the requested bandwidth. The composite GSM of the full structure is interpolated at the remaining frequencies via two different orders of rational function, and an error estimate is computed from their difference at each frequency. The next knot is selected as that frequency with the largest error estimate. A full analysis is performed at this knot, and new interpolations are performed incorporating the new data. The process continues until the error estimate remains less than -80 dB for three consecutive iterations. The strict termination criterion employed in PSSFSS for this algorithm makes it absolutely reliable, in the author's experience.

Additional details of the theory and implementation for PSSFSS can be found in [5].

C. Program features

Currently supported element types include rectangular strips, meanderlines, loaded and filled crosses, sinuous and manji crosses, Jerusalem crosses, split rings, and polyrings. The latter are able to model concentric rectangular loops or polygonal rings. All element types are fully parameterized for easy specification and optimization. The user manual [4] includes a gallery of supported element types.

Available output quantities include scattering parameters (magnitudes, phases, or complex) using a TE/TM, Ludwig 3, or LHCP/RHCP polarization basis, axial ratio, and others.

D. Program usage

PSSFSS is run in a Julia script. The geometry to be analyzed is specified as a vector of two or more dielectric `Layers` and zero or more `RWGSheets`. The latter define the FSS/PSS sheets and are instantiated by calling constructors such as `meander`, `strip`, `polyring`, etc. After also specifying the desired scan angles (or unit cell incremental phase shifts) and frequencies to be analyzed, a call to the `analyze` function performs the analysis. Outputs are requested using a tiny domain-specific language implemented by the `@outputs` macro. As an example, providing `@outputs s21db(L,R) ar22db(v)` as the second argument to the `extract_results` function will produce a matrix whose columns contain 1) transmission amplitude in dB to LHCP pol exiting port 2 due to a RHCP wave incident at port 1, and 2) reflected axial ratio in dB exiting port 2 due to an incident Ludwig 3 vertical wave at port 2. The outputs can be further post-processed and/or plotted in the same interactive or batch Julia session.

IV. EXAMPLE RESULTS

A. Symmetric strip grid

This example consists of a symmetric strip grating, i.e., a grating where the strip width is half the unit cell

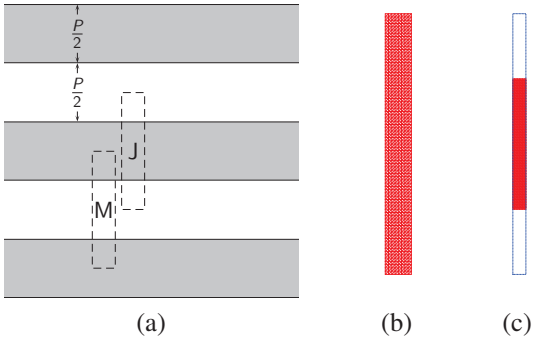

Fig. 1. Symmetric strip grid: (a) Gray areas represent metalization, Dashed lines show two possible choices for unit cell location, (b) Triangulation used for both J and M choice of unit cell, and (c) Triangulation with unit cell boundary also shown.

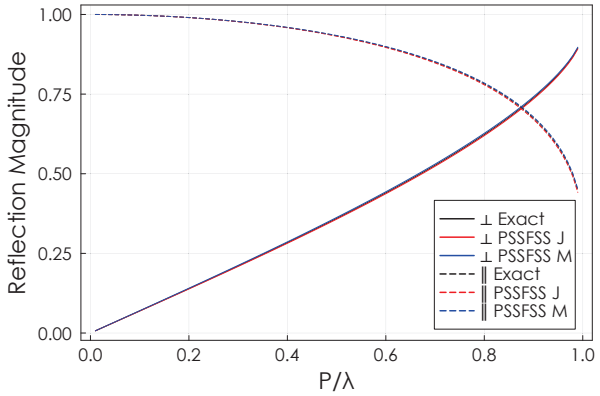

Fig. 2. Reflection magnitude for symmetric strip grid.

period P, as shown in part (a) of Fig. 1. The grating lies in the $z = 0$ plane with free space on both sides. The shaded areas represent metalization. The dashed lines show two possible choices for the unit cell location: "J" for a formulation in terms of electric surface currents, and "M" for magnetic surface currents. The same triangulation (parts (b) and (c) of the figure) can be used for either choice. The length of the unit cell in the x direction is arbitrary, here chosen to be one tenth of the strip width. The triangulation shown uses 8 edges in the x direction and 80 in the y direction for a total of 640 squares bisected into 1280 triangles. The PSSFSS analysis covered 99 frequencies where period normalized to wavelength (P/λ) varied from 0.01 to 0.99, requiring about 9 seconds of execution time. Normal incidence reflection coefficient magnitudes and phases computed by PSSFSS are compared with the exact solution ([16], [17, Prob. 10.6]) for the electric field parallel ($\|$) and perpendicular ($\perp$) to the direction of the grid (the y axis) in Figs. 2 and 3. The maximum magnitude error for either polarization is about

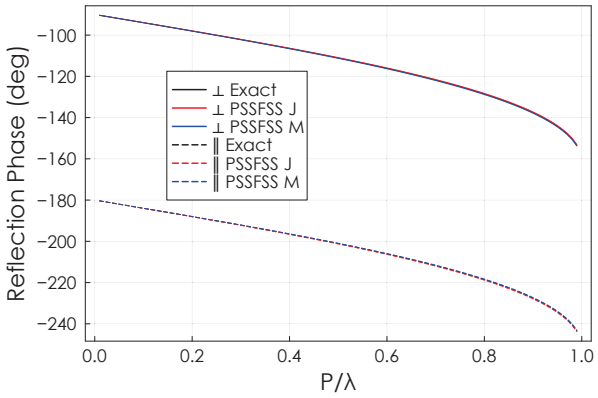

Fig. 3. Reflection phase for symmetric strip grid.

0.006 at the highest frequency. Maximum phase error is about 0.35°, also at the highest frequency. In all cases the solutions for the M and J unit cells bracket the exact solution. Presentation of the Julia script needed to run this example is omitted here; it can be found in the online manual [4].

B. Over-sized Jerusalem cross slot

This example, taken from [18] and illustrated in the inset of Fig. 4, constitutes a severe test of the fast sweep algorithm. The unit cell is a 2.5 cm square. The FSS is etched on a 0.02 cm thick dielectric slab with $\epsilon_r = 2.0 - j0.1$. The incidence angle is $(\theta, \phi) = (45°, 1°)$ so that higher-order free-space Floquet modes begin propagating at 7.025, 12.292, 12.542, 14.051, 16.665, and 17.060 GHz. Figure 4 shows how the computed transmission coefficient for TM polarization converges as the discretization is made finer. All of the traces overlay for frequencies below about 17 GHz. The fast sweep results for the final case are also shown, and they are indistinguishable from the discrete sweep results. The maximum fast sweep error for any of the 381 frequencies plotted is less than 0.0006 dB. The "glitches" in the traces between 16 GHz and 18 GHz are resonances associated with blazing frequencies. Swept frequency timing for discrete and fast sweeps are shown in Table 1. This analysis and all others reported in this paper were performed on a 3 GHz Core i7-9700 CPU. As shown in the table, fast sweeps for this example exhibited a speedup of about 4×. Greater speedups are usually obtained, but the many modes passing out of cut-off in this band make this case especially difficult. Here, about 90 of the 381 requested analysis frequencies required a full PMM solve in the fast sweep. The worst convergence of the model is obtained at the highest frequency, 20 GHz. The final column of Table 1 shows how the computed transmission coefficient at this frequency changes with number of triangles in the discretization. Applying Richardson extrapolation

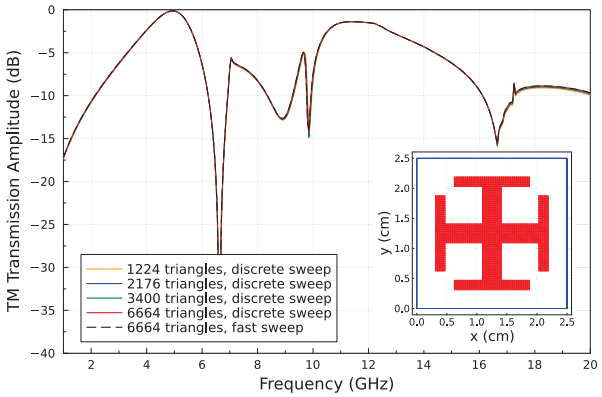

Fig. 4. TM transmission coefficient for the over-sized Jerusalem cross slot from [18]. The inset triangulation contains 3400 triangles; a blue dashed line demarks the 2.5 cm unit cell.

Table 1: Timing and convergence for the Jerusalem cross

Number of Triangles	Sweep Time (s) Discrete	Fast	Fast Sweep Speedup	T at 20 GHz (dB)
1224	199.3	58.3	3.4	-9.97
2176	627.5	155.2	4.0	-9.83
3400	1732.1	420.1	4.1	-9.75
6664	9182.0	2096.8	4.4	-9.66

[19] to this series results in a predicted converged value of -9.54 dB, about 0.1 dB away from the 6664 triangle result. Listing 1 contains the code used to generate the fast sweep PSSFSS data and geometry plot for the 3400 triangle case.

C. 5-Sheet meanderline/strip CPSS

This example, from [20], consists of a 5-sheet, sequentially rotated, circular polarization selective surface (CPSS). The top images in Fig. 5 are the individual sheet triangulations. Each sheet shares the same unit cell, a 5.2 mm square. Sheets are etched on dielectric substrates separated from their neighbors by foam layers. The structure consists of 9 dielectric layers and 5 FSS sheets. Below the sheet triangulations is a plot of computed insertion loss and transmitted axial ratio (AR) for a right-hand circular polarization (RHCP) wave normally incident on the structure, both computed by PSSFSS and CST, the latter digitized from plots in [20]. The differences in the two models' results are attributed to finite metalization thickness used in the CST model, a feature not yet supported by PSSFSS. Analysis of the 5-sheet composite structure at 101 frequencies required only 20 s for PSSFSS, compared to the 17 min and 1 hr reported in [20] for CST using a coarse and fine mesh, respectively. The speed of PSSFSS for this case is due to multiple factors: 1) analysis is fastest at normal incidence, 2) meanderlines and strips are triangulated using structured meshes which are exploited by PSSFSS to avoid redundant calculations, 3) the elements used herein fill only a small portion of the unit cell and are not resonant, reducing the number of triangles required, and 4) the smoothly varying GSM over this analysis bandwidth required only 13 full solutions out of 101 analysis frequencies in the fast sweep algorithm.

Listing 2 is a fragment of the log file created by PSSFSS when analyzing the CPSS. It recapitulates the layup of the structure and displays the number of Floquet modes assigned to each dielectric layer in the final

Listing 1 Julia script used to produce the triangulation plot and compute the fast sweep performance shown in Fig. 4.

```
using PSSFSS, Plots
P = 2.5 # unit cell period
sheet = jerusalemcross(class='M', ntri=3400, P=P,
                       w=P/8, L1=3P/4, L2=P/8,
                       A=P/2, B=P/16, units=cm)
pl = plot(sheet, unitcell=true, linecolor=:red,
          size=(600,600))
strata = [Layer()
          sheet
          Layer(ϵr=2.0, tanδ=0.05, width=0.02cm)
          Layer()]
freqs = 1:0.05:20; steering = (ϕ=1, θ=45)
reslt = analyze(strata, freqs, steering)
T_TM = extract_result(reslt, @outputs s21db(tm,tm))
```

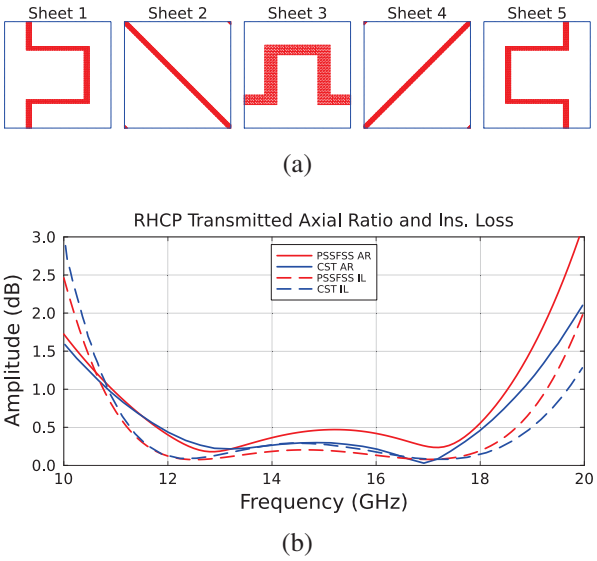

Fig. 5. 5-Sheet CPSS from [20]: (a) All 5 sequentially rotated sheets share the same 5.2 mm unit cell and (b) RHCP → RHCP axial ratio and insertion loss computed by PSSFSS and CST Microwave Studio.

column. The layers labeled 1 and 11 are the semi-infinite vacuum regions on either side of the FSS structure. Note that the thin substrates adjacent to the FSS sheets, labeled as layers 2, 4, 6, 8, and 10, are assigned zero modes. This is because a very large number of modes would be required to cascade GSMs for very thin layers adjacent to FSS sheets. Instead, PSSFSS defines a so-called "GSM Block" consisting of the sheet and any neighboring thin layers. A single, composite GSM is computed for this GSM Block using the stratified media Green's functions. For the remaining foam spacer layers, it is observed that 10 modes are used in the 3.81 mm layers 3 and 9, while 18 modes are used in the thinner 2.61 mm layers 5 and 7.

Listing 2 Portion of the log file produced by PSSFSS when analyzing the CPSS of Fig. 5.

```
 Layer Width units  epsr   tandel  mur  mtandel modes
 ----- ----------- ------ ------  ------ ------ -----
     1   0.000  mm   1.00 0.0000   1.00 0.0000     2
     2   0.127  mm   2.17 0.0009   1.00 0.0000     0
 =================  Sheet   1  ======================
     3   3.810  mm   1.04 0.0017   1.00 0.0000    10
     4   0.127  mm   2.17 0.0009   1.00 0.0000     0
 =================  Sheet   2  ======================
     5   2.610  mm   1.04 0.0017   1.00 0.0000    18
 =================  Sheet   3  ======================
     6   0.127  mm   2.17 0.0009   1.00 0.0000     0
     7   2.610  mm   1.04 0.0017   1.00 0.0000    18
     8   0.127  mm   2.17 0.0009   1.00 0.0000     0
 =================  Sheet   4  ======================
     9   3.810  mm   1.04 0.0017   1.00 0.0000    10
 =================  Sheet   5  ======================
    10   0.127  mm   2.17 0.0009   1.00 0.0000     0
    11   0.000  mm   1.00 0.0000   1.00 0.0000     2
```

Of course, this use of multi-mode GSM cascading is only possible because all sheets in this structure share the same periodicity. For structures with sheets of different periodicity, PSSFSS employs the usual approximation where only the principal TE and TM Floquet modes are included in the GSMs used for cascading.

D. Loaded cross slots bandpass filter

This example, originally from [21, Fig. 7.9], was also used in [22]. The geometry, shown in Fig. 6, consists of two identical loaded cross slot-type elements separated by a 6 mm layer of dielectric constant 1.9. Outboard of each sheet is a 1.1 cm layer of dielectric constant 1.3. The closely spaced sheets provide another good test of the generalized scattering matrix cascading formulation implemented in PSSFSS. Analysis of this structure with PSSFSS at 381 frequencies over a 20:1 bandwidth was performed for a few different mesh discretizations. A total of 18 Floquet modes in the center dielectric layer was selected by the code to accurately model interactions between the two closely spaced FSS sheets. Computed transmission amplitudes from PSSFSS and HFSS are compared in Fig. 7, where good agreement is observed over a very wide dynamic range of nearly 80 dB.

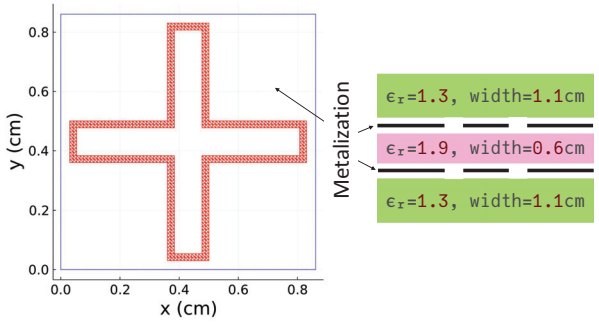

Fig. 6. Bandpass filter geometry consisting of two identical loaded cross slots in a three-layer, symmetrical, dielectric sandwich structure.

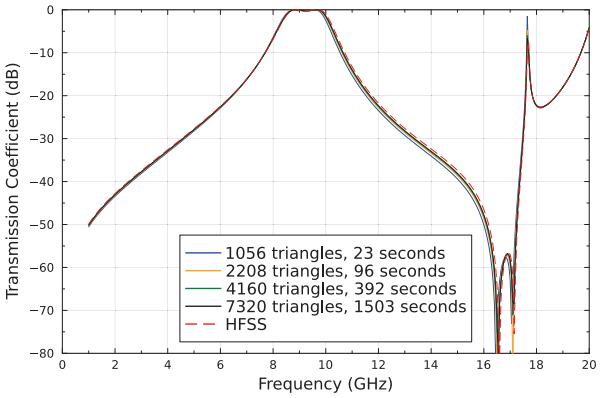

Fig. 7. Normal incidence transmission amplitude versus frequency for the bandpass filter.

Timings for the different discretizations are given in the figure legend.

E. Other

The complete scripts for all the above cases along with numerous other usage examples can be found in [4], including reflectarray elements, rabsorbers, and a fully worked-out design optimization for a CPSS using an evolutionary algorithm.

V. CONCLUSIONS

An open-source code PSSFSS for analysis of polarization and frequency selective surfaces has been described. PSSFSS can be obtained, installed, and used easily and without cost. It is written in the relatively new Julia programming language; therefore, some of the features of Julia that were especially convenient and useful in developing PSSFSS were highlighted. PSSFSS employs multi-threading and several novel algorithms to enhance computational efficiency. Examples were provided that demonstrate the speed, ease of use, and accuracy of the code.

REFERENCES

[1] P. S. Simon, "PSSFSS — Analysis of polarization and frequency selective surfaces in Julia," [Online]. Available: https://github.com/simonp0420/PSSFSS.jl

[2] *The Julia Programming Language*. [Online]. Available: https://julialang.org

[3] JuliaHub. *Parallel Supercomputing for Astronomy*. [Online]. Available: https://juliahub.com/case-studies/celeste

[4] P. S. Simon. *PSSFSS User Manual*. [Online]. Available: https://simonp0420.github.io/PSSFSS.jl/stable/manual

[5] P. S. Simon, "PSSFSS theory documentation," Tech. Report, May 2021. [Online]. Available: https://github.com/simonp0420/PSSFSS.jl/blob/main/docs/TheoryDocs/theorydoc.pdf

[6] P. S. Simon, "Modified RWG basis functions for analysis of periodic structures," *2002 IEEE MTT-S Int. Microwave Symp. Dig.*, vol. 3, pp. 2029-2032, Seattle, WA, June 2002.

[7] P. S. Simon, "Efficient Green's function formulation for analysis of frequency selective surfaces in stratified media," *Dig. 2001 IEEE AP-S Int. Symp.*, vol. 4, pp. 374-377, Boston, MA, July 2001.

[8] J. R. Shewchuk, "Triangle: Engineering a 2D quality mesh generator and delaunay triangulator," *Applied Computational Geometry: Towards Geometric Engineering*, ser. Lecture Notes in Computer Science, M. C. Lin and D. Manocha, Eds. Springer-Verlag, vol. 1148, pp. 203-222, May 1996.

[9] StaticArrays—statically sized arrays for Julia. [Online]. Available: https://github.com/JuliaArrays/StaticArrays.jl

[10] D. R. Wilton, S. M. Rao, A. W. Glisson, D. H. Schaubert, O. M. Al-Bundak, and C. M. Butler, "Potential integrals for uniform and linear source distributions on polygonal and polyhedral domains," *IEEE Trans. Antennas Propagat.*, vol. AP-32, no. 3, pp. 276-281, Mar. 1984.

[11] K. A. Michalski and J. R. Mosig, "Multilayered media Green's functions in integral equation formulations," *IEEE Trans. Antennas Propagat.*, vol. 45, no. 3, pp. 508-519, Mar. 1997.

[12] M. Frigo and S. G. Johnson, "The design and implementation of FFTW3," *Proceedings of the IEEE*, vol. 93, no. 2, pp. 216-231, 2005.

[13] R. Redheffer, "Inequalities for a matrix riccati equation," *Journal of Mathematics and Mechanics*, pp. 349-367, 1959.

[14] R. C. Rumpf, "Improved formulation of scattering matrices for semi-analytical methods that is consistent with convention," *Progress In Electromagnetics Research B*, vol. 35, pp. 241-261, 2011.

[15] Y. Ding, K.-L. Wu, and D. G. Fang, "A broadband adaptive-frequency-sampling approach for microwave-circuit em simulation exploiting Stoer-Bulirsch algorithm," *IEEE Trans. Microwave Theory Tech.*, vol. 51, no. 3, pp. 928-934, 2003.

[16] L. A. Weinstein, *The Theory of Diffraction and the Factorization Method: Generalized Wiener-Hopf Technique*. Golem Press, 1969.

[17] R. E. Collin, *Field Theory of Guided Waves*, 2nd ed. IEEE Press, 1991.

[18] X. Wang and D. H. Werner, "Improved model-based parameter estimation approach for accelerated periodic method of moments solutions with application to the analysis of convoluted frequency selected surfaces and metamaterials," *IEEE Trans. Antennas Propag.*, vol. 58, no. 1, pp. 122-131, 2010.

[19] G. Dahlquist and Å. Björck, *Numerical Methods in Scientific Computing, Volume I*. SIAM, 2008.

[20] A. Ericsson and D. Sjöberg, "Design and analysis of a multilayer meander line circular polarization selective structure," *IEEE Trans. Antennas Propag.*, vol. 65, no. 8, pp. 4089-4101, 2017.

[21] B. A. Munk, *Frequency Selective Surfaces: Theory and Design*. John Wiley & Sons, Inc., 2000.

[22] L. Li, D. H. Werner, J. A. Bossard, and T. S. Mayer, "A model-based parameter estimation technique for wide-band interpolation of periodic moment method impedance matrices with application to genetic algorithm optimization of frequency selective surfaces," *IEEE Trans. Antennas Propag.*, vol. 54, no. 3, pp. 908-924, 2006.

Peter S. Simon is a retired antenna engineer and a Life Senior Member of the IEEE. He received the B.S. and M.S. degrees in electrical engineering from the University of Illinois at Urbana/Champaign and the Ph.D. degree in electrical and computer engineering from the University of California at Santa Barbara. He served in the United States Navy as both an enlisted man and later as a commissioned officer. During his engineering career he worked at Raytheon Electromagnetic Systems Division (now Raytheon Intelligence & Space), Goleta, CA, in positions involving antenna design and computational electromagnetics, where he ultimately attained the rank of Principal Engineer. Following his stint at Raytheon, he joined Space Systems/Loral (now Maxar Technologies Space Systems), Palo Alto, CA, where his work again involved computational electromagnetics, analysis, and design applied to reflector antennas, feed horns, fre-

quency and polarization selective surfaces, and feed networks for commercial satellite applications. In 2014 he was selected among the first group of SSL employees to be awarded the title of Distinguished Engineer. He is the author or coauthor of five patents and several papers relating to antennas. Since his retirement he has been involved in developing open-source software using the Julia programming language.

Wide-Angle Scanning and High Isolation Dual-Polarized Base Station Antennas for Sub-6 GHz Applications

Fang-Fang Fan, Pei-Pei Ma, and Qing-Lin Chen

Key Laboratory of Antennas and Microwave Technology
Xidian University, Xi'an, 710071, China
fffan@mail.xidian.edu.cn, 3305559651@qq.com, 929938860@qq.com

***Abstract* –** This paper presents a wide-angle scanning and high isolation base station antenna array. The antenna element employs a compact dual-polarized umbrella-shaped printed dipole with a small size of $0.23\lambda_0 \times 0.23\lambda_0 \times 0.26\lambda_0$, which provides the possibility for a small element spacing array. The antenna element possesses wide 3 dB beamwidth of 84.6° benefiting from the pulling down of the dipole arms. Then, a dual-layer metal superstrate structure and metal wall is adopted to mitigate different kinds of mutual coupling between the dual-polarized antenna elements in the array. Owing to the wide beamwidth of the element and the low mutual coupling between the elements, the final 4×6 antenna array can achieve a good beam-scanning capability with maximum scanning angle up to ±55° and a small gain variation of less than 3 dB over the operation band 3.3-3.8 GHz. The fabricated array shows the measured isolation between all ports of the antennas is increased to more than 20 dB. Scanning characteristics also agree well with the simulated results. With the merits of wideband, low-cost (simple design and easy fabrication), wide-angle beam-scanning capacity, and good radiation performance, the proposed design has potential for application in 5G base station systems.

***Index Terms* –** 5G base station antenna, dual-polarized antenna, high isolation, phased array antenna, wide-angle scanning.

I. INTRODUCTION

Fifth-generation (5G) communication technology has brought high data rate, large channel capacity, and low latency transmission experience to users. One of the 5G key technologies is beam-scanning arrays, which can realize multi-target communication and tracking. For 5G base station applications, dual-polarized capability should be required, which can extend system capacity without increasing size, and implement polarization diversity technology to achieve multipath fading resistance. Thus, designing a dual-polarized wide-angle scanning base station antenna array is an urgent task for researchers. To date, many efforts have been devoted to the single polarized wide beam-scanning array [1–5]. Few papers focus on both the dual-polarized and wide beam-scanning at sub-6 GHz simultaneously [6–8]. Actually, high isolation between the elements in the array is essential for wide-angle beam-scanning, otherwise serious mutual coupling would deteriorate the impedance matching and the radiation patterns of the array antennas. Single and dual-polarized array decoupling has been done recently [9–18]. Mutual coupling between the elements in the array is mainly blamed for the space wave coupling and surface wave coupling. Different decoupling methods have been used, such as DGS [9], EBG [10], and neutral line [11], which are devoted to reducing surface wave coupling. The DGS structure might introduce back radiation, and have narrow decoupling bandwidth. EBG requires more area to get better decoupling performance, which is not suitable to be used in closely packed antenna. The neutral line network needs a complicated design. Moreover, these methods are difficult to be applied in the dual-polarized antenna array. For space wave decoupling, frequency selective surface (FSS) [12], array-antenna decoupling surface (ADS) [13], meta-surface superstrate [14], baffle [15], dielectric stub [16] and hybrid decoupling array [17–18] have been employed to get better isolation.

In this paper, a dual-layer superstrate structure with periodic metal patches, referred to as a metal superstrate, has been introduced on top of the antenna to achieve distinct decoupling performance. Meanwhile, a separation metal wall is inserted between the columns of the array to reduce the cross polarization between the elements. Finally, a 4×6 antenna array is designed and fabricated. The measured results show that the mutual coupling between elements in the array is reduced to below -20 dB in the wideband range while maintaining stable radiation patterns. The array can achieve a good beam-scanning capability with maximum scanning angle up to ±55°and a small gain variation of less than 3 dB over the band 3.3-3.8 GHz.

Submitted On: April 27, 2023
Accepted On: March 16, 2024

https://doi.org/10.13052/2024.ACES.J.390208

II. DESIGN AND WORK MECHANISM

A. Antenna element configuration

Figure 1 (a) depicts the configuration of the proposed compact dual-polarized umbrella-shaped dipole. The antenna is composed of two orthogonal substrates, a microstrip balun, and two pairs of umbrella-shaped dipoles printed on both sides of the substrate. The ground plane is utilized to achieve directional radiation. The two substrates with thickness of 0.5 mm are made of FR4 with a relative dielectric constant of 4.4. Figure 1 (c) shows the detailed structure of the feeding balun. Compared with the conventional T-shaped dipole as shown in Fig. 1 (b), the proposed dipole has a more compact size, as the length of the substrate denoted *Ln1* has been reduced from 33 mm to *L1*=28 mm, which would contribute to the high isolation between the elements when the elements are formed into a compact array. Moreover, the beamwidth of the dipole has been widened from 78° to 84.6° as shown in Fig. 2 (c). Figure 2 (a) shows the simulated reflection coefficient and the port isolation. We can conclude the proposed element has a bandwidth of 14.1% (3.3-3.8 GHz) and high port isolation of more than 40 dB. The radiation patterns are stable in the whole band with the cross polarization more than 20 dB, as shown in Fig. 2 (b).

B. Antenna array decoupling scheme

With the small element distance in the array, strong coupling would deteriorate the impedance matching characteristics and the radiation patterns of the array antennas. A feasible hybrid decoupling method is employed in this paper. A separation metal wall is vertically placed between antenna elements, and a dual-layer metal superstrate structure is placed directly above the antenna array. These methods work together to realize a wideband decoupling within 3.3-3.8 GHz. The decoupling steps and mechanism will be illustrated in detail.

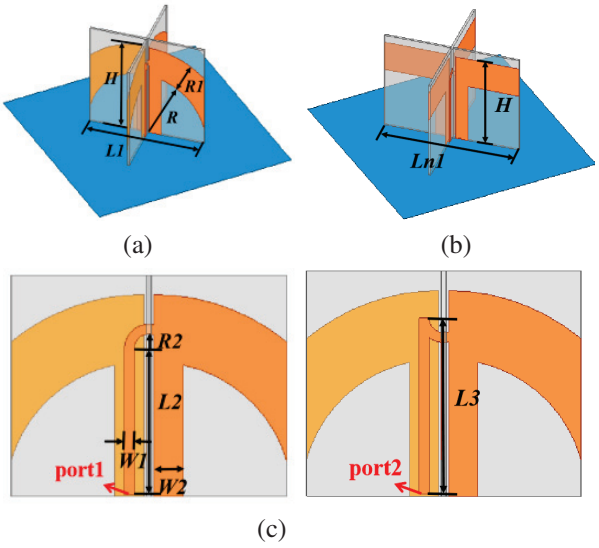

Fig. 1. Configuration of the antenna unit: (a) proposed antenna unit, (b) conventional dipole, and (c) side view of the proposed antenna (*L1*=28 mm, *R*=14 mm, *R1*=7 mm, *H*=21 mm, *Ln1*=33 mm, *R2*=2.5 mm, *L2*=15.4 mm, *W1*=1 mm, *W2*=3 mm, *L3*=18 mm).

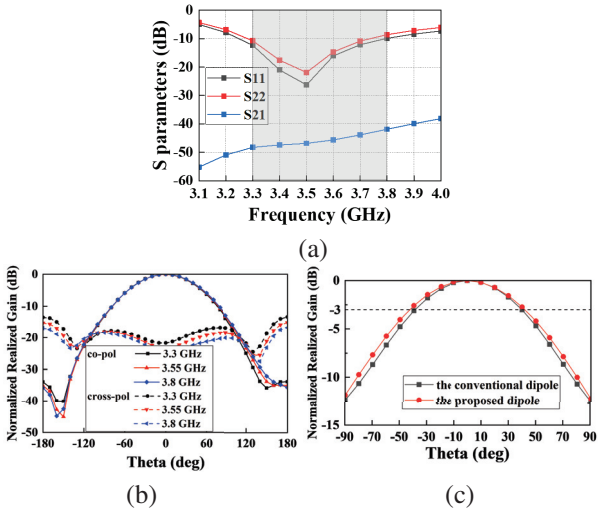

Fig. 2. Simulation results of the dipole: (a) S-parameters, (b) radiation patterns at different frequencies, and (c) comparison of the beamwidth between the conventional and the proposed dipole.

(1) Separation metal wall and lower metal superstrate for decoupling

As shown in Fig. 3 (a), it is a 1×4 linear array with the element distance of 33 mm ($0.4\lambda_0$, where λ_0 is the free space wavelength at 3.55 GHz). The port number has been marked in Fig. 3 (a). The separation metal wall is placed between two adjacent antennas, which block the propagation of spatially coupled waves and contribute to the suppression of cross-polarized coupling. The decoupling mechanism of the separation metal wall is based on the partition principle. Moreover, a lower metal superstrate is located directly on the top array as shown in Fig. 3 (b), which is used to further reduce the cross-polarized coupling between the elements. At the same time, the lower metal superstrate can also broaden the bandwidth of the antenna array. Figure 4 shows the simulated S-parameters of the 1×4 antenna array with/without the lower metal superstrate and metal wall. It is obvious that the reflection coefficients have been improved with the decoupling structure since they were deteriorating owing to the coupling, especially the higher frequency band. The co-polarized coupling achieves lower than -15 dB, and cross-polarized

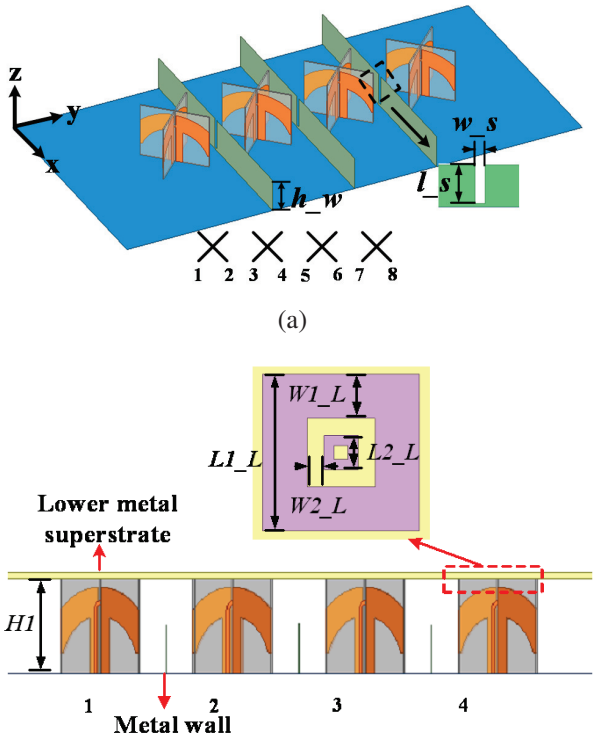

Fig. 3. The 1×4 dual-polarized antenna array: (a) with the separation metal wall and (b) with the separation metal wall and lower metal superstrate (*w_s*=2 mm, *l_s*=11 mm, *h_w*=12 mm, *W1_L*=6.5 mm, *W2_L*=1.5 mm, *L1_L*=23 mm, *L2_L*=5 mm, *H1*=23 mm).

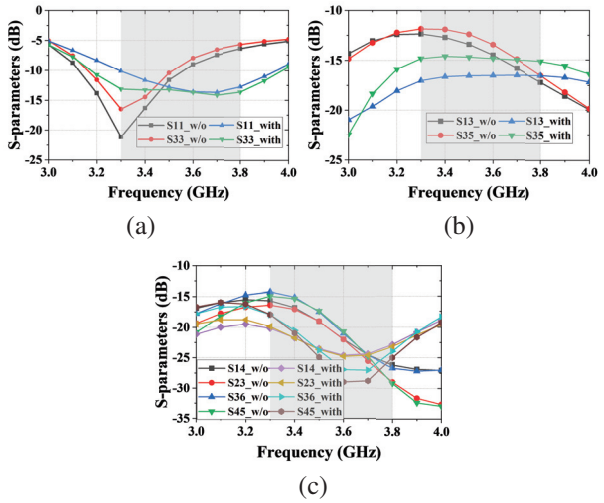

Fig. 4. S-parameters of the 1×4 antenna array with/without the separation metal wall and the lower metal superstrate: (a) reflection coefficients, (b) co-polarized coupling, and (c) cross-polarized coupling.

couplings are improved to -20 dB, almost the entire frequency band with the two decoupling structures.

(2) Upper metal superstrate for co-polarized decoupling

The addition of lower metal superstrate and separation metal wall can reduce the cross-polarized coupling to -20 dB and the co-polarized coupling to -15 dB, which cannot meet the requirements of high isolation. Therefore, the upper superstrate is employed above the array to further improve the co-polarized isolation. The distance between the ground plane and upper metal superstrate is *H2*=36.5 mm. Figure 5 shows the structure and the operating principle of the upper metal superstrate. The electromagnetic wave emitted by Antenna 1 can be reflected by the upper metal superstrate and an additional superstrate and an additional wave path is produced. When the reflected and coupling waves have the same amplitude but opposite phases, they cancel each other, reducing the mutual couplings. Figure 6 shows the simulated S-parameters of the 1×4 antenna array with/without the upper metal superstrate. It can be seen that the co-polarized coupling has been suppressed to -20 dB. Moreover, the reflection coefficients and cross-polarized coupling get better results with the upper metal superstrate. It can be observed from Fig. 7 that when an element is excited, the electric field coupled to its neighboring antenna is significantly weakened after loading the decoupling structure.

(3) Decoupling parametric study

In order to illustrate how the lower and upper metal superstrates affect the mutual coupling depression, a simulated parametric study is performed. Figure 8 (a) shows that when the parameter of the patch length

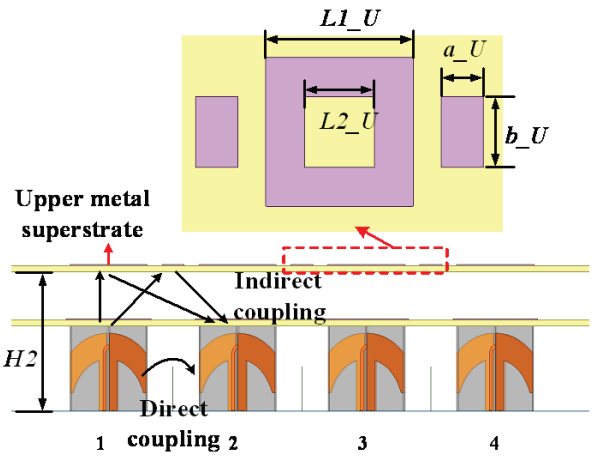

Fig. 5. The 1×4 antenna array with upper metal superstrate (*L1_U*=21 mm, *L2_U*=10 mm, *a_U*=6 mm, *b_U*=10 mm).

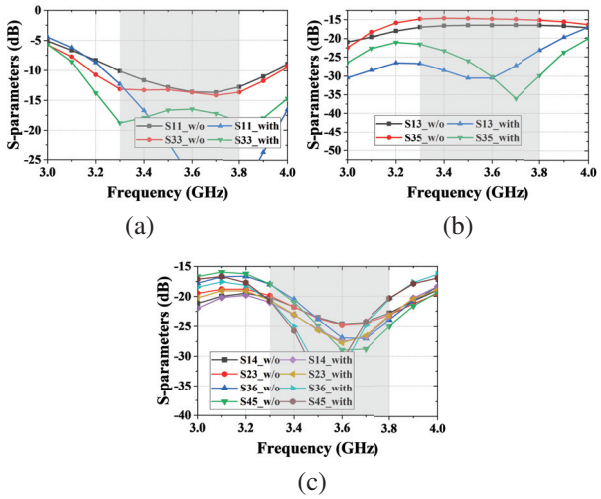

Fig. 6. S-parameters of the 1×4 antenna array with/without the upper metal superstrate: (a) reflection coefficients, (b) co-polarized coupling, and (c) cross-polarized coupling.

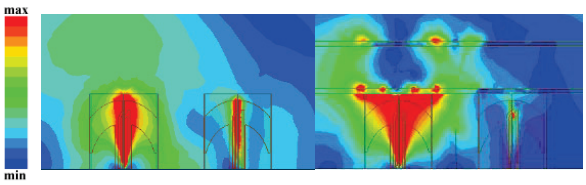

Fig. 7. Electric field distribution of the two-element array (a) without and (b) with loading decoupling structure at 3.5 GHz.

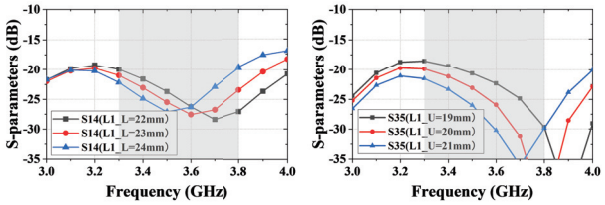

Fig. 8. S-parameters of the 1×4 antenna array with and without the upper metal superstrate: (a) patch size analysis on the lower metal superstrate and (b) patch size analysis on the upper metal superstrate.

L1_L on the lower metal superstrate increases, the cross-polarization decoupling frequency point shifts to higher frequency. Figure 8 (b) shows how the parameter of the patch length *L1_U* on the upper metal superstrate influences the co-polarized decoupling. When *L1_U* increases, the co-polarized decoupling frequency point shifts to the lower frequencies. That is to say, the decoupling frequency can be controlled simply by changing the size of periodic patch cells on the superstrate.

III. ARRAY DESIGN AND RESULTS

To obtain the wide-angle scanning performance for the large-scale array, generally, the following three aspects should be considered: (a) the coupling among array elements which would lead to the scanning blindness, (b) the wide beamwidth of the array element to ensure the lower gain reduction at the large scanning angle, and (c) the small spacing to minimize the grating lobes. In this paper, the coupling has been reduced to -20 dB and the element is compact to guarantee the small spacing.

To verify the above analysis, a 4×6 array is designed. The array configuration can be seen in Fig. 9

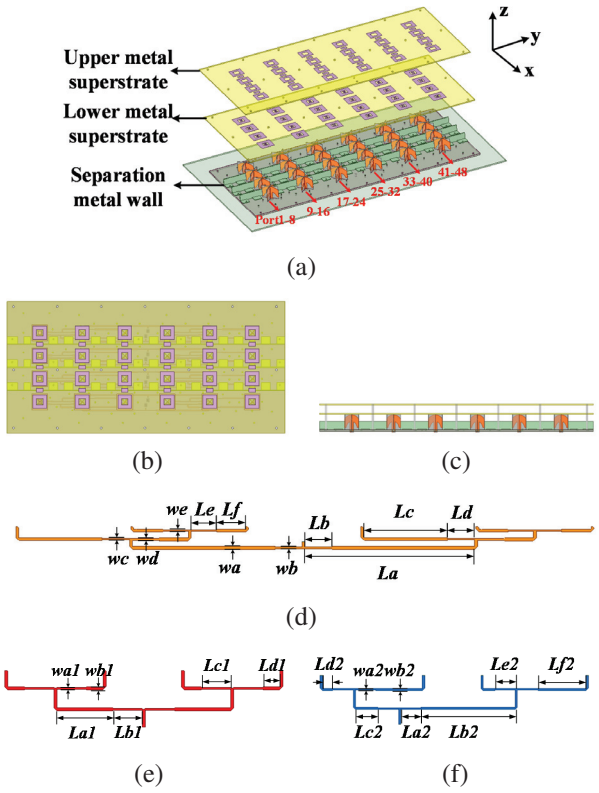

Fig. 9. Proposed 4×6 antenna array: (a) three-dimensional view of the model, (b) top view, (c) side view, (d) feeding network of the 4×6 array, (e) feeding network for broadside radiation, and (f) feeding network for 55° radiation (*La* = 95.96 mm, *Lb* = 15.38 mm, *Lc* = 47.3mm, *Ld* = 15.48 mm, *Le* = 14.43 mm, *Lf* = 16.6 mm, *Lb1* = *Lc1* = *La2* = *Le2* = 15.12 mm, *La1* = 28.54 mm, *Ld1* = 8.54 mm, *Lb2* = 68.64 mm, *Lc2* = 16.44 mm, *Lf2* = 33.94 mm, *Ld2* = 8.44 mm, *wa* = 1.545 mm, *wb* = *we* = 0.888 mm, *wc* = 0.61mm, *wd* = 1.13 mm, *wa1* = 0.87 mm, *wb1* = 1.56 mm, *wa2* = 0.89 mm, *wb2* = 1.56 mm).

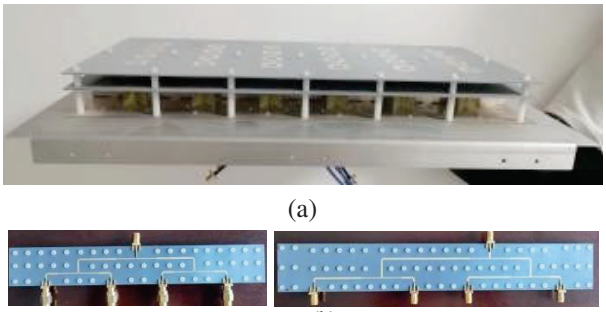

(a) (b)

Fig. 10. Photograph of (a) fabricated 4×6 antenna array and (b) fabricated power divider.

(a), the element distance in y-axis is 65 mm (0.77 λ_0, where λ_0 is the free space wavelength at 3.55 GHz). Note that power dividers used to feed the subarrays are omitted in the figure for clearer illustration. Figure 9 (a-c) illustrates the simulated model of the 4×6 antenna array and the 1 to 6 power divider model are shown in Fig. 9 (d). Figures 9 (e-f) are the 1 to 4 power dividers to feed the four subarrays in order to realize the broadside and wide-angle scanning. Figures 10 (a-b) illustrate the fabricated 4×6 antenna array model and power divider model.

The simulated and measured S-parameters are shown in Fig. 11. It is seen that the measured reflection coefficients correspond well to the simulated ones. Both the co-polarized and cross-polarized mutual coupling are reduced to below -20 dB. Figure 12 shows the simulated active reflection coefficients of the subarrays in the array

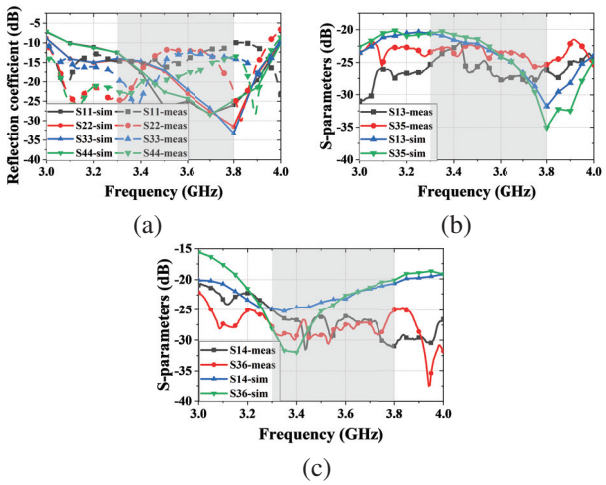

(a) (b) (c)

Fig. 11. Measured and simulated S-parameters of the 4×6 dual-polarized antenna array with the decoupling method: (a) reflection coefficient, (b) S13 and S35, and (c) S14 and S36.

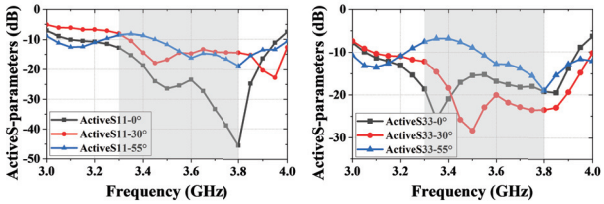

(a) (b)

Fig. 12. Simulated active reflection coefficients of the subarrays in the array and at different scanning angles: (a) port 1 and (b) port 3.

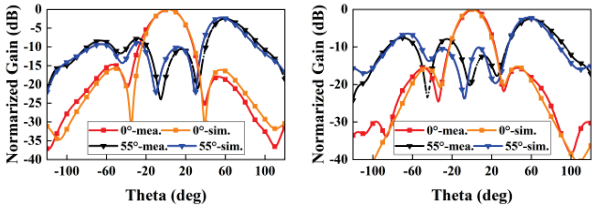

(a) (b)

Fig. 13. Simulated and measured scanning performance of the proposed array: (a) 3.3 GHz and (b) 3.8 GHz.

and at different scanning angles. It can be observed that even at wide scanning angle, the active reflection coefficients are less than -10 dB, which would guarantee the realization of wide-angle scanning. The radiation patterns and the scanning performance of the antenna array at 3.3 GHz / 3.55 GHz / 3.8 GHz are also presented in Fig. 13. It can be concluded that the main beam is able to scan up to -55° and the scan losses are lower than 2.5 dB at 3.3 GHz and 3.8 GHz. The measured and simulated realized gain are also given in Fig. 14. The measured gain is up to 19.4 dBi, which is about around 1 dB lower than the simulated gain. It may be mainly caused by fabrication and measurement errors.

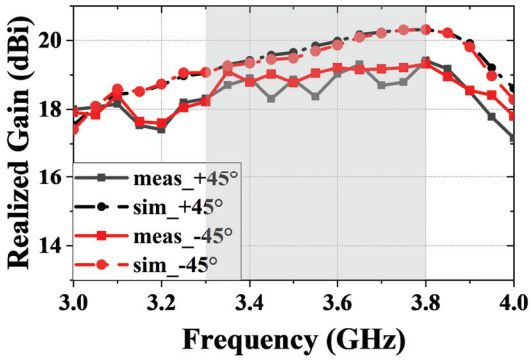

Fig. 14. Measured and simulated realized gain of the 4×6 dual-polarized antenna array.

Table 1: Comparison of the related arrays

Ref.	BW (GHz) (%)	Polarization	AS	MSA	GF	ID
[6]	4.4-5 (10.5%)	±45° dual linear	4×4	60°	3.0 dB	>20 dB
[7]	5.2-5.3 (2.1%)	dual linear	6×6	66°	3.5 dB	>16 dB
[17]	1.7-2.22 (5.6%)	±45° dual linear	4×4	-	-	>20 dB
[19]	3.3-3.8 (14.1%)	±45° dual linear	1×4	55°	>3.0 dB	>13 dB
This work	3.3-3.8 (14.1%)	±45° dual linear	4×6	55°	3.0 dB	>20 dB

BW = Bandwidth, AS = Array scale, MSA = Maximum scanning angle, GF = Gain fluctuation, ID = Inter-port decoupling

In Table 1, the comparison between our work and other antenna arrays is presented. The proposed antenna array has a broader operating bandwidth than the designs in [6–7] and [17] owing to the wideband characteristic of the proposed antenna and the decoupling structure. Meanwhile, the proposed antenna in this paper exhibits higher isolation than [19].

IV. CONCLUSION

A wide-angle beam-scanning with high isolation base station antenna array has been proposed in this paper, benefiting from the compact element and effective hybrid decoupling methods. The measured 4×6 antenna array achieved a good beam-scanning capability with maximum scanning angle up to ±55° and a small gain variation of less than 3 dB over the whole band. Plus, the measured isolation between all ports of the array is increased to more than 20 dB. With the merits of wideband, low-cost (simple design and easy fabrication), wide-angle beam-scanning capacity, and good radiation performance, the proposed design has potential for application in large-scale 5G base station systems.

REFERENCES

[1] Y. Feng, J.-Y. Li, L.-K. Zhang, X.-J. Yu, Y.-X. Qi, D. Li, and S.-G. Zhou, "A broadband wide-angle scanning linear array antenna with suppressed mutual coupling for 5G Sub-6G applications," *IEEE Antennas and Wireless Propagation Letters*, vol. 21, no. 2, pp. 366-370, Feb. 2022.

[2] S. Kim and S. Nam, "A compact and wideband linear array antenna with low mutual coupling," *IEEE Transactions on Antennas and Propagation*, vol. 67, no. 8, pp. 5695-5699, Aug. 2019.

[3] Z. Wang, Y. Dong, Z. Peng, and W. Hong, "Hybrid metasurface, dielectric resonator, low-cost, wide-angle beam-scanning antenna for 5G base station application," *IEEE Transactions on Antennas and Propagation,* vol. 70, no. 9, pp. 7646-7658, Sep. 2022.

[4] E. Adas, F. De Flaviis, and N. G. Alexopoulos, "Realization of scan blindness free finite microstrip phased arrays based on mode-free radiating electromagnetic bandgap materials," *IEEE Transactions on Antennas and Propagation*, vol. 66, no. 7, pp. 3375-3382, July 2018.

[5] G. Yang, Y. Zhang, and S. Zhang, "Wide-band and wide-angle scanning phased array antenna for mobile communication system," *IEEE Open Journal of Antennas and Propagation*, vol. 2, pp. 203-212, 2021.

[6] G. Yang and S. Zhang, "Dual polarized wide-angle scanning phased array antenna for 5G communication system," *IEEE Transactions on Antennas and Propagation,* vol. 70, no. 9, pp. 7427-7438, Sep. 2022.

[7] Y.-Q. Wen, S. Gao, B.-Z. Wang, and Q. Luo, "Dual-polarized and wide-angle scanning microstrip phased array," *IEEE Transactions on Antennas and Propagation*, vol. 66, no. 7, pp. 3775-3780, July 2018.

[8] G.-F. Gao, X. Ding, Y.-F. Cheng, and W. Shao, "Dual-polarized wide-angle scanning phased array based on multimode patch elements," *IEEE Antennas and Wireless Propagation Letters*, vol. 18, no. 3, pp. 546-550, Mar. 2019.

[9] K. Wei, J. Li, L. Wang, Z. Xing, and R. Xu, "Mutual coupling reduction by novel fractal defected ground structure bandgap filter," *IEEE Transactions on Antennas and Propagation*, vol. 64, no. 10, pp. 4328-4335, Oct. 2016.

[10] F. Yang and Y. Rahmat-Samii, "Microstrip antennas integrated with electromagnetic band-gap (EBG) structures: A low mutual coupling design for array applications," *IEEE Transactions on Antennas and Propagation*, vol. 51, no. 10, pp. 2936-2946, Oct. 2003.

[11] Y. Wang and Z. Du, "A wideband printed dual-antenna with three neutralization lines for mobile terminals," *IEEE Transactions on Antennas and Propagation*, vol. 62, no. 3, pp. 1495-1500, Mar. 2014.

[12] F. Merzaki, P. Besnier, M. Himdi, X. Castel, M. Sergolle, T. Levavasseur, and P. Caldamone, "A compact double-sided FSS absorbing wall for decoupling 5G antenna arrays," *IEEE Transactions on Electromagnetic Compatibility*, vol. 64, no. 2, pp. 303-314, Apr. 2022.

[13] C. Wei, K. Wu, X. Mei, and Z. Zhang, "Array-antenna decoupling surface," *IEEE Transactions on*

Antennas and Propagation, vol. 65, no. 12, pp. 6728-6738, Dec. 2017.

[14] J. Tang, F. Faraz, X. Chen, Q. Zhang, Q. Li, Y. Li, and S. Zhang, "A metasurface superstrate for mutual coupling reduction of large antenna arrays," *IEEE Access*, vol. 8, pp. 126859-126867, 2020.

[15] M. Li, X. Chen, A. Zhang, W. Fan, and A. A. Kishk, "Split-ring resonator loaded baffles for decoupling of dual-polarized base station array," *IEEE Antennas Wireless Propagation Letters*, vol. 19, no. 10, pp. 1828-1832, Oct. 2020.

[16] P. Mei, Y. M. Zhang, and S. Zhang, "Decoupling of a wideband dual-polarized large-scale antenna array with dielectric stubs," *IEEE Transactions on Vehicular Technology*, vol. 70, no. 8, pp. 7363-7374, Aug. 2021.

[17] B. Liu, Y. Da, X. Chen, and A. A. Kishk, "Hybrid decoupling structure based on neutralization and partition schemes for compact large-scale base station arrays," *IEEE Antennas Wireless Propagation. Letters*, vol. 21, no. 2, pp. 267-271, Feb. 2022.

[18] J. Li, H. Zhai, L. Zhao, T. Chen, Y. Wang, S. Yang, and W. Xu, "High-capacity compact massive MIMO array with hybrid decoupling scheme," *IEEE Transactions on Antennas and Propagation*, vol. 70, no. 10, pp. 9292-9304, Oct. 2022.

[19] Z. Wang and Y. Dong, "Broadband dual-polarized phased array with dynamic scanning control for intelligent mobile communication application," *IEEE Transactions on Vehicular Technology*, vol. 72, no. 10, pp. 12480-12490, Oct. 2023.

Fang-Fang Fan received a Ph.D. degree in Electromagnetic Field and Microwave Technology from Xidian University in 2011. Currently, she is an associate professor at Xidian University. Her current research interests include antenna arrays, gap waveguide technology and base station antennas for 5G application.

Pei-Pei Ma received her bachelor's degree from Hainan University in July 2019 and she is currently pursuing the master's degree at Xidian University from September 2021. Her research interests mainly concentrate on base station antennas and filters.

Qing-Lin Chen received his bachelor's degree in electronic information engineering from Xidian University, China, in July 2020. From September 2020, he studies for the master's degree in electronic and communication engineering at Xidian University, China. His current interests are to research and design millimeter wave antenna array for 5G application.

Analysis of EM Properties of High-speed Moving Cone-sphere Target Coated with Plasma Sheath based on Lorentz-FDTD Method

Xian-Min Guo[1], Hai-Yan Li[1], Yong Bo[1,2*], Wei Chen[1], Li-Xia Yang[1], Zhi-Xiang Huang[1], and An-Qi Wang[1]

[1]Information Materials and Intelligent Sensing Laboratory of Anhui Province
Anhui University, Hefei, 230601, China

[2]East China Research Institute of Electronic Engineering
Hefei, 230600, China
*Corresponding author: boyong@ahu.edu.cn

***Abstract* –** The study of the interaction between moving plasma-coated objects and electromagnetic (EM) waves is the essential factor for the EM problems of high-speed targets. In this paper, the physical model of a moving dispersive medium is developed based on the principle of special relativity to study the EM properties of high-speed moving targets coated with plasma sheath. First, the Lorentz transform is used to introduce the incident plane wave into moving frame. Second, based on the proposed EM model, the EM problems are solved in moving frame by the shift-operator (SO) FDTD numerical algorithm. Finally, the EM results are further converted back into the laboratory frame to analyze the scattered properties of high-speed plasma coated objects. The validity of the proposed algorithm is verified by comparison with the reference solution. On this basis, the influence of relativistic effects produced by the motion of the object and the EM properties of the plasma on the scattering fields of high-speed targets are investigated. This work expands the applicability of the FDTD method and provides a theoretical foundation for solving the scattering properties of high-speed plasma-coated complex shape objects through numerical methods.

***Index Terms* –** Electromagnetic (EM) scattering, finite difference time domain (FDTD), moving plasma, relativistic effects.

I. INTRODUCTION

When a high-speed vehicle performs a highly maneuverable cruise mission in the near space, it will generate violent friction with the surrounding atmosphere, which will promote the ionization of the air around the vehicle, resulting in the formation of plasma sheath wrapping around the vehicle [1, 2]. On the one hand, the plasma sheath will seriously interfere with the wireless communication between the target and the detection radar, and will bring irreversible effects on the electromagnetic (EM) transmission, scattering, and imaging characteristics of high-speed moving targets [3–5]. On the other hand, the relativistic effect due to the high-speed motion of the radar target will modulate the EM wave as well. Therefore, the influence of relativistic effects must be considered in the study of EM scattering properties of high-speed moving targets coated with plasma sheaths.

In real application environments, the acquisition of the realistic flow field environment excited around a high-speed target would be time-consuming and expensive [6], which aggravates the difficulty of the research and analysis of the EM problems about high-speed moving targets coated with plasma sheaths. Numerous EM numerical simulation approaches play a crucial role in real-world applications as computer technology advances. The finite-difference time-domain (FDTD) approach can be used to solve EM problems in a wide range of complicated situations with high accuracy and efficiency, and it can also be effectively integrated with other methods [7–9]. Zheng et al. proposed to introduce the Lorentz transformation into the FDTD method for calculating the EM scattering characteristics of a high-speed moving conductor plate [10]. The EM transmission characteristics of a high-speed moving multilayer dielectric plate are further investigated by using the Lorentz-FDTD method [11]. To analyze the transmission characteristics of EM waves obliquely incident into a high-speed moving left-handed metamaterial, the authors establish a connection between the Lorentz transformation with the ADE-FDTD method [12]. The total energy scattering, extinction, and absorption cross section of incident EM waves by a high-speed moving target are analyzed based on the relativistic principles [13–14]. By transforming LFM waves into the moving frame, the 1D range profile of a high-

Submitted On: June 29, 2023
Accepted On: October 22, 2023

https://doi.org/10.13052/2024.ACES.J.390209

speed moving target is researched in [15] based on the Lorentz-FDTD method. The interaction between EM waves and spatiotemporally non-uniform moving plasma plates is revealed in [16]. In [17], absorption characteristics of EM waves by a non-uniform plasma moving at high velocities were investigated by using the Wentzel-Kramers-Brillouin method.

In summary, various numerical methods have been developed and applied to study the EM scattering characteristics of high-speed targets [7–12, 15] and the effect of moving plasma plates on the EM transmission characteristics [16–19]. However, there remains a dearth of studies on the EM properties of high-speed moving complex-shaped targets coated with plasma sheath based on the relativity effect. In this paper, we investigate the influence of relativistic effects and EM parameters of plasma sheath on the scattering characteristics of high-speed targets by using the Lorentz-FDTD method.

In Section II, the EM scattering model of the moving dispersive medium is established, and the procedure for the calculation of the moving dispersive medium by the Lorentz-FDTD method is derived. In Section III, the validity and accuracy of the proposed algorithm is verified. In Section IV, the EM scattering problem from a uniformly moving conical-spherical metal object and that object coated with a plasma has been investigated and analyzed. The conclusion of this research is presented in Section V.

II. RESEARCH METHOD

The fundamental principle of the calculation of a high-speed moving dispersive medium target by the Lorentz-FDTD method can be divided into two steps. First, the dynamic EM scattering problem in the radar frame (denote by K frame) is converted to the motion frame (denote by K' frame), which remains relatively stationary with the moving target according to the principle of relativity. Second, the EM problem is solved by the conventional FDTD method in the K'frame, and then the EM solution is further transformed into the K frame according to the inverse Lorentz transformation. The relationship between the two frames is shown in Fig. 1. Before the solution of the dynamic EM problem for high-speed targets by the conventional FDTD method, the incident plane EM waves and the spatial-temporal separation intervals in both frames need to be converted according to the relativistic principle. The algorithm flow of the Lorentz-FDTD method for calculating the motion dispersion medium is shown in Fig. 2.

A. Physical model of moving plasma

When EM waves propagate in a moving isotropic medium, their frequency will be shifted due to the Doppler effect. Assuming that the angle between the EM wave propagation vector $\vec{k}$ and the object velocity $\vec{v}$ is θ,

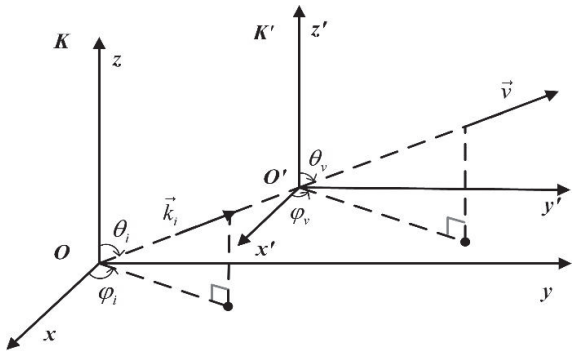

Fig. 1. Sketch of the two coordinate systems.

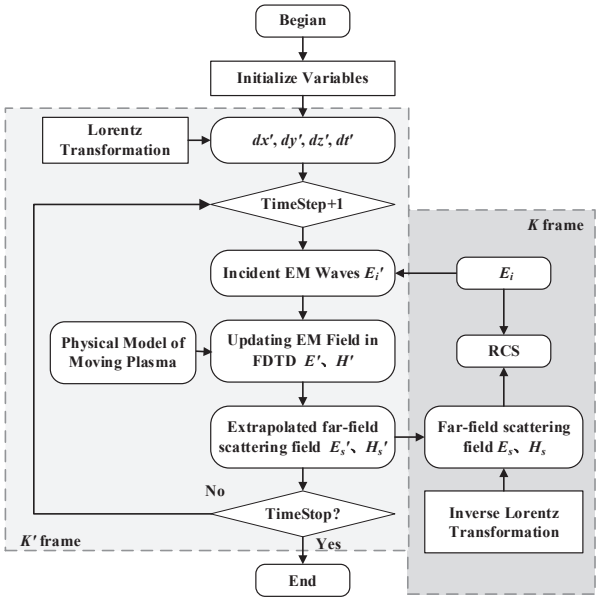

Fig. 2. Flowchart of Lorentz-FDTD algorithm for the calculation of motion dispersion media.

the EM wave frequency ω' after the Doppler shift can be calculated as [16]

$$\omega' = \gamma\omega(1-\beta\cos\theta), \tag{1}$$

where $\gamma = 1/\sqrt{1-\beta^2}, \beta = v/c$. c is the velocity of light in free space.

The dielectric coefficient ε_r of a magnetized cold plasma is generally described using Appleton's formula.

$$\varepsilon_r(\omega) = 1 - \frac{\omega_p^2}{\omega^2+\omega_c^2} - j\frac{\omega_c}{\omega}\frac{\omega_p^2}{\omega^2+\omega_c^2}, \tag{2}$$

where ω_p is the plasma cut-off frequency and ω_c is the plasma collision frequency. ω is the operating frequency of EM waves.

The EM wave frequency ω' in the K' frame will be red-shifted when the object moves away from the detection radar radiation. Conversely, the ω' will be blue-shifted when the object is moves toward the direction of

EM wave propagation. Therefore, the dielectric coefficient ε_r of plasma in the K' frame can be further written as

$$\varepsilon_r'(\omega') = 1 - \frac{\omega_p^2}{\omega'^2 + \omega_c^2} - j\frac{\omega_c}{\omega'}\frac{\omega_p^2}{\omega'^2 + \omega_c^2}. \quad (3)$$

The EM field update equation for a moving plasma based on the shift-operator (SO-FDTD) method [20–22] is derived as follows. First, as the dielectric coefficient of the plasma will change with the EM wave frequency, the electric field frequency domain intrinsic relationship of the moving plasma can be expressed as

$$\boldsymbol{D}'(\omega') = \varepsilon_0 \varepsilon_r'(\omega')\boldsymbol{E}'(\omega'), \quad (4)$$

where the rational fraction of ε_r in the SO-FDTD method is expressed in the form

$$\varepsilon_r'(\omega') = \frac{\sum_{n=0}^{N} p_n (j\omega')^n}{\sum_{m=0}^{M} q_m (j\omega')^m}, \quad (5)$$

where p_n and q_n denote the numerator and denominator coefficients of the relative permittivity, respectively.

To simplify the equation, we define the velocity factor $C=\gamma(1-\beta\cos\theta)$, then establish the equation $j\omega'=C\,j\omega$. The time domain forms of the electric field and relative dielectric coefficients of plasma can be transitioned by the conversion operator $j\omega = \partial/\partial t$ between the time and frequency domains. Therefore, the time-domain form of (5) can be deduced further as

$$\varepsilon_r'\left(\frac{\partial}{\partial t'}\right) = \frac{\sum_{n=0}^{N} p_n C^n (\frac{\partial}{\partial t})^n}{\sum_{m=0}^{M} q_m C^m (\frac{\partial}{\partial t})^m}. \quad (6)$$

The time-domain intrinsic form of the electric field can be acquired by bringing (6) into the electric field intrinsic structure relation (4).

$$\left[\sum_{m=0}^{M} q_m C^m \left(\frac{\partial}{\partial t}\right)^m\right]\boldsymbol{D}'(t') = \varepsilon_0\left[\sum_{n=0}^{N} p_n C^n \left(\frac{\partial}{\partial t}\right)^n\right]\boldsymbol{E}'(t'). \quad (7)$$

By discretizing the time derivative in (7) with the central difference $\left(\frac{\partial}{\partial t}\right)^l \to \left(\frac{2}{\Delta t}\cdot\frac{z_t-1}{z_t+1}\right)^l$, where z_t denotes the discrete time-domain shift operator and l represents the order of time derivative [21]. The electric field update equation in the SO-FDTD method is given by

$$\begin{aligned}&\left\{\left[q_0' + q_1'\frac{2}{\Delta t} + q_2'\left(\frac{2}{\Delta t}\right)^2\right]z_t^2 + \left[2q_0' - 2q_2'\left(\frac{2}{\Delta t}\right)^2\right]z_t + \right.\\ &\left.\left[q_0' - q_1'\frac{2}{\Delta t} + q_2'\cdot\left(\frac{2}{\Delta t}\right)^2\right]\right\}\boldsymbol{D}_x'^n =\\ &\left\{\left[p_0' + p_1'\frac{2}{\Delta t} + p_2'\left(\frac{2}{\Delta t}\right)^2\right]z_t^2 + \left[2p_0' - 2p_2'\left(\frac{2}{\Delta t}\right)^2\right]z_t + \right.\\ &\left.\left[p_0' - p_1'\frac{2}{\Delta t} + p_2'\left(\frac{2}{\Delta t}\right)^2\right]\right\}\varepsilon_0\boldsymbol{E}_x'^n. \end{aligned} \quad (8)$$

The differential form of the electric field update equation for a moving dispersive medium is as follows:

$$\begin{aligned}\boldsymbol{E}'^{n+1} = \frac{1}{b_0}\left\{\frac{1}{\varepsilon_0}\left(a_0\boldsymbol{D}'^{n+1} + a_1\boldsymbol{D}'^{n} + a_2\boldsymbol{D}'^{n-1}\right)\right.\\ \left. - b_1\boldsymbol{E}'^{n} - b_2\boldsymbol{E}'^{n-1}\right\},\end{aligned} \quad (9)$$

where the coefficients $a_0, a_1, a_2, b_0, b_1, b_2$ are as follows:

$$\begin{cases} a_0 = q_0' + q_1'\left(\frac{2}{\Delta t}\right) + q_2'\left(\frac{2}{\Delta t}\right)^2, & b_0 = p_0' + p_1'\left(\frac{2}{\Delta t}\right) + p_2'\left(\frac{2}{\Delta t}\right)^2 \\ a_1 = 2q_0' - 2q_2'\left(\frac{2}{\Delta t}\right)^2, & b_1 = 2p_0' - 2p_2'\left(\frac{2}{\Delta t}\right)^2 \\ a_2 = q_0' - q_1'\left(\frac{2}{\Delta t}\right) + q_2'\left(\frac{2}{\Delta t}\right)^2, & b_2 = p_0' - p_1'\left(\frac{2}{\Delta t}\right) + p_2'\left(\frac{2}{\Delta t}\right)^2 \end{cases}, \quad (10)$$

where $q_n' = C^n q_n$, $p_n' = C^n p_n$ $(n = 0,1,2)$, and the coefficients q_n and p_n are determined by the EM parameters of plasma.

B. Lorentz transformation of space-time increments

When the Lorentz transformation is introduced into the FDTD method according to the principle of special relativity, the relationship between the space-time increments of two inertial systems satisfy the Lorentz transformation equation. Suppose that the K' frame is moving with constant velocity $\vec{v}$ relative to the K frame, and the origin of the two frames coincide at the instantaneous moment $t = t' = 0$. The space-time increment between the two inertial frames is given by (11).

$$\begin{pmatrix}\Delta x\\ \Delta y\\ \Delta z\end{pmatrix} = \begin{pmatrix} 1+(\gamma-1)\frac{v_x^2}{v^2} & (\gamma-1)\frac{v_x v_y}{v^2} & (\gamma-1)\frac{v_x v_z}{v^2} \\ (\gamma-1)\frac{v_x v_y}{v^2} & 1+(\gamma-1)\frac{v_y^2}{v^2} & (\gamma-1)\frac{v_y v_z}{v^2} \\ (\gamma-1)\frac{v_x v_z}{v^2} & (\gamma-1)\frac{v_y v_z}{v^2} & 1+(\gamma-1)\frac{v_z^2}{v^2} \end{pmatrix} \cdot \begin{pmatrix}\Delta x'\\ \Delta y'\\ \Delta z'\end{pmatrix}, \quad (11\text{-a})$$

$$\Delta t = \frac{1}{\sqrt{1-\beta^2}}(1 - \beta\hat{a}_s\cdot\hat{a}_v)\Delta t', \quad (11\text{-b})$$

where $v_x = |\vec{v}|\sin\theta_v\cos\varphi_v, v_y = |\vec{v}|\sin\theta_v\sin\varphi_v$, $v_z = |\vec{v}|\cos\theta_v$. θ_v is the elevation angle of $\vec{v}$ with $+z$ axis, φ_v is the angle between the projection of $\vec{v}$ on xOy and $+x$ axis. The symbol $\hat{a}_s$ and $\hat{a}_v$ denotes the unit vectors of the scattered field and velocity, respectively.

C. Incident EM field transformation

In order to solve the dynamic EM problem for high-speed targets by the FDTD method, the incident plane EM wave in the K frame need to be converted to the K' frame. Assume that the unit vector of incident EM wave propagating along arbitrary direction in the K frame is defined as $\overrightarrow{k}_i$. According to the phase-invariant principle of EM waves [23], the wave vector $\overrightarrow{k}_i'$, angular frequency ω_i' and amplitude $\overrightarrow{E}_i'$ transformation equations of

the incident plane EM wave in the K' frame are given by (12)-(14).

$$\vec{\mathrm{k}}_i^{'} = \gamma\vec{\mathrm{k}}_i\left(1-\beta\frac{\vec{\mathrm{k}}_i\cdot\vec{\mathrm{v}}}{|\vec{\mathrm{v}}|}\right), \tag{12}$$

$$\omega_i^{'} = \gamma\omega_i\left(1-\beta\frac{\vec{\mathrm{k}}_i\cdot\vec{\mathrm{v}}}{|\vec{\mathrm{v}}|}\right), \tag{13}$$

$$|\vec{E}_i^{'}| = \sqrt{(\vec{E}_0\cos\theta)^2+\gamma^2(\vec{E}_0\sin\theta+|\vec{v}\times\vec{B}|)^2}, \tag{14}$$

where the ω_i, $\vec{E}_0$are the angle frequency and amplitude of the incident EM waves in the K frame.

D. Near- to far-field extrapolation

In the frame K', the near-field scattered field of the moving target can be obtained by using the time domain EM field iteration of conventional FDTD. The far-field scattered EM field can be obtained by extrapolation from the near-field data. First, a closed virtual boundary is set as the extrapolation boundary in the FDTD scattering field region according to the equivalence principle. Second, the tangential current and tangential magnetic current on the virtual boundary are calculated, and the equivalent EM current on this surface is extrapolated according to the Huygens's principle. In addition, the 10-level uniaxial anisotropy perfectly matched (UPML) layer as absorbing boundary is used to terminate the outward propagating EM field in space. The 3D far-field equation in the frame K' can be expressed as

$$\begin{aligned} e_\theta^{s'}(t') = {} & u_x'\sin\varphi_s' - u_y'\cos\varphi_s' - \eta\left(w_x'\cos\theta_s'\cos\varphi_s'\right. \\ & \left.+w_y'\cos\theta_s'\sin\varphi_s' - w_z'\sin\theta_s'\right) \end{aligned}, \tag{15-a}$$

$$\begin{aligned} e_\varphi^{s'}(t') = {} & u_x'\cos\theta_s'\cos\varphi_s' + u_y'\cos\theta_s'\cos\varphi_s' - u_z'\sin\theta_s' \\ & +\eta\left(w_x'\sin\varphi_s' - w_y'\cos\varphi_s'\right) \end{aligned}, \tag{15-b}$$

where η is the wave impedance in free space. $\boldsymbol{w}'(t)$ and $\boldsymbol{u}'(t)$ can be obtained by performing the inverse Fourier transform on (16).

$$\begin{aligned} \overrightarrow{\boldsymbol{W}}' &= jk\rightarrow\mathbf{A}' \\ &= jk\frac{\exp(-jk'r')}{4\pi r'}\int_A\left(\hat{n}\times\rightarrow\mathbf{H}_s'\right)\exp\left(jk'\boldsymbol{r}'\cdot\hat{\boldsymbol{e}}_{r'}'\right)ds' \end{aligned}, \tag{16-a}$$

$$\begin{aligned} \overrightarrow{\boldsymbol{U}}' &= jk\overrightarrow{\boldsymbol{F}}' \\ &= jk\frac{\exp(-jk'r')}{4\pi r'}\int_A-\left(\hat{n}\times\overrightarrow{\boldsymbol{E}}_s'\right)\exp\left(jk'\boldsymbol{r}'\cdot\hat{\boldsymbol{e}}_{r'}'\right)ds' \end{aligned}, \tag{16-b}$$

E. Inverse Lorentz transformation of EM field

As the Maxwell system of equations satisfies the covariance principle, its rotational equations remain in the same form in all inertial systems. Therefore, Maxwell's rotational equations in K' can be expressed as

$$\frac{\partial\vec{\boldsymbol{D}}^{'}}{\partial t'} = \nabla\times\vec{\boldsymbol{H}}^{'}, \tag{17}$$

$$\frac{\partial\vec{\boldsymbol{H}}^{'}}{\partial t'} = -\frac{1}{\mu_0}\nabla\times\vec{\boldsymbol{E}}^{'}. \tag{18}$$

In the previous section, the far-field scattered fields $\overrightarrow{\boldsymbol{E}}_{s\theta}'$ and $\overrightarrow{\boldsymbol{E}}_{s\varphi}'$ of the high-speed target were obtained by near to far-field extrapolation. The electric and magnetic field components will change in the two inertial systems due to the relative motion between the K frame and the K' frame. The relationship between the EM fields in the two frames follows the Lorentz transformation equation. The inverse Lorentz transformation equation for the far-field scattered EM field between two frames is given by (20)-(21).

$$\vec{\boldsymbol{E}} = \gamma(\vec{\boldsymbol{E}}^{'}-\vec{v}\times\vec{\boldsymbol{B}}^{'})+(1-\gamma)\frac{\vec{\boldsymbol{E}}^{'}\cdot\vec{v}}{v^2}\vec{v}, \tag{19}$$

$$\vec{\boldsymbol{B}} = \gamma(\vec{\boldsymbol{B}}^{'}-\frac{1}{c^2}\vec{v}\times\vec{\boldsymbol{E}}^{'})+(1-\gamma)\frac{\vec{\boldsymbol{B}}^{'}\cdot\vec{v}}{v^2}\vec{v}, \tag{20}$$

where spatial electric field $\overrightarrow{\boldsymbol{E}}'$ and magnetic field $\overrightarrow{\boldsymbol{B}}'$ are represented in FDTD with Cartesian coordinates. Therefore, the far-field $\overrightarrow{\boldsymbol{E}}_{sx}'$, $\overrightarrow{\boldsymbol{E}}_{sy}'$, $\overrightarrow{\boldsymbol{E}}_{sz}'$ can be obtained by performing a coordinate transformation on $\overrightarrow{\boldsymbol{E}}_{s\theta}'$ and $\overrightarrow{\boldsymbol{E}}_{s\varphi}'$. In the SO-FDTD method, the far-field scattered field in the K frame is derived as follows. The Lorentz transformation equation of the spatial electric field in FDTD is given below.

$$\begin{aligned} \begin{pmatrix}\overrightarrow{\boldsymbol{E}}_x\\ \overrightarrow{\boldsymbol{E}}_y\\ \overrightarrow{\boldsymbol{E}}_z\end{pmatrix} &= \gamma\begin{pmatrix}\overrightarrow{\boldsymbol{E}}_x'\\ \overrightarrow{\boldsymbol{E}}_y'\\ \overrightarrow{\boldsymbol{E}}_z'\end{pmatrix}-\gamma\begin{pmatrix}\hat{x} & \hat{y} & \hat{z}\\ v_x & v_y & v_z\\ \overrightarrow{\boldsymbol{B}}_x' & \overrightarrow{\boldsymbol{B}}_y' & \overrightarrow{\boldsymbol{B}}_z'\end{pmatrix} \\ &\quad+(1-\gamma)\frac{\overrightarrow{\boldsymbol{E}}_x'v_x+\overrightarrow{\boldsymbol{E}}_y'v_y+\overrightarrow{\boldsymbol{E}}_z'v_z}{v^2}\overrightarrow{\boldsymbol{v}}. \end{aligned} \tag{21}$$

The frequency domain field value $\overrightarrow{E}_i(f)$ of the incident EM wave can be obtained by Fourier transforming the time domain incident field $\overrightarrow{E}_i(t)$. The 3D radar scattering cross section (RCS) can be calculated by (25).

$$\mathrm{RCS}(f) = \lim_{r\to\infty}\left\{10\log\left(4\pi r^2\left|\frac{\vec{E}_s(f)}{\vec{E}_i(f)}\right|^2\right)\right\}. \tag{22}$$

F. Stability and dispersion

It is necessary to ensure the stability and dispersion stability of Lorentz–FDTD method in the analysis the moving target coated with plasma sheath. Assume the time and space grids of the Lorentz–FDTD in the frame K' are set to $dx' = dy' = dz' = \delta$ and $dt' = \delta/2c$. The Courant stability criterion for the FDTD in the K' frame

is given by equation (23), according to the principle of invariance of the speed of light [22]:

$$\Delta t' \le \frac{\delta}{\sqrt{3}c}. \tag{23}$$

Given that the EM wave will be modulated by the velocity of the target and the effect of strong dispersion of the plasma, to guarantee the dispersion stability of the FDTD is necessary, and it can be achieved by selecting a suitable spatial increment δ. The spatial grid parameters to satisfy the FDTD dispersion stability in the frame K' are given in (24) [23]:

$$\delta \le \frac{\lambda'}{12}, \tag{24}$$

where λ' is the minimum wavelength in plasma sheath corresponding to the maximum frequency after the blue-shift of the EM wave, which can be calculated according to the frequency-resolved formula for the scattered field of a moving target [16]. Equation (24) reveals that the velocity of the object affects the EM wave frequency and thus imposes certain restrictions on the spatial grid of the FDTD. In turn, the maximum frequency f_{max} that can be calculated with the FDTD is determined once the space-time increments are set. Therefore, the dispersion stability of the FDTD can be guaranteed when the velocity is less than the critical velocity (herein, the critical velocity is defined as the maximum frequency equal to the f_{max} after the blue-shift of the EM wave frequency caused by the target moving at that velocity). Simulating higher velocities of the moving object can be achieved by reasonably reducing the space-time increments of the FDTD.

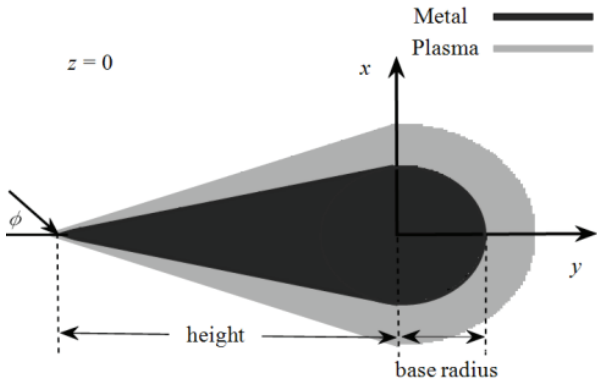

Fig. 3. Shape of cone-sphere target is in the xOy plane.

III. VALIDITY AND ACCURACY

A. Validation of Lorentz-FDTD method

As a validation example, the monostatic RCS of a high-speed moving metal sphere with radius of 1 m is calculated using the proposed algorithm. The space-time increment of Lorentz-FDTD is set to $dx'= dy'= dz'=$ 0.05 m and $dt'= dx'/ 2c$. In frame K', the incident plane EM wave is a Gaussian pulse source is defined with the parameters of $\tau = 40dt'$ and $t_0 = \tau$. The EM propagation angles are set to $\theta_i = 90^\circ$ and $\varphi_i = 90^\circ$, and the incident electric field is polarization along the +z-direction. This target is moving with the velocity v of $0.1c$ along the direction of θ_v=90° and φ_v=90°.

Figure 4 presents the comparison of the RCS results calculated in this article with the RCS results in [23]. It can be seen in Fig. 4 that the RCS of the moving metal sphere complies perfectly with the results in [23] in terms of the variation pattern with the EM wave frequency when the target moves at velocity v of 0 and $0.1c$. The maximum error between the two results of RCS is less than 2.0 dB, which can be a good verification of the proposed algorithm in the analysis scattered fields from moving targets.

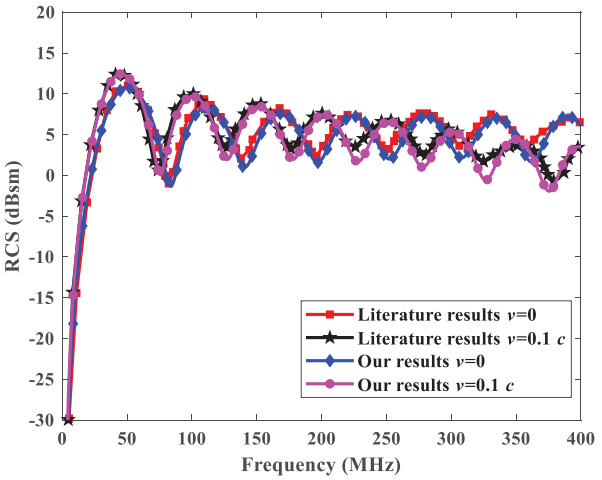

Fig. 4. The monostatic RCS from moving metal sphere target compared with the RCS results in literature.

B. Accuracy in analysis of moving dispersive medium

Here, we adopt a plasma sphere with a diameter of 7.5 mm as a validation example for dispersive media, where the plasma frequency ω_p is 1.8×10^{11} rad/s and the collision frequency ω_c is 20 GHz. The Lorentz–FDTD method is used to calculate the monostatic RCS of the plasma sphere, and the results would be compared with that calculated with Mie theory to verify the validity and accuracy of the proposed algorithm in analyzing EM scattering from dispersive-medium objects. The spatial and time increments of the Lorentz–FDTD are set as $dx'= dy'= dz'=$ 0.05 mm and $dt'= dx'/ 2c$. A Gaussian pulsed plane wave with a pulse width τ of $60dt'$ is incident along the directions $\theta_i = \pi / 2$ and $\varphi_i = \pi / 2$.

Figure 5 presents the results of monostatic RCS calculated with the Lorentz–FDTD and Mie theory

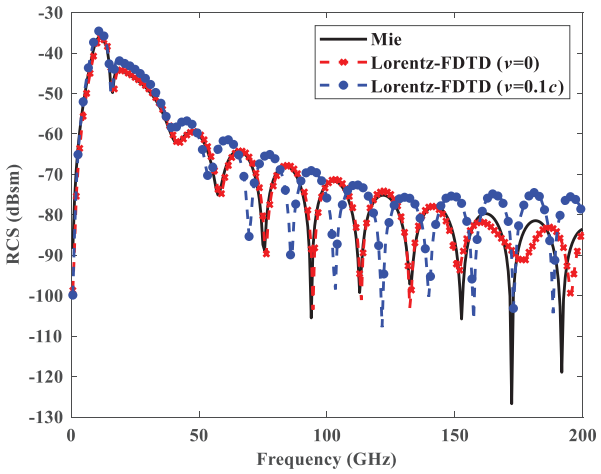

Fig. 5. The monostatic RCS from moving plasma sphere target compared with the Mie's resolution.

respectively for the plasma sphere. From Fig. 5, we can see that when the plasma target is stationary, the RCS results calculated with two methods are nearly consistent. When the plasma target moves away from the incident EM wave source with a velocity of $0.1c$, the monostatic RCS is significantly modulated toward lower frequencies by the motion property of the plasma target, which can be conformed to the expected Doppler effect.

IV. NUMERICAL RESULTS

A. High-speed moving metal cone-sphere target

In this section, the EM scattered properties of a 3D metal cone-sphere target without plasma sheath coating are investigated. The cone-sphere target has a height of 15 cm and base radius of 5 cm. The model of this target in the xOy plane is shown in Fig. 3. The time and space increment of Lorentz–FDTD are set to $dx' = dy' = dz' = \lambda/20$ and $dt' = dx'/2c$, where $\lambda = c/f_0$ is the wavelength of the EM wave at the modulation frequency. The simulation space is defined as $T_x \times T_y \times T_z = (180 \times 180 \times 180)\delta$. The incident plane wave source is a modulated Gaussian pulse with the parameters of center frequency of $f_0 = 4$ GHz, bandwidth of $B = 4$ GHz, pulse width of $\tau = 1.7/B$, and time delay of $t_0 = 0.8\tau$. The plane EM wave was introduced in the SO-FDTD method by using the 3D TF-SF boundary based on the equivalence principle. The mathematical expression of the incident signal is given in

$$E_i'(t') = E_0' \cos\left(2\pi f_0' t'\right) \exp\left(-\frac{4\pi\gamma_t^2 (t'-t_0)^2}{\tau^2}\right), \quad (25)$$

where the E_0' is the amplitude of incident wave in the K'frame, and $\gamma_t = \gamma(1 - \beta\cos\theta)$. The direction of incidence is $\theta_i = 90°$ and $\varphi_i = 90°$, the polarization angle α is set to 90°, the receiving angle $\theta_s = 90°$ and $\varphi_s = 270°$. The corresponding calculation time to update EM field components 3×10^3 times is 0.5 h by using a microcomputer.

Figure 6 shows the backscattering properties of the target with different velocities. The results in Fig. 6 (a) illustrate that when the target moves along the incident direction, the scattered waves in the time domain are delayed and the amplitude decreases slightly, whereas the opposite phenomenon is observed when moving close to the incident wave. In Fig. 6 (a), as the target moves away from the incident wave at $v = 0.02c$, the scattered waveform received in the time domain delays about 0.075 ns compared with that received when the target is stationary. And the time delay will be 0.15 ns for the receding velocity v of $0.04c$. Conversely, the

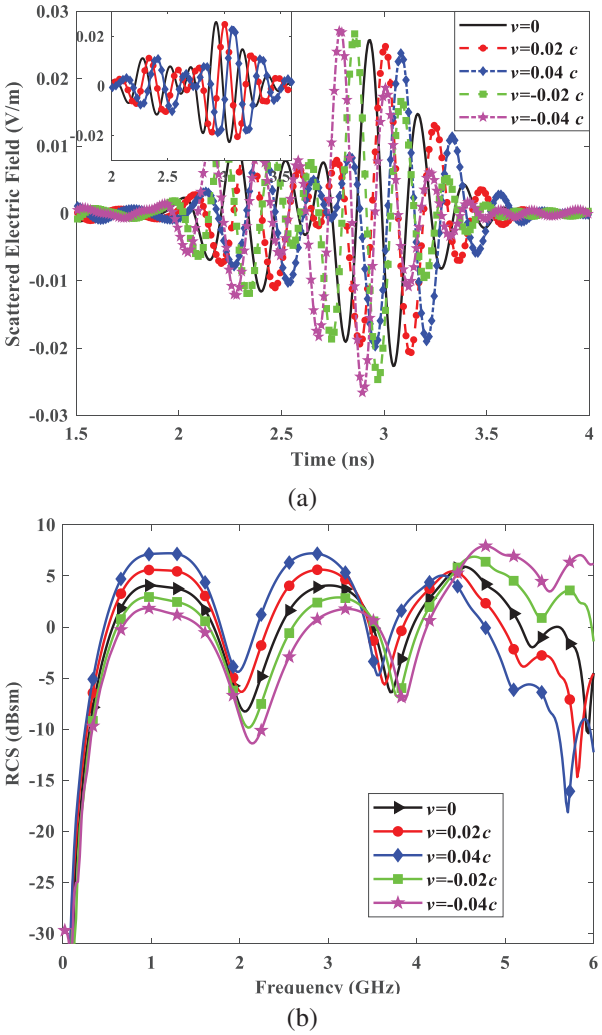

Fig. 6. Scattering fields radiated from a metallic cone-sphere target with motion direction as $\theta_v = 90°$ and $\varphi_v = 90°$: (a) Scattering field in the time domain and (b) monostatic RCS.

scattered waveform in the time domain will advance by about 0.075 ns for v of 0.02c when the target is moving close to the incident source. Further simulations reveal that the time delay of the scattered waveform caused by the motion will differ if the shape of the target is changed. As shown in Fig. 6 (b), the monostatic RCS has a frequency shift toward the low-frequency band if the object moves along the incident direction ($v > 0$). Conversely, RCS has a frequency shift to the high-frequency band while the target moves toward the incident waves ($v < 0$).

For a high-speed moving rotating target, the EM scattering strongly depends on its state of motion, orientation, and shape [14]. To further investigate the relationship between the backward echo characteristics and the velocity of a moving target, the EM echoes of a high-speed moving-cone-sphere target are simulated for different ratios, where the ratio is defined as *ratio = height / base radius*. The details of the target dimensions at different ratios are given in Table 1. The incident wave is incident along the tip of the moving target, and the distance of the plane wave to each cone tip is ensured to be constant.

Table 1: Dimension parameters of cone-sphere target

Ratios	Height (cm)	Base Radius (cm)
0.1	1.5	15
0.5	5.5	11
1.0	17	17
5.0	25	5
10	34	3.4

Figure 7 (a) shows the time-domain waveform of the incident signal. Figures 7 (b)-(f) present the time tracks of backscattered pulse fields of the cone-sphere targets with different ratios and at different velocities. The result in Fig. 7 shows that the backscattered waveform from the target contains abundant information about the target. First, the variation of the scattered wave in terms of delay and amplitude reflects the motion velocity of the object. Second, the waveform variation of the scattered field in the time domain is strongly correlated with the ratio of the target. The maximum amplitude of the scattered field decreases with the target ratio raising, and the scattered field lags significantly in the time domain. For the different ratios and same motion velocity of target, the time delay of the scattered field from the targets has a big difference, and the degree of time delay slightly increases with ratio enlarging. However, as the velocity is 0.04c, the time delay (compared with the stationary target) is twice as long as that when the velocity is 0.02c for all cone ratios.

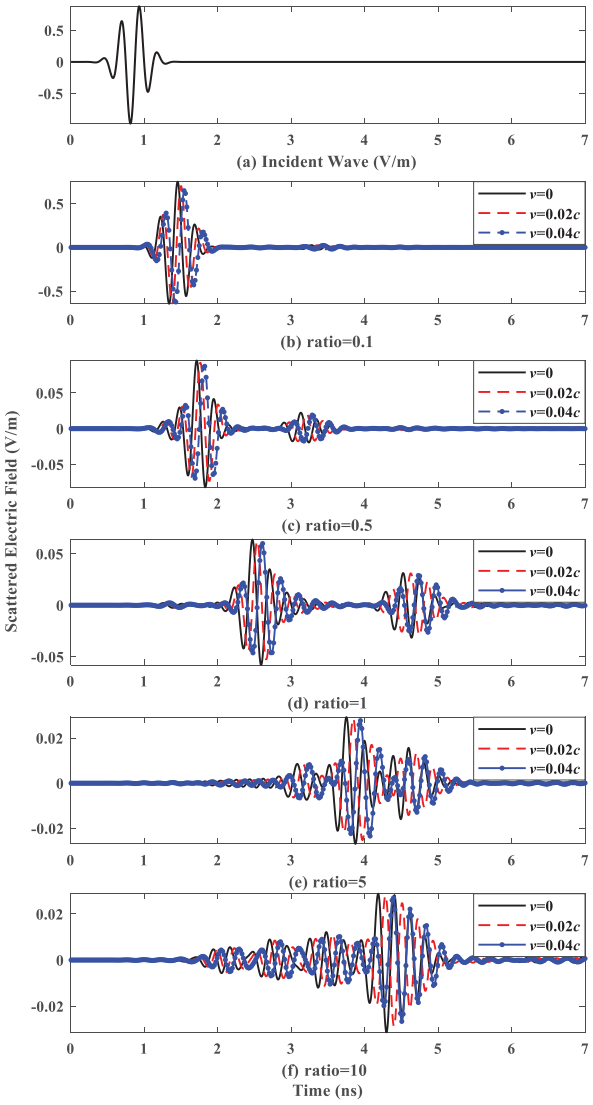

Fig. 7. The incident signal and backscattered waveform of moving cone-sphere targets with different ratios.

B. Moving cone-sphere target coated with plasma sheath

In this section, the influence of the typical EM characteristic parameters of the plasma sheath on the scattered field of the moving cone-sphere target is studied by referring to the measured data of the flow field around a high-speed vehicle [26–27]. A modulated Gaussian pulse source with parameters of f_0 = 4 GHz, B = 4 GHz, τ = 1.7 / B, and $t_0 = 0.8\tau$ is applied to irradiate the moving target. The space-time increment of Lorentz–FDTD are set to $dx' = dy' = dz' = \lambda$ / 54 and $dt' = dx'/2c$. The cone-sphere target with a height of 0.045 m and a base radius of 0.015 m moves at 0.01c along the +y axis. The direction of incident wave is $\theta_i = 90^\circ$ and $\varphi_i = 90^\circ$ in

Table 2: EM parameters of the plasma sheath

Case	Electron Density n_e ($\times$ 1016 m^{-3})	Collision Frequency ω_c (GHz)	Incident Angle ϕ_i (°)
a	1, 5, 10, 20, 100	20	0
b	10	1,5, 10, 20	0
c	20	5	0, 30, 45, 60

simulations of case (a) and (b). In simulation of case (c), the angle of incidence $\theta_i = 90°$, and φ_i is given in Table 2. The EM parameters of the plasma sheath and incident angle are given in Table 2. In additional, the calculation time for the computer to update EM field 4.2×10^3 times is 0.8 h.

Figure 8 displays the variation in monostatic RCS under different plasma electron densities when the target moves at $0.01c$ along the $+y$ axis. It can be seen that the monostatic RCS varies substantially at different electron densities because the cut-off frequency of plasma increases as electron density increases. When the operating frequency of the EM wave is less than the cut-off frequency of plasma ($f < 2$ GHz), the backscattering ability of the plasma sheath for EM waves increases with increased electron density. Therefore, monostatic RCS increases with increased electron density in the low-frequency band. However, when the operation frequency is greater than the cutoff frequency of plasma (f belongs to 2-12 GHz), the reflection caused by plasma decreases, and the absorption of EM waves increases. Eventually, RCS decreases rapidly as electron density increases. Moreover, the maximum absorption position of the RCS for EM waves gradually shifts toward high frequencies with the increase in electron density. When the electron density of plasma is set to 1×10^{18} m^{-3}, the cut-off frequency of plasma is greater than other values, but monostatic RCS decreases very rapidly. This finding is due to most of the EM waves being scattered in the forward-scattering direction, thereby causing a rapid decrease in backscattering direction.

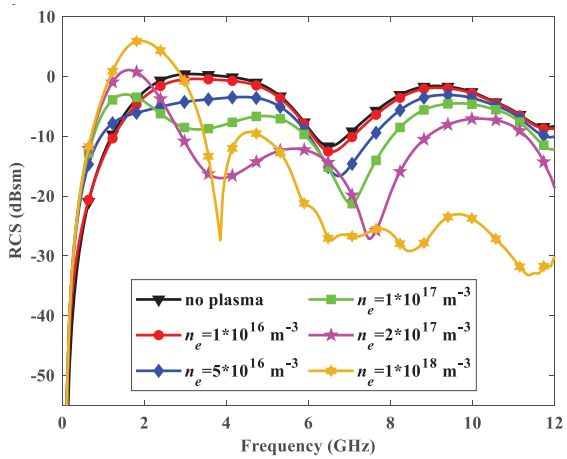

Fig. 8. Monostatic RCS of cone-sphere target coated by plasma sheath with different electron densities n_e.

Figure 9 shows the change in monostatic RCS under different plasma collision frequencies ω_c. When the EM wave operating frequency f ranges within 0-2 GHz, monostatic RCS increases with decreased collision frequency. RCS has a more dramatic change with collision frequency when the plasma frequency is close to the cut-off frequency of EM waves. When the operating frequency f is 2-4 GHz, monostatic RCS decreases first and then increases with increased collision frequency, and decay is maximum at collision frequency $\omega_c = 5$ GHz. This finding is due to that the absorption of EM waves is more remarkable by the plasma sheath when collision frequency wave is close to the cut-off frequency. The monostatic RCS decreases rapidly with increased collision frequency when the operating frequency is greater than the cut-off frequency.

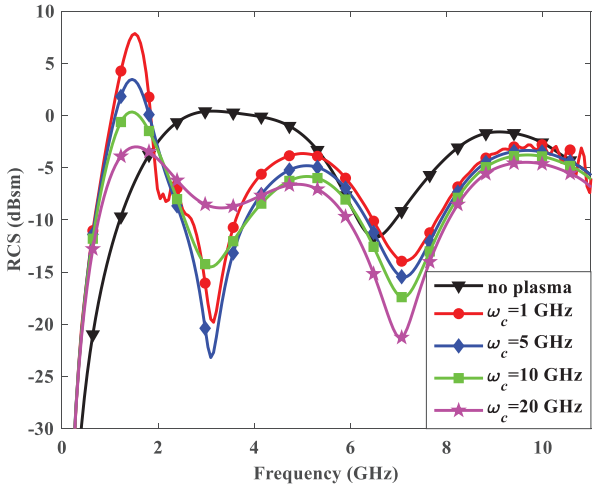

Fig. 9. Monostatic RCS of cone-sphere target coated by plasma sheath with different collision frequencies ω_c.

Figure 10 shows monostatic RCS variation with the angle of the incident wave. The angle of the incidence plane wave has a remarkable effect on monostatic RCS when the operating frequency f ranges within 2-5 GHz. In this frequency range, RCS increases significantly as the incident angle increases. This is mainly because the frequency of EM waves is close to the cut-off frequency, and in this condition the direction of incidence of EM waves has a greater influence on the monostatic RCS. However, the monostatic RCS does not increase with the increase of the incident angle when the operating frequency of EM waves is higher than the cut-off frequency ($f > 6$ GHz).

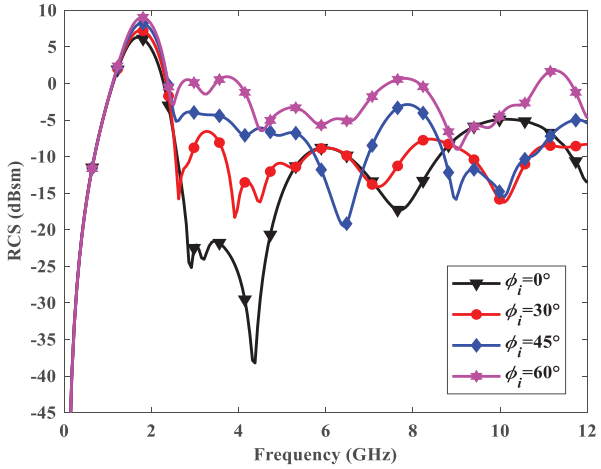

Fig. 10. Monostatic RCS of cone-sphere target coated by plasma sheath with different angles ϕ_i of incident wave.

To illustrate the effect of the electron density of a plasma sheath at different operating frequencies on the EM-scattering ability of the moving cone-sphere target, the bistatic RCS of the cone-sphere target varies with different electrons at different operating frequencies f of 1, 4, and 9 GHz. The operating frequency f = 1 GHz is less than the plasma frequency, f = 4 GHz is within the range of plasma frequency, and f = 9 GHz is greater than the plasma frequency. The collision frequency ω_c of the plasma sheath is 20 GHz, and the thickness of the plasma sheath is 1 cm. The target moves along the $+y$ axis with velocity $0.01c$. The plane wave is incident in the direction of $\theta_i = 90°$ and $\varphi_i = 90°$, and the electric field is polarized along the $+z$ direction. When the scattering angle $\theta_s = 90°$, the bistatic RCS in the xOy scattering plane is observed. The bistatic RCS of moving the cone-sphere target at different operation frequencies of EM waves is shown in Fig. 9.

Figure 11 (a) shows that bistatic RCS increases with the increase electron densities of plasma sheath in both the forward-scattering direction $\varphi_s = 90°$ and the backscattering direction $\varphi_s = 270°$. The increased reflection of the EM wave is caused by the increased electron densities of the plasma sheath when the operating frequency f is less than the plasma cutoff frequency. In Fig. 11 (b), the bistatic RCS increases as the electron densities increases in the forward-scattering direction at $\varphi_s = 90°$. In the backscattering direction at φ_s =270°, the RCS reaches its minimum when the electron densities $n_e = 2\times10^{17}$ m^{-3}. This occurs because the cutoff frequency of plasma at electron densities $n_e = 2 \times 10^{17}$ m^{-3} matches the operating frequency of EM waves, leading to the most pronounced absorption of EM waves by the plasma. Figure 11 (c) shows that the bistatic RCS in the forward-scattering direction $\varphi_s = 90°$

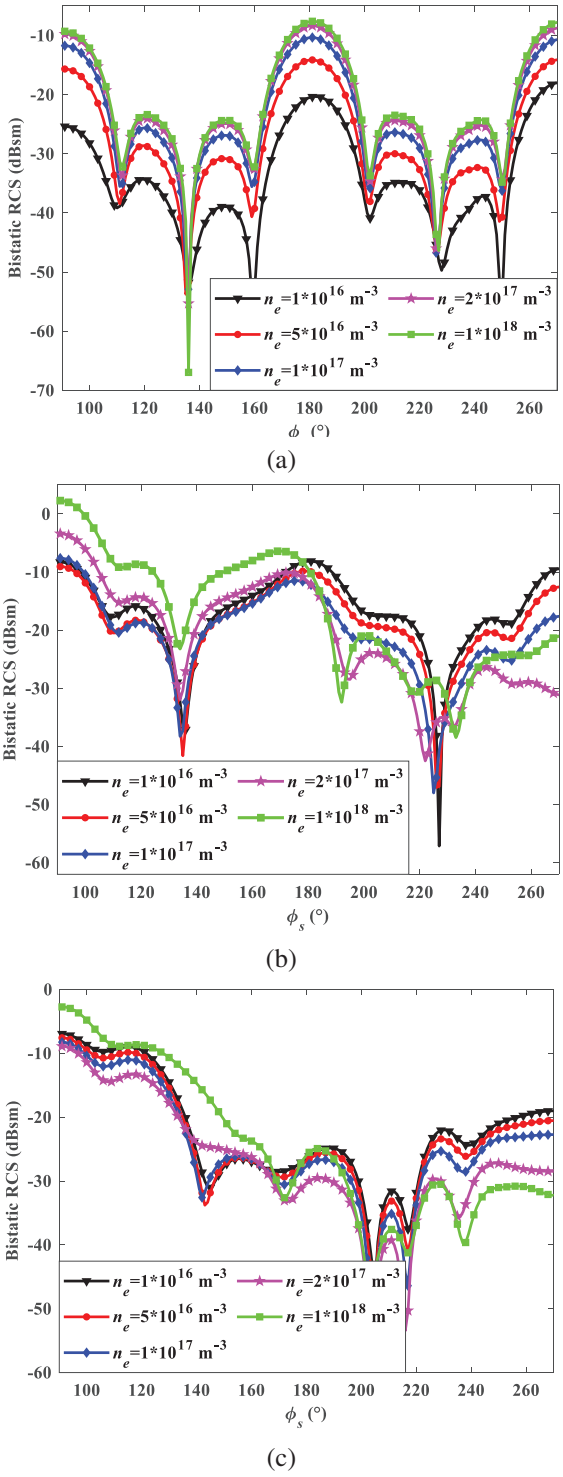

Fig. 11. (a) HIS structure and (b) Equivalent circuit.

decreases with increased electron densities when $n_e \leq 2 \times 10^{17}$ m^{-3}, but increases at $n_e = 1 \times 10^{18}$ m^{-3} and decreases rapidly with increasing electron density in the backscattering direction $\varphi_s = 270°$. The RCS changes

more considerably in the backscattering direction than in the forward-scattering one. Figure 8 (a) can be verified again. When the electron density $n_e = 1 \times 10^{18}$ m^{-3}, the reason for the rapid decreases of monostatic RCS at high frequencies is that the EM wave is scattered to the forward-scattering direction.

C. Doppler effect on scattered field

In this section, we examine the impact of the velocity on the Doppler effect of the scattered field of a high-speed target. The parameters of the FDTD grid and the dimensions of the target are the same as in Section B. The EM parameters of the plasma sheath are set as the electron density n_e of 3×10^{16} m^{-3} and 3×10^{17} m^{-3}, ω_c of 10 GHz, and a plasma thickness of 1 cm. The incident direction is set to $\theta_i = \pi/2$ and $\varphi_i = \pi/2$. This object is moving at velocities $\boldsymbol{v}$ of 0.02c, 0.04 c, -0.02c, and -0.04c along the incident direction.

It is evident from Fig. 12 that the RCS experiences a red-shift when the target moves away the incident wave ($v > 0$) and a blue-shift when the target moves toward the source. This phenomenon bears resemblance to the frequency modulation law observed in moving metal targets. However, the complexity of the amplitude modulation law increases. Due to the variation in electron density, the RCS exhibits different levels of reduction across various frequency bands of EM waves. As depicted in Fig. 12 (a), when the electron density $n_e = 3 \times 10^{16}$ m^{-3}, the operation frequency f of EM waves significantly exceeds the cut-off frequency of the plasma. Therefore, there is a lower absorbing and higher scattering of plasma on the EM waves. Figure 12 (b) presents the variation of RCS with velocity when the electron density $n_e = 3 \times 10^{17}$ m^{-3}. It can be seen that when the operation frequency f is in the range of 3.5-5.0 GHz, the RCS when the velocity v of 0.04 c is significantly stronger than at the velocity v of -0.04 c. This finding is due to the variations of the target velocity changes the relative dielectric coefficient of plasma, which in turn influences the absorbing and scattering of plasma on EM waves. With the target moving away from the source, the red-shift will decrease the frequency of EM waves, which increases the scatter of plasma on EM waves. By contrast, the blue-shift due to the target moving toward the source will increase the EM wave frequency, which increases the absorbing of plasma on EM waves. The scattering EM echo from this plasma coated target at different velocities is presented in Fig. 13.

Finally, to investigate the impact of velocity on the Doppler shift of the scattered field from the target, a time-harmonic signal with a carrier frequency of 4 GHz was used to irradiate the target. The backscattered field in the time domain was then recorded. Further, the analysis of the variation of Doppler shift with object velocity

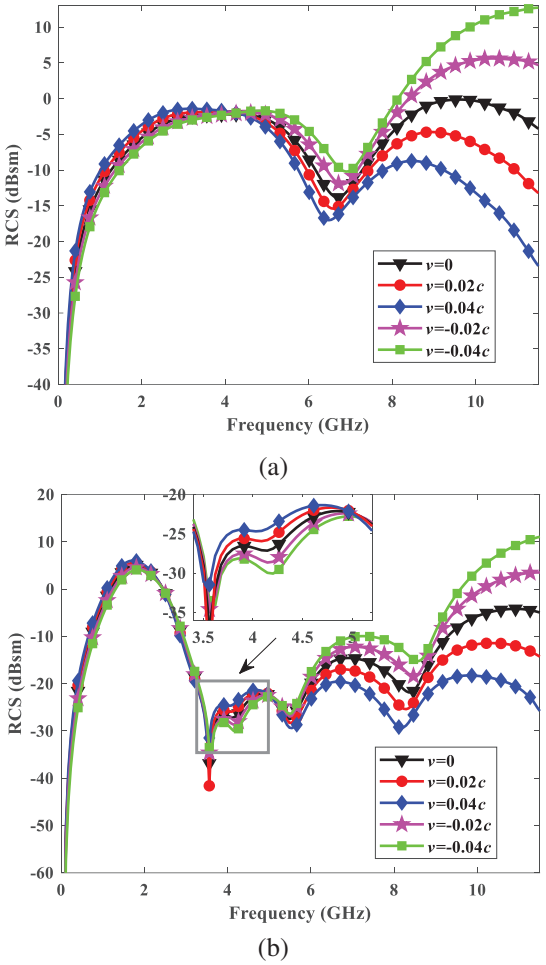

Fig. 12. Monostatic RCS in different velocities when the target coated with a plasma sheath with electron densities (a) n_e=3×10^{16} m^{-3} and (b) n_e=3×10^{17} m^{-3}.

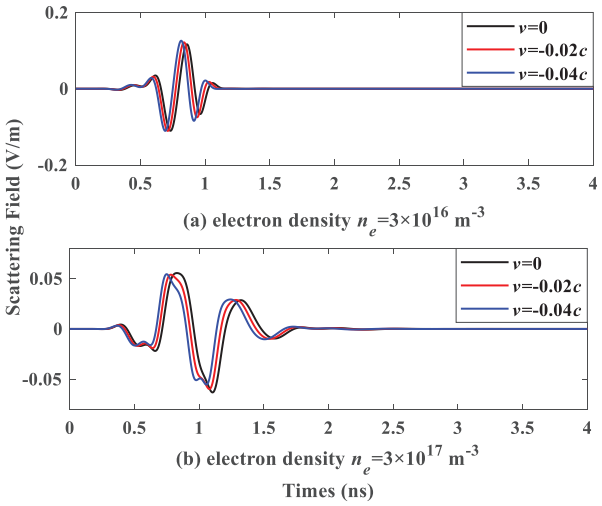

Fig. 13. EM echo in different velocities when the plasma coated target with electron densities n_e of 3×10^{16} and 3×10^{17} m^{-3}.

Table 3: Doppler shift and relative error of scattered field in different velocities

Velocity	Numerical Results (GHz)	Theoretical Results (GHz)	Error
0.02c	3.8435	3.8431	0.013%
0.04c	3.6929	3.6923	0.016%
-0.02c	4.1637	4.1633	0.010%
-0.04c	4.3338	4.3333	0.012%

can be conducted through the examination of the echo spectrum. Table 3 presents the numerical and theoretical results (26) of the frequency of the scattered field for a high-speed target. The results indicate that the relative error between the two outcomes falls within an acceptable range. This finding further supports the accuracy and validity of the proposed method:

$$\omega_s = \gamma\omega' \left(1 - \beta \frac{\cos\theta + \beta}{1 + \beta\cos\theta}\right). \tag{26}$$

V. CONCLUSION

In this paper, the EM model of a moving dispersive medium is established by utilizing the relativistic principle. In this study, we aim to investigate the scattering properties of high-speed moving plasma coated targets and their interaction with EM waves. To achieve this, we present and analyze two cases in order to reveal the nature of this work.

The first research example reveals that scattering and echo characteristics of the object exhibit a significant dependence on the velocity of the target, the direction of its motion, and the shape of the object. The second example examines the impact of plasma parameters, incidence direction, frequency of electromagnetic waves, and object velocity on the scattered field. The research findings indicate that the relative dielectric coefficient of the plasma sheath undergoes changes as a result of the object's velocity, thereby influencing the scattering and absorption of electromagnetic waves by the plasma. Additionally, the RCS exhibits distinct variations in pattern with target velocities when subjected to EM waves at different operating frequencies.

In future research, the Lorentz-FDTD algorithm will be applied to investigate and analyze more-complex EM scattering scenarios, such as considering the flow field properties of plasma sheaths and investigating the effect of spatial-temporal non-uniformity of plasma on EM imaging of high-speed moving object.

ACKNOWLEDGMENT

This work was supported by the National Natural Science Foundation of China (Nos. 62071003, 62201001), the Key Basic Research Project of the State Administration of Science, Technology and Industry for National Defense, China, the Open Project of the Key Laboratory of Computational Intelligence and Signal Processing, Ministry of Education (Grant No. 2020A008), the Natural Science Foundation of Education Department of Anhui Province, China (Grant No. KJ2020A0024), Anhui Provincial Natural Science Foundation (No. 2208085QF184), the Open Research Fund of Advanced Laser Technology Laboratory of Anhui Province, China (No. AHL2020KF04), the Open Project of the State Key Laboratory of Millimeter Waves (Grant No. K202222).

The authors are with the Information Materials and Intelligent Sensing Laboratory of Anhui Province, Anhui University, Hefei 230601, China, and also with the Anhui province Key Laboratory of Target Recognition and Feature Extraction, Luan 237000, China (The corresponding author is Yong Bo, email: boyong@ahu.edu.cn).

REFERENCES

[1] J. P. Rybak and R. J. Churchill, "Progress in reentry communications," *IEEE Transactions on Aerospace and Electronic Systems*, AES-7, NO.5:879-894, 1971.

[2] K. Lemmer, *Use of a Helicon Source for Development of a Re-entry Blackout Amelioration System*, 1-23, Michigan: University of Michigan, 2014.

[3] T. C. Lin and L. K. Sproul, "Influence of reentry turbulent plasma fluctuation on EM wave propagation," *Comput. Fluids*, vol. 35, no. 7, pp. 703-711, Aug. 2006.

[4] M. Kundrapu, J. Loverich, K. Beckwith, P. Stoltz, A. Shashurin, M. Keidar, and A. Ketsdever, "Modeling radio communication blackout and blackout mitigation in hypersonic vehicles," *J. Spacecr. Rockets*, vol. 52, no. 853, pp. 2-27, 2015.

[5] L. Shi, B. L. Guo, Y. M. Liu, and J. T. Li, "Characteristics of plasma sheath channel and its effect on communication," *Progress in Electromagnetic Research*, vol. 123, no. 2, pp. 321-336, 2012.

[6] C. T. Swift, F. B. Beck, J. Thomson, and S. L. Castellow, "RAM C-III S-band diagnostic experiment," in *Proc. NASA SP-252 4th Plasma Sheath Symp,* Washington, DC, USA, pp. 137-155, Jan. 1971.

[7] M. Chung and S. S, "FDTD simulations on radar cross sections of metal cone and plasma covered metal cone," *Vacuum: Technology Applications & Ion Physics: The International Journal & Abstracting Service for Vacuum Science & Technology*, vol. 86, no. 7, pp. 970-984, 2012.

[8] B. T. Nguyen, A. Samimi, and J. J. Simpson, "Recent advances in FDTD modeling of electromagnetic wave propagation in the iono-

sphere," *Applied Computational Electromagnetics Society (ACES) Journal*, vol. 29, no. 12, pp. 1003-1012, 2014.

[9] M. Pourbagher and S. A. Sahafi, "Three dimensional FDTD algorithm for wave propagation in cold plasma media using Forth-Order schemes," *Applied Computational Electromagnetics Society (ACES) Journal*, vol. 28, no. 12, pp. 1153-1161, 2013.

[10] K. S. Zheng, J. Z. Li, G. Wei, and J. D. Xu, "Analysis of Doppler effect of moving conducting surfaces with Lorentz-FDTD method," *Journal of Electromagnetic Waves and Applications*, vol. 27, no. 2, pp. 149-159, Feb. 2013.

[11] K. S. Zheng, X. P. Liu, Z. Mu, and W. Gao. "Analysis of scattering fields form moving multilayered dielectric slab illuminated by an impulse source," *IEEE Antennas Wireless Propag. Lett*, vol. 16, pp. 2130-2134, Jul. 2017.

[12] Y. Zhao and S. Chaimool, "Relativistic finite-difference time-domain analysis of high-speed moving metamaterials," *Scientific Reports*, vol. 8, no. 1, pp. 7686, 2017.

[13] T. J. Garner, A. Lakhtakia, J. K. Breakall, and C. F. Bohren, "Lorentz invariance of absorption and extinction cross sections of a uniformly moving object," *Physical Review A*, vol. 96, no. 5, pp. 053839, 2017,

[14] T. J. Garner, C. F. Bohren, A. Lakhtakia, and J. K. Breakall, "Electromagnetic pulse scattering by a spacecraft nearing light speed," *Applied Optics*, vol. 56, no. 22, pp. 6206-6213, 2017,

[15] G. Z. Niu, Y. M. Liu, B. W. Bai, and D. Yi, "A numerical simulation method of radar echo from a high-speed target," *IEEE Antennas Wireless Propag. Lett*, vol. 20, no. 10, pp. 1958-1962, Aug. 2021.

[16] L. Man, H. C. Deng, Y. Bo, Z. H. Xiao, and L.X. Yang, "Interaction between relative moving plasma plate and electromagnetic wave," *Chinese Journal of Radio Science*, vol. 38, no. 1, pp. 164-172, May 2022.

[17] L. J. Guo and L. X. Guo, "Absorption of electromagnetic waves by a moving non-uniform plasma," *Physics of Plasmas*, vol. 24, no.4, pp. 042119, 2017.

[18] Z. Bian, J. T. Li, L. X. Guo, and X. Luo, "Analyzing the electromagnetic scattering characteristics of a hypersonic vehicle based on the inhomogeneity zonal medium model," *IEEE Transactions on Antennas and Propagation*, vol. 69, no. 2, pp. 971-982, 2021.

[19] X. M. Guo, Y. Bo, L. X. Yang, M. P. Jin, Z. X. Huang, and H. Y. Li, "Study on Scattering Properties of Moving Cone-Sphere Shape Coated with Plasma Sheath," *2022 IEEE 5th International Conference on Electronic Information and Communication Technology*, pp. 775-778, 2022.

[20] H. W. Yang, R. S. Chen, and Y. Zhang, "SO-FDTD method and its application to the calculation of electromagnetic wave reflection coefficients of plasma," *Chinese Physics*, vol. 55, no. 7, pp. 3464-3469, 2006.

[21] Z. K. Zhou, X. H. Wan. X. L. Li, J. Zhang, Y. S. Zhou, X. P. Ren, and Y. R. Shi, "SO-FDTD analysis on transmission characteristics of terahertz wave in plasma," *Physics of Plasmas*, vol. 28, no. 7, pp. 1-8, 2021.

[22] C. Wei, L. X. Yang, Z. X. Huang, and L. X Guo, "Research on the propagation characteristics of THz waves in spatial inhomogeneous and time-varying and weakly ionized dusty plasma," *IEEE Trans. Plasma Sci*, vol. 47, no. 10, pp. 4745-4752, Oct. 2019.

[23] K. S. Zheng, Y. Li, L. Xu, J. T. Li, and G. Wei, "Electromagnetic properties of a complex pyramid-shaped target moving at high speed," *IEEE Trans. Antennas Propag*, vol. 66, no. 12, pp. 7472-7476, Dec. 2018.

[24] Jinau Kong, *Electromagnetic Waves Theory* 2, *Higher Education Press*, 2000.

[25] D. B. Ge and Y. B. Yan, *The Finite-Difference Time-Domain Method for Electromagnetic Wave*, 151-155. Xi'an, China: Xidian Univ. Press, 2011.

[26] Y. G. Lv, L. X. Guo, and J. T. Li, *Hypersonic Vehicle Plasma Sheath and Electromagnetic Characteristics Data Manual*, Beijing, China: Science Press, 2019.

[27] Z. W. Liu, W. M. Bao, X. P. Li, and D. L. Liu, "A segmentation calculation method for plasma collision frequency considering the electromagnetic wave driving effect," *Acta Phys. Sinica*, vol. 63, no. 23, 2014,

Xian-Min Guo was born in Xianyang City, Shanxi Province, China, in 1999. She received the B.S. degree in electronic information engineering from Shandong University of Technology, Zibo, China, in 2021. She is currently working toward the master's degree in electromagnetic field and microwave technology of Electronic Information with the School of Electronic Information Engineering, Anhui University, Hefei, China.

Her current research interest is computational electromagnetism and plasma physics.

Hai-Yan Li was born in Huaibei City, Anhui Province, China, in 1999. She received the B.S. degree in electronic information engineering from Huainan Normal University, Huainan, China, in 2021. She is currently working toward the master's degree in electromagnetic field and microwave technology of Electronic Information with the School of Electronic Information Engineering, Anhui University, Hefei, China.

Her current research interest is computational electromagnetism.

Yong Bo was born in Shandong Province, China, on November 11, 1989. He received the B.S. degree in Shandong University of Science and Technology, Qingdao, China, in 2012, and the Ph.D. degree from the Center for Information Geoscience, University of Electronic Science and Technology of China, Chengdu, China.

He is currently a lecturer with the University of Anhui, Hefei, China. The main subjects of his interest include computational electromagnetic, wave propagation in plasmas, and low temperature plasma technology and application.

Wei Chen was born in Jiangsu Province, China, in 1987. He received the B.S. and M.S. degrees from Jiangsu University, Jiangsu, China, in 2010 and 2013, respectively, and the Ph.D. degree from Xidian University, Xi'an, China, in 2018.

He is currently a lecturer with the School of Electronics and Information Engineering, Anhui University, Hefei, China. His current research interests include numerical methods in electromagnetic scattering from plasma and wave propagation in complex systems.

Li-Xia Yang was born in Ezhou, Hubei, China, in 1975. He received the B.S. degree in physics from Hubei University, Wuhan, China, in 1997, and the Ph.D. degree in radio physics from Xidian University, Xi'an, China, in 2007.

Since 2010, he has been an associate professor with the Communication Engineering Department, Jiangsu University, Zhenjiang, China. From 2010 to 2011, he was a postdoctoral research fellow with the Electro Science Laboratory (ESL), Ohio State University, Columbus, OH, USA. From 2015 to 2016, he was a visiting scholar with the Institute of Space Science, University of Texas at Dallas, Dallas, TX, USA. From 2016 to 2019, he was a professor, a Ph.D. supervisor, and the chairman of the Communication Engineering Department, Jiangsu University. Since 2020, he has been a distinguished professor, a Ph.D. supervisor, and the vice dean with the School of Electronic and Information Engineering, Anhui University, Hefei, China. His research interests include wireless communication technique, radio sciences, computational electromagnetics, and the antenna theory and design in wireless communication systems. He is a member of the Editorial Board of Radio Science Journal in China.

Zhi-Xiang Huang was born in Anhui, China, in 1979. He received the B.S. and Ph.D. degrees from Anhui University, Hefei, China, in 2002 and 2007, respectively. He was a visiting scholar with Iowa State University, USA, from September 2010 to September 2011. From August 2013 to October 2013, he was a visiting professor with The University of Hong Kong. From February 2014 to February 2015, he was a visiting professor with the Beijing National Laboratory for Condensed Matter Physics, Institute of Physics, Chinese Academy of Sciences. He has published one monograph on the symplectic finite-difference time-domain method and two book chapters at CRC Press and In Tech Publishers. He has published 60 peer-reviewed journal articles included in the Web of Science Core Collection. His current research interests include time-domain numerical methods, metamaterials, and active metamaterials. He is a member of the OSA. In 2015, he was awarded the second prize of Science and Technology from the Anhui Province Government, China, and the National Science Foundation for Outstanding Young Scholar of China, in 2017.

An-Qi Wang was born in Anhui, China, in 1986. She received the B.S. and Ph.D. degrees from Xidian University, Xi'an, China, in 2007 and 2013, respectively. Her current research interests include computational electromagnetics and the electromagnetic wave scattering characteristics of rough surface and targets.

Anomalous Magnetization Spikes in the Locally Corrected Nyström Discretization of Static Volume Integral Equation using Tetrahedral Cells

John C. Young[1], Robert J. Adams[1], and Stephen D. Gedney[2]

[1]Department of Electrical & Computer Engineering
University of Kentucky, Lexington, Kentucky 40506, USA
john.c.young@uky.edu, robert.adams@uky.edu

[2]Department of Electrical Engineering
University of Colorado – Denver, Denver, Colorado 80204, USA

***Abstract* –** A locally corrected Nyström (LCN) discretization of a magnetostatic volume integral equation is presented. Anomalous magnetization spikes can occur when the underlying mesh uses tetrahedral cells regardless of discretization order. The mechanism for the anomalous magnetization spikes is discussed, and mitigation of the spikes through use of an LCN-to-Moment Method conversion is investigated. Results are presented validating that the LCN-to-Moment Method suppresses the anomalous spikes.

***Index Terms* –** integral equation methods, locally corrected Nyström method, moment method.

I. INTRODUCTION

The locally corrected Nyström (LCN) method [1–3] is one of the primary methods for discretizing integral equations. Advantages of the LCN method over the Moment Method (MoM) include not having to explicitly enforce continuity of physical quantities across mesh cell boundaries, less strict mesh conformality requirements, more efficient system matrix fill, and ease of implementing higher-order codes. Divergence-conforming formulations require that normal components of quantities such as fields and currents be continuous (unless physically discontinuous) across mesh cell boundaries. Although the Nyström method does not explicitly enforce this normal continuity, the underlying Nyström degrees-of-freedom should permit the proper space and continuity properties required by the formulation to be achieved.

In this paper, a magnetostatic volume integral equation is presented that is discretized by the locally corrected Nyström method [4]. Results are provided in which anomalous (non-physical) magnetization [5] are observed for complex geometries when tetrahedral mesh elements are used in the discretization. The mechanism for the anomalous magnetization spikes is discussed by noting that the typical Nyström representation does not span the same mixed-order divergence-conforming space that commonly used Moment Method bases span. Further, use of an LCN-to-MoM conversion [7, 8] of the discretized LCN system is observed to suppress the anomalous magnetization spikes since the LCN-to-MoM conversion provides a representation with the appropriate degrees-of-freedom to model a mixed-order divergence-conforming space as well as the appropriate normal continuity.

II. LCN FORMULATION FOR TETRAHEDRA

Consider the magnetostatic volume integral equation (VIE)

$$\boldsymbol{\chi}^{-1}\cdot\mathbf{M}(\mathbf{r}) = H^{\text{excitation}}(\mathbf{r}) + \mathbf{H}^{m}(\mathbf{r}),\ \ \mathbf{r}\in V, \qquad (1)$$

defined over a material volume V where $\mathbf{M}$ is the magnetization, $\boldsymbol{\chi}$ is the magnetic susceptibility tensor, and $\mathbf{H}^m$ is the demagnetizing field

$$\mathbf{H}^{m}(\mathbf{r}) = \iiint_{V} \nabla\nabla\cdot\left[\frac{1}{4\pi|\mathbf{r}-\mathbf{r}'|}\mathbf{M}(\mathbf{r}')\right]dv'. \qquad (2)$$

The VIE in (1) is discretized using the locally corrected Nyström (LCN) method. For simple geometries, good results and convergence have been obtained for both hexahedral and tetrahedral cells. For sphere and spherical shell geometries with isotropic, homogeneous magnetic susceptibility, high-order convergence is obtained for higher basis orders when higher-order mesh representations are used. For some complex geometries, however, the magnetization is observed to exhibit anomalous spikes for tetrahedral meshes. Similar spikes in the magnetization are not observed for hexahedral meshes of the same geometry when using a mixed-order LCN formulation [10].

For basis order $p = 0$, the phenomenon seems to be at least partially due to the inability of the underlying function space of the Nyström representation of the magnetization to sufficiently model the continuity of the normal component of magnetization across tetrahedral cell

Submitted On: July 31, 2023
Accepted On: September 26, 2023

https://doi.org/10.13052/2024.ACES.J.390210

boundaries. More generally, for order $p \geq 0$ the standard Nyström representation on tetrahedral cells (and similarly on triangular cells) does not span the same space as typical divergence-conforming MoM representations (e.g,, [9]). The ability to maintain continuity across all cell boundaries is discussed for the basis order $p = 0$ and $p = 1$ representations. For orders $p > 1$, analogous results hold. Further, the number of degrees-of-freedom of the standard Nyström representation and mixed-order divergence-conforming MoM representations are not the same, indicating different spaces are being spanned.

Consider the set of tetrahedral cells depicted in Fig. 1. A primary cell T_c is adjacent to four secondary cells T_k for $k = 0,1,2,3$. The boundary face S_k is shared by cells T_c and T_k. Local coordinates are defined such that u^{ix} is the coordinate along the ith unitary axis for i=1,2,3. A dependent local coordinate $u^{0x} = 1 - u^{1x} - u^{2x} - u^{3x}$ is also defined. The local coordinates are such that $u^{kx} = 0$ on face S_k in cell T_x. For i=1,2,3, $\mathbf{u}_{ix}\left(u^{1x}, u^{2x}, u^{3x}\right)$ is the ith unitary vector and $\mathbf{u}^{ix}\left(u^{1x}, u^{2x}, u^{3x}\right)$is the ith reciprocal unitary vector in cell x. Furthermore, $\mathbf{u}^{0x} = -\left(\mathbf{u}^{1x} + \mathbf{u}^{2x} + \mathbf{u}^{3x}\right)$. The cell vertices are ordered such that the outward normal to boundary S_k is $-\mathbf{u}^{kc}$ in cell T_c and is $-\mathbf{u}^{kk}$ in cell T_k, and, so, $\mathbf{u}^{kc} = -\mathbf{u}^{kk}$ on S_k.

Let the Nyström degrees-of-freedom be cast onto a set of bases within tetrahedron x with degrees-of-freedom $\alpha_{ix,j}$ for the jth degree-of-freedom associated with the ith unitary direction. The pth-order polynomial-complete basis representation on tetrahedron x is

$$\mathbf{M}_x^p\left(u^{1x}, u^{2x}, u^{3x}\right) = \frac{1}{\sqrt{g_x}} \sum_{i=1}^{3} f_{ix}^p\left(u^{1x}, u^{2x}, u^{3x}\right) \mathbf{u}_{ix}, \quad (3)$$

where $\sqrt{g_x\left(u^{1x}, u^{2x}, u^{3x}\right)}$ is the cell Jacobian and f_{ix}^p is a polynomial of degree p. Note that on the boundary face S_k, $\sqrt{g_c} = \sqrt{g_k}$ at each point on the face. Hence, in the following development, the cell Jacobians will cancel for constraints on S_k. For both the $p = 0$ and $p = 1$ discussion, the degrees-of-freedom in cell T_k are considered fixed, and the degrees-of-freedom in cell T_c will be constrained (if possible) to achieve continuity of normal magnetization across all faces.

For $p = 0$, there are three Nyström degrees-of-freedom and three bases, and

$$f_{ix}^0\left(u^{1x}, u^{2x}, u^{3x}\right) = \alpha_{ix,0}^0. \quad (4)$$

Enforcing continuity at each face S_k for k=0,1,2,3 gives the constraints

$$\left[u^{kc} \cdot \frac{1}{\sqrt{g_c}} \sum_{i=1}^{3} \alpha_{ic,0}^0 u_{ic}\right]_{u^{kc}=0} = \left[u^{kc} \cdot \frac{1}{\sqrt{g_k}} \sum_{i=1}^{3} \alpha_{ik,0}^0 u_{ik}\right]_{u^{kk}=0}. \quad (5)$$

Since the set of unitary and reciprocal unitary vectors are orthonormal, the constraints in (5) reduce to

$$\alpha_{kc,0}^0 = -\alpha_{kk,0}^0, \ k = 1,2,3, \quad (6)$$

and

$$\sum_{k=1}^{3} \alpha_{kc,0}^0 = -\sum_{k=1}^{3} \alpha_{k0,0}^0, \ k = 0. \quad (7)$$

Note there are only three degrees-of-freedom in cell T_c but four constraints that must be satisfied. The three degrees of freedom within the cell permit the normal component of the magnetization to be matched continuously at three of the tetrahedral cell faces. However, there are insufficient degrees-of-freedom within the cell to match the normal component of magnetization at all four of the faces of the cell as required in a divergence-conforming formulation.

For $p = 1$, there are twelve Nyström degrees-of-freedom and twelve bases, and [3]

$$f_{ix}^1\left(u^{1x}, u^{2x}, u^{3x}\right) = \alpha_{ix,0}^1 + \alpha_{ix,1}^1 u^{1x} + \alpha_{ix,2}^1 u^{2x} + \alpha_{ix,3}^1 u^{3x}. \quad (8)$$

Enforcing continuity at each face S_k for k=0,1,2,3 gives the constraints

$$\left[\frac{\mathbf{u}^{kc}}{\sqrt{g_c}} \cdot \sum_{i=1}^{3}\left(\alpha_{ic,0}^1 + \alpha_{ic,1}^1 u^{1c} + \alpha_{ic,2}^1 u^{2c} + \alpha_{ic,3}^1 u^{3c}\right)\mathbf{u}_{ic}\right]_{u^{kc}=0} = \left[\frac{\mathbf{u}^{kc}}{\sqrt{g_k}} \cdot \sum_{i=1}^{3}\left(\alpha_{ik,0}^1 + \alpha_{ik,1}^1 u^{1k} + \alpha_{ik,2}^1 u^{2k} + \alpha_{ik,3}^1 u^{3k}\right)\mathbf{u}_{ik}\right]_{u^{kk}=0}. \quad (9)$$

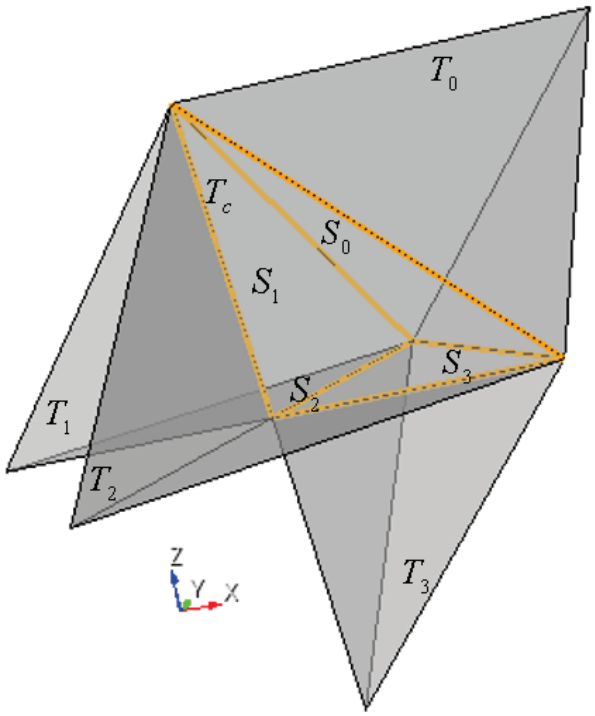

Fig. 1. Primary tetrahedral cell T_c adjacent to four secondary tetrahedral cells T_k. Shared face S_k is shared by T_c and T_k.

The constraints in (9) then reduce to

$$\left(\alpha^1_{ic,0}+\alpha^1_{ic,1}u^{1c}+\alpha^1_{ic,2}u^{2c}+\alpha^1_{ic,3}u^{3c}\right)\Big|_{u^{kc}=0} = -\left(\alpha^1_{ik,0}+\alpha^1_{ik,1}u^{1k}+\alpha^1_{ik,2}u^{2k}+\alpha^1_{ik,3}u^{3k}\right)\Big|_{u^{kk}=0}, \tag{10}$$

for $k = 1,2,3$. For each k=1,2,3, three degrees-of-freedom on T_c are specified leaving 3 remaining degrees-of-freedom to match continuity across S_0. For S_0, the constraint reduces to

$$\sum_{i=1}^{3}\left(\alpha^1_{ic,0}+\alpha^1_{ic,1}u^{1c}+\alpha^1_{ic,2}u^{2c}+\alpha^1_{ic,3}u^{3c}\right)\mathbf{u}^{0c}\cdot\mathbf{u}_{ic} = \sum_{i=1}^{3}\left(\alpha^1_{i0,0}+\alpha^1_{i0,1}u^{10}+\alpha^1_{i0,2}u^{20}+\alpha^1_{i0,3}u^{30}\right)\mathbf{u}^{0c}\cdot\mathbf{u}_{i0}. \tag{11}$$

Given the normal

$$\mathbf{u}^{0c} = -\left(\mathbf{u}^{1c}+\mathbf{u}^{2c}+\mathbf{u}^{3c}\right) = -\mathbf{u}^{00}, \tag{12}$$

at S_0 and $u^{1x}+u^{2x}+u^{3x}=1$ on the shared face, there are three constraints and maintaining normal continuity is possible. Note that [5] mistakenly indicates normal continuity is not possible for $p \geq 1$ using the polynomial-complete representation.

In the p = 0 case, the Nyström degrees-of-freedom are insufficient by one DoF to be able to enforce normal continuity at all four faces simultaneously. The p = 1 case allows a linear tangential, linear normal representation instead of the typical linear tangential, constant normal representation. However, the linear tangential, linear normal representation includes degrees-of-freedom associated with the null space of the divergence operator, which is undesirable.

In general, the order p divergence-conforming interpolatory vector basis set for tetrahedral cells in [9] give the number of boundary face bases and internal cell bases as

$$2\left(p+1\right)\left(p+2\right), \tag{13}$$

and

$$p\left(p+1\right)\left(p+2\right)/2, \tag{14}$$

respectively. Table 1 lists the number of degrees-of-freedom for the Nyström representation and a divergence-conforming interpolatory [9] representation on a tetrahedral cell for basis orders p = 0 through p = 2. It is noted that there are fewer Nyström bases than divergence-conforming bases. What is missing from the Nyström function space are mixed-order p+1 terms that ensure that the divergence of the basis function space is complete to order p. Without these terms, the divergence of the Nyström basis space is only of order p-1. In addition, for the p = 0 basis, the divergence is zero.

For $p > 0$, while the Nyström basis is sufficient to represent the magnetization to order p and provide normal continuity, it has insufficient DoF to represent the charge to order p. Therefore, the Nyström basis has an insufficient number of DoF to represent the mixed-order divergence-conforming space to order p. Furthermore, it over specifies the p-1 function space. Hence, the standard Nyström representation on tetrahedra (and triangles) cannot be truly divergence-conforming although the method seems to provide very good solutions across a wide range of problems.

Table 1: Total degrees-of-freedom (DoF) in Nystrom and an interpolatory divergence-conforming representations versus basis order p. (Number of boundary face and internal cell DoF in parenthesis)

Basis Order *p*	**Nyström DoF**	**Interpolatory Divergence Conforming DoF**
0	3	4 (4,0)
1	12	15 (12, 3)
2	30	36 (24, 12)

For higher-order LCN representations, a variety of quadrature rules with differing numbers of points and properties exist thus complicating the discussion. For Nyström discretizations with $p > 0$, it is desirable to choose a quadrature rule of degree q = $2p$, but, for $p > 1$, rules of degree $q = 2p$ usually lead to non-square local correction matrices. Non-square local correction matrices may compromise the stability of the solution, so choosing quadrature rules of degree $q \geq (p+1)$ such that the number of points equals the number $\sum_{k=1}^{p+1} p\left(p+1\right)\left(p+2\right)/6$ of Nyström bases for each vector component at order p is recommended. The quadrature rules need not be symmetric even though symmetric rules are preferred when available.

The magnetization spike phenomenon is not observed for hexahedral meshes. For example, for the p = 0 Nyström representation on hexahedral cells, a mixed-order representation [10] has six degrees-of-freedom which are sufficient to match continuity of the normal magnetization at each of the six faces of the cell. If the Nyström degrees-of-freedom are cast onto a set of bases within the cell, the basis representation is

$$M^0_x = \frac{1}{\sqrt{g_x}}\sum_{i=1}^{3}\left(\alpha^0_{ix,0}+\alpha^0_{ix,1}u^{ix}\right)u_{ix}, \tag{15}$$

Along each unitary direction there are two degrees-of-freedom allowing for a constant plus linear representation of the magnetization so that the magnetization at one face can vary sufficiently to its opposite face (unlike the p = 0 tetrahedral representation). Furthermore, the hexahedral Nyström degrees-of-freedom span the same space that a typical divergence-conforming Moment Method basis set spans. A polynomial-complete representation on hexahedral cells, however, does not span the proper divergence-conforming space and may suffer from other spurious effects [10].

III. LCN-TO-MOM FORMULATION

Nyström methods are desirable since the system matrix fill avoids the costly double integrations that arise in

Method of Moment (MoM) discretizations. An LCN-to-MoM conversion [7, 8] allows an LCN system to be easily converted to a MoM system without sacrificing too many of the LCN method's advantages. Further, for the magnetostatic VIE formulation presented, it is not necessary to strictly enforce the continuity of MoM bases across tetrahedral cell faces. Hence, independent half-MoM bases can be assigned to each face in each tetrahedral cell, which further simplifies the LCN-to-MoM conversion. For the magnetostatic formulation, independent half-MoM bases must be assigned to shared faces between two cells that have different susceptibilities.

In the LCN-to-MoM conversion on tetrahedral cells, an order p MoM representation requires the LCN system to be filled at order (p+1) to accommodate the polynomial space requirements of divergence-conforming bases [9]. In view of Table 1, the (p+1) Nyström representation has too many degrees-of-freedom for the analogous divergence-conforming representation. Hence, the LCN-to-MoM conversion matrices can be viewed as the appropriate constraints to remove the extraneous degrees-of-freedom in a Nyström representation and achieve a divergence-conforming representation.

IV. DISCUSSION

First, a convergence analysis was performed for a locally-corrected Nyström (LCN) discretization of (1) for a magnetic spherical shell. The inner radius is 0.9 m, the outer radius 1.0 m, and the relative permeability is 50. The shell was meshed with a sequence of three tetrahedral meshes with 1514, 3320, and 6426 cells, respectively for mesh orders $o = 1$ (linear) and $o = 2$ (quadratic). The convergence analysis was performed for LCN basis orders $p = 0$, 1, and 2. The magnetic field was computed at various points outside the shell, and the average relative error was calculated using the analytic solution [4] as a reference. The results of the convergence analysis are plotted in Fig. 2. Also plotted are the relative

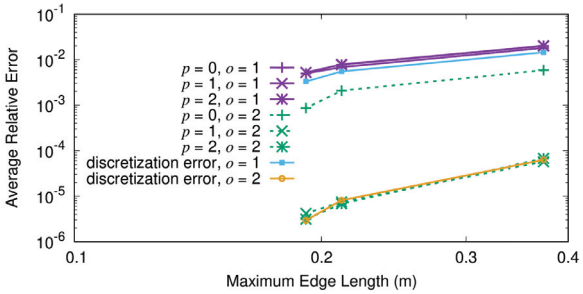

Fig. 2. Average relative field error in Nyström solution of (1) for a magnetic spherical shell vs. maximum mesh edge length for various basis orders p and mesh orders o. The relative mesh discretization error for the spherical shell surface area is also plotted.

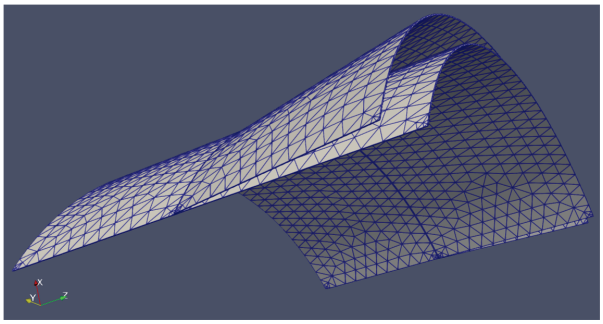

Fig. 3. Subsection of circular-cylindrical shell with extending circular frustrum shell overlaid with tetrahedral mesh.

mesh discretization error of the total surface area of the shell. The average relative error is observed to be limited by the mesh discretization error. However, the convergence rate increases with basis order until limited by the mesh discretization error. Hence, when the geometry is fairly smooth and uncomplicated, the LCN method usually produces good results.

As a second example, a subsection of a circular-cylindrical shell with a hollow circular-cylindrical frustrum extending outward, depicted in Fig. 3, was analyzed. The cylinder has a height of 6 m, an outer radius of 5 m, a wall thickness of 2 cm and is aligned on the z axis and centered at the origin. The frustrum has a height of 3 m, a wall thickness of 2 cm, and extends out from the cylinder to a final outer radius of 5.5 m. Only the subsection of the structure for $x > 3$ m is retained. The circular-cylindrical shell has a relative permeability of 150, and the frustrum extension has a relative permeability of 100. The excitation $H^{\text{excitation}} = -\hat{z}$ A/m, and the geometry was meshed with a 28728 cell, linear tetrahedral mesh.

The LCN simulation was performed at $p = 0$, and the LCN-to-MoM conversion used the Schaubert-Wilton-Glisson (SWG) bases [6] with four degrees-of-freedom per tetrahedral cell. Independent half-MoM bases were applied to each shared face. Plots of the magnetization for the LCN solution and LCN-to-MoM solution are provided in Fig. 4 (a) and Fig. 4 (b), respectively. In Fig. 4 (c) is shown the magnetization for a $p = 0$ LCN solution using a hexahedral mesh. The LCN-to-MoM solution and hexahedral LCN solutions are observed to be regular while the tetrahedral LCN solution exhibits anomalous spikes in magnetization across the mesh. The maximum magnetization magnitude for the tetrahedral LCN-MoM solution is approximately 156 A/m while the tetrahedral LCN solution spikes to almost 1275 A/m. Furthermore, some of the spikes in LCN magnetization occur at smooth parts of the mesh and not near edges or other complex features.

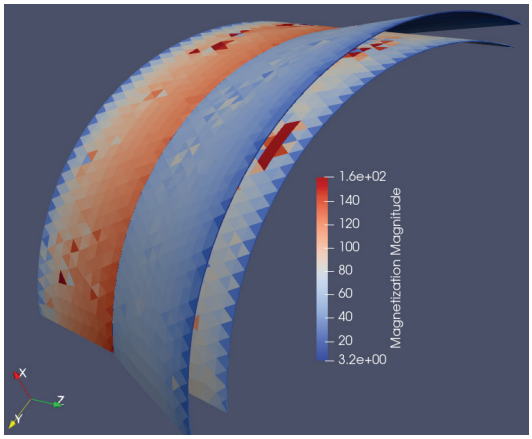

(a)

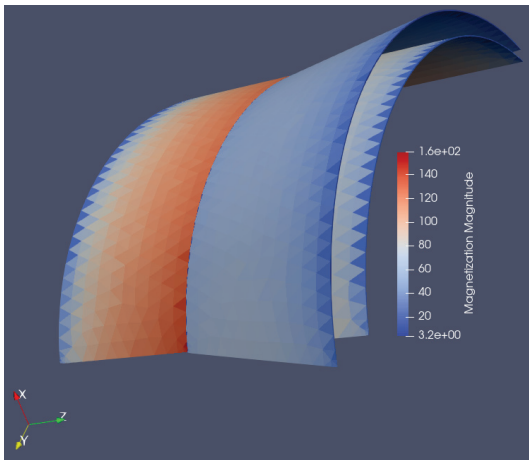

(b)

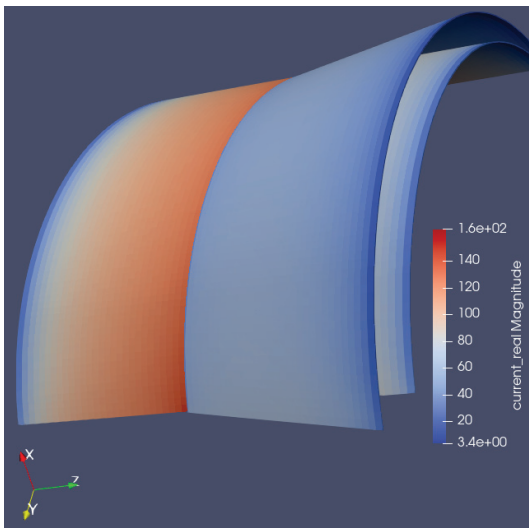

(c)

Fig. 4. Magnitude of magnetization in circular-cylindrical shell section with circular-cylindrical frustrum shell extension for (a) tetrahedral LCN simulation (b) tetrahedral LCN-to-MoM simulation, and (c) hexahedral LCN simulation.

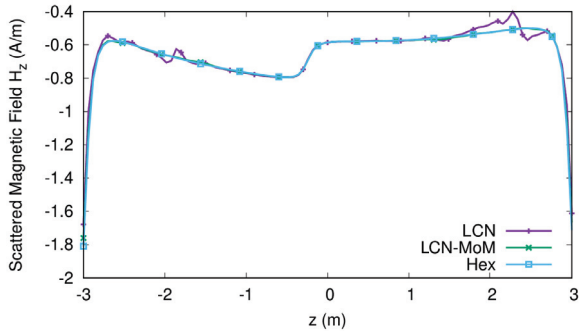

Fig. 5. Scattered magnetic field H_z along a line centered at x = 4.9 m, y = 0 m for the cylindrical shell section with frustrum extension example. Included are the fields due to the tetrahedral LCN solution, the tetrahedral LCN-MoM solution, and the hexahedral LCN solution.

In Fig. 5 is plotted the z-component of the scattered magnetic field vs z along a line centered at $(x, y) = (4.9, 0)$ m for the tetrahedral LCN, tetrahedral LCN-to-MoM, and hexahedral LCN solutions. The line passes close to some of the magnetization spikes observed in Fig. 4 (a) for the tetrahedral LCN solution. While the scattered field of the LCN-to-MoM and hexahedral LCN are visually identical, the field of the tetrahedral LCN solution is seen to be corrupted by the spurious magnetization.

V. CONCLUSION

The locally-corrected Nyström (LCN) method was observed to potentially produce anomalous spikes in magnetization when used to solve magnetostatic volume integral equations with tetrahedral mesh cells to model geometry. The failure of the LCN method for tetrahedra was discussed in terms of the inability of the Nyström representation to appropriately model a typical divergence-conforming space. Further, it was also observed that the p = 0 LCN discretization for tetrahedra does not allow continuity of normal magnetization between mesh cells to be appropriately modeled. For $p >$ 0, the LCN basis does allow continuity, but fails to represent the charge to order p, and does not fully represent the divergence-conforming basis to order p.

An LCN-to-MoM discretization, however, does appropriately model a mixed-order divergence-conforming space since the MoM bases are constructed to be divergence-conforming. Further, proper continuity of the normal magnetization across cell boundaries is modeled at all orders even though it is not required to explicitly enforce the MoM bases to be continuous across cell boundaries. Hence, many of the advantages of an LCN method are maintained in an LCN-to-MoM discretization.

Convergence results for a spherical magnetic shell were presented that showed the LCN method usually performs well for simple structures. Higher-order convergence was achieved until stagnated by mesh discretization error. However, for a more complicated model, the LCN method produced anomalous spikes while the LCN-to-MoM did not.

In conclusion, it is remarkable that the typical LCN representations used with tetrahedral meshes perform as well as they do as the representation do not span the appropriate space. Still, over a wide range of problems, no issues are observed, and good convergence characteristics are achieved. It is extremely difficult to predict a priori for a specific geometry whether the LCN method will produce spurious results. For large complex geometries with millions of cells, the probability of anomalous spikes occurring greatly increases. Although mesh quality can affect both the LCN and LCN-to-MoM solution, mesh quality seems to be more important to obtain robust LCN results when using tetrahedral cells. Refining the mesh may help suppress the spikes in some cases, but the increase in system size, as well as not knowing a priori whether the refinement is sufficient, is prohibitive for very large problems. Further, while the spikes seem to be local in nature and do not seem to corrupt the whole solution, fields in the vicinity of the spikes may have significant errors. Hence, the use of the LCN-to-MoM is advisable when working with tetrahedral meshes.

ACKNOWLEDGMENT

This work was supported in part by Office of Naval Research Grants N00014-16-1-3066 and N00014-23-1-2138.

REFERENCES

[1] L. F. Canino, J. J. Ottusch, M. A. Stalzer, J. L. Visher, and S. M. Wandzura, "Numerical solution of the Helmholtz equation in 2D and 3D using a high-order Nyström discretization," (in English), *Journal of Computational Physics,* vol. 146, no. 2, pp. 627-663, Nov. 1, 1998.

[2] S. D. Gedney and J. C. Young, "The locally corrected Nyström method for electromagnetics," in *Computational Electromagnetics: Recent Advances and Engineering Applications*, R. Mittra, Ed. New York: Springer, 2014, pp. 149-198.

[3] M. S. Tong, Z.-G. Qian, and W. C. Chew, "Nyström method solution of volume integral equations for electromagnetic scattering by 3D penetrable objects," *IEEE Transactions on Antennas and Propagation*, vol. 58, no. 5, pp. 1645-1652, May 2010.

[4] J. C. Young and S. D. Gedney, "A Locally Corrected Nyström formulation for the magnetostatic volume integral equation," *IEEE Transactions on Magnetics,* vol. 47, no. 9, pp. 2163-2170, Sep. 2011.

[5] J. C. Young, R. J. Adams, and S. D. Gedney, "Anomalous current spikes in the kocally corrected Nyström discretization of volume integral equations," *2023 International Applied Computational Electromagnetics Society Symposium*, Denver, CO, March 26-March 30, 2023.

[6] D. Schaubert, D. Wilton, and A. Glisson, "A tetrahedral modeling method for electromagnetic scattering by arbitrarily shaped inhomogeneous dielectric bodies," *IEEE Transactions on Antennas and Propagation,* vol. 32, no. 1, pp. 77-85, 1984.

[7] R. A. Pfeiffer, J. C. Young, R. J. Adams, and S. D. Gedney, "Locally corrected Nyström to moment method conversion for volume integral equations," *IEEE Transactions on Magnetics,* vol. 55, no. 4, pp. 1-7, 2019.

[8] M. Shafieipour, I. Jeffrey, J. Aronsson, and V. I. Okhmatovski, "On the equivalence of RWG method of moments and the locally corrected Nyström method for solving the electric field integral equation," *IEEE Transactions on Antennas and Propagation,* vol. 62, no. 2, pp. 772-782, Feb. 2014.

[9] R. D. Graglia and A. F. Peterson, *Higher-Order Techniques in Computational Electromagnetics*, Sci-Tech Publishing, 2016.

[10] S. D. Gedney, A. Zhu, and C.-C. Lu, "Study of mixed-order basis functions for the locally corrected Nyström method," *IEEE Transactions on Antennas and Propagation*, vol. 52, no. 11, pp. 2996-3004, Nov. 2004.

John C. Young received the B.E.E. degree in electrical engineering from Auburn University in 1997, the M.S. degree in electrical engineering from Clemson University in 2000, and the Ph.D. degree in electrical engineering also from Clemson University in 2002.

From January 2003 to April 2003, he served as a post-doctoral researcher at Clemson University, and from 2003 to 2005, he served as a post-doctoral researcher at Tokyo Institute of Technology, Tokyo, Japan. From 2005 to 2008, he worked at Japan Radio Co. Since 2008, he has been with the Department of Electrical and Computer Engineering at the University of Kentucky, Lexington, KY where he is currently an associate professor.

Dr. Young's research interests include integral equation methods, finite element methods, electromagnetic theory, waveguides, array antennas, and magnetic signature modeling of hysteretic materials. He is a member

of IEEE, the Applied Electromagnetics Society (ACES), and URSI Commission B. He currently serves as an Associate Editor for the IEEE Transactions on Antennas and Propagation and on the Education Committee of the Antennas and Propagation Society. He also served (2020-2023) on the Board of Directors of ACES where he is currently Secretary.

Robert J. Adams received the B.S. degree from Michigan Technological University, Houghton, MI, USA, in 1993, and the M.S. and Ph.D. degrees in electrical engineering from Virginia Polytechnic Institute and State University (Virginia Tech), Blacksburg, VA, USA, in 1995 and 1998, respectively.

From 1999 to 2000, he was a Research Assistant Professor with Virginia Tech. Dr. Adams joined the University of Kentucky in 2001, where he is currently a Professor with the Department of Electrical and Computer Engineering.

He has made novel contributions to mesh and frequency stable integral equation formulations of electromagnetic problems, constraint-based methods for high-order MOM discretizations, spectral splitting methods for implementing shadowing effects in integral equations at high frequencies, and sparse direct solution methods for low-to-moderate frequency electromagnetics applications. Dr. Adams is a senior member of the IEEE.

Stephen D. Gedney received the B.Eng.-Honors degree from McGill University, Montreal, P.Q., in 1985, and the M.S. and Ph.D. degrees in Electrical Engineering from the University of Illinois, Urbana-Champaign, IL, in 1987 and 1991, respectively.

He is currently the Don and Karen White Professor of the Department of Electrical Engineering at the University of Colorado Denver (CUD). Previously he was a Professor of Electrical Engineering at the University of Kentucky from 1991 – 2014. He worked for the U.S. Army Corps of Engineers, Champaign, IL ('85-'87). He was a visiting Professor at the Jet Propulsion Laboratory, (92', 93'), HRL laboratories ('96-'97) and Alpha Omega Electromagnetics ('04-'05). He received the Tau Beta Pi Outstanding Teacher Award in 1995 and 2013. From 2002 – 2014, he was the Reese Terry Professor of Electrical and Computer Engineering at the University of Kentucky. He was titled as a Distinguished Professor of the University of Colorado in 2022. He is a past Associate Editor of the IEEE Transactions on Antennas and Propagation (1997 – 2004), a member of the IEEE Antennas and Propagation Society ADCOM (2000 – 2003), and served as the chair of the IEEE Antennas and Propagation Society Membership Committee (1995 – 2002). He is a Fellow of the IEEE and member of Tau Beta Pi.